ENP Engineering Science Journal

SSN: 2716-912X
E-ISSN: 2773-4293
https://doi.org/10.53907

Edited by Ecole Nationale Polytechnique, 10 Avenue des Frères Oudek, El-Harrach, 16200, Algiers, Algeria.

SCOPE

Ecole Nationale Polytechnique (ENP) is an academic and research institution where thousands of Engineers and PhDs have been educated during the last 6 decades. Its alumna and alumnus have had a positive impact on industry and science all over the world. ENP aims to disseminate high-quality academic work to contribute to technology and science advances for humanity.

The ENP Engineering Science journal (ENPESJ) is a peer-reviewed open-access journal. It publishes reviews and full original research papers covering all aspects of recent advances in engineering dealing with:

- Electrical and Computer Engineering
- Industrial Engineering
- Mechanical and Materials Engineering
- Civil and Hydraulic Engineering
- Chemical and Environmental Engineering

The journal would focus also on technology with industry applications, it plans to publish special issues on up-to-date emerging technologies and new research directions. ENPESJ promotes Open Science through truly free open access peer-reviewed journal articles.

ENPESJ (New ISSN 2716-912X) (formerly named *AJOT (Algerian Journal of Technology)*, Old ISSN 1111-357X) is administrated and sponsored by Ecole Nationale Polyetchnique. The ENP Engineering Science Journal is published online with a frequency of two issues per year: http://enpesj.enp.edu.dz

Vol. 1 No. 2 (2021): ENP Engineering Science Journal
https://doi.org/10.53907/enpesj.v1i12

CONTENTS

Magnetic Field Calculation for Flat Permanent-Magnet Linear Machines Using a Hybrid Analytical Model

Brahim Ladghem-Chikouche, Kamel Boughrara, Frédéric Dubas, Lazhar Roubache, and Rachid Ibtiouen

Abstract−This paper proposes an improved two-dimensional (2-D) hybrid analytical method (HAM) in Cartesian coordinates, based on the exact subdomain (SD) technique and the finite-difference method (FDM). It is applied to flat permanent-magnet (PM) linear machines with dual-rotor. The magnetic field solution is obtained by coupling an exact SD model, calculated in all regions having relative permeability equal to unity, with FDM in ferromagnetic regions. The analytical model and FDM are connected in both axes (x, y) of the (non-)periodicity direction (i.e., in the interface between the tooth regions and all its adjacent regions as slots and/or air-gap). To provide accuracy solutions, the current density distribution in slot regions is modeled by using Maxwell's equations. It is found that, whatever the iron core magnetic parameters, the developed HAM gives accurate results for no- and on-load conditions. Finite-element analysis (FEA) demonstrates excellent results of the developed technique.

***Keywords*− Hybrid magnetic model, exact subdomain technique, finite difference method, finite-element analysis.**

I. Introduction

Flat PM linear machines with dual-rotor present many important industrial applications due to their multiple advantages compared to conventional machines, namely: compactness, high-torque density, precise control, and dynamic performance.

Recently, several design models have been proposed and developed for these machines in view to introduce the nonlinearity of the *B(H)* curve into the analytical solution, such as the analytical approach (e.g., based on the exact SD technique) or/and the HAM. The latter has become important and is preferred for different reasons, such as the accuracy, the saturation effect, and the computation time.

One of the critical deficiencies of the different published methods and techniques concerns the magnetic characteristic of ferromagnetic core, when the authors, to facilitate their calculations, suppose that the iron core relative permeability is equal to infinity. This problem has been solved by different technique such as the HAM which has been proposed by different techniques:

i. In [1]-[2], a coupling between the Maxwell-Fourier methods and FEA is achieved via the boundary integral term in the air-gap region. The proposed method eliminates the need for finite-elements in the air-gap. In [2], the saturation effect is considered.
ii. In [3]-[12], a coupling between the Maxwell-Fourier methods and the magnetic equivalent circuit (MEC) are presented for no- and on-load conditions. In [3], the magnetic potential drop can be replaced by equivalent current sheets in the slots in order to represent the nonlinearity magnetostatic effect for loaded conditions. The hybrid method is used for the analysis of axial or radial flux rotating or tubular linear machines. Some of them can consider the saturation effect on the exact SD technique. The armature winding currents is represented by equivalent magneto-motive force (MMF).
iii. Improved conformal mapping coupled with MEC is presented in [13]-[16]. This technique has been validated for any complex stator. It is suitable for machines with small number of slots per pole and phase.
iv. In [17]-[18], a direct coupling between FEA and MEC is proposed. However, in [18], the proposed MEC is used to predict the no-load characteristics firstly and then the proposed 2-D equivalent FEA is used to predict the load characteristics at the preliminary design stage.
v. In [19]-[22], a coupling between FDM and FEA is developed.
vi. The electromagnetic performances are calculated by means of a 2-D HAM combining the SD technique and FDM [23]-[24].

This paper deals with new HAM based on the Maxwell-Fourier methods, based on the exact SD technique, and FDM. It covers comprehensively any modeling related to a complex electromagnetic device. In this paper, the HAM is applied to flat PM linear machines with dual-rotor. The main contribution is to establish a direct coupling between the SD technique and numerical method based on the finite-difference in the interface separating the iron core and the vacuum. In order to accurately predict the electromagnetic performances, a direct coupling is assumed in both directions

Manuscript received May 5, 2021; revised July 26, 2021.
Brahim Ladghem-Chikouche is with the Department of Electrical Engineering, Faculty of Technology, University of M'sila, Algeria and with Laboratoire de Recherche en Electrotechnique (LRE-ENP), Ecole Nationale Polytechnique, Algeria (e-mail: brahim.lch@univ-msila.dz).
Kamel Boughrara, and Rachid Ibtiouen are with LRE-ENP, Ecole Nationale Polytechnique, (e-mail: kamel.boughrara@g.enp.edu.dz, rachid.ibtiouen@gmail.com).
Frédéric Dubas is with Département ENERGIE, FEMTO-ST, CNRS, Univ. Bourgogne Franche-Comté, F90000 Belfort, France (e-mail: fdubas@gmail.com).
Lazhar Roubache is with the Department of Electrical Engineering, Faculty of Technology, University of M'sila, Algeria (e-mail: roubache.lazhar@gmail.com).

Digital Object Identifier (DOI): 10.53907/enpesj.v1i2.36

(x- and y-edges) considering the finite permeability of the ferromagnetic core.

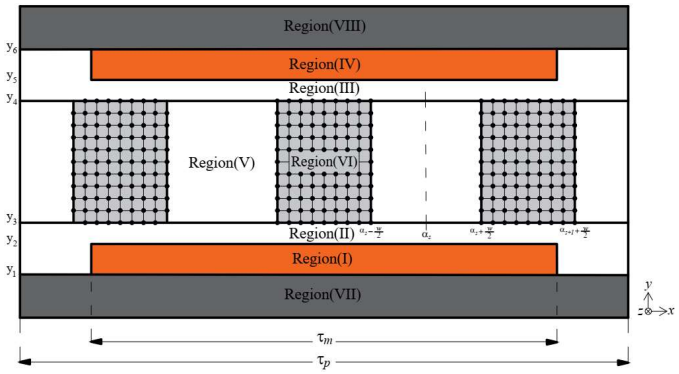

Fig. 1: Proposed flat linear PM synchronous machine with dual-rotor having a radial magnetization and a single-layer concentrated winding.

TABLE .I
MACHINE CHARACTERISTICS

Symbol	Parameter (unit)	Value
B_{rm}	Remanent of flux density of PMs (T)	1.25
-	Magnetization type	Radial
Q	Number of stator slots per pole	3
y_1	Inner magnet height (mm)	7
y_2	Outer magnet height (mm)	12
y_3	Inner slot height (mm)	12.5
y_4	Outer slot height (mm)	27.5
y_5	Outer magnet height (mm)	28
y_6	Inner magnet height (mm)	33
y_7	Outer yoke height (mm)	40
β	PM pole-width to pole-pitch ratio	100%
w	Slot opening width (mm)	12
τ_p	Pole pitch (mm)	60
J_m	Armature current density (A/m^2)	$15{\cdot}10^6$
L	Axial length (mm)	50
nh	Harmonics number	140

To evaluate the efficacy of the proposed HAM, the magnetic flux density distribution in the whole electromagnetic device was compared with those obtained by the 2-D FEA [25]. FEA demonstrates highly accurate results of the developed technique. The 2-D HAM is ≈ 2 times faster than 2-D FEA with high accuracy.

II. PROBLEM DESCRIPTION AND ASSUMPTIONS

The proposed flat PM linear synchronous machine with rotor-dual is depicted in Fig. 1. The main geometrical and physical parameters are listed in Table I. This machine is composed of:

- PMs: Region I and IV;
- Vacuum: Region II and III;
- Q slots with coils: Region V;
- Q teeth: Region VI;
- Iron yokes: Region VII and VIII.

The rotor topology is constituted of multi-poles PMs mounted on the rotor surface with a radial magnetization. The moving PMs can have a more diversity of magnetization. The stator slots topology is proposed with a radial-sided surface. The spatial distribution of *3*-phases winding is configurated in a standard manner with a single-layer in the slot (i.e., non-overlapping or concentrated winding).

In the 2-D cartesian coordinate system, some assumptions are made in this paper to limit the mathematical efforts, as in [26]-[27].

III. FORMULATION OF HAM

A. Introduction

In this paper, a 2-D HAM based on the SD technique and FDM is presented. Each SD of the proposed machine is modeled under fixed absolute permeability $\mu = C^{st}$. The SDs are expressed by a partial differential equation (PDE) in terms of $\boldsymbol{A}$ [27].

$$\nabla^2 \boldsymbol{A} = -[\mu\, \boldsymbol{J} + \mu_0\, \nabla \times \boldsymbol{Mr}] \tag{1}$$

where J is the current density (due to supply currents) vector, $\boldsymbol{Mr}$ is the remanent magnetization vector (with $\boldsymbol{Mr} = 0$ for the vacuum/iron or $\boldsymbol{Mr} \neq 0$ for the PMs according to the magnetization direction), and $\mu = \mu_0 \mu_r$ is the absolute magnetic permeability of the magnetic material in which μ_0 and μ_r are respectively the vacuum permeability and the relative permeability of the magnetic material (with $\mu_r = 1$ for the vacuum or $\mu_r \neq 1$ for the PMs/iron).

B. 2-D Exact SD Technique

From Equation (1), the general PDEs in terms of $\boldsymbol{A}$ in the Region I to V can be written as:

$$\nabla^2 \boldsymbol{A} = -\mu_o\, \nabla \times \boldsymbol{Mr} \quad \text{in Region I and IV} \tag{2a}$$

$$\nabla^2 \boldsymbol{A} = 0 \quad \text{in Region II and III} \tag{2b}$$

$$\nabla^2 \boldsymbol{A} = -\mu_0\, \boldsymbol{J} \quad \text{in Region V} \tag{2c}$$

The remanent magnetization vector of PMs can be expressed by

$$\boldsymbol{Mr} = Mr_x\, \boldsymbol{u_x} + Mr_y\, \boldsymbol{u_y} \tag{3}$$

where Mr_x and Mr_y are respectively the x- and y-component of $\boldsymbol{Mr}$.

The field vectors $\boldsymbol{B} = \{B_x; B_y; 0\}$ and $\boldsymbol{H} = \{H_x; H_y; 0\}$ are coupled by the magnetic material equation

$$\boldsymbol{B} = \mu_m\, \boldsymbol{H} + \mu_o\, \boldsymbol{Mr} \quad \text{in Region I and IV} \tag{4}$$

$$\boldsymbol{B} = \mu_0\, \boldsymbol{H} \quad \text{in other regions} \tag{5}$$

Using $\boldsymbol{B} = \nabla \times \boldsymbol{A}$, the components of $\boldsymbol{B}$ can be deduced by

$$B_x = \frac{\partial A_z}{\partial y} \quad \& \quad B_y = -\frac{\partial A_z}{\partial x} \tag{6}$$

In Cartesian coordinates (x, y), Equation (2) in terms of $\boldsymbol{A} = \{0; 0; A_z\}$ can be rewritten as

- in Region I and IV (i.e., Poisson's equation):

$$\frac{\partial^2 A_z^{I,IV}}{\partial x^2} + \frac{\partial^2 A_z^{I,IV}}{\partial y^2} = -\mu_o \cdot \left(\frac{\partial Mr_y}{\partial x} - \frac{\partial Mr_x}{\partial y}\right) \tag{7}$$

- in Region II and III (i.e., Laplace's equation):

$$\frac{\partial^2 A_z^{II,III}}{\partial x^2} + \frac{\partial^2 A_z^{II,III}}{\partial y^2} = 0 \tag{8}$$

- in Region V (i.e., Poisson's equation):

$$\frac{\partial^2 A_z^{V}}{\partial x^2} + \frac{\partial^2 A_z^{V}}{\partial y^2} = -\mu_0 \cdot J_z \tag{9}$$

In order to obtain the solution of Laplace's and Poisson

equations in different regions, the PDEs (7) ~ (9) can be solved by using the separation of variables method and the Dubas' superposition technique [27]. All regions of the proposed machine are described by Fourier series expression in both directions (i.e., x- and y-edges). Hence, the general solution of A_z, in SDs is the superposition of two components in x- and y-directions [26]-[27]:

- in Region I and IV:

$$A_z^{I,IV} = \sum_n \begin{pmatrix} C_{3n}^{I,IV} \cdot e^{K_n y} + \\ C_{4n}^{I,IV} \cdot e^{-K_n y} + \Gamma_s \end{pmatrix} \cdot \sin(K_n x) + \sum_n \begin{pmatrix} C_{5n}^{I,IV} \cdot e^{K_n y} + \\ C_{6n}^{I,IV} \cdot e^{-K_n y} + \Gamma_c \end{pmatrix} \cdot \cos(K_n x) \quad (10a)$$

where

$$K_n = \frac{\pi n}{\tau_p}, \quad \Gamma_s = -\mu_o \cdot \frac{M r_{ycn}}{K_n}, \quad \Gamma_c = \mu_o \cdot \frac{M r_{ysn}}{K_n} \quad (10b)$$

τ_p is the pole pitch.

- in Region II and III:

$$A_z^{II,III} = \sum_n \begin{pmatrix} C_{3n}^{II,III} \cdot e^{K_n y} + \\ C_{4n}^{II,III} \cdot e^{-K_n y} \end{pmatrix} \cdot \sin(K_n x) + \sum_n \begin{pmatrix} C_{5n}^{II,III} \cdot e^{K_n y} + \\ C_{6n}^{II,III} \cdot e^{-K_n y} \end{pmatrix} \cdot \cos(K_n x) \quad (11)$$

- in Region V:

$$A_{zs}^V = C_{s1}^V + C_{s2}^V \cdot y - \frac{1}{2} \cdot \mu_o \cdot J_{zs} \cdot y^2 + \sum_m G_{sm}^{Vx} \cdot \cos\left[\beta_m^V \cdot \left(x - \alpha_s + \frac{w}{2}\right)\right] + \sum_v G_{sv}^{Vy} \cdot \sin[\lambda_v^V \cdot (y - y_3)] \quad (12a)$$

$$G_{sm}^{Vx} = C_{s3m}^V \cdot e^{\beta_m^V y} + C_{s4m}^V \cdot e^{-\beta_m^V y} \quad (12b)$$

$$G_{sv}^{Vy} = \begin{matrix} C_{s5v}^V \cdot \sinh\left[\lambda_v^V \cdot \left(x - \alpha_s + \frac{w}{2}\right)\right] + \\ C_{s6v}^V \cdot \sinh\left[\lambda_v^V \cdot \left(x - \alpha_s - \frac{w}{2}\right)\right] \end{matrix} \quad (12c)$$

with

$$J_{zs} = J_m \cdot [1 \ 1 \ 0 \ -1 \ -1 \ 0 \ 1 \ 1 \ 0 \ -1 \ -1 \ 0] \quad (13)$$

where J_m is the current density peak, w is the slot-opening, α_s is the position of s[th] slot, m and v are the spatial harmonic orders, β_m^V and λ_v^V are the spatial frequency (or periodicity) in both directions defined by:

$$\beta_m^V = \frac{m\pi}{w} \quad \& \quad \lambda_v^V = \frac{v\pi}{y_4 - y_3} \quad (14)$$

C. 2-D FDM

In Region VI, the solution of magnetic vector potential distribution can be achieved from numerical Maxwell's equations. According to Fig. 2, the grill nodes located in the ferromagnetic region is obtained with a uniform mesh. The magnetic flux can be written as:

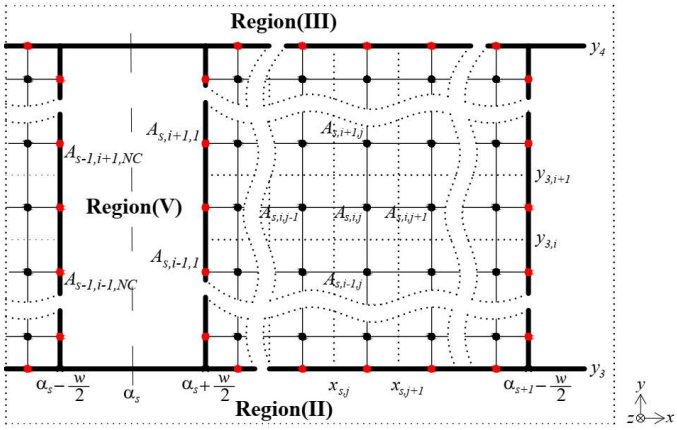

Fig. 2: Uniform mesh of the Region VI discretized into several nodes

$$\frac{\Delta^2 A_z^{VI}}{\Delta x^2} + \frac{\Delta^2 A_z^{VI}}{\Delta y^2} = 0 \quad (15)$$

Equation (6) should be rewritten using numerical differentiation defined as the limit of a difference quotient as:

$$B_x(x) = \lim_{\Delta y \to 0} \left(\frac{\Delta A}{\Delta y}\right) \quad \& \quad B_y(y) = \lim_{\Delta x \to 0} \left(-\frac{\Delta A}{\Delta x}\right) \quad (16)$$

The difference quotient $B_x(x)$ and $B_y(y)$ is a derivative approximation. This improves as Δx and Δy become smaller. Δx and Δy are the spacing between two adjacent nodes in the x- and y-direction, respectively

$$\Delta x = x_{s,j+1} - x_{s,j} \quad (17a)$$

$$\Delta y = y_{3,i+1} - y_{3,i} \quad (17b)$$

According to Equation (15) and Fig. 2, each term of the PDE at the particular node is replaced by a finite-difference approximation. The distribution of A_z in the Region VI can be rewritten as:

$$\frac{A_{zs,i,j+1}^{VI} - 2A_{zs,i,j}^{VI} + A_{zs,i,j-1}^{VI}}{\Delta x^2} + \frac{A_{zs,i+1,j}^{VI} - 2A_{zs,i,j}^{VI} + A_{zs,i-1,j}^{VI}}{\Delta y^2} = 0 \quad (18)$$

IV. Boundary and Interface Conditions

The special feature of this paper is to establish a direct coupling between the two models, especially between regions that do not have the same relative permeability, such as the Region VI and its adjacent regions (namely, II, III and V). For simplicity and to limit the mathematical efforts, the Region VII and VIII are not introduced in the system to be solved. The relative permeability of these regions is supposed to be equal to infinity. It is easy to add these regions in the HAM. For this case and,

- At $y = y_3$ and for the index $s = 1, \cdots, Q$:

$$A_{zs,1,j}^{VI} = \frac{1}{\Delta x} \int_{x_{s,j}}^{x_{s,j+1}} A_z^{II}(x,y)dx \quad (19)$$

$$\left(A_{zs}^V(x,y) = A_z^{II}(x,y)\right)\Big|^{\alpha_s - \frac{w}{2} \le x \le \alpha_s + \frac{w}{2}} \quad (20)$$

$$H_x^{II}(x,y) = \sum_s \begin{pmatrix} H_{xs}^V(x,y)\Big|^{\alpha_s - \frac{w}{2} \le x \le \alpha_s + \frac{w}{2}} \\ + H_{xs}^{VI}(x,y)\Big|^{\alpha_s + \frac{w}{2} \le x \le \alpha_{s+1} - \frac{w}{2}} \end{pmatrix} \quad (21)$$

In order to satisfy Equation (21), the magnetic flux intensity $H_{xs}^{VI}(x,y)$ by applying Equation (16) should be written as:

$$H_{xs}^{VI}(x,y) = \frac{1}{\mu_0\mu_r}\sum_{j=2}^{Nc-1}\left(\frac{A_{s,2,j}^{VI} - A_{s,1,j}^{VI}}{\Delta y}\right) f_v \quad (22a)$$

$$f_v = \sum_v [h_{xsv}^{VI}\sin(K_n x) + h_{xcv}^{VI}\cos(K_n x)] \quad (22b)$$

where h_{xsv}^{VI} & h_{xcv}^{VI} are the Fourier's constants, and Nc is the number of grid nodes in the x-direction.

- At $y = y_4$ and for the index $s = 1, \cdots, Q$:

$$A_{zs,NL,j}^{VI} = \frac{1}{\Delta x}\int_{x_{s,j}}^{x_{s,j+1}} A_z^{III}(x,y)dx \quad (23)$$

$$\left(A_{zs}^{V}(x,y) = A_z^{III}(x,y)\right)\Big|^{\alpha_s - \frac{w}{2} \le x \le \alpha_s + \frac{w}{2}} \quad (24)$$

$$H_x^{III}(x,y) = \sum_s \begin{pmatrix} H_{xs}^{V}(x,y)|^{\alpha_s - \frac{w}{2} \le x \le \alpha_s + \frac{w}{2}} \\ +H_{xs}^{VI}(x,y)|^{\alpha_s + \frac{w}{2} \le x \le \alpha_{s+1} - \frac{w}{2}} \end{pmatrix} \quad (25)$$

In order to satisfy Equation (25), the magnetic flux intensity $H_{xs}^{VI}(x,y)$ by applying Equation (16) should be written as:

$$H_{xs}^{VI}(x,y) = \frac{1}{\mu_0\mu_r}\sum_{j=2}^{Nc-1}\left(\frac{A_{s,Nl,j}^{VI} - A_{s,Nl-1,j}^{VI}}{\Delta y}\right) f_v \quad (26)$$

On the y-direction, viz., on the edges of the Region V and VI and for the index $s = 1, \cdots, Q$:

- for $x = \alpha_s + w/2$:

$$A_{zs,i,1}^{VI} = \frac{1}{\Delta y}\int_{y_{3,i}}^{y_{3,i+1}} A_{zs}^{V}(x,y)dy \quad (27)$$

$$H_{ys}^{VI}(x,y) = H_{ys}^{V}(x,y) \quad (28)$$

where

$$H_{ys}^{VI}(x,y) = \frac{1}{\mu_r\mu_0}\sum_{i=2}^{Nl-1}\sum_v\left(-\frac{A_{zs,i,2}^{VI} - A_{zs,i,1}^{VI}}{\Delta x}\right) \cdot h_{ysv}^{VI}\sin[\lambda\cdot(y - y_2)] \quad (29)$$

where Nl is the number of grid nodes in the y-direction and h_{ysv}^{VI} is the Fourier's constants.

For the index $s = 2, \cdots, Q$ and,

- for $x = \alpha_s - w/2$:

$$A_{zs,i,Nc}^{VI} = \frac{1}{\Delta y}\int_{y_{3,i}}^{y_{3,i+1}} A_{z(s-1)}^{V}(x,y)dy \quad (30)$$

$$H_{rs}^{VI}(x,y) = H_{r(s-1)}^{V}(x,y) \quad (31)$$

where

$$H_{ys}^{VI}(x,y) = \frac{1}{\mu_r\mu_0}\sum_{i=2}^{Nl-1}\sum_v\left(-\frac{A_{zs,i,Nc}^{VI} - A_{zs,i,Nc-1}^{VI}}{\Delta x}\right) \cdot h_{ysv}^{VI}\sin[\lambda\cdot(y - y_2)] \quad (32)$$

Anti-periodic BCs are applied and given as:

$$A_{zQs,i,Nc}^{VI} = -\frac{1}{\Delta y}\int_{y_{3,i}}^{y_{3,i+1}} A_{z1}^{V}(x,y)dy \quad (33)$$

$$H_{xQs}^{VI}(x,y) = -H_{x1}^{V}(x,y) \quad (34)$$

V. Comparison of HAM and Numerical Calculations

About the FEA, FEMM designer was used, and the analytical calculations were computed by MATLAB. The number of nodes and elements are 84,019 and 167,089, respectively. These results have been calculated under an acceptable amount of discretization of the Region VI (viz., $Nc = 25$ and $Nl = 15$).

Figs. 3 ~ 4 shown a comparison of the air-gap flux density distribution with a radial magnetization pattern and for the open-circuit calculated by HAM and FEA with different values of iron core relative permeability (viz., $\mu_r = 2$ and 1,000) under geometrical and physical parameters given in Table I.

Figs. 5 ~ 6 shown the air-gap magnetic flux density distribution for the armature reaction. The maximal current density is equal to J_m [see Table I].

Excellent agreement is achieved between HAM and FEM.

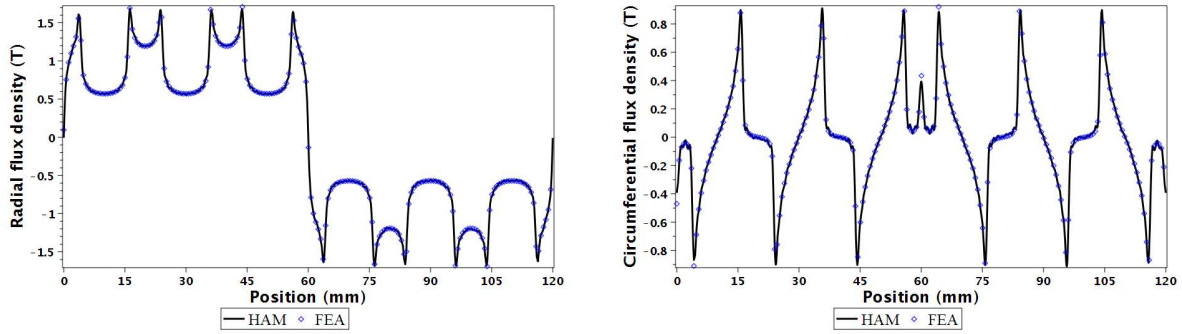

Fig. 3: Comparison of HAM and FEA predicted for the open-circuit magnetic flux density distribution with a radial magnetization pattern in the middle of the Region II for $\mu_r = 1{,}000$ in all ferromagnetic regions.

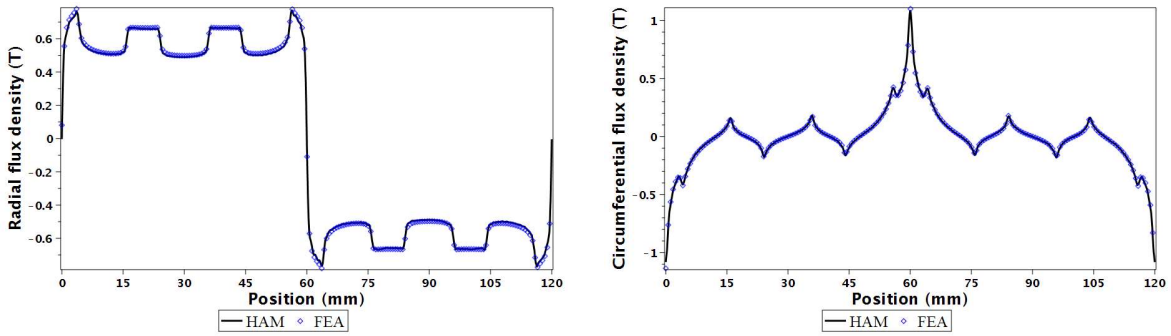

Fig. 4: Comparison of HAM and FEA predicted for the open-circuit magnetic flux density distribution with a radial magnetization pattern in the middle of the Region II for $\mu_r = 2$ in all ferromagnetic regions.

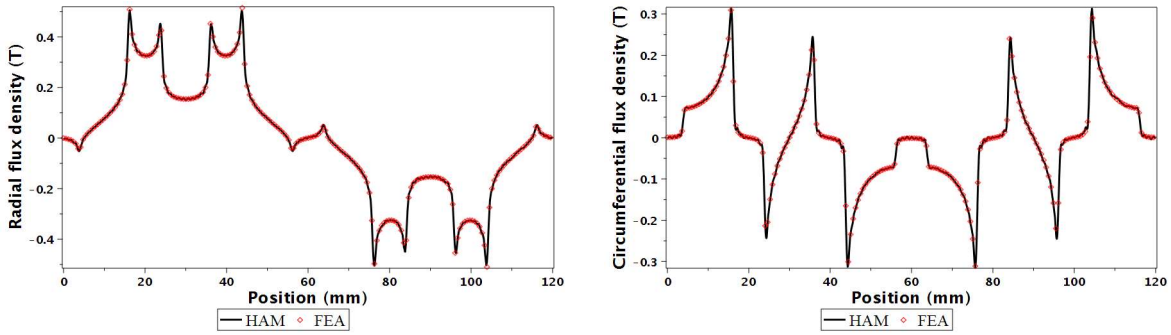

Fig. 5: Comparison of HAM and FEA predicted of the armature reaction magnetic flux density in the middle of the Region II for $\mu_r = 1{,}000$ in all ferromagnetic regions.

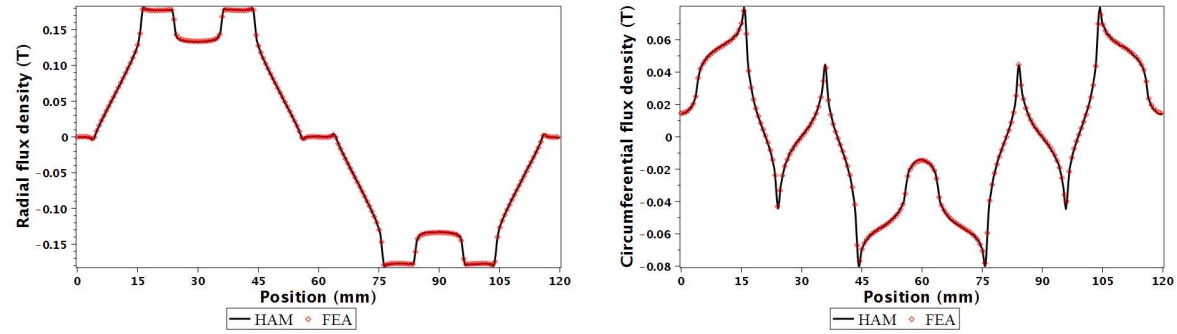

Fig. 6: Comparison of HAM and FEA predicted of the armature reaction magnetic flux density in the middle of the Region II for $\mu_r = 2$ in all ferromagnetic regions.

TABLE II.
2-D COMPUTATIONAL TIME FOR VARIOUS METHODS

Method	HAM	FEA
	$nh = 140$ $Nc = 25, Nl = 15$	Two poles 84,019 nodes
Time (sec)	~3	~7.5

Figs. 7 ~ 10 show the magnetic flux density distribution in all parts of an electrical machine calculated by HAM and compared to FEA with different values of iron core relative permeability (viz., $\mu_r = 2$ and 1,000) as well as the error level calculated by

$$\|\boldsymbol{B}_{error}\| = \frac{|\,\|\boldsymbol{B}_{\mathbf{FEA}}\| - \|\boldsymbol{B}_{\mathbf{HAM}}\|\,|}{\text{mean}(\|\boldsymbol{B}_{\mathbf{FEA}}\|)} \times 100\% \qquad (35)$$

Each SDs of the proposed machine is divided into 50 levels in the *y*-direction and each level is composed to 1,200 points in the *x*-direction. We can observe that the errors can be localized in the interface between two adjacent regions or in the edges of PMs and that because of the fluctuations due to limiting number of Fourier series harmonics.

Table II shown the computation time for the magnetic flux density calculation by HAM and FEA.

VI. CONCLUSION

This paper presents a new HAM based on an accurate SD model and FDM for the flat PM linear synchronous machine with rotor-dual having a radial magnetization and a single-layer concentrated winding. The proposed approach is modeled in 2-D Cartesian coordinates using Maxwell's equations. The coupling between the two models is performed especially in the interface when two adjacent regions have not the same magnetic parameters (e.g., in the interface between teeth regions and all its adjacent regions). It was performed in both directions (*x*- and *y*-edges) in order to gives accurate results, especially in case of saturation effect.

The HAM was used to predict the magnetic flux density components whatever the loading conditions (i.e., the open-circuit and the armature reaction) and the iron core relative permeability. The comparison with 2-D FEA demonstrates excellent results of the developed approach. The computational time is ≈ 2 times smaller than FEA.

The high impact contributions of this approach can now focus our attention on the optimization of the machine performances, in particular with the local saturation effect through elementary SD technique [28] by inserting the *B(H)* curve which will be proposed in a future contribution.

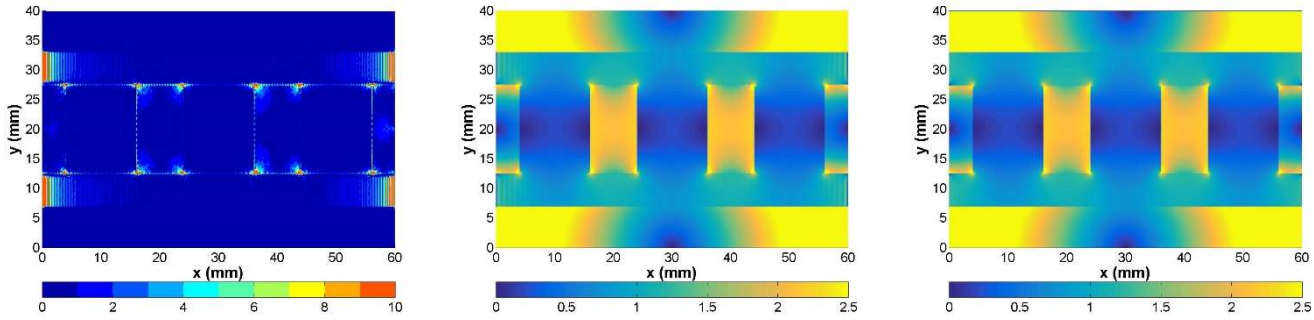

a) b) c)

Fig. 7: a) $\|\boldsymbol{B}_{error}\|(\%)$ distribution calculated by the difference between b) HAM and c) FEA under no-load condition for $\mu_r = 1{,}000$.

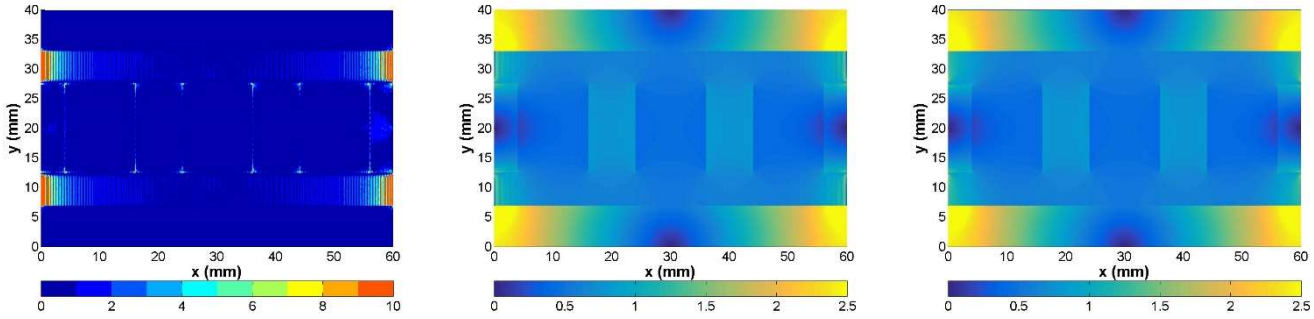

a) b) c)

Fig. 8: a) $\|\boldsymbol{B}_{error}\|(\%)$ distribution calculated by the difference between b) HAM and c) FEA under no-load condition for $\mu_r = 2$.

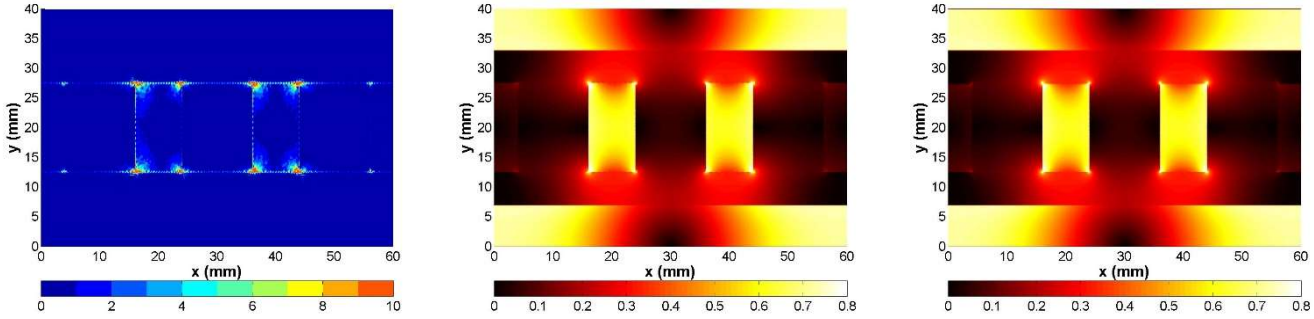

a) b) c)

Fig. 9: a) $\|\boldsymbol{B}_{error}\|(\%)$ distribution calculated by the difference between b) HAM and c) FEA under armature reaction condition for $\mu_r = 1{,}000$.

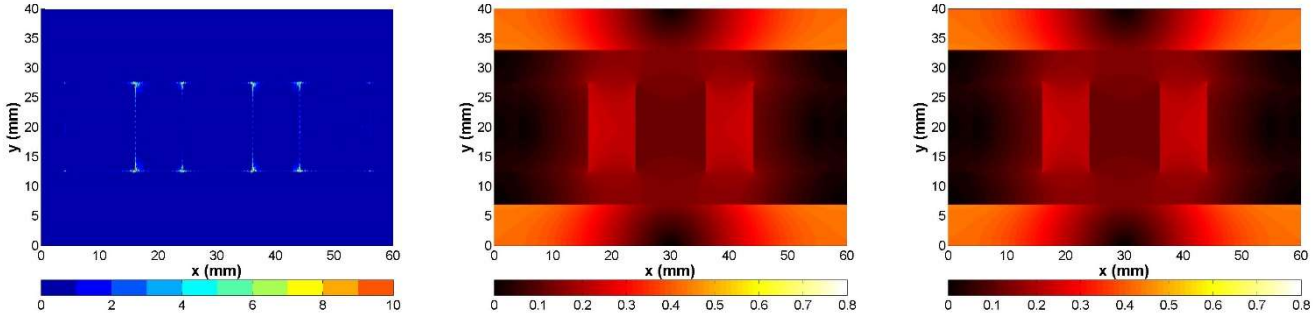

a) b) c)

Fig. 10: a) $\|\boldsymbol{B}_{error}\|(\%)$ distribution calculated by the difference between b) HAM and c) FEA under armature reaction condition for $\mu_r = 2$.

ACKNOWLEDGMENT

The authors acknowledge the financial support of the General Directorate of Scientific Research and Technological Development (DGRSDT) of Algeria.

REFERENCES

[1] K. Lee, M.J. DeBortoli, M.J. Lee, S.J. Salon, "Coupling Finite Elements and Analytical Solution in the Airgap of Electrical Machines," *IEEE Trans. Magn.*, vol. 27, no. 5, Sep. 1991, pp. 3955-3957, doi: 10.1109/20.104969.

[2] M. Shen, P-D. Pfister, C. Tang, and Y. Fang, "A hybrid model permanent-magnet machines combining Fourier analytical model with finite element method, taking magnetic saturation into account," *IEEE Trans. Magn*, vol. 57, no. 2, Feb. 2021, doi: 10.1109/TMAG.2020.3005802.

[3] L. Wu, H. Yin, D. Wang, and Y. Fang, "On-load field prediction in SPM machines by a subdomain and magnetic circuit hybrid model," *IEEE Trans Ind.* Elec., vol. 67, no. 9, pp. 7190-7201, Sep. 2020, doi: 10.1109/TIE.2019.2942561.

[4] H.S. Zhang, Z.X. Deng, M.L. Yang, Y. Zhang, J.Y. Tuo, and J. Xu, "Analytical prediction of Halbach array permanent magnet machines considering finite tooth permeability," *IEEE Trans. Magn.*, vol. 56, no. 6, June 2020, Art. no. 8101010, doi: 10.1109/TMAG.2020.2982844.

[5] S. Ouagued, Y. Amara, and G. Barakat, "Comparison of hybrid analytical modelling and reluctance network modelling for pre-design purposes," *Mathematics and Computers in Simulation*, vol. 130, pp. 3-21, Dec. 2016, doi: 10.1016/j.matcom.2016.05.001.
[6] S. Ouagued, Y. Amara, and G. Barakat, "Cogging force analysis of linear permanent magnet machines using a hybrid analytical model," *IEEE Trans. Magn*, vol. 52, no. 7, July 2016, Art. no. 8202704, doi: 10.1109/TMAG.2016.2521825.
[7] Y. Benmessaoud, F. Dubas, and M. Hilairet, "Combining the magnetic equivalent circuit and Maxwell-Fourier method for eddy-current loss calculation," Math. Comput. Appl., vol. 24, no. 2, p. 60, June 2019, doi: 10.3390/mca24020060.
[8] Y. Benmessaoud, D. Ouamara, F. Dubas, and M. Hilairet, "Investigation of volumic permanent-magnet eddy-current losses in multi-phase synchronous machines from hybrid multi-layer model," *Math. Comput. Appl*., vol. 25, no. 1, p. 14, Mar. 2020, doi: 10.3390/mca25010014.
[9] D. Ceylan, L.A. J. Friedrich, K.O. Boynov, and E.A. Lomonova, "Convergence analysis of the fixed-point method with the hybrid analytical modeling for 2-D nonlinear magnetostatic problems," *IEEE Trans. Magn*, Jan. 2021, Art. no. 7500105, doi: 10.1109/TMAG.2020.3024539.
[10] J. Bao, B.L.J. Gysen, and E.A. Lomonova, "Hybrid analytical modeling of saturated linear and rotary electrical machines: Integration of Fourier modeling and magnetic equivalent circuits," *IEEE Trans. Magn*, vol. 54, no. 11, Nov. 2018, Art. no. 8109905, doi: 10.1109/TMAG.2018.2837896.
[11] B. Ladghem-Chikouche, K. Boughrara, F. Dubas, and R. Ibtiouen, "Analytical Magnetic Field Calculation for Flat Permanent-Magneti Linear Machines with dual-rotor by using improved 2-D hybrid analytical method", *COMPEL - Int. J.* Comput. Math. Electr. Electron. Eng., vol. 40, no. 3, pp. 602-623, August, 2021, doi: 10.1108/COMPEL-02-2021-0039.
[12] B. Ladghem-Chikouche, K. Boughrara, F. Dubas, and R. Ibtiouen, "Two-dimensional hybrid model for magnetic field calculation in electrical machines: Exact subdomain technique and magnetic equivalent circuit", *COMPEL - Int. J. Comput. Math. Electr. Electron. Eng*., vol. 40, no. 3, pp. 535-560, June, 2021, doi: 10.1108/COMPEL-01-2021-0008.
[13] A. Hanic, D. Zarko, D. Kuhinek, and Z. Hanic "On-load analysis of saturated surface permanent magnet machines using conformal mapping and magnetic equivalent circuits," *IEEE Trans. Magn*, vol. 33, no. 3, Sep. 2018, pp. 915-924, doi**:** 10.1109/TEC.2017.2789322.
[14] A. Hanic, D. Zarko, and Z. Hanic, "A novel method for no-load magnetic field analysis of saturated surface permanent-magnet machines using conformal mapping and magnetic equivalent circuits," *IEEE Trans. Magn*, vol. 31, no. 2, Nov. 2016, pp. 740-749, doi: 10.1109/TEC.2015.2507704.
[15] Y. Liu, Z. Zhang, W. Geng, and J. Li, "A simplified finite-element model of hybrid excitation synchronous machines with radial/axial flux paths via magnetic equivalent circuit," *IEEE Trans. Magn*, vol. 53, no. 11, Nov. 2017, Art. no. 7403004, doi: 10.1109/TMAG.2017.2696568.
[16] M. Farhadian, M. Moallem, B. Fahimi, "Analytical calculation of magnetic field components in synchronous reluctance machine accounting for rotor flux barriers using combined conformal mapping and magnetic equivalent circuit methods," *Journal of Magnetism and Magnetic Materials*, vol. 505, no. 1, July 2020, 166762, https://doi.org/10.1016/j.jmmm.2020.166762.
[17] L.J. Wu, Z. Li, X. Huang, Y. Zhong, Y. Fang, and Z. Q. Zhu, "A hybrid field model for open-circuit field prediction in surface-mounted PM machines considering saturation," *IEEE Trans. Magn*, vol. 54, no. 6, June 2018, Art. no. 8103812, doi: 10.1109/TMAG.2018.2817178.
[18] B. Nedjar, L. Vido, S. Hlioui, Y. Amara, and M. Gabsi, "Hybrid coupling: magnetic equivalent circuit coupled to finite element analysis for PMSM electromagnetic modeling," *in Proc.* ISIE, pp. 858-862, Hangzhou, China, 28-31 May 2012, doi: 10.1109/ISIE.2012.6237201.
[19] R. Benlamine, F. Dubas, S-A. Randi, D. L. hotellier, and C. Espanet, "3-D numerical hybrid method for PM eddy-current losses calculation: Application to axial-flux PMSMs," *IEEE Trans. Magn.*, vol. 51, no. 7, July 2015, Art. no. 8106110, doi: 10.1109/TMAG.2015.2405053.
[20] A. Demenko, J. K. Sykulski, "Analogies between Finite Difference and Finite Element Methods for Scalar and Vector Potential Formulations in Magnetic Field Calculations," *IEEE Trans. Magn*, vol. 52, no. 6, June 2016, Art. no. 7004206, doi**:** 10.1109/TMAG.2016.2521345.
[21] Q. Sun, R. Zhang, Q. Zhan, and Q. H. Liu, "3-D implicit–explicit hybrid finite difference/spectral element/finite element time domain method without a buffer zone," *IEEE Trans. Antennas Propag*., vol. 67, no. 8, Aug. 2019, pp. 5469-5476, doi: 10.1109/TAP.2019.2913740.
[22] Q. Sun, Q. Ren, Q. Zhan, and Q. H. Liu, "3-D domain decomposition based hybrid finite-difference time-domain/finite-element time-domain method with nonconformal meshes," *IEEE Trans. Microw. Theory Tech.*, vol. 65, no. 10, Oct. 2017, pp. 3682-3688, doi**:** 10.1109/TMTT.2017.2686386.
[23] B. Yan, Y. Yang X. Wang, "A semi-numerical method to assess start and synchronization performance of a line-start permanent magnet synchronous motor equipped with hybrid rotor," *IET Elect. Power Appl.,* vol. 15, no. 4, pp. 487-500, Feb. 2021, doi: 10.1049/elp2.12043.
[24] T. Carpi, Y. Lefèvre, and C. Henaux, "Hybrid modeling method of magnetic field of axial flux permanent magnet machine", XIII International Conference on Electrical Machines (ICEM), Greece. pp.766-772, Sep. 2018, doi: 10.1109/ICELMACH.2018.8506756.
[25] D.C. Meeker, "Finite Element Method Magnetics", Version 4.2, 2019, Build, http://www.femm.info.
[26] B. Ladghem-Chikouche, K. Boughrara, F. Dubas, and R. Ibtiouen, "2-D semi-analytical magnetic field calculation for flat permanent-magnet linear machines using exact subdomain technique," *IEEE Trans. Magn.*, Early Access Article, doi**:** 10.1109/TMAG.2021.3068326.
[27] F. Dubas, and K. Boughrara, "New scientific contribution on the 2-D subdomain technique in Cartesian coordinates: Taking into account of iron parts," *Math. Comput. Appl.*, vol. 22, no. 1, p. 17, Feb. 2017, doi: 10.3390/mca22010017.
[28] L. Roubache, K. Boughrara, F. Dubas, and R. Ibtiouen, "Elementary subdomain technique for magnetic field calculation in rotating electrical machines with local saturation effect," *COMPEL - Int. J. Comput. Math. Electr. Electron. Eng.*, vol. 38, no. 1, pp. 24-45, Jan. 2019, doi: 10.1108/COMPEL-11-2017-0481.

Brahim Ladghem-Chikouche was born in M'sila, Algeria, in 1981. He received the Engineer Diploma degree from the University of M'sila, M'sila, Algeria, in 2005, the Magister and the Ph.D degree from Ecole Nationale Polytechnique (ENP), Algiers, Algeria, in 2009 and 2018 respectively. Before joining the University of M'sila in 2009, he has served in the industrial equipment maintenance sector, and electricity production company SPE-SONELGAZ, M'sila. He is currently a Lecturer at the department of Electrical Engineering, Faculty of Technology, University of M'sila, Algeria and member of the Laboratoire de Recherche en Electrotechnique (LRE-ENP), Ecole Nationale Polytechnique, Algiers, Algeria.
His current research interests include electromagnetic actuation systems modeling and design.

Kamel Boughrara was born in Algiers, Algeria, in 1969. He received the Engineer Diploma degree from Ecole Nationale Polytechnique (ENP), Algiers, in 1994, the Magister degree from the University of Sciences and Technology Houari Boumediene, Algiers, in 1997, and the Ph.D. degree from ENP, in 2008. He is currently a Professor with ENP, where he is also the head of department of Electrical Engineering.
His current research interests include the modeling and control of electrical machines.

Frédéric Dubas was born in Vesoul, France, in 1978. He received the M.Sc. degree and the Ph.D. degree from the "Univ. Bourgogne Franche-Comté" (Besançon, France) in 2002 and 2006, respectively, with a focus on the design and the optimization of high-speed surface-mounted permanent-magnet (PM) synchronous motor for the drive of a fuel cell air-compressor.
From 2014 to 2016, he has been the Head of "Unconventional Thermal and Electrical Machines" Team. He is the Head of the "Electrical Actuators" group in the "Hybrid & Fuel Cell Systems, Electrical Machines (SHARPAC)" Team. He works with ALSTOM Transports (Ornans, France), and RENAULT Technocenter (Guyancourt, France), where he is involved in the modelling, design and optimization of electrical systems and, in particular, induction and PM synchronous (radial and/or

axial flux) machines, creative problem solving, and electrical propulsion/traction. He is currently an Associate Professor with the Dép. ENERGIE, FEMTO-ST Institute affiliated to the CNRS and jointly with the “Univ. Bourgogne Franche-Comté” (Besançon, France).
He has authored over 100 refereed publications and he holds a patent about the manufacturing of axial-flux PM machines with flux-focusing. Dr. Dubas received: i) the Prize Paper Awards in the IEEE Conference Vehicle Power and Propulsion (VPPC) in 2005, ii) the Prize Presentation Awards in the 19th International Conference on Electrical Machines and Systems (ICEMS) in 2017, iii) the RENAULT Internal Award (Direction Engineering Alliance – Innovation) in 2019.

Lazhar Roubache was born in M’sila, Algeria, in 1991. He received the master’s degree and the Ph.D. degree from Ecole Nationale Polytechnique (ENP), Algiers, Algeria, in 2015 and 2019.
From 2019 to 2020, he was R&D engineer at Société d'Accélération du Transfert de Technologie Satt-Nord (Lille, France).
His current research interests include designs, modeling, optimization, and control of electrical machines.

Rachid Ibtiouen received the Ph.D. degree in electrical engineering from Ecole Nationale Polytechnique (ENP), Algiers, Algeria, and the Institut National Polytechnique de Lorraine, Nancy, France, in 1993. He was with the Groupe de Recherche en Électrotechnique et Électronique de Nancy (GREEN), Nancy, from 1988 to 1993. From 2005 to 2013, he was the Director of the Laboratoire de Recherche en Electrotechnique (LRE) with ENP.
His current research interests include the modelling electric systems and drives, and, in particular, electrical machines.

Comparative Study between precooled Claude Liquefaction Cycle and an Active Magnetic Regeneration Cycle applied to Hydrogen Liquefaction

Mustapha BELKADI and Arezki SMAILI

Abstract−The present work aims at performing a comparative study between precooled Claude cycle and an Active Magnetic Regeneration Cycle (AMR cycle) applied to hydrogen liquefaction. It deals with a comparison between performances and energy consumption evaluated for the two systems at similar operating conditions. For Claude system, energy and material balances have been performed by using Aspen Hysys simulator. Thus, liquefaction power, energy consumption and coefficient of performance (COP) have been calculated. While, the AMR system considered is constituted of 6 stages operating in cascade. Each stage contains two regenerator beds, composed of a typical magnetic material, through which a carrier fluid is forced to follow alternatively between two heat reservoirs. Thermal analysis and evaluation of performances have been performed at once by a numerical model, developed on the basis of energy equations for fluid and solid within the regenerator bed, and Aspen Hysys simulator. Using the following magnetic materials (Gd, Dy, Tb and Ho), the COP found for the AMR system is 0.096. This value is higher than Claude cycle efficiency for which a COP of 0.094 was found. In terms of energy consumption, the value found for the AMR cycle is 0.053 kW which can be neglected compared to the Claude cycle consumption (14.5 kW).

***Keywords*−Magnetic Refrigeration, Active Magnetic Refrigeration Cycle, Magnetic Materials, Hydrogen Liquefaction, Conventional Liquefaction Cycles.**

I. INTRODUCTION

Liquefaction of hydrogen has the advantage that very high hydrogen storage densities can be attained at atmospheric pressure: the density of saturated liquid hydrogen at 1 bar is 70 kg/m^3 [1]. Therefore, it is a suitable solution making possible large-scale hydrogen storage and long distance transportation. Liquid hydrogen has x characteristics such as lower weight and volume and higher energy content than the gaseous hydrogen [2]. The development of large hydrogen energy storage systems will facilitate the evolution of renewable energy sources, mitigate concerns arising from damage to the environment and eliminate the problem of energy demand fluctuations of renewable energy grids by storing the excess energy generated during times of high production to be consumed during times of low production.

Liquid hydrogen, under atmospheric pressure, can be obtained at 20.3 K. The liquefaction is carried out by extracting of 4914 kJ/kg of heat (divided between sensible heat, latent heat and conversion heat from n-H_2 to p-H_2). This liquefaction requires the use of some high level cryogenic technology whether to liquefy it or to keep it in the liquid state. In general, three processes are applied: Claude cycle, Brayton cycle and magneto-thermal cycles (i.e. magnetic refrigeration, based on the magnetocaloric effect (MCE) phenomenon) [3].

Manuscript received March 14, 2021; revised August 2, 2021.
M. Belkadi is with SONATRACH / Central Direction of Research and Development, Boumerdes, ALGERIA (e-mail: mustapha.belkadi@sonatrach.dz).
A. Smaili is with the Laboratory of Mechanical Engineering and Development-LGMD, Ecole Nationale Polytechnique, Algiers, ALGERIA (e-mail: arezki.smaili@g.enp.edu.dz).

Digital Object Identifier (DOI): 10.53907/enpesj.v1i2.12

The use of magnetic refrigeration to liquefy hydrogen is based on the magneto-caloric effect (MCE) phenomenon, which occurs in some materials when they are subjected to external magnetic field changes. The MCE is defined as the change of material temperature when applying or removing the magnetic field (magnetization /demagnetization process). In fact, if a magnetic material is placed in a magnetic field, there is usually an increase in its temperature. Conversely, demagnetization process has a cooling effect on it. Liquefaction could be carried out by cooling the gas through a thermomagnetic cycle, known as Active Magnetic Regeneration (AMR cycles) cycles. An AMR cycle consists essentially of a regenerator bed (magnetic material) which is subjected to cyclic changes in magnetic-field intensity, alternating between zero-field and the maximum field. Temperature span induced by the magnetization and demagnetization process is amplified by forcing a working fluid to move alternatively through the regenerator bed between two heat sources (hot and cold reservoirs). Thus, a large temperature span can be obtained [4].

Application of Magnetic Refrigeration to hydrogen liquefaction is performed by absorbing the liquefaction power from the gas to be liquefied via an AMR regenerator cycle. The liquefaction power absorbed is the cooling power which can be produced by the AMR cycle. This cooling power can be evaluated through modeling of magnetic refrigeration phenomena, based on characterization of heat transfer between working fluid and magnetic material and EMC calculation. In this context, several research activities related to performance investigation of AMR cycle or development of new magnetic materials have been conducted. We show here, e.g., the work of Smaili et al. [5] related to thermodynamic investigations of optimum active magnetic regenerators, Aprea et al. [6] who proposed a flexible numerical model to study an active magnetic refrigerator for near room temperature applications, Chiba et al. [7] study

related to thermal investigations of an experimental active magnetic regenerative refrigerator operating near room temperature.

The interest in magnetic refrigeration for hydrogen gas liquefaction started in the early to mid-1970s by W.A. Steyert, joined by J.A. Barclay in 1977 and C.B. Zimm in 1983, at the Los Alamos National Laboratory (LANL) [8]. Later, research activities have been increased substantially and several works have been published by different researchers globally [9]- [16]. This entire work are related to exergy analysis, cooling capacity and COP investigation or design optimization of hydrogen liquefier operating between 77 K and 20K, after being precooled, in most cases by liquid nitrogen. Exception is found for Smaili et al. paper [15] where a numerical study on the first stage hydrogen magnetic liquefier operating over the temperature range: 298-233 K has been reported. The authors investigated the cooling capacity and the COP of the AMR cycle as function of mass flow rate, cycle frequency, and magnetic field.

Recently, Belkadi and Smaili [17] published in 2018 a work about thermal analysis of a multistage Active Magnetic Regenerator (AMR) cycle for hydrogen liquefaction starting from room temperature. The proposed liquefier operates with a magnetic material, assumed having a constant EMC, as refrigerant and hydrogen gaseous as carrier fluid. The number of stages, the coefficient of performance (COP) and the required volume of magnetic material has been investigated. To liquefy 1kg/h of hydrogen supplied at 298 K, a minimum required volume of 2.96 L, corresponding to COP value of 1.23 has been found for a liquefier constituted of 6 AMR cycles operating in series (cascade).

For conventional systems, liquefaction of hydrogen was first performed in 1898 by Sir James Dewar. Some years later, a pre-cooled Linde Hampson system was used as the first simple laboratory system to liquefy hydrogen [18]. Then, the process was improved by Georges Claude, the forefather of the French company ''Air Liquide'' [19].

As a review, Krasae-in *et al.* [18], published in 2010 a paper related to the development of large-scale hydrogen liquefaction processes from 1898 to 2009. This paper retraces the history of hydrogen liquefaction development starting from the first system of Sir James Dewar. A brief process description and comparison between energy consumption and overall cycle exergy efficiency were given by the authors for different liquefaction systems, including theoretical liquefaction systems (Linde-Hamson system, Helium refrigerant system and Precooled-Claude system), current plants and conceptual plants. As reported by the authors, it is found that every current plant is based on the Precooled-Claude system, which is still the same as was 50 years ago with little improvement and low exergy efficiency of just between 20–30%.

There are two main fundamental reasons as to why the liquefaction of hydrogen has low exergy efficiency and requires a substantial input of energy: (i) the extremely low boiling point of hydrogen (20 K at 1 bar) and (ii) the fact that hydrogen gas does not cool down during throttling processes (adiabatic, isenthalpic expansion) for temperatures above around 200 K (inversion temperature of hydrogen). The latter problem requires precooling in the liquefaction process, most often by the evaporation of liquid nitrogen [1].

In order to solve the problem of the low exergy efficiency of the current liquefaction plants, several research activities are oriented to find a new configuration with more efficient system. In this purpose, Krasae-in et al. [20]- [22] proposed a multi-component refrigerant (MR) refrigeration cycle for which, three studies have been published between 2010 and 2011. The first study investigates the simulation of a small-scale laboratory liquid hydrogen plant with a new innovative multi-component refrigerant (MR) refrigeration system that was capable of liquefying a feed of 2 kg/h of normal hydrogen gas at 21 bar and 298 K to normal liquid hydrogen at 2 bar and 23 K. In the second one, a test rig was constructed to verify the simulation of the proposed small-scale laboratory hydrogen liquefaction plant. The third paper presents a proposed liquid hydrogen plant using a multi-component refrigerant (MR) refrigeration system where a cycle that is capable of producing 100 tons of liquid hydrogen per day is simulated. The authors found that the overall power consumption of the proposed plant is 5.35 kWh/kgLH_2. The system shows very low energy consumption compared to the current plant in Ingolstadt used as a reference by the authors, which has an energy consumption of 13.58 kWh /kgLH_2.

In same way, a large-scale hydrogen liquefier, utilizing mixed-refrigerant (MR) pre-cooling, has been developed by Berstad *et al* [23] in 2010. The liquefier employs MR refrigerant to pre-cool hydrogen until the temperature of 75 K. Below this temperature, a reversed helium/neon Brayton cycle provides the requisite cooling. Two MR-based liquefier models have been performed. In the first, Joule–Thomson throttling valves are employed for MR expansion, while these have been replaced by liquid expanders in the second. With 21bar hydrogen feed pressure and an ambient temperature of 300 K, the resulting figures for specific liquefaction power presented by the authors for the two models are respectively 6.48 and 6.15 kWh/kgLH_2.

In 2017, a novel large-scale plant for hydrogen liquefying, with a production capacity of 100 tons per day, is proposed and analyzed by Aasadnia M *et al.* [24]. The liquefaction plant is proposed to provide the required LH_2 for a large urban area with 100 000-200 000 hydrogen vehicles supply. In the precooling section of the process, a new mixed refrigerant (MR) refrigeration cycle, combined with a Joule-Brayton refrigeration cycle, precool gaseous hydrogen feed from 298 K to the temperature of 75 K. A new refrigeration system with six simple Linde-Hampson cascade cycles cools low-temperature gaseous hydrogen from 75 K to temperature of 20 K. The process specific energy consumption is 7:69 kWh/kgLH2 as reported by the authors.

In addition, a large review and analysis of basic cycles of hydrogen liquefaction is presented by Aasadnia M et al. [2] in 2018. The review includes hybrid conceptual plants where various renewable-energy may be used in different combined configuration within hydrogen liquefaction plants. The promising role in the cost reduction and the increasing contribution of this new approach is demonstrated. As reported by the authors, results of thermodynamic analysis, of a combined refrigeration system comprising a conventional vapor-compression cycle cascaded with an absorption refrigeration cycle assisted by geothermal energy, show that the conventional cycle energy consumption is approximately 37% and 54% more than the combined system under the same operating conditions.

In the same context of assistance by geothermal energy, Gaddalla et al. [25] presented an extensive investigation for an integrated absorption cooling-hydrogen liquefaction system. The pre-cooling process of hydrogen can be achieved by using absorption system which runs on low grade heat instead of electricity.

Otherwise, enhancement of hydrogen liquefaction efficiency can also be performed by optimizing operating parameters and reducing heat losses in the main equipment of the liquefaction system. In this, approach, Skaugen et al. [26] presented a work in 2020 about exergy losses comparison and evaluation of the potential of catalyst-filled plate-fin and spiral-wound heat exchangers for use in a large-scale Claude hydrogen liquefaction process. In addition to the comparison made on characteristics, behavior and performances, maps of the local exergy destruction in the heat exchangers have also been presented. This is to reveal avenues which can be followed to further improve the process.

To reduce energy consumption, a refrigeration strategy that gives minimum entropy production/exergy destruction in a plate-fin heat exchanger that cools the hydrogen from 47.8 K to 29.3 K has been discussed in 2019 by Hande et al. [27]. Two reference cases have been studied; one where the feed stream enters at 20bar, and one where it enters at 80 bar.

In the present work, a comparative study between conventional liquefaction cycle and AMR liquefaction cycle has been performed. It deals with a comparison between performances and energy consumption evaluated for the two systems at similar operating conditions. This is to situate the AMR systems, which are now at laboratory scale, in relation to conventional systems which are already industrialized.

For the first one, precooled Claude cycle has been considered. Here, energy and material balances have been performed by use of Aspen Hysys simulator. Thus, liquefaction power, energy consumption and coefficient of performance (COP) have been calculated. While, the second one is based on a multistage AMR cycles operating in cascade. Each stage contains two regenerator beds, composed of appropriate typical magnetic material. thermal analysis and performance calculation have been performed. First, for the AMR cycle by considering energy equations for fluid and solid within the regenerator bed. A numerical model has been developed in order to determine heats exchanged between the solid (magnetic material) and the carrier fluid at each stage. Then, heats exchanged are introduced as input in Aspen Hysys simulator to perform energy and material balances and calculate performances of the liquefier (COP, work input, etc.). For this purpose, a simulation method published by Belkadi and Smaili [17] has been used to simulate the AMR liquefier with Aspen Hysys which allows rapid and rigorous calculations.

II. Conventional basic cycles applied to hydrogen liquefaction

As mentioned before, every current plant is based on the Precooled-Claude system. Improvement has been conducted, for often, in the precooling section. In this section, a brief description of basic cycles of hydrogen liquefaction is presented.

A. Basic Claude cycle

The basic Claude cycle uses hydrogen itself as working medium after being compressed, chilled and expanded through a Joule-Thomson Valve (JT valve). A part of compressed H_2 gas is expanded in the expansion turbine to generate colder gas. This colder gas is combined with saturated vapor, coming from the flash end separator, to be used for cooling of the compressed hydrogen gas (figure 1). Energy analysis performed by Asadria et al. [2] illustrates a COP of 0.055 and a specific energy consumption of 22.1 kWh/kgLH_2.

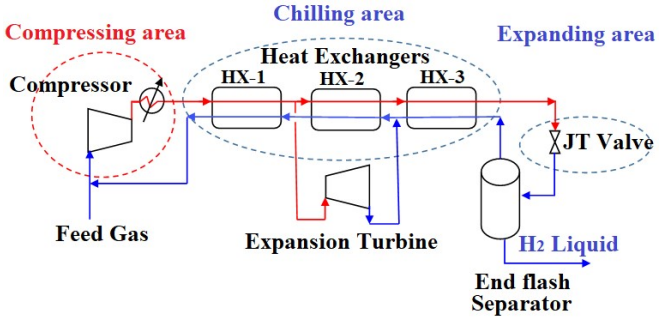

Fig. 1 Simple Claude cycle of hydrogen liquefaction.

B. Brayton cycle.

Brayton cycle uses helium, often mixed with neon, as an external refrigerant as illustrated in figure 2. It includes:

- A compressor to bring helium from 3 to 17 bars,
- Two parallel turbines expanding helium gas from 17 to 3 bars,
- An ambient-refrigerant heat-exchanger to cool the compressed helium.
- A cold box where hydrogen is first precooled by nitrogen and then liquefied by helium refrigerant after being expanded to 3 bars.

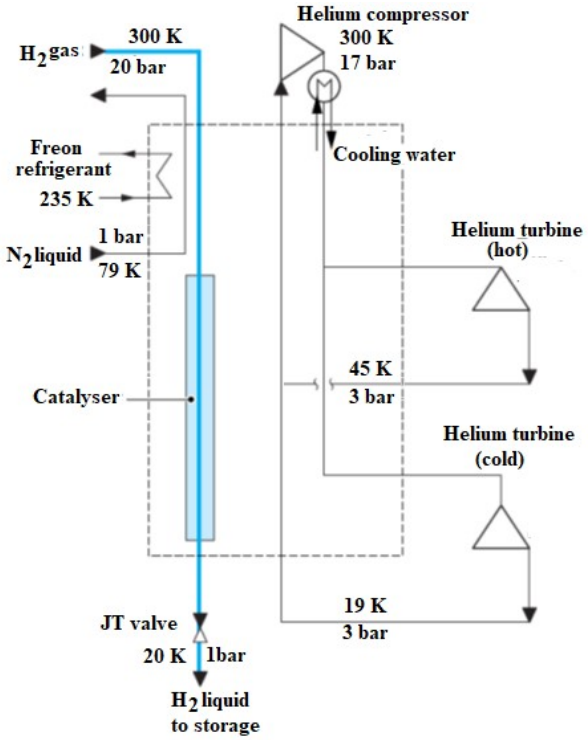

Fig.2 Brayton liquefaction cycle [adapted from 19]

C. Liquid-nitrogen pre-cooled cycles

As the maximum inversion temperature of hydrogen (i.e. 205 K) is below ambient, pre-cooling is an inevitable necessity of the basic simple cycle modification. Basic Claude cycle, Brayton cycle and Linde-Hampson system that utilized for air liquefying can be improved, by adding a precooling medium, e.g. liquid nitrogen bath (LN_2 bath), to be used for hydrogen liquefaction [2]. Fig. 3 depicts the process flow diagram (PFD) of a LN_2 pre-cooled Linde-Hampson cycle applied for hydrogen liquefaction.

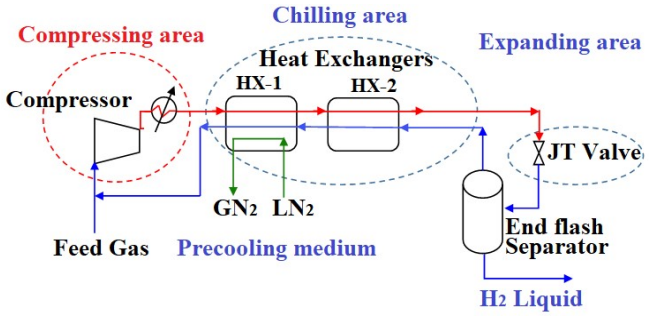

Fig. 3 Pre-cooled Linde-Hampson cycle for hydrogen liquefaction.

D. Precooled Claude cycle

In Precooled Claude system, liquefaction of hydrogen at 20.3 K is obtained by the combined effect of cooling and adiabatic expansion of gas after it has been previously compressed as illustrated in figure 4. Expansion can be carried out through two turbines (hot turbine and cold turbine) followed by a Joule-Thomson valve (JT valve) to avoid liquid formation at the end of the cold turbine.

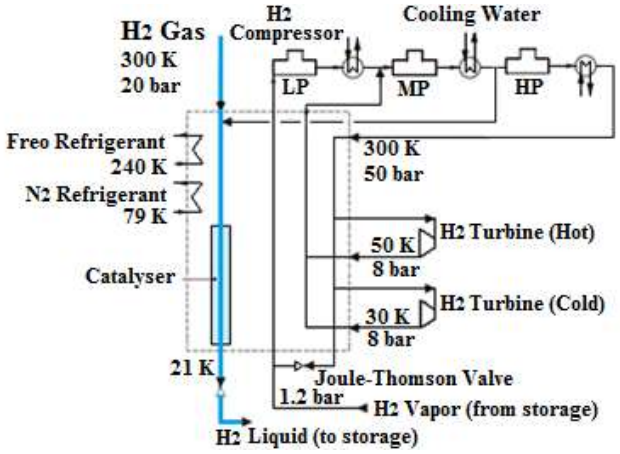

Fig. 4 Precooled Claude liquefaction Cycle [adapted from 19].

The optimum pressure for hydrogen liquefaction is generally above the critical pressure, between 15 and 25 bars. It can be supplied at the liquefaction pressure if it is produced by a hydrocarbon or methanol reforming. It should be compressed before purification and liquefaction if it is produced by an electrolyze device operating at atmospheric pressure [19].

In order to avoid hydrogen liquid losses which can be involved by the heat of conversion, a catalyzer should be provided during the liquefaction to accelerate the conversion from the normal-hydrogen, n-H_2 (25% para-hydrogen and 75% ortho-hydrogen), to para-hydrogen (p-H_2) [19].

E. Mixed refrigerant pre-cooled cycle

Mixed refrigerant (MR) is a mixture of hydrocarbon components (N_2, Methane, Ethane, Propane, Butane) used to precool hydrogen gas to a temperature of 75 K. Figure 5 shows the overall process diagram of a MR precooled system working according to Claude cycle.MR refrigeration is a mature technology for liquefied naturel gas (LNG) applications, but has not yet been realized commercially for hydrogen liquefaction, where open nitrogen pre-cooling is the standard [26].With MR precooling, high efficiency and minimum energy consumption can be reached.

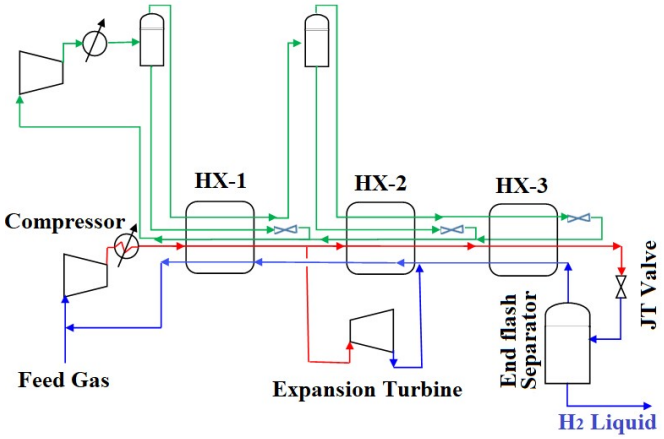

Fig. 5 Mixed refrigerant pre-cooling simple Claude cycle.

III. AMR LIQUEFACTION CYCLE

The concept of magnetic refrigeration is based on the Magnetocaloric Effect (MCE), which occurs in some materials when they are subjected to external magnetic field changes (Magnetization / Demagnetization process) through an AMR regenerator cycle. Its Application to hydrogen liquefaction consists in performing a thermal contact between the AMR regenerator cycle and the gas to be liquefied as illustrated in figure 6.Liquefaction is performed by absorbing an amount of heat from the gas (Q_L), equal to the total cooling power of the AMR liquefier, and rejecting into the atmospheric environment an amount of heat equal to Q_{Ha}.

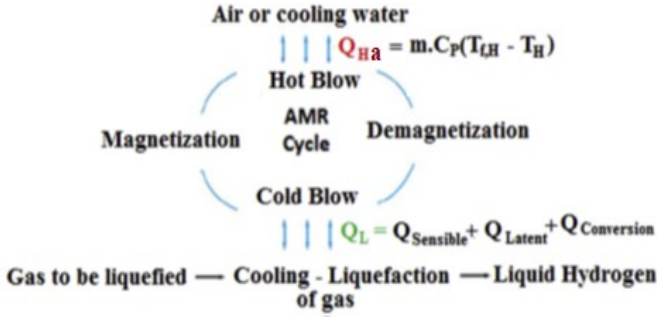

Fig. 6. Hydrogen liquefaction process via AMR cycle.

Furthermore, the use of one AMR cycle is not suitable to provide the large temperature span required for hydrogen liquefaction. Thus, applying magnetic refrigeration to the liquefaction of hydrogen is performed by assembling a number of AMR cycles operating in series (cascade cycles) as illustrated in figure 8. The cooling power produced by one stage is used to cool hydrogen entering the stage and absorbs heat rejected by the lower stage. The required cooling power of each stage is regulated by adjusting the volume of the regenerator beds (adjusting the volume of magnetic material used in each stage).

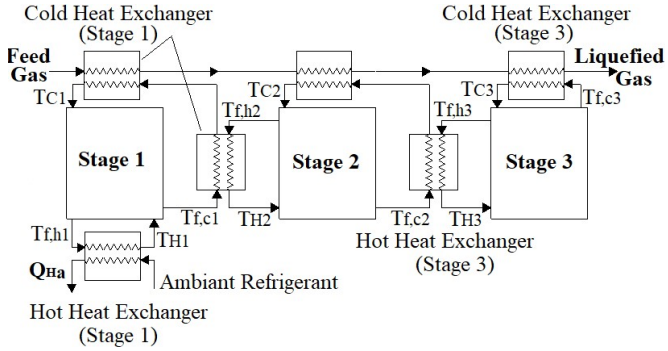

Fig. 8 Multistage AMR liquefaction system

In the present paper, the AMR cycle considered for each stage is mainly constituted, as illustrated in figure 7, of the following components [17]:

- Two Regenerator beds working alternately, AMR_A and AMR_B, (when the first regenerator bed is magnetized, the second one is demagnetized) to provide a continuous production of the cooling powerthrough the regenerator beds (Q_C).
- Reciprocating displacer which is able to move the fluid alternatively;
- Magnetic field source able to magnetize and demagnetize the regenerator beds;
- Hot heat exchanger able to reject the thermal energy (Q_H) into the hot reservoir;
- Cold heat exchanger able to receive the thermal energy from the cold reservoir (Cooling power Q_C).

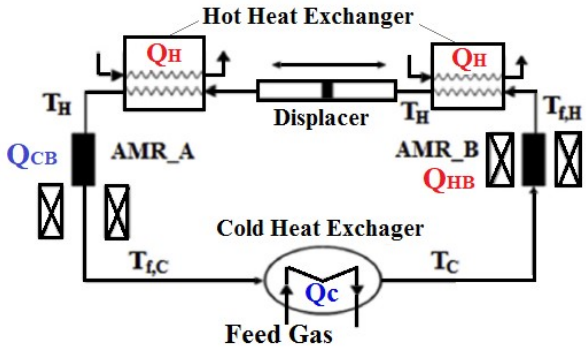

Fig.7. AMR device with two regenerator beds.

A complete AMR cycle consisting of two isentropic steps (adiabatic magnetization / demagnetization process) and two isofield steps (Cold and Hot blows) which can be described as follows) [20]:

1. Adiabatic demagnetization step:
   By reducing magnetic field from given strength B to 0 with no flow, the bed is demagnetized adiabatically.

2. Cold Blow at zero fields:
   The fluid is then forced by the displacer to move from the hot to the cold exchangers. Upon entering the demagnetized bed, the fluid temperature T_f is equal to the hot reservoir temperature T_H, exchanging heat with the bed it drops to $T_{f,C}$below the cold reservoir T_C at the cold end. Passing through the cold heat exchanger, the fluid absorbs heat from the cold reservoir (gas to be liquefied) at a rate Q_C, which represents the cooling power of the regenerator:

$$Q_C = \dot{m}_f Cp_f\left(T_C - T_{f,C}\right). \quad (1)$$

3. Adiabatic magnetization step:
   The bed is magnetized adiabatically when the magnetic field increases from 0 to B, with no flow.

4. Hot Blow at applied field:
   The fluid is then forced from the cold to the hot ends, entering the bed at the temperature equal to T_C. Since the bed temperature rises along the flow direction, the fluid temperature will also be increased, and it leaves the bed at a temperature $T_{f,H}$ higher than T_H. Passing through the hot exchanger, the fluid temperature drops to T_H, rejecting heat to the hot reservoir at a rate:

$$Q_H = \dot{m}_f Cp_f\left(T_{f,H} - T_H\right). \quad (2)$$

in addition to Q_H and Q_C given by equations 1 and 2, the exchanged heats with the regenerator beds, Q_{HB} and Q_{CB}, can be calculated according to the fluid entering temperatures in the regenerator beds T_H and T_C, respectively during the cold blow and the hot blow, and the exit temperatures $T_{f,C}$ and $T_{f,H}$.

$$Q_{CB} = \dot{m}_f Cp_f\left(T_H - T_{f,C}\right). \quad (3)$$

$$Q_{HB} = \dot{m}_f Cp_f\left(T_{f,H} - T_C\right). \quad (4)$$

Calculation of the exchanged heats by equations 1-4 involves development of a numerical model based on the fundamental equations of energy conservation considered for the fluid and the solid (magnetic material), during the cold and hot blows, and characterization of the MCE during the magnetization and demagnetization of material. For pure magnetic materials (Gd, Tb and Dy), the MCE characterization can be performed according to the Molecular Field Theory (MFT) [15, 17].

The time period of fluid flow for either blow is considered equal to τ. The adiabatic demagnetization and magnetization processes are assumed to occur instantaneously at the time τ and 2τ. This information shows the periodic operation of the AMR system; each period (2τ) constitutes a regenerative cycle where a temperature span is observed in the regenerator bed. This temperature span is amplified by alternating the carrier fluid between the two heat reservoirs, until reaching the steady state.

When the steady state is reached, the AMR cycle efficiency can be evaluated by using the coefficient of performance (COP), which is usually defined as follows:

$$COP_{AMR} = \frac{Q_C}{Q_H - Q_C + W}. \quad (5)$$

Where Q_H is the heat rejected into the hot reservoir, Q_C is the heat absorbed from the cold reservoir and W is the power input used to move the carrier fluids through the regenerator beds.

However, the overall AMR liquefier efficiency is calculated by using the overall COP as follow:

$$COP = \frac{Q_L}{Q_{Ha} - Q_L + W_{in}}. \quad (6)$$

Where Q_{Ha} is the heat rejected into the atmospheric environment at the hot heat exchanger of the first stage (stage

1), Q_L is the total heat absorbed from the gas to be liquefied (the total cooling power of the AMR liquefier) and W_{in} is the total power input used to move the carrier fluids through the regenerator beds.

IV. Comparative Study between Claude and AMR Hydrogen Liquefaction Cycles

To perform comparison between conventional and magnetic liquefaction systems, thermal analysis of the two systems has been performed by means of Aspen Hysys simulator which is a powerful software developed by AspenTech to simulate gas processing plants, oil refineries and petrochemical plants. The Simulation consists of building a Process Flow Diagram (PFD) of the liquefaction system, performing material and energy balances and calculating heat transfer and energy consumption.

A. Claude cycle simulation

The cycle considered in this work is based on the precooled Claude cycle where hydrogen gas is first precooled by a mechanical refrigerant until 245 K, then by nitrogen gas refrigerant until 83 K as illustrated in figure 4. The liquefaction part is carried out by cold hydrogen refrigerant after being expanded, from 50 bar to 3 bar, through two turbines. Nitrogen refrigerant loop includes two-stage compressor with intercooling, to compress nitrogen to 10 bar, and an Expander to expand it until 1.2 bar after being cooled in parallel with hydrogen in the precooling heat exchangers.

Two case studies have been performed. In the first case, hydrogen gas to be liquefied has been assumed to be supplied at liquefaction pressure. In the second case, hydrogen gas is supplied at atmospheric pressure and then compressed to the liquefaction pressure.

To calculate the cycle efficiency, we first need to determine the heat absorbed from the gas to be liquefied (Colling power Q_L) and compression consumedpower(W_C) by performing energy and material balances for the overall liquefaction cycle. This can be performed by Aspen Hysys and all operating parameters of the cycle will be determined from the simulation flow sheet.

The cycle efficiency is then computed by introducing the coefficient of performance (COP) which is defined as the ratio of heat absorbed from the gas to be liquefied (Q_L) to the net absorbed power of the cycle (Compression power W_C), as follows:

$$COP = \frac{Q_L}{W_C}. \quad (7)$$

where, Q_L is the total heat absorbed from hydrogen and W_C is the total compression power consumed.

B. AMR cycle simulation

Thermal analysis of the AMR cycle has been performed by Aspen Hysys simulator according to the simulation method published by Belkadi and Smaili [17]. The method consists of modeling the AMR system, once the steady state is reached, by an ordinary system where the magnetized regenerator is idealized as a heater, whereas the demagnetized one is idealized as a cooler (figure 9). The carrier fluid flows continuously through the cycle, absorbing form the heater an amount of heat equal to the heat absorbed from the regenerator bed during the hot blow (Q_{HB}). The carrier fluid rejects through the cooler an amount of heat equal to the heat exchanged with the regenerator bed during the cold blow (Q_{CB}).

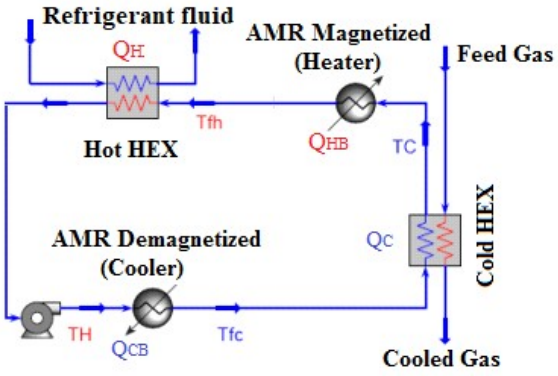

Fig. 9 AMR cycle Simulation method

The exchanged heats with the regenerator beds, Q_{HB} and Q_{CB}, should be calculated, according the equations 3 and 4, by the numerical model developed separately and introduced as input in Aspen Hysys simulation.

V. Results and Discussion

As mentioned in section II, hydrogen can be supplied at the liquefaction pressure if it is produced by a hydrocarbon or methanol reforming. However, it should be compressed before purification and liquefaction if it is produced by an electrolyze device operating at atmospheric pressure [19]. In this logic, simulation of precooled Claude cycle has been performed, first, for a device where hydrogen is supplied at liquefaction pressure. Then a device where hydrogen is supplied at atmospheric pressure is considered. The simulation has been performed for different liquefaction pressures in order to determine the optimum pressure which should be considered as operating pressure. Figure 10 illustrates the evolution of the COP and power consumption (W_C) as function of liquefaction pressure (P_L) when hydrogen is supplied at liquefaction pressure. Results show the increase of the COP with the pressure. This rise becomes insignificant from the pressure of 30 bar. Thus, the optimum pressure can be taken between 15 bar and 30 bar. At 20 bar the total power required to liquefy 1kg/h is 13kW. The corresponding COP is 0.105 (10.5%). This efficiency is not so far compared with published values. Pre-cooled Claude exergy efficiency, e.g., as published by Krasae-in [18], is situated between 6.2%-8.8% (noting that for the same system, exergy efficiency is higher compared to energy efficiency).

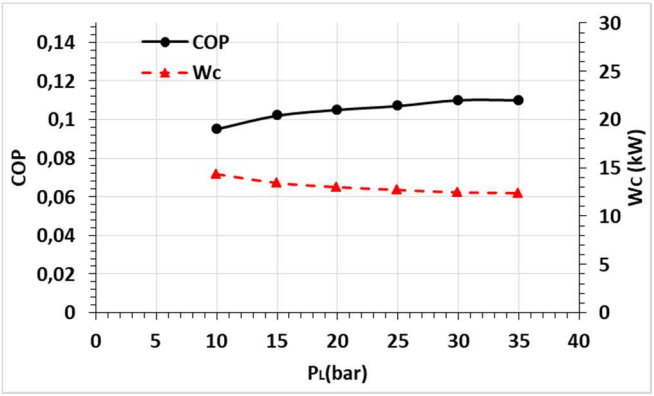

Fig.10. Evolution and COP and power required of precooled Claude cycle as function of liquefaction pressure when hydrogen is supplied at liquefaction pressure.

When hydrogen is supplied at atmospheric pressure, it should be compressed to the required liquefaction pressure. in this case the power required to compress 1kg/h from 1 bar to 20 bars is 1.5 kW. The total power required rises to 14.5 kW. Evolution of the COP of precooled Claude system and the total power required to liquefy 1kg/h of hydrogen supplied at 1 atm, as function of liquefaction pressure (P_L), is illustrated on figure 11.

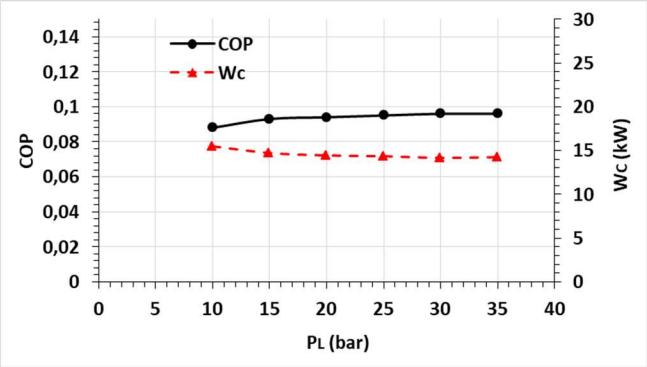

Fig. 11 Evolution of COP and power consumption of precooled Claude cycle as function of liquefaction pressure when hydrogen is supplied at atmospheric pressure.

For magnetic liquefaction, the AMR considered is composed of 6 stages operating in cascade. The hydrogen gas to be liquefied is supplied at ambient temperature under atmospheric pressure. Using Gadolinium (Gd), Terbium (Tb), Dysprosium (Dy) and Holmium (Ho) [11] as magnetic materials, thermal analysis has been performed by use of Hysys simulator as presented in section 3.2. The total volume (V) of the magnetic materials to be installed, liquefaction COP and power consumption (W_{in}) are calculated. The relation between the COP and the total volume of magnetic materials has been investigated. Results obtained are presented in figure 12. Results show that the most efficient volume is 124 liters. The corresponding COP is 0.096 (9.6%). Here, the total work input used to move the carrier fluid through the regenerator beds is insignificant (0.053 kW to liquefy 1 kg/h of H_2 supplied at atmospheric pressure).

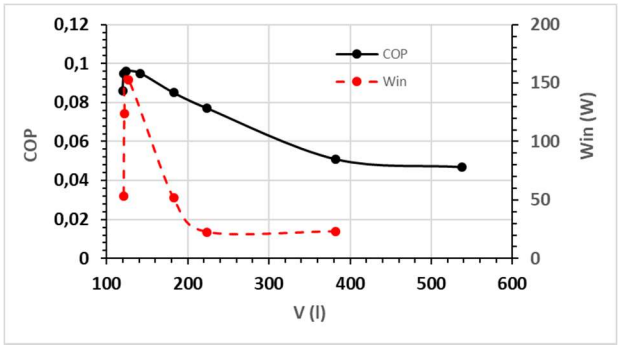

Fig.12. COP and the total work input of AMR cycle as function of magnetic material volume

To highlight the difference between the two systems, efficiency and energy consumption, calculated according to the thermal analysis procedure presented in section 3, are illustrated in table 1.

Table I
Comparison between conventional system and AMR system.

	P_L (bar)	COP	W_C (kW)	W_{in} (kW)
Claude cycle	20	0.105	13	
	20	0.094	14.5	
AMR system	1	0.096		0.053

It is found that, in terms of efficiency, the two systems have the same COP. However, the power consumption for conventional systems is very high compared to the AMR systems. These performances can be improved for the AMR liquefier by the use of other magnetic materials having large EMC.

VI. Conclusion

In this study, an AMR liquefaction system, constituted of 6 stages operating in cascade, has been considered to be compared with a precooled Claude system. COP and energy consumption have been calculated for the two systems at similar conditions.

In conventional systems, liquefaction can be obtained by the combined effect of cooling and adiabatic expansion of gas after it has been previously compressed. This liquefaction requires the use of large amounts of energy through cooling loops and at the recompression of gas. 13 kW is the required power found to liquefy 1kg/h supplied at 20 bar. The corresponding COP found is 0.105. When hydrogen is supplied at atmospheric pressure and compressed to be liquefied at 20 bar, the power required rises to 14.5 kW and the COP decreases to 0.094.

By use of real magnetic materials (Gadolinium Gd, Terbium Tb, Dysprosium Dy and Holmium HoN) in 6 stages AMR liquefier, the COP found is 0.096. This value is very close of the one found for precooled Claude cycle. However, the total work input used to move the carrier fluid through the regenerator beds is insignificant compared to the energy consumed in Claude system: 0.053 kW of power to liquefy 1 kg/ of H_2 supplied at atmospheric pressure against 14.5 kw for Claude system. These results can be enhanced by the use of other magnetic materials having large EMC. However, the use of a large amount of magnetic materials as solid refrigerant stills the main disadvantage of the magnetic systems: 124 litters is the volume of magnetic materials found for the AMR to be considered.

Acknowledgements

The support from Directorate-General for Scientific Research and Technological Development (DG-RSDT) of Algerian government in the form of research grant is gratefully acknowledged.

References

[1] J. Andersson, S. Grönkvist, Large-scale storage of hydrogen, International Journal of Hydrogen Energy 44 (2019) 11901-11919. https://doi.org/10.1016/j.ijhydene.2019.03.063
[2] M. Aasadnia, M. Mehrpooya, Large-scale liquid hydrogen production methods and approaches: A review, Applied energy 212 (2018) 57-83. https://doi.org/10.1016/j.apenergy.2017.12.033
[3] P. Malbrunot, Th. Alleau, Mémonto de l'hydrogène, Fiche 4.3 (2019).
[4] JA. Barclay, The theory of an active magnetic regenerative refrigerator, New Mexico: Los Alamos National Laboratory; 1982. LA-UR-83e1251; CONF-821237-1.
[5] A. Smaili, R. Chahine, Thermodynamic investigations of optimum active magnetic regenerators. Cryogenics 38(1998) 247-252.
[6] C. Aprea, A. Maiorino, a flexible numerical model to study an active magnetic refrigerator for near room temperature applications, Appl. Energy 87(2010) 2690-2698.
[7] Y. Chiba, A. Smaili, C. Mahmed, M. Balli, O. Sari, Thermal investigations of an experimental active magnetic regenerative refrigerator operating near room temperature, International Journal of Refrigeration 37(2014) 36-42.
[8] Jr. K.A. Gschneidner, V.K. Pecharsky, Thirty years of near room temperature magnetic cooling: where we are today and future prospects, International Journal of Refrigeration 31(2008) 945-961.

[9] L. Zhang, S.A. Sherif, T.N. Veziroglu, J.W. Sheffield, Performance analysis of reciprocating magnetic liquefiers, Int. Journal of Hydrogen Energy 19(1994) 945-956.
[10] L. Zhang, S.A. Sherif, T.N. Veziroglu, J.W. Sheffield, On exergy losses in AMR hydrogen liquefier, Int. Journal of Hydrogen Energy, 19(1994) 447-452.
[11] L. Zhang, S.A. Sherif, A.J. DeGregoria, C.B Zimm, T.N. Veziroglu, Design optimization of a 0.1- ton/day active magnetic regenerative hydrogen liquefier, Cryogenics 40 (2000) 269-278.
[12] W. Iwasaki, Magnetic refrigeration technology for an international clean energy network using hydrogen energy (WE-NET), Int. Journal Hydrogen Energy 28(2003) 559-567.
[13] T. Nakagawa, T.A. Yamamoto, T. Numazawa, Research on a magnetic refrigeration cycle for hydrogen liquefaction, Cryocoolers 14 (2007) 645-653.
[14] K. Matsumoto, T. Kondo, M. Ikeda, T. Numazawa, Numerical analysis of active magnetic regenerators for hydrogen magnetic refrigeration between 20 and 77K, Cryogenics 51 (2011) 353-357.
[15] A. Smaili, S. Aı¨t Ali, R. Chahine, Performance predictions of a first stage magnetic hydrogen liquefier, Int. Journal of Hydrogen Energy 36(2011) 4169-4177.
[16] I. Park, Y. Kim, J. Park, S. Jeong, Design method of the layered active magnetic regenerator (AMR) for hydrogen liquefaction by numerical simulation, Cryogenics 70 (2015) 57-64 https://doi.org/10.1016/j.cryogenics.2015.04.007
[17] M. Belkadi, A. Smaili, Thermal analysis of a multistage active magnetic regenerator cycle for hydrogen liquefaction, International Journal of Hydrogen Energy 43(2018) 3499-3511.
[18] S. Krasae-in, J. Stang, P. Neksa, Development of large-scale hydrogen liquefaction processes from 1898 to 2009, International Journal of Hydrogen Energy 35(2010) 4524-4533.
[19] J. Gallarda, Liquéfaction de l'hydrogène. Technique de l'Ingénieur, j3603 (2001).
[20] S. Krasae-in, J. Stang, P. Neksa, Exergy analysis on the simulation of a small-scale hydrogen liquefaction test rig with a multi-component refrigerant refrigeration system, Int Journal of Hydrogen Energy 35 (2010) 8030-8042.
[21] S. Krasae-in, A. Bredesen, J. Stang, P. Neksa, Simulation and experiment of a hydrogen liquefaction test rig using a multi-component refrigerant refrigeration system, Int. Journal of Hydrogen Energy 36 (2011) 907-919.
[22] S. Krasae-in, J. Stang, P. Neksa, Simulation on a proposed large-scale liquid hydrogen plant using a multi-component refrigerant refrigeration system, Int. Journal of Hydrogen Energy 35(2010) 12531-12544.
[23] D. O. Berstad, J.H. Stang, P. Neksa, Large-scale hydrogen liquefier utilizing mixed-refrigerant pre-cooling, International Journal of Hydrogen Energy 35(2010) 4512-4523.
[24] M. Asadnia, M. Mehrpooya, A novel hydrogen liquefaction process configuration with combined mixed refrigerant systems, International Journal of Hydrogen Energy 42(2017)15564-15585. https://doi.org/10.1016/j.ijhydene.2017.04.260
[25] M.A. Gadalla, T.A.H. Ratlamwala, I. Dincer, M. Kanoglu, Performance assessment of an integrated absorption cooling-hydrogen liquefaction system using geothermal energy, Int. J. Exergy 12(213) 205-225.
[26] G. Skaugen, D. Berstad, Ø. Wilhelmsen, Comparing exergy losses and evaluating the potential of catalyst-filled plate-fin and spiral-wound heat exchangers in a large-scale Claude hydrogen liquefaction process, Int. Journal of Hydrogen Energy 45(2020) 6663-6679. https://doi.org/10.1016/j.ijhydene.2019.12.076
[27] R. Hande, Ø. Wilhelmsen, Minimum entropy generation in a heat exchanger in the cryogenic part of the hydrogen liquefaction process: On the validity of equipartition and disappearance of the highway, Int. Journal of Hydrogen Energy 44(2019) 15045-15055. https://doi.org/10.1016/j.ijhydene.2019.03.229

Mustapha BELKADI is a researcher with extensive experience and management skills and works for the Algerian National Company SONATRACH. He is a Manager of Development & Valorization Department at Central Direction of Research and Development of SONATRACH. He received his Engineer Diploma in Mechanical Engineering from National Institute of Mechanical Engineering (Ex-INGM), Boumerdes in 1994, Specialist Engineer in Gas Engineering (LNG specialist) from Algeria Institute of Petroleum (IAP-Boumerdes), Master of Sciences in Renewable Energy from Ecole Nationale Polytechnique (ENP), Algiers in 2012, and Doctor of Sciences in Mechanical Engineering from ENP, Algiers in 2020. Prior to joining SONATRACH in 2005, where he worked as a technical-commercial Engineer at Marketing Activity and Teacher Researcher at IAP-Boumerdes, Mr. Mustapha Belkadi worked as a Process Engineer at Algerian-Japanese Company of Engineering and Construction (ex-SAJEC-SPA, Subsidiary of JGC Japan Gas Company).

Arezki Smaili is a Professor of Mechanical Engineering and Director of Research Laboratory of Mechanical Engineering (Laboratoire de ''Génie Mécanique et Développement-LGMD'', at Ecole Nationale Polytechnique (ENP), Algiers. He received his engineer diploma in Mechanical Engineering from University of Sciences and Technologies Houari Boumediene (USTHB), Algiers in 1988, M.S. in Mechanical Engineering from Laval University, Québec (Canada) in 1991, and his PhD in Energy Sciences from University of Québec (Canada) in 1998. He joined the ENP in 2006. He was formerly research scientist at "Ecole de Technologie Supérieure", Montreal (Canada). He has been involved with wide range of energy conversion applications, particularly in the area of thermal analysis of clean and renewable energy systems and aerodynamics of wind turbines since the 1992.

A Simplified Diagnosis Method for CHBMIs under Open-circuit Switch or Battery Faults

Omar Kherif, Tahar Zebbadji, Youcef Gherbi, Mohamed Larbi Azzouze, and Madjid Teguar

Abstract—This paper deals with the diagnosis of cascaded H-bridge multilevel inverters controlled by a sinusoidal level-shifted pulse-width modulation technique. For this purpose, the behaviour of 3, 5, 7 and 9-level inverters is studied for regular and faulty operation modes. Three types of recurring faults are considered, namely open-circuit of a switch, damaged and disconnected battery. Under a single fault, the output voltage signals are presented where the impact of each fault is discussed. In order to detect, identify and localise the three types of fault, a signal processing method is proposed, elaborating the output voltage of inverters with and without fault. The obtained results are convincing for the considered cases. The study shows no real correlation between the selected features from one to the other type of fault. Indeed, each fault type has its own trajectory with respect to the evolution of the output voltage characteristics. Thus, localizing the faulty component within the multilevel inverter can be made with no ambiguity. Such findings obviously solve a large part of problems associated with the presence of faults in multilevel inverters. They can help improving the reliability of the inverter in such way it continues working.

***Keywords*—Cascaded H-Bridge, Diagnosis, Multilevel inverter, Industrial electronics, Voltage source inverter.**

I. Introduction

Multilevel inverters represent an ideal choice of the high-power demands for electric drives and renewable energies exploitation. These inverters might be considered as an important alternative in the area of high-power medium-voltage energy control with almost a high-quality output with low harmonic distortion [1]. Among many inverter's topologies, cascaded H-bridge multilevel inverter (CHBMI) presents an easier topology to implement with practically reduced harmonics [2]. CHBMIs are typically used to eliminate the bulky transformer required in the case of conventional multiphase inverters. These inverter also used to eliminate the clamping diodes and the flying capacitors required, respectively, in the case of diode and flying capacitor inverters [3, 4]. However, these, on one hand, require a large number of isolated voltage sources to supply each cell and, on the other hand, the number of switches needed increases accordingly. Thus, the fault probability of the accompanying system raises [5, 6].

The reliability of CHBMI has received much attention from researchers due to the occurrence of various faults within the system (e.g., [7–10]). An unbalanced voltage is generated when a fault occurs which can produce permanent damage to the load or complete system failure [8]. Most of these faults occur in switching devices, circuit boards, capacitors, and power sources [11]. If these faults are not fixed, a considerable negative impact on the performance of the inverter and the system to which it is connected will be observed [11]. The thermal factor might be considered as a source of disturbance that has more impact on the reliability of power electronics components and systems with a rate of 55%. Indeed, other factors such as humidity and vibrations are very often linked to the degradation of power devices [12].

In fact, CHBMI are currently utilized in an enormous variety of industrial applications, including variable speed AC drives. However, these inverters are quite susceptible to switch failures due to their complexity and exposure to several stresses [5]. According to [12], semiconductor defects account for 34% of failures in converter systems. Based on more than 200 products from 80 companies, semiconductor power devices were selected by 31% of respondents as being the most fragile components [12]. Capacitor faults include open-circuit/short-circuit, displacement of materials between electrodes creating a conductive path, dielectric breakdown, etc. [13]. In addition, PCB defects include broken metal pipes, corrosion or cracking of traces, misalignment of components, delamination of boards and cold welds [13].

Choi et *al.* [12] analysed the different methods of study and treatment of switch failures, giving statistics on this aspect. According to [8], on one hand, the short-circuit fault is difficult to handle because an abnormal over-current which can cause serious damage to other parts is produced immediately. On the other hand, the open-switch fault increases total harmonic distortion and adversely affects the grid, which is connected to. In literature, there is a great interest in detecting the faults that could occur in the controllable devices of multilevel inverters (e.g., [6, 14–16]). In [6] and [14], the detection method used a wavelet packet transform and a neural network algorithm without additional devices. Also, the current pattern by the

Manuscript received March 29,2021; revised August 2,2021.

O. Kherif is with The Advanced High Voltage Engineering Research Centre, School of Engineering, Cardiff University, CF24 3AA Cardiff, U.K. (e-mail: KherifO@cardiff.ac.uk).

T. Zebbadji, Y. Gherbi, M.L. Azzouze and M. Teguar are with Laboratoire de Recherche en Electrotechnique (LRE), Ecole Nationale Polytechnique, Algiers 16200, Algeria (e-mail: tahar.zebbadji@g.enp.edu.dz, youcef.gherbi@g.enp.edu.dz, mohamed_larbi.azzouze@g.enp.edu.dz).

Digital Object Identifier (DOI): 10.53907/enpesj.v1i2.23

open-switch fault of the two-level topology was used, in which, the detection method has been carried out using a differential equation of currents [15]. Therefore, most of the diagnostic methods for open-circuit faults have been practically focused on the occurrence of single faults. In addition, other works have the capability to handle and identify multiple failures (e.g., [10]). The average absolute values have been used here as prime quantities to formulate the diagnostic variables.

Indeed, any failure at a given level of the multi-level converter can cause abnormal operation of the electrical system. In electric drives, such a failure can cause the motor to overheat, increasing harmonics and acoustic noises, etc. Sometimes the need to shut down the entire drive system arises to avoid serious damage. To reduce downtime and therefore improve productivity, it is necessary to detect faults in converters in order to fix them [17]. It is well known that diagnosing faults in multilevel inverters is a difficult task requiring efficient and rapid decision-making procedures especially under extreme noisy measurement conditions, strongly interdependent data, large number of inputs and a complex interaction between symptoms and faults [1]. The diagnosis consists in locating the fault, and this, by comparing the current state of the system according to the readings of the sensors compared to that of normal operation [18]. Better understanding of the system dynamics might be a key factor that leads to a successful application, decreasing losses and improving the quality of the output voltage waveforms.

In this paper, simulation tests have been carried out to study a CHBMI under different possible faults. One switching device within the inverter has been affected by open-circuit faults. Also, the malfunction or disconnection of one DC link has been considered. Based on the output voltage records, the effects of the selected faults have been examined and the output voltage has been presented accordingly. The obtained results show the possibility to visually distinguish the fault features compared with the regular operation mode. Using the output voltages, THD, a_0, A_f, RMSE and STD have been used to extract information corresponding to the fault detection, identification and localisation. The obtained results confirm the effectiveness of the proposed fault diagnostic approach for 3, 5, 7, and 9-level inverters. Diagnostic results and the information on the identified faulty switches and batteries in multilevel converters can help to reduce the downtime cost of industrial power electronic systems.

II. Inverter Topology and Control Strategy

A. CHBMI Topology

Fig. 1 shows the circuit configuration of the selected three-phases power-conversion multilevel inverter.

The circuit has N-number of H-Bridge per phase, providing approximately a sinusoidal output voltage. For each phase, this later is the sum of the voltages that are generated by each cell. A given H-Bridge has been made up of four switches namely S_{1i}, S_{3i}, S_{2i} and S_{4i}, having an independent DC voltage source $V_{in} = E = E_i$.

The output voltage phase is synthesized by the sum of inverter outputs. Each single-phase full bridge inverter can generate three level outputs, $+E$, 0, and $-E$. This is made possible

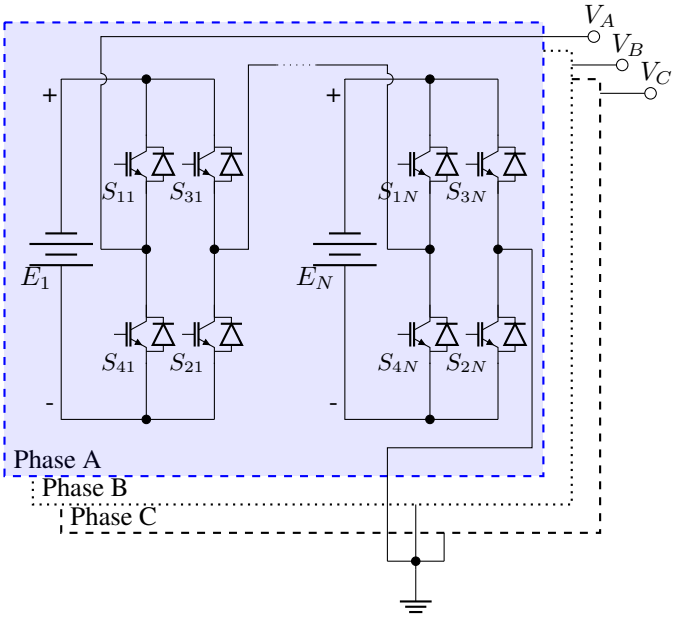

Fig. 1: Circuit configuration of the three-phase CHBMI

by connecting the DC sources sequentially to the AC side via the four semiconductor power devices. Fig. 2 illustrates the voltage polarities according to the switching states for each H-bridge(positive, zero and negative polarities in Figs. 2(a), 2(b) and 2(c), respectively).

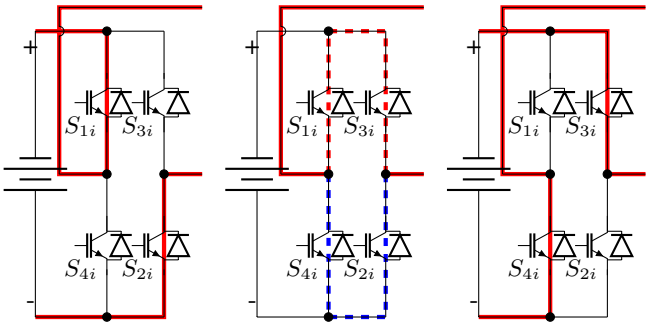

(a) Positive polarity (b) Zero polarity (c) Negative polarity

Fig. 2: Output voltage polarities for each H-bridge

From Fig. 2, a positive polarity is obtained for the case where S_{1i} is activated and S_{3i} is deactivated. The negative polarity appears for the complementary case. Moreover, the zero polarity is obtained during the simultaneous activation or deactivation of the switches (S_{1i} and S_{3i}). Table I summarizes the switching states of the 3-level inverter (only one H bridge). It is worth noting that the state of switch is designted by 1 or 0 when it is on ON-state or OFF-state, respectively.

For 5, 7 and 9-level inverter, a second, third and fourth block (bridge H) are added in cascade per phase, respectively. Each inverter will have the same three voltage levels, namely $+E$, 0 and $-E$ for every cycle. By cascading the output voltage of the H-bridge inverters per phase, a stepped voltage waveform is produced. It is well known that the level number of the output voltage is defined by $m = 2s + 1$, in which s is the number of DC sources or the cascaded H-bridges per leg. It is worth noting that the three output voltages of the three-phase cascaded

Table. I
SWITCHING STATES OF A H-BRIDGE INVERTER

Output voltage	Switching states	
V_A	S_{1i}	S_{3i}
E	1	0
0	1	1
0	0	0
-E	0	1

inverters can be connected in either wye or delta connection. The line voltage is equal to the phase voltage in delta connection. However, the line voltage is obtained by subtracting two phase voltages in wye connection. In this topology, the maximum number of levels is $m = 4s + 1$ and triplen harmonics are eliminated.

B. Control and Modulation Strategy

Multi-carrier PWM method is embraced in this investigation to achieve an approximately sinusoidal output voltage waveform per phase. In this method, PWM signals are generated by comparing a reference signal of sinusoidal form with triangular carriers. Three sinusoidal signals, shifted by $(2\pi/3)$–angle, are required for the three output voltages. Recall that for an inverter of N levels, there must be $(N-1)$ triangular carriers with the same frequency and amplitude, constituting the level shifted PWM (LS-PWM). Fig. 3 shows an example of the control signals for generating the pulses of the switches of a 5-level CHBMI, in which a switching frequency $F_c = 1kHz$ has been selected with a modulation ratio $M_i = 1$.

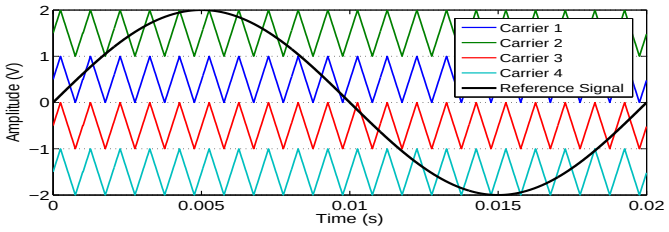

Fig. 3: PWM strategy for the 5-level CHBMI

Phase disposition strategy is used for the carrier arrangements (i.e., in phase with each other), which have the same peak to peak amplitude and F_c frequency. In this modulation technique, the sinusoidal reference is constantly compared with each of the triangular signals. If the reference is greater than the triangular signal, the switch corresponding to this modulation is active. Otherwise, the switch in question is in the ON state. For each sine signal, four features are obtained with respect to the four carriers. Fig. 4 illustrates an example of the triggering pulses obtained for the 5-level CHBMI.

III. FAULTY OPERATION MODE RESULTS

In this section, regular and faulty operation modes of the three-phase 3, 5, 7 and 9-level CHBMI have been presented. Each inverter has been simulated in MATLAB environment to assess the proposed fault detection technique. DC voltage sources of $30V$ have been considered with a fundamental frequency (f) of 50Hz and sampling (f_s) of 5kHz.

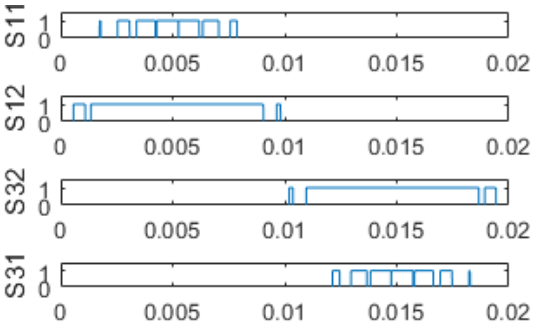

Fig. 4: Triggering pulses for the 5-level CHBMI

A. Open-Circuit Fault (Type I)

In this part, simulations have been carried out to show the effect of switches' open-circuit faults on the inverter output voltages. Fig. 5 shows the output voltage patterns, recorded for fault of one selected switch in the considered inverter. Figs. 5(a), 5(b), 5(c) and 5(d) show the effect of open–fault in CHBMI of 3, 5, 7, and 9 levels, respectively.

For regular operation mode (Fig. 5), each output voltage can be represented by Fourier series, in which the waveform is given as follows:

$$V(t) = \sum_{n=1}^{\infty} V_n \sin(n\omega t), \qquad \omega = 2\pi f \tag{1}$$

where, V_n is the amplitude of n-th voltage harmonic that is given by:

$$V_n = \begin{cases} \frac{4}{n\pi} \sum_{k=1}^{s} V_{dc} \cos(n\alpha_k) & \text{for odd n} \\ 0 & \text{for even n} \end{cases} \tag{2}$$

in which, s is the number of H-bridges and α_k is the switching angle used in the study $(2\pi/3)$.

Compared to the regular operation mode, one can see that all fault features in open-circuit cases could be visually detected. Fault in a particular switch within a given leg leads to a deformation on the output voltage of the corresponding phase related to this leg. For a single H-bridge, the failure of a switch causes the disappearance of the positive or negative part of the output voltage. The distorted output signal due to the open circuit type fault of switch S_{11} is exactly the same as that of S_{21} where only the negative part of the signal appeared. Regarding a fault at switch S_{31} or S_{41} (they have the same waveform), the output voltage contains only the positive part of the signal associated with regular operation. Therefore, only one spectrum can be found, describing the open circuit fault in a 3-level inverter as shown in Fig. 5(a)

Referring to the results of Fig. 5(b), three types of deformations have been noticed at the level of the output signal: two waveforms for a fault in H_1 and another waveform for H_2. The first one consist in the absence of $\pm 2E$ $(\pm 60V)$ levels in some intervals. For the second voltage waveform, there is a disappearance of $\pm E$ $(\pm 30V)$ levels with zero voltage levels during a time interval greater than half period. The complete absence of either positive or negative sequences is characterising the third waveform. Indeed, a type I fault of S_{11} and S_{31} brings out the same

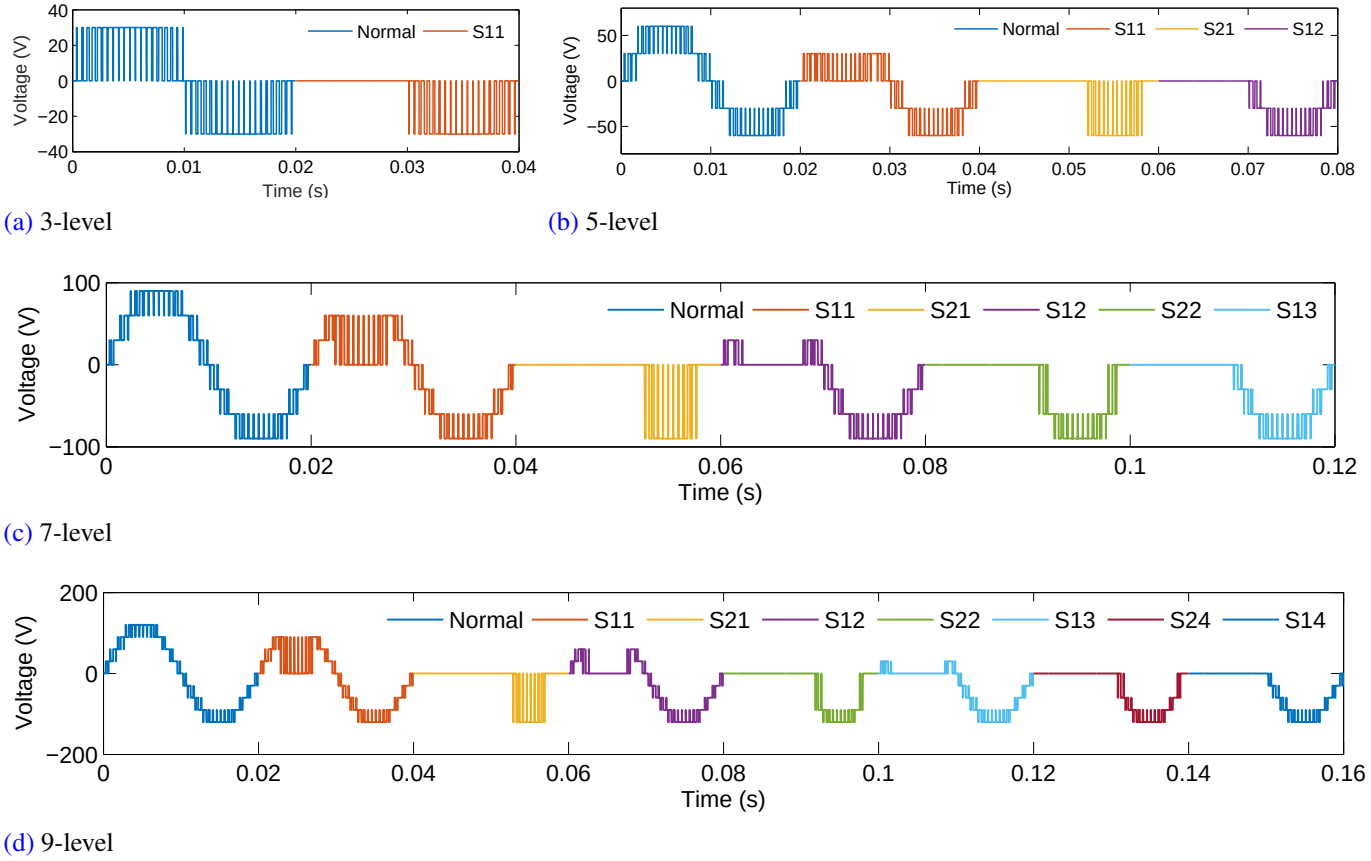

(a) 3-level (b) 5-level

(c) 7-level

(d) 9-level

Fig. 5: Output voltage of the 3, 5, 7 and 9-level inverters during a type I fault and normal operation mode

waveform with symmetrical characteristics with respect to the time axis. The same observation is perceived for the following pairs of switches: (S_{41} and S_{21}), (S_{12} and S_{32}) and (S_{22} and S_{42}). It should be noted that the waveform obtained for a type I fault of S_{12} and S_{22} are identical. Thus, if we consider the spectrum of the output voltage signal, three waveforms can be identified: the first waveform concerns the switches S_{11} and S_{31}, the second one is related to those of S_{21} and S_{41} and the last one is linked to those of S_{12}, S_{22}, S_{32}, and S_{42}.

From the results of Figs. 5(c) and 5(d), one can generalize the study to an N-level inverter system according to the output signals associated to a type I fault of a given switch. In this condition, a number $(N-2)$ of signal waveforms is obtained for an N-level inverter. Thereafter, the waveforms for each H-bridge are briefly described as follows:

1. Type I fault on H_1 :
   - In the switch S_{11} (S_{31} respectively): The deformation consists in the disappearance of the last level $(N-1)E/2$ in the positive (negative respectively) cap. In addition, during the interval where S_{11} (S_{31} respectively) is active, the voltage levels vary from 0 to $((N-1)/2-1)E$ in the positive (negative respectively) cap.
   - In the switch S_{41} (S_{21} respectively): The output voltage is zero except for the operating interval of S_{11} (S_{31} respectively) where it varies directly between 0 and $(N-1)E/2$.
2. Type I fault on H_i :
   - In the switch S_{1i} (S_{3i} respectively): The voltage is null during the ON-state interval of S_{1i} (S_{3i} respectively).
   - In the switch S_{4i} (S_{2i} respectively): The voltage is null during the whole period except the ON-state interval of S_{1i} (S_{3i} respectively).
3. Type I fault on H_N : The distorted output voltage following the appearance of a fault in S_{1n} is exactly the same as that in S_{2n}. The same observation is obtained for the two other switches (S_{3n} and S_{4n}). These two signals are also symmetrical with respect to the time axis with a phase shift of π.

B. Battery Fault Type II

Under particular conditions such as the batteries ageing, a DC source might be lost. The effect of such a fault has been investigated in this part where the internal resistor has been neglected. Fig. 6 shows the output voltages of the 9-level inverter such that the bridges H_1, H_2, H_3 and H_4 are in sequence way one after one under the type II fault.

In this figure, the obtained four signals can be overlapped to clarify the difference between the defected batteries. A common result between these four signals is the loss of the last level of voltage $(N-1)E/2$ ($4E$ in this case). It is true that there are 3 levels of voltage left, however, the arrangement of the remaining

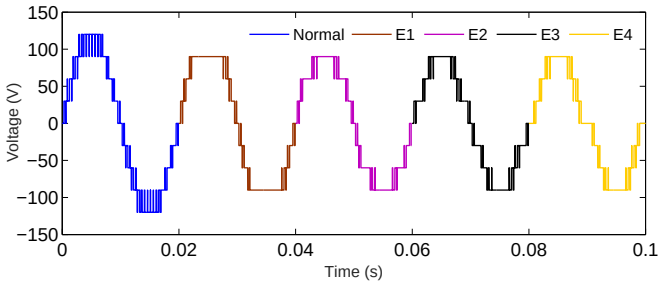

Fig. 6: Output voltages under type II fault in the CHBMI

levels is different. One can notice that a type II fault on the H_1 bridge, the 120V level is replaced by the one of 90V. A type II fault affecting the H_2 bridge generates the same waveform of signal found previously but with a slight decrease in the duration of the $90V$ level. For the fault concerning the H_3 bridge, we note that the duration of the $60V$ level has decreased slightly compared to that of the fault of the H_2 bridge. Whereas, for the fault concerning bridge H_4, the duration of the $30V$ level has decreased compared to that of the fault of bridge H_3. This means that the duration of each level is directly linked to the fault affecting a given bridge (H_i). This duration can be quantified by the control sequences of the different switches of a given bridge (see Fig. 6).

C. Battery Fault Type III

In this part, the battery of a given bridge is totally disconnected, hence, open-circuit at the input side of this bridge is obtained. Fig. 7 shows the V_{AN} output voltages of the 9-level inverter respectively for a fault in the battery disconnection of H_1, H_2, H_3 and H_4.

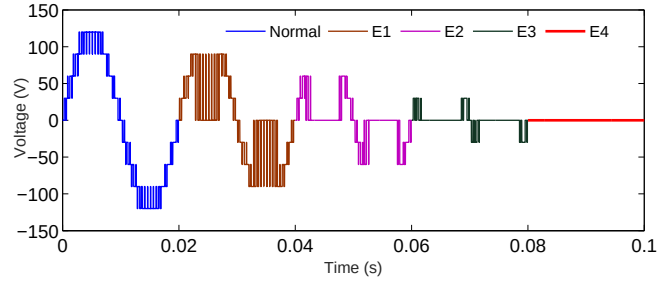

Fig. 7: Output voltages under type III fault in the CHBMI

Each battery contributes in a different way depending on its order of connection within the multilevel inverter. This means that the time contribution for each level is different from the other (see Fig. 7). Disconnecting a battery from a given bridge completely opens the phase for a well-defined period. By disconnecting the battery from the H_1 and for a modulation index equal to the unit, we notice the same phenomenon as that obtained for a simultaneous type I fault of S_{11} and S_{31}. Likewise, a type III fault affecting the H_i bridge is equivalent to a simultaneous type I fault of the switches S_{1i} and S_{3i}. By disconnecting the battery from the H_n bridges, one can notice that during the application of its own voltage E, the output voltage (V_{AN}) is null. It can be noted that the application duration of the voltage E associated to H_4 is observed throughout the period. Therefore, the voltage V_{AN} is null for the entire duration of the type III fault.

IV. Fault Diagnosis Method

A. Features Extraction Technique

In this section, a signal processing technique is presented, allowing the analysis of electrical signals in order to extract information useful for the detection and characterization of type faults (I, II and III). This method is based on the frequency decomposition of the signals, and this allows computing the THD, the mean value, the standard deviation and the root mean square error of the signals to be analysed in MATLAB environment. The frequency spectrum of a signal has been computed with and without faulty operation. Thereafter, the different parameters have been calculated.

Fourier series decomposition helps with the computation of the signal THD and the fundamental amplitude, which describe the quality of the output waveform. The signal mean value of the output voltage is the average of the instantaneous values measured over a full period, corresponding to the first component of the signal FFT. In addition, the standard deviation indicates the degree of variation or dispersion compared to the average (average or expected value). A low standard deviation indicates that the data points tend to be very close to the mean, while a high standard deviation indicates that the data is spread over a wide range of values.

B. Features Extraction Results for Type I Fault

1— Type I Fault in 3-level CHBMI: For the 3-level inverter, Table II illustrates the computed values of the parameters used in this study. These parameters have been calculated with and without a faulty operation.

Table. II
FEATURES OF THE 3-LEVEL INVERTER UNDER TYPE I FAULT

Operation with/without type I fault	$\mathbf{V_{AN}}$				
	THD (%)	**A_f (V)**	**a_0 (%)**	**STD**	RMSE (%)
Without	52.36	29.99	0	23.93	0
S_{11} or S_{21}	85.87	14.99	−63.68	13.97	29.25
S_{31} or S_{41}	85.87	14.99	+63.68	13.97	29.25

From Table II, the results show remarkable differences between the values obtained during regular operation mode and that under fault. Indeed, the fault of one open-circuit switch generates a remarkable increase in THD from 52.36 % to 85.87 %, accompanied by a decrease in the amplitude of the fundamental (denoted A_f) from 29.99 V to 14.99 V. This is to say that this fault generates a strong voltage distortion. In addition, this anomaly causes an increase of the relative error of the output voltage signal, up to 29.25%. Moreover, a decrease in the standard deviation of the signal from 23.93 to 13.97 was recorded. In faultless operation of the inverter, the voltage signal is characterized by its null mean value. The type I fault generates a signal distortion for the S_{11} and S_{21} switches symmetrically compared to that of S_{41} and S_{31}, that is why the same mean output voltage value; having opposite signs, has been obtained.

From the disparities between the obtained results, it is concluded that the selected features are capable of detecting and locating the fault by indicating the opening of a switch on the same path,

i.e., S_{11} or S_{21} on one hand, or S_{31} or S_{41} on the other hand, without indicating the exact position of the open-circuit switch.

2— Type I Fault in 5-level CHBMI: In the case of 5-level inverter, Table III illustrates the different values of the features used during this investigation.

Table. III
FEATURES OF THE 5-LEVEL INVERTER UNDER TYPE I FAULT

Operation with/without type I fault	$\mathbf{V_{AN}}$				
	THD (%)	$\mathbf{A_f}$ (V)	$\mathbf{a_0}$ **(%)**	**STD**	RMSE **(%)**
Without	26.91	60.10	0	43.99	0
S_{11}	67.89	36.53	−35.93	31.22	23.01
S_{31}	67.89	36.53	+35.93	31.22	23.01
S_{21}	110.54	23.52	−55.73	24.79	36.26
S_{41}	110.54	23.52	+55.73	24.79	36.26
S_{12} or S_{22}	57.72	30.05	−63.68	24.52	24.52
S_{32} or S_{42}	57.72	30.05	+63.68	24.52	24.52

According to the results of Table III, the operating mode with an anomaly can be detected when the THD value is greater than 26.91%. The fault in this case can be classified into 3 groups, corresponding to the three waveforms of signals shown in Fig. 5(b). The first group represents a fault in the lower switches of H_1 (S_{41} and S_{21}) with a THD of 110.54%. The second group characterises a fault in the upper switches (S_{11} and S_{31}) of H_1 with a THD of 67.89%. Finally, the third group is related to an open-circuit fault in all switches of H_2, having a THD of 57.72%. Regarding the sign of the mean value (positive or negative), one can locate the faulty switch within the three given groups as follows:

- Group 1: positive value means that the fault is on S_{41}, otherwise S_{21}.
- Group 2: positive value means that the fault is on S_{31}, otherwise it is on S_{11}.
- Group 3: positive (respectively negative) value means that the fault is on S_{42} or S_{32} (respectively S_{12} or S_{22}).

In general, the followed approach allows locating the default position of the switch, with the exception of the last bridge (H_2) where it is possible to distinguish between the pairs of switches (S_{12} or S_{22}) and (S_{42} or S_{32}).

3— Type I Fault in 7-level CHBMI: Table IV summarizes the different values of the proposed features for the 7-level inverter with and without type I defect.

The difference in THD values allows identifying four groups of switches. The group 1, made up of the switches S_{41} and S_{21}, stands out with a THD of 130.51%. The signals whose THD is 62.63% (default on S_{11} and S_{31} with the upper switches of the bridge H_2) compose the group 2. For a fault in the lower switches of H_2, the THD is 69.84%. The group 4 concerns the fault of all the switches of H_3, which is characterised by a THD of 50.56%.

Table. IV
FEATURES OF THE 7-LEVEL INVERTER UNDER TYPE I FAULT

Operation with/without type I fault	$\mathbf{V_{AN}}$				
	THD (%)	$\mathbf{A_f}$ (V)	$\mathbf{a_0}$ **(%)**	**STD**	RMSE **(%)**
Without	18.26	89.92	0	64.63	0
S_{11}	60.94	60.48	−26.16	50.06	18.80
S_{31}	60.94	60.48	+26.16	50.06	18.80
S_{21}	130.51	29.50	−53.65	34.25	41.67
S_{41}	130.51	29.50	+53.65	34.25	41.67
S_{12}	62.63	47.31	−53.25	39.47	27.57
S_{32}	62.63	47.31	+53.25	39.47	27.57
S_{22}	69.84	42.63	−59.11	36.76	31.07
S_{42}	69.84	42,63	+59.11	36.76	31.07
S_{13} or S_{23}	50.56	44,95	−63.68	35.63	29.29
S_{33} or S_{43}	50.56	44.95	+63.68	35.63	29.29

At this point, one can use the other parameters such as the fundamental amplitude, the absolute value of the DC component, STD or RMSE to obtain two complementary subgroups (belong to the group 2). The first subgroup 2.1 is formed by the upper switches of H_1 (S_{11} and S_{31}) whose fundamental value is equal to 60.48V. The subgroup 2.2 contains the two switches of H_2 (S_{42} and S_{22}) with the fundamental value of around 40V. Moreover, to distinguish between the switches of each group/subgroup, the sign of the mean values has been elaborated as follows:

- Group 1: positive (respectively negative) value means that the fault is on S_{41} (respectively S_{21}).
- Subgroup 2.1: positive value means that the default is on S_{41}, otherwise S_{21}.
- Subgroup 2.2: positive value means that the default is on S_{32}, otherwise it is on S_{12}.
- Group 3: positive value means that the default is on the switch S_{42}, otherwise it is on S_{22}.
- Group 4: positive value indicates that the fault is on S_{43} or S_{33}, otherwise it is on S_{13} or S_{23}.

It is important to note that this approach requires more precision to distinguish between either the switches of subgroups 2.1 and 2.2 or the pairs (S_{13} or S_{23}) and (S_{33} or S_{43}) due to the fact that the parameters values are close to each other.

4— Type I Fault in 9-level CHBMI: Table V illustrates the different values of the parameters used for the 9-level inverter for the type I fault.

Based on the results of the computed THD, five groups of switches can be obtained as follows:

- Group 1 is associated to a fault on S_{41} and S_{21}, which has a THD of 145.22%.

Table. V
FEATURES OF THE 9-LEVEL INVERTER UNDER TYPE I FAULT

Operation with/without type I fault	$\mathbf{V_{AN}}$				
	THD (%)	$\mathbf{A_f}$ (V)	$\mathbf{a_0}$ **(%)**	**STD**	RMSE **(%)**
Without	13.83	120	0	85.64	0
S_{11}	56.61	85.47	-21.27	69.44	16.18
S_{31}	56.61	85.47	$+21.27$	69.44	16.18
S_{21}	145.22	34.51	-52.68	43.02	45.47
S_{41}	145.22	34.51	$+52.68$	43.02	45.47
S_{12}	64.52	66.91	-45.03	56.31	25.43
S_{32}	64.52	66.91	$+45.03$	56.31	25.43
S_{22}	81.75	53.07	-56.77	48.47	33.36
S_{42}	81.75	53.07	$+56.77$	48.47	33.36
S_{13}	56.08	61.23	-58.36	49.64	28.58
S_{33}	56.08	61.23	$+58.36$	49.64	28.58
S_{23}	58.51	58.75	-60.83	48.13	30.01
S_{43}	58.51	58.75	$+60.83$	48.13	30.01
S_{14} or S_{24}	47.65	59.99	-63.69	46.99	29.29
S_{34} or S_{44}	47.65	59.99	$+63.69$	46.99	29.29

- Group 2 represents an open-circuit fault of the upper switches of H_1 (S_{11} and S_{31}) and all those of H_3 where the THD is around 57%.
- Group 3 characterises faults in the upper switches of H_2 (S_{12} and S_{32}) with a THD equal to 64.52%.
- Group 4, having THD equal to 81.75%, is related to faults of the lower switches of H_2 (S_{42} and S_{22}).
- Group 5 is linked to open-circuit of the H_4 with a THD of 47.65%.

It is worth noting that each group contains at least 2 switches. To overcome the localisation problem, the maximum value of the fundamental, the absolute value of the DC component, STD and RMSE have been exploited. For instance, as with the 7-level inverter, the sign of the mean values (a_0) might be used as follows :

- Group 1: positive value of a_0 means that the fault is on S_{41}, otherwise it is on S_{21}.
- Group 2 : this group, containing 6 switches, has been subdivided into the following subgroups :
  - Subgroup 2.1: positive (respectively negative) value of 52.68V means that the fault is on S_{41} (respectively S_{21}).
  - Subgroup 2.2: positive (respectively negative) mean value of 58.36V concerns fault is on S_{33} (respectively S_{13}).
  - Subgroup 2.3: this subgroup is identified by mean value of 60.83V, which is related to a fault on S_{43} (respectively S_{23}) if its sign is positive (respectively negative).
- Group 3: positive value of a_0 means that the fault is on S_{32}, otherwise it is S_{12}.
- Group 4: positive (respectively negative) value of a_0 indicates that the fault is on S_{42} (respectively S_{22}).
- Group 5: positive value of a_0 means that the fault is on S_{43} or S_{34}, otherwise, it is on S_{14} or S_{24}.

C. Features Extraction Results for Type II Fault

The same aforementioned features have been taken into account to deal with the fault localisation of a faulty battery in a 9-level inverter. The extracted features have been computed and illustrated in Table VI.

Table. VI
FEATURES OF THE 9-LEVEL INVERTER UNDER TYPE II FAULT

Operation with/without type II fault	$\mathbf{V_{AN}}$				
	THD (%)	$\mathbf{A_f}$ (V)	$\mathbf{a_0}$ **(%)**	**STD**	RMSE **(%)**
Without	13.83	120	0	85.64	0
E_1	16.86	102.7	0	73.65	13.99
E_2	19.15	90.35	0	65.05	24.05
E_3	19.90	84.67	0	61.04	28.72
E_4	24.40	82.19	0	59.82	30.15

According to this table, one can observe that the mean value is null for all cases of this type of fault. This observation is due to the fact that the signals extracted after the appearance of a fault always remain symmetrical with respect to the time axis. This parameter no longer fits into the fault localisation. From the THD readings, the type II fault of battery E_1 and E_4 can be easily detected because their respective THD is 16.86% and 24.4% compared to the regular operation mode (THD=13.83%).

For the fault of battery E_2 and E_3, their THD values are practically close: 19.15 % and 19.90 %. To overcome this situation, the fundamental amplitude, STD and RMSE have been used. For type II fault of battery E_2 or E_3, these parameters are respectively equal to (90.35V, 65.05, 24.05%) and (84.67V, 61.04, 28.72%).

D. Features Extraction Results for Type III Fault

In this part, features have been extracted from the output voltage of the 9-level inverter under a type III fault. Table VII illustrates the different values of the selected parameters.

For this type of fault in a 9-level inverter, Table VII shows a remarkable difference in all features except for the mean value, which remains null. For the case of fault of the first three batteries (E_1, E_2, and E_3), one can note that the values of each parameter vary (increase or decrease) for a given feature compared to the regular operation mode. This is to say that such a fault is easily detected. For the localisation purpose, the THD and RMSE increase from fault in the battery E_1 to E_3. The intermediate values of THD and RMSE allow concluding that the battery E_2 is defected. In addition, fault in the battery E_1 is identified by a higher value of the fundamental amplitude (50.96V), which decreases to 13.85V and 2.49V for a fault in the

Table. VII
FEATURES OF THE 9-LEVEL INVERTER UNDER TYPE III FAULT

Operation with and without type III fault	$\mathbf{V_{AN}}$				
	THD (%)	**A_f** (V)	**a_0 (%)**	**STD**	RMSE (%)
Without	13.83	120	0	85.64	0
E_1	113.52	50.96	0	54.51	36.35
E_2	274.96	13.85	0	28,66	66.54
E_3	684.09	2.49	0	12.17	85.79
E_4	–	0	0	0	100

battery E_2 and E_3, respectively. For the case of the last battery (E_4), almost all the parameters are null for the output voltage with the exception of RMSE (100%) and the THD. Therefore, for a right diagnosis, it would be wise to take into account the phase-to-phase voltage.

E. Features Extraction Comparison

From the obtained results of the proposed diagnostic method, it is possible to distinguish between regular operation mode (without fault) and that in the presence of a type I, II or III fault. This distinction is ensured by the use of the vector [THD, A_f, a_0, STD, RMSE]. One can recall that obtaining a non-null mean value, a_0, of the voltage signal, means that a type I fault is faced. However, a null mean value, of this, implies a type II or III fault. Parameters, other than the average value, make possible distinguish between these last two types of fault. In addition to the mean value a_0, two parameters (THD and A_f) are largely sufficient, in the actual case, to separate between the different types or at least between those of II and III, as illustrated in Fig. 8.

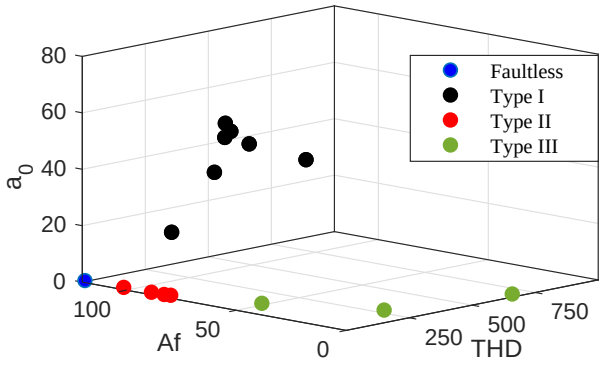

Fig. 8: Parameters distribution with respect to the type of faults for 9-level inverter

Regular operation is indicated by the blue dot. Likewise, the three assemblies presenting the three types of faults are isolated from each other. Since the features round up in separated groups in Fig. 8, the proposed method confirms the absence of correlation between the different types of faults considered. In general, the more uncorrelated the features, the better the classifier performance, which improves the identification process.

V. CONCLUSION

This paper dealt with the diagnosis of CHBMI under typical faults where their effects have been examined. First, fault in one of the controllable components has been considered, in which an open-fault case has been selected (Type I). Then, DC link faults have been studied for defected (Type II) and disconnected (Type III) battery. Simulations show the possibility to visually distinguish the fault features from the output voltage signal compared to the regular one. Based on the obtained results, a diagnostic method has been proposed using THD, A_f (amplitude of the fundamental), a_0 (mean value), STD (standard deviation) and RMSE (the mean square error) of the output voltage signal. The first three parameters are largely sufficient to distinguish between the three types of faults. This is due to the total lack of correlation between these faults. The location of faults is done by a classification according to their THD. Faults in switches with the same THD order have been classified in the same group. The other parameters allow further decision between the groups formerly considered. The three types of faults can be identified since the selected features are round up in separated groups. Such findings and the proposed technique might be used to extract a general fault diagnosis method to detect and locate the fault in higher level CHBMIs. The diagnostic results and the information on the identified faulty switches in multilevel converters can help the reduction of the downtime cost of industrial power electronic systems.

REFERENCES

[1] P. Lezana, J. Pou, T. Meynard, J. Rodriguez, S. Ceballos and F. Richardeau, , "Survey on fault operation on multilevel inverters", *IEEE Trans.Indus. Elect.*, vol. 57, no. 7, pp. 2207–2218, Jul. 2010. https://doi.org/10.1109/TIE.2009.2032194

[2] H. Mhiesan, Y. Wei, Y.P. Siwakoti and H.A. Mantooth, "A Fault-Tolerant Hybrid Cascaded H-Bridge Multilevel Inverter", *IEEE Trans. Power Elect.*, vol. 35, no. 12, pp. 12702–12715, Dec. 2020. https://doi.org/10.1109/TPEL.2020.2996097

[3] G. Sani Shehu, A. Bala Kunya, I. Shanono and T. Yalcinoz, "A Review of Multilevel Inverter Topology and Control Techniques", *International Journal of Automation and Control*, vol. 4, no. 3, pp. 233–241, Jun. 2016. https://doi.org/10.1109/MEPCON.2017.8301344

[4] Grain Adam, S.J. Finney, A.M. Massoud and B. Williams, "Capacitor Balance Issues of the Diode-Clamped Multilevel Inverter Operated in a Quasi Two-State Mode", *IEEE Trans. Indus. Elect.*, vol. 55, no. 8, pp. 3088–3099, Sep. 2008. https://doi.org/10.1109/TIE.2008.922607

[5] J.O. Estima and A.J.M. Cardoso, "A new algorithm for real-time multiple open-circuit fault diagnosis in voltage-fed PWM motor drives by the reference current errors," *IEEE Trans. Indus. Elec.*, vol. 60, no. 8, pp. 3496–3505, Aug. 2013. https://doi.org/10.1109/TIE.2012.2188877

[6] M.A.S.K. Khan and M. Azizur-Rahman, "Development and implementation of a novel fault diagnostic and protection technique for IPM motor drives," *IEEE Transactions on Industrial Electronics*, vol. 56, no. 1, pp. 85–92, Jan. 2009. https://doi.org/10.1109/TIE.2008.2004662

[7] A. Anand, A. Vinayak, N. Raj, G. Jagadanand and S. George, "A Generalized Switch Fault Diagnosis for Cascaded H-Bridge Multilevel Inverters Using Mean Voltage Prediction", *IEEE Trans. Indus. Apps.*, vol. 56, no. 2, pp. 1563–1574 , Mar./Apr. 2020. https://doi.org/10.1109/TIA.2019.2959540

[8] J.S. Lee and K.B. Lee, “An Open-Switch Fault Detection Method and Tolerance Controls Based on SVM in a Grid-Connected T-Type Rectifier With Unity Power Factor," *IEEE Trans. Indus. Elect.*, vol. 61, no. 12, pp. 7092–7104, Dec. 2014. https://doi.org/10.1109/TIE.2014.2316228

[9] S. Khomfoi and L. M. Tolbert, “Fault Diagnosis and Reconfiguration for Multilevel Inverter Drive Using AI-Based Techniques," *IEEE Trans. Indus. Electronics*, vol. 54, no. 6, pp. 2954–2968, Dec. 2007. https://doi.org/10.1109/TIE.2007.906994

[10] J.S. Lee and K.B. Lee, “A Fault Detection Method and a Tolerance Control in a Single-Phase Cascaded H-bridge Multilevel Inverter," *IFAC PapersOnline*, vol. 50, no. 1, pp. 7819–7823, Jul. 2017. https://doi.org/10.1016/j.ifacol.2017.08.1058

[11] W. Qiao and D. Lu, “A survey on wind turbine condition monitoring and fault diagnosis—Part I: Components and subsystems", *IEEE Trans. Indus. Elect.*, vol. 62, no. 10, pp. 6536–6545, Oct. 2015. https://doi.org/10.1109/TIE.2015.2422112

[12] U. Choi, F. Blaabjerg and K. Lee, “Study and handling methods of power IGBT module failures in power electronic converter systems", *IEEE Trans. Power Elect.*, vol. 30, no. 5, pp. 2517–2533, May 2015. https://doi.org/10.1109/TPEL.2014.2373390

[13] M.L. Hossain, A. Abu-Siada and SM. Muyeen, “A hybrid multilevel power electronic inverter and fault location identification of switching devices", *IEEE 2018 Condition Monitoring and Diagnosis (CMD)*, pp. 1–4, 2018. https://doi.org/10.1109/CMD.2018.8535618

[14] Y.J. Ko, K.B. Lee, D.C. Lee, and J.M. Kim, “Fault diagnosis of three-parallel voltage-source converter for a high power wind turbine," *IET Power Electronics*, vol. 5, no. 7, pp. 1058–1067, Aug. 2012. https://doi.org/10.1109/ECCE.2011.6063863

[15] W.S. Im, J.M. Kim, D.C. Lee, and K.B. Lee, “Diagnosis and fault-tolerant control of three-phase ac-dc PWM converter systems," *IEEE Transactions on Industrial Applications*, vol. 49, no. 4, pp. 1539–1547, Jul./Aug. 2013. https://doi.org/10.1109/TIA.2013.2255111

[16] O. Kherif, Y. Benmahamed, D. Maadjoudj, M. Teguar, M. Bounabi and C. Larbes, “Fault Diagnosis Method for Cascaded H-bridge Multilevel Inverters under Switching Device Failure," *2019 19th Int. Symp. Electromagnetic Fields in Mechatronics, Electrical and Electronic Engineering (ISEF)*, Nancy, France, France, 29–31 Aug. 2019. https://doi.org/10.1109/ISEF45929.2019.9096978

[17] J. Amini and M. Moallem, “A fault-diagnosis and fault-tolerant control scheme for flying capacitor multilevel inverters", *IEEE Trans. Indus. Elect.*, vol. 64, no. 3, pp. 1818–1826, Mar. 2017. https://doi.org/10.1109/TIE.2016.2624722

[18] M. Ardakani, M. Askarian, A. Shokry, et *al.*, “Optimal features selection for designing a fault diagnosis system", *Computer Aided Chemical Engineering*, vol. 38, pp. 1111–1116, Jun. 2016. https://doi.org/10.1016/B978-0-444-63428-3.50190-9

Omar KHERIF received a M.Eng. and Ph.D. degrees in electrical engineering from the Ecole Nationale Polytechnique (ENP) in 2015 and 2019, respectively. He was a mathematical-analysis teacher with ENP from 2016 to 2018. He was also researcher with the Laboratoire de Recherche en Electrotechnique (LRE) of the ENP, where he co-supervised several M.S. theses. He is currently a KTP Associate with Cardiff University and a Technical Consultant with Kingsmill Industries Ltd (UK). His main interests are in high voltage engineering, electromagnetic transients, earthing and power system protection. Dr Kherif is a member of IEEE and some of IEEE societies since 2017.

Tahar ZEBBADJI Tahar received his Engineer Diploma from the Ecole Nationale Polytechnique (ENP) of Algiers in 1984 and then obtained the Master degree from the University of Colorado, Boulder, USA in 1987. He is currently a senior lecturer in the department of electrical engineering with the Ecole Nationale Polytechnique of Algiers. He is also a member of the research team of the Laboratoire de Recherche en Electrotechnique (LRE), ENP, Algiers. His main area of interests includes the modelling and control of power electronics.

Youcef GHERBI was born on April 23rd, 1997 in Algiers. He received a M.S. and Engineer degrees in Electrical Engineering from Ecole Nationale Polytechnique (ENP) in 2020. He was also researcher with the Laboratoire de Recherche en Electrotechnique of the ENP. Mr Gherbi is currently an Instrumentation & Control Engineer in the Oil & Gas industries. His main research interests are in power electronics and renewable energies.

Mohamed Larbi AZZOUZE received a M.S. and Engineer degrees in electrical engineering from Ecole Nationale Polytechnique (ENP) in 2020. He was also researcher with the Laboratoire de Recherche en Electrotechnique of the ENP. Mr AZZOUZE is currently a MSc student in Global Purchasing and Supply Chain Management at Audencia Business School. His main research interests are in power electronics and diagnosis.

Madjid TEGUAR received the degree in electrical engineering, the master’s degree, and the Ph.D. degree in high voltage engineering from the École Nationale Polytechnique (ENP) of Algiers, in 1990, 1993, and 2003, respectively. He is currently a Professor of Electrical Engineering with ENP. His research interests include insulation systems, insulation coordination, earthing of electrical power systems, and polymeric cables insulation.

Polluted Barrier Effect on the Electric Field Distribution in Point-Plane Air Gaps under AC Applied Voltage: Based on Experimental Model

Mohamed Abdelghani Benziada, Ahmed Boubakeur, and Abdelouahab Mekhaldi

Abstract− The aim of this paper is to study the effect of the surface condition of an insulating barrier on the electric field distribution in point-plane air gaps with the presence of a space charge, under AC voltage. The pollution was modelled as a uniform conductive layer on the barrier surface. Electric field analysis was carried out by changing the conductivity, permittivity, and thickness of the pollution layer. Using the Finite Element Method (FEM), the geometric model has been implemented in COMSOL Multiphysics software. This method is used to solve the partial differential equations that describe the field with the presence of space charge. The electric field increases when the conductivity and thickness of the polluted layer increases. Uniform pollution on the side of the high voltage point greatly reduces the insulation quality of the barrier. In addition, a limit level of pollution, from which its minimal electric strength is equivalent to that of a conductive barrier, has been determined. This model has been validated by comparing with the experimental results of a point-barrier-plane configuration with a distance between electrodes equal to 5cm. The distribution of the electric field predicted by the numerical model is in accordance with the experimental results. The latter indicate that this model has a great contribution in the physics of discharges in the air under various polluted environments.

Keywords− barrier surface condition, conductive layer, electric field, finite element, numerical method, point-plane air gap, space charge.

I. Introduction

The improvement of the dielectric strength of the non-uniform field air gaps by the insertion of insulating barriers has been well demonstrated under a clean and dry atmosphere and under AC, DC or impulse voltages [1-7].

In the high-voltage domain, pollution is a serious problem that must be taken into account when designing insulating systems. This is due to the formation of more or less conductive layers on the surface of the barriers, which used between electrodes in high voltage technique. These electrodes can be either the metal parts of different live equipment or the conductors of overhead lines or high-voltage terminals in testing laboratories. These polluting deposits covering the insulating surfaces can cause a considerable reduction in the dielectric strength of the high-voltage systems.

Knowledge of the degree of pollution is, therefore, a prerequisite and indispensable condition for a suitable insulation dimensioning.

Awad [8] studied the behavior of polluted barriers in point-point and point-plane air gaps of less than 12 cm in length. The voltages used were 50 Hz industrial frequency and switching impulse. It has been found that the breakdown voltage decreases when the surface conductivity increases and then tends to a constant value for a surface conductivity greater than or equal to 3 µS in the case where the polluted surface is in front of the point electrode.

In 1979, A. Boubakeur [9] studied the influence of a polluted barrier covered by a semiconducting or a conductive layer on the dielectric strength of a point-barrier-plane system. The semiconducting layers on the barrier correspond to the practice of using the barrier in polluted conditions. As soon as the surface conductivity of the semiconductor layers exceeds 1.6µS [10], the electrical discharge develops in two steps, as in the case of a metal barrier [11,12]. With a semiconductor surface barrier, the breakdown voltage of the point-plane air gaps varies between the values obtained with the insulating barrier with clean surfaces and those obtained with the metal barrier of the same shape.

The most recent works are those carried out by S. Mouhoubi [13,14] and concern the case of point-barrier-plane systems under DC and AC voltage. The pollution applied to the upper surface of the barrier facing the point causes an increase in the electric field at the plane, whatever the position of the barrier. Nevertheless, the completely polluted barrier causes a greater increase of the electric field, compared to the case where the barrier is only polluted on its upper surface.

With the growing development of computing electromagnetic software, it is now possible to obtain fast and accurate results. Among the numerical methods available and applicable to electromagnetic field calculations, the finite element method is the most used one. Thus, its use through the COMSOL Multiphysics commercial software was selected to carry out the various simulations.

In this work, the electric field distribution in a point-barrier-plane air gap was determined under an AC applied voltage. Conductivity, permittivity, and thickness of the pollution layer were varied to investigate their effect on the electric field distribution. The 2D model from COMSOL Multiphysics was used for modelling. To interpret the results

Manuscript received March 29, 2021; revised August 5, 2021.

M. A. Benziada, A. Boubakeur and A. Mekhaldi are with the Electrical Engineering Department, Ecole Nationale Polytechnique, Algiers, ALGERIA,
(e-mail: mohamed_abdelghani.benziada@g.enp.edu.dz, ahmed.boubakeur@g.enp.edu.dz, abdelouahab.mekhaldi@g.enp.edu.dz).

Digital Object Identifier (DOI): 10.53907/enpesj.v1i2.21

of our model, the simulation results are compared with experimental data obtained by S. Mouhoubi [13,14].

II. SIMULATION MODEL

To simulate the electric field in the air, a drift-diffusion model is used. This model describes the generation, the annihilation and the movement of three species (electrons, positive ions, and negative ions) [15]. It includes a set of mass conservation equations for the charge carriers in the gas coupled with the Poisson's equation for the calculation of the electric field and is described by the equations (1) and (2) [15,16]:

$$\frac{\partial N_{e,p,n}}{\partial t} + \nabla.\left(-N_{e,p,n}W_{e,p,n} - D_{e,p,n}\nabla N_{e,p,n}\right) = R_{e,p,n} \quad (1)$$

$$(-\varepsilon_0\varepsilon_r\nabla V) = q\left(N_p - N_e - N_n\right),\ E = -\nabla V \quad (2)$$

The subscripts *e, p,* and *n* indicate the quantities related to electrons, positive ions, and negative ions, respectively. *N* stands for the charge carrier density, [m^{-3}]; *D* is the diffusion coefficient, [$m^2\ s^{-1}$]; ***E*** is the vector of electric field, [Vm^{-1}]; V is the electric potential, [V]. *t* stands for time, [s]; and *R* specifies source terms (rates of the processes in discharge plasma), [$m^{-3}\ s^{-1}$]; $q = 1.6\cdot10^{-19}$ [C] is the elementary charge, and $\varepsilon_o = 8.854\cdot10^{-12}$ [Fm^{-1}] is the permittivity of vacuum [15].

The resulting process rates for the different charged particles can be expressed as follows [15,16]:

$$\begin{aligned} R_e &= R_{ion} + R_{det} + R_0 - R_{att} - R_{ep} \\ R_p &= R_{ion} + R_0 - R_{pn} - R_{ep} \\ R_n &= R_{att} - R_{det} - R_{pn} \end{aligned} \quad (3)$$

R_0 represents the rate of background ionization in zero field limit; $R_{ion} = \alpha N_e W_e$ is the rate of electron impact ionization (α stands for Townsend's ionization coefficient, m^{-1}); $R_{att} = \eta N_e W_e$ is the rate of electron attachment to electronegative molecules (η is attachment coefficient, m^{-1}); and $R_{det} = k_{det}N_eN_n$ is the rate of detachment of electron from negative ions (k_{det} is detachment coefficient, m^3/s).

Two types of recombinations are considered, electron-ion and ion-ion, with the rates $R_{ep} = \beta_{ep}N_eN_p$ and $R_{pn} = \beta_{pn}N_pN_n$, respectively ($\beta$ stands for corresponding recombination coefficient, m^3/s).

In our study, the used model parameters, the boundary and initial conditions used are adopted from [15,16] and are implemented in COMSOL Multiphysics.

A. Modeling of thin conductive layer

To study the influence of pollution on the distribution of the electric field, the pollution layer was modelled as a thin conductive layer uniformly distributed over the insulating barrier. The parameters of the polluted layer are given in the table 1.

Table. I

POLLUTION PARAMETERS

	Permittivity [F/m]	Conductivity [mS/cm]
Insulating barrier	5.8	0
Polluted barrier [17]	15 and 80	0.0235
		0.45
		1
		2

The used thickness for polluted layers are 0.1mm, 0.3mm and 0.5mm. The algorithm developed to calculate the electric field is represented in Fig 1. For our simulation, t_{out} is equal to 100 ms and the peak value of the AC voltage is used.

The input parameters for initializing calculations are the dimensions of the physical domain, gas pressure, potentials of the electrodes, number of nodes in the computational grid, desired output times and the initial distribution of space charges (if any).

The routine "Output Electric field" calculates data needed for the main solvers and calls subroutine "Resolution of the Poisson's equation", which solves the Poisson's equation (2). The output from it is the distribution of the electric field in the discharge gap (after the first call it gives the electrostatic field distribution if no space charge was set initially). Then the routine "Resolution of mass conservation equations" is called for solving system (1) – (3).

This routine calculates the time step advances the profiles of the densities of charged particles taking into account the source terms and computes the space charge density profiles using the electric field distribution obtained earlier. Then, the current time is updated and the routine subroutine "Resolution of the Poisson's equation" is called again to calculate the electric field corresponding to the new space charge distribution. If the current time is not greater than the desired output time, the loop "Resolution of mass conservation equations" – "Resolution of the Poisson's equation" is repeated until the condition is fulfilled [15].

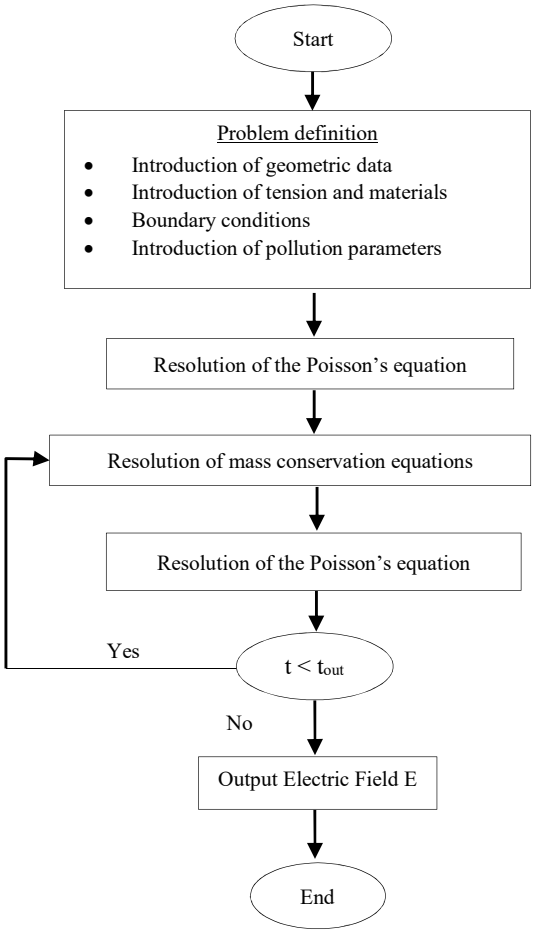

Fig.1: Simulation chart.

B. Implementation

In Fig 2, the geometry of the used point-plane electrode system with an insulating barrier is presented. To simulate our model, an AC voltage 50 HZ has been applied to the high-voltage electrode (point) and the plane is grounded considering that atmospheric conditions are normal.

A 2D simulation was performed for a point-plane electrode arrangement. The boundary conditions used in our simulation are given in Fig 3.

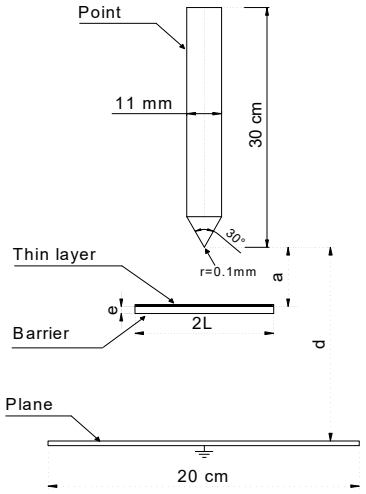

Fig.2: Point-barrier-plane configuration.

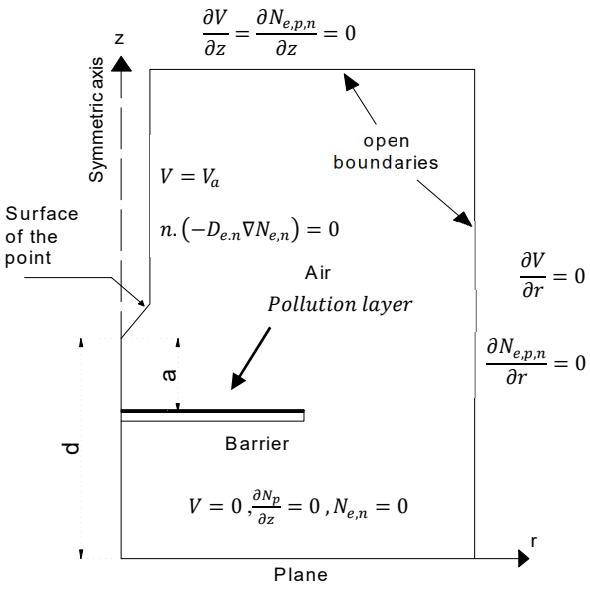

Fig.3: Computational domain, **n** is the unit vector normal to the boundary.

C. Validation of the model

To validate our model, a comparison is made with experimental results of investigations already performed using a capacitive probe carried out at the University of Cardiff by Mouhoubi and Boubakeur (Fig 2) [13,14].

D. Experimental Set-up and Measurement Method

The experimental set-up and measurement method are based on experiments measuring electric field under AC stress [13,14].

The capacitive probes is a portable probe, which is generally used for measurements of the electric field on site (apparatus, lines, stations, etc.). It consists of a surface element S isolated from the grounded circular plane (Fig 4). The S probe is connected to an electrical measuring circuit, introduced into a grounded housing, acting as a screen (Fig 5). Two 9-volt batteries power it. The design of the probe as well as elements of the electrical circuit is obtained by simulation using a software package Slim (Electromagnetic Engineering Alstom).

Considering equation (4), the electric field can be determined using a memory oscilloscope or a PC with an interface, which allows the V_c probe signal corresponding to the voltage across the capacitor C_{11} (Fig 6).

$$E = \frac{C_{11}.V_c}{\varepsilon_0.S} \qquad (4)$$

Where V_c is the voltage across the capacitance C_{11}.

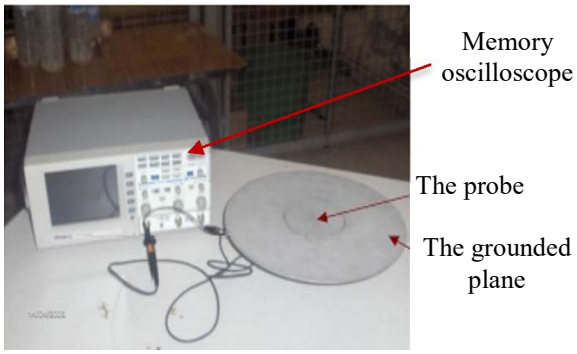

Fig.4: Photograph of the capacitive probe [13].

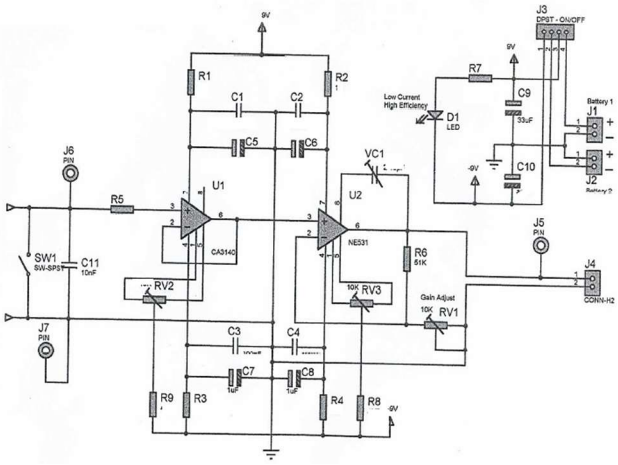

Fig.5: Electric circuit diagram of the capacitive probe [13].

Knowing the surface of the probe S as well as the value of the capacitance C_{11} :

$$E = 14.388 \times V_c \text{ (kV/m)} \qquad (5)$$

For a voltage of 10 kV applied to the high voltage electrode, the V_c voltage recorded across the capacitance of the probe is shown in Fig 6. The field probe schema as well as its characteristics used in the experimental tests are represented below (Fig 7):

- The radius of the probe (S_0): r = 2.235 mm.
- The inside radius of the electrode (E_1): re = 2,270 mm, which gives an air gap g = 0,035 mm and an effective radius of the probe rm = 2.2525 mm.

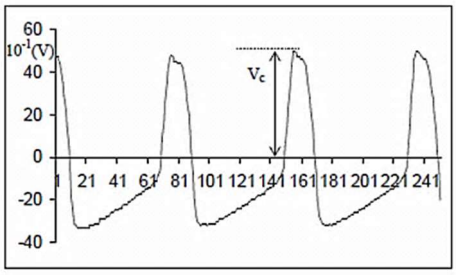

Fig.6: Oscillogram of the voltage V_c of the capacitive probe [14].

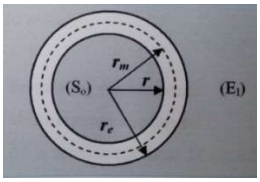

Fig.7: Field probe schema [14].

III. RESULTS AND DISCUSSIONS

The results in this work concern the electric field distribution at the plane in the presence of a space charge density in the medium, which varies from $[1 \div 50]x10^{-7}C/m^3$. This range

of values gives better results compared to the experimental model. Several parameters, such as conductivity, permittivity, and thickness of the pollution layer are considered. We studied the influence of these parameters on one side of the barrier (in front of the point and in front of the plane) and on the two sides of the barrier. The influence of variation of the barrier length is not studied in this paper and is considered equal to 15 cm.

To better understand the performance of this method, an analysis that illustrates the relative error of the method compared to the experimental results in the calculation of the electric field at the plane was performed.

A. Influence of polluted barrier

We begin by studying the influence of a polluted barrier on its upper surface on the electric field at the plane in comparison with the experimental results obtained by Mouhoubi [13,14].

Fig 8 shows the influence of the polluted barrier on the variation of the electric field at the plane as a function of the voltage V. The electric field increases by increasing the applied voltage. We also note that the pollution increases the electric field at the plane [18]. A good correlation between experimental and calculated results for the insulating barrier (error < 6%), and a slight difference for the polluted barrier has been found (error < 10%).

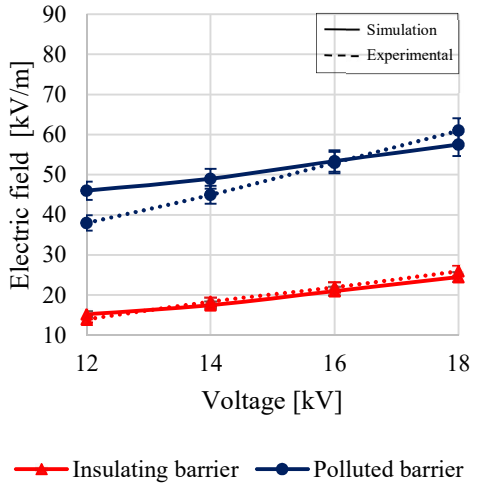

Fig.8: Influence of the polluted barrier on the variation of the electric field at the plane as a function of the voltage V (d = 5 cm, a/d = 0%, 2L = 15 cm, e=2.1mm, σ=0.45 mS/cm).

Fig 9 shows the variation of the electric field as a function of the applied voltage at the point, for two positions of the barrier, a/d = 0% and 20%, in the case of the polluted barrier facing the point.

The pollution applied to the upper face of the barrier causes the increase of the electric field at the plane, regardless of the position of the barrier [18]. It is useful to note that the electric field at the plane in the case of a polluted barrier, as for the clean barrier, increases by moving the barrier away from the point. Consequently, the dielectric strength decreases by increasing the ratio a/d [14].

There is a difference between the simulation results and the experimental data especially when the voltages are greater than 16 kV for the position a/d=0% and 14 kV for the position a/d=20%, and when the voltages are close to the indicated values, the simulation is closer to the experimental results.

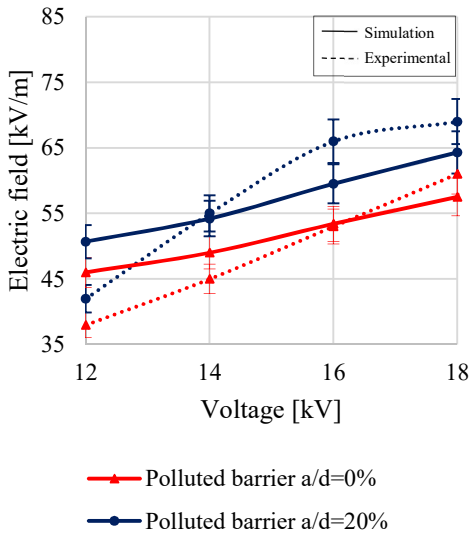

Fig.9: Influence of the position of the polluted barrier on the variation of the electric field at the plane as a function of the voltage V (d = 5 cm, 2L = 15 cm, e=2.1mm, σ=0.45 mS/cm).

B. Influence of pollution mode

The influence of the mode of pollution on the variation of the electric field at the plane as a function of the voltage V for a polluted barrier is shown in Fig 10.

From this figure, it can be observed that whatever the mode of pollution applied to the barrier, the electric field is higher than that of the clean barrier. In particular, the completely polluted barrier causes a greater increase of the electric field compared to the case where the barrier is only polluted on its upper surface [18]. For the insulating barrier, we observe that the simulation results are close to the experimental ones and the error is less than 5%. On the other side, for the polluted barrier, the experimental and the simulation data are within an error tolerance of +/- 10%. We also observe that the simulation results are close to the experiment ones, especially for high voltage values.

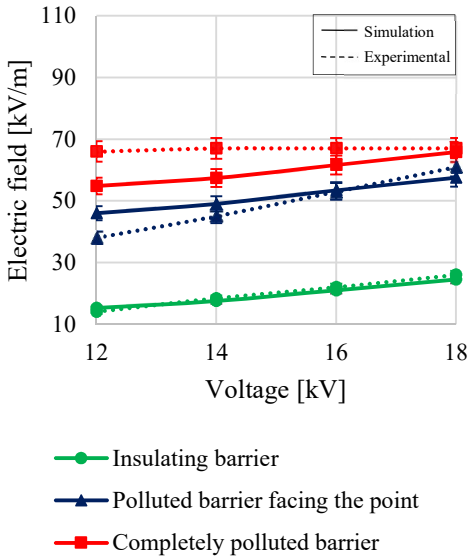

Fig.10: Influence of the pollution mode on the variation of the electric field at the plane as a function of the voltage V for a polluted barrier (d = 5 cm, a/d = 0%, 2L = 15 cm, e=2.1mm, σ=0.45 mS/cm).

C. Influence of layer conductivity

We examine now the effect of the layer conductivity on the electric field distribution at the plane for the three cases: polluted barrier facing the point, facing the plane, and completely polluted.

The x-axis (position on the plane) represents the distance between the center and the edge of the plane.

The results, presented in Fig 11,12 and 13, were obtained for an AC voltage equal to 22 kV, conductivity values of 0 S/m (clean barrier), 0.0235mS/cm, 0.45mS/cm, 1mS/cm and 2mS/cm, and for permittivity thin layer value of 80. Pollution layer thickness was kept constant at 0.1 mm.

From these figures, we note that the electric field depends on the pollution layer conductivity. As a first observation, a polluted barrier reduces the dielectric strength compared to that of the clean barrier, whatever the mode of application of the pollution but remains superior to that of the conductive barrier.

In Fig 11, the electric field distribution as a function of a polluted barrier facing the pointed electrode was presented. From this figure, we observe that when the conductivity of the pollution layer increases, the electric field increases [19].

The influence of the pollution layer facing the grounded electrode is presented in Fig 12. We notice the more the conductivity of the pollution layer increases, the electric field slightly increases but remain far from the case of the polluted barrier facing the point [19]. The pollution on the ground side does not significantly affect the dielectric strength of the system.

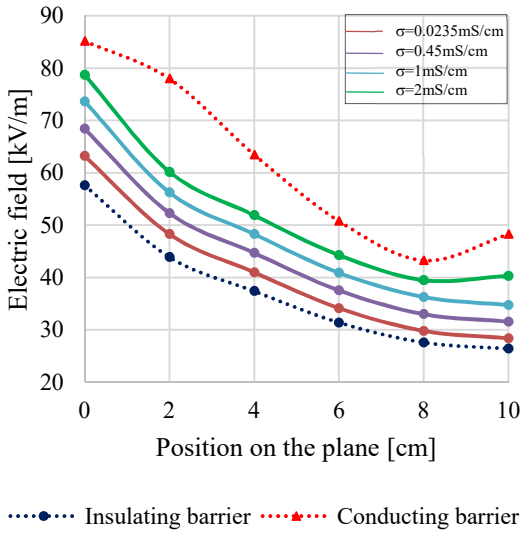

Fig.11: Distribution of the electric field at the plane (V=22kV, d = 5 cm, a/d = 0%, 2L = 15 cm, e=5mm, εr = 80, ep =0.1mm).

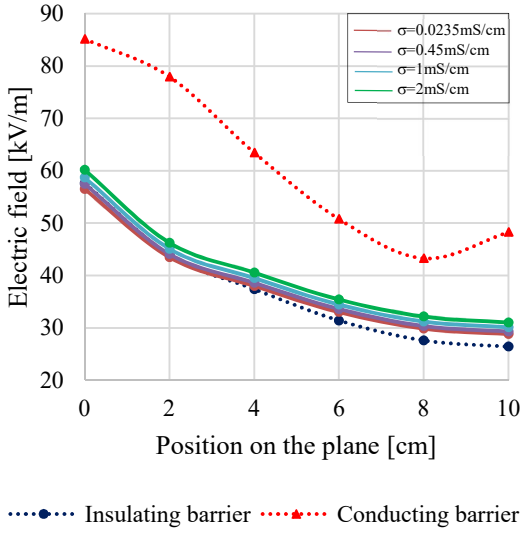

Fig.12: Distribution of the electric field at the plane (V=22kV, d = 5 cm, a/d = 0%, 2L = 15 cm, e=5mm, εr = 80, ep =0.1mm).

Finally, we tested the influence of a completely polluted barrier on the distribution of the electric field (Fig 13).

From this figure, we notice that the variation of the electric field is almost the same as the case of a polluted barrier facing the pointed electrode [19]. The pollution on the side of the point greatly reduces the insulation quality of the barrier.

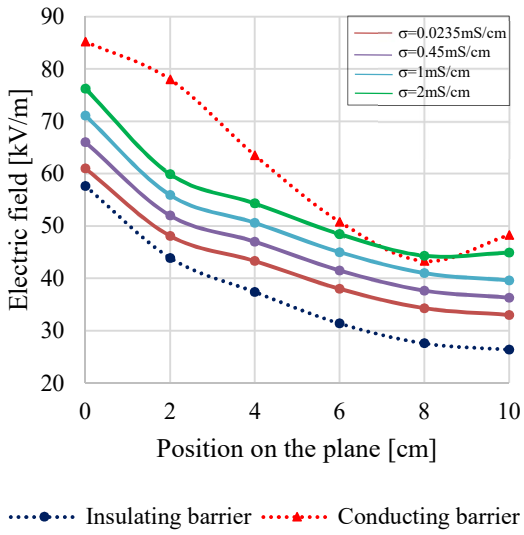

Fig.13: Distribution of the electric field at the plane (V=22kV, d = 5 cm, a/d = 0%, 2L = 15 cm, e=5mm, εr = 80, ep =0.1mm).

D. Influence of layer permittivity

In order to study the influence of the layer permittivity on the electric field distribution at the plane, two permittivity values: 15 and 80 respectively were used. We used also two conductivity values: σ=0.0235mS/cm and σ=1mS/cm, and the thickness of the pollution is equal to 0.1 mm.

Based on the simulation results (Fig 14), it has been observed that the influence of the permittivity on the electric field distribution at the plane is remarkable for low conductivity values. With the growth of the conductivity value, the effect of the permittivity decreases [18].

In fact, the thin layer becomes a better conductive layer entering in resistive regime making the electric field distribution uniform. In this type of regime, the influence of permittivity is not noticeable as we can observe when we compare the green curve, pollution conductivity of 1mS/cm and pollution permittivity of 80F/m, with the blue curve, pollution conductivity of 1 mS/cm and permittivity of 15F/m. These curves are substantially equal.

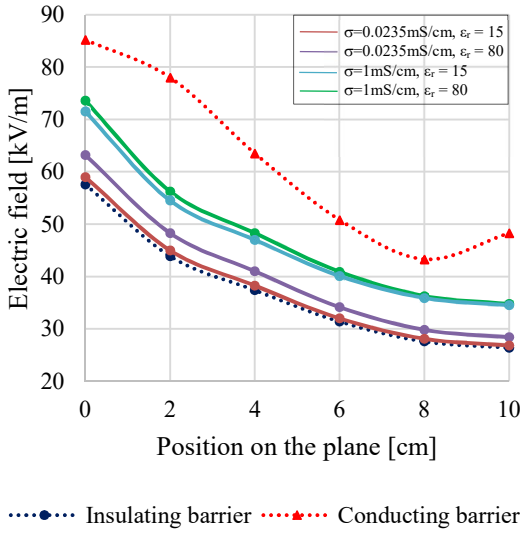

Fig.14: Distribution of the electric field at the plane (V=22kV, d = 5 cm, a/d = 0%, 2L = 15 cm, e=5mm, e_p =0.1mm).

E. Influence of layer thickness

The study of the effect of the thickness of pollution layers on the electric field distribution at the plane is of great importance to determine the dielectric strength of the point-barrier-plane arrangement.

To do this, three thicknesses e_p=0.1, 0.3 and 0.5mm were used. We also used two values of conductivity σ=0.0235 and σ=1mS/cm which represent two different levels of pollution. The value of the permittivity was kept constant and equal to 80.

From Fig (15,16), It can be observed that when the thickness of the pollution increases, the electric field increases. This increase in field strength is much greater when the conductivity of the pollution layer increases. For low values of conductivity and in the case of a polluted barrier on its upper surface (Fig 15), the electric field increases but remains far from that one obtained in the case of the conductive barrier.

If the conductivity and the thickness increase at the same time (Fig 16), the distribution of the electric field increases and converges towards the value of the conductive barrier [18].

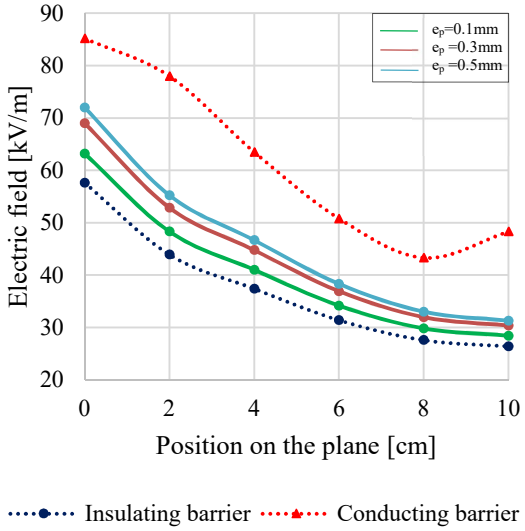

Fig.15: Distribution of the electric field at the plane (V=22kV, d = 5 cm, a/d = 0%, 2L = 15 cm, e=5mm, σ=0.0235mS/cm, εr = 80).

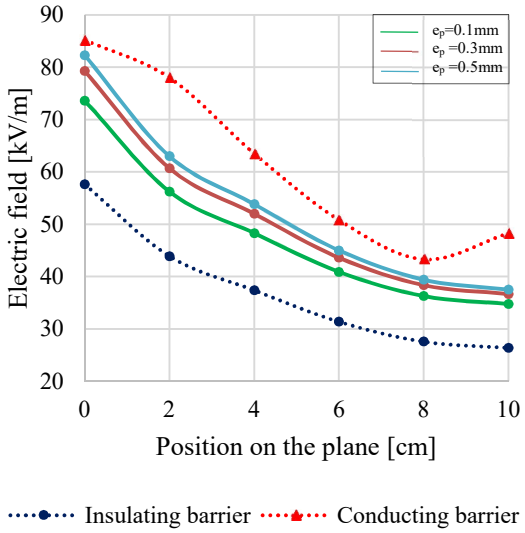

Fig.16: Distribution of the electric field at the plane (V=22kV, d = 5 cm, a/d = 0%, 2L = 15 cm, e=5mm, σ=1mS/cm, εr = 80).

F. Polluted barrier vs conductive barrier

To complete our study, the limit value of the conductivity from which the polluted barrier gives almost the same result as the conductive one in the case of polluted barrier facing the point was determined (fig 17).

From this figure, we observe that the polluted barrier has almost the same behavior in comparison with the conducting barrier for the position x=0 (center of the plane) and when the conductivity is close to 2.25 mS/cm [18].

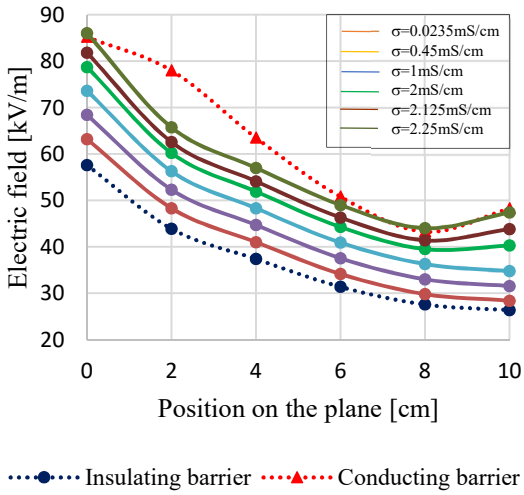

Fig.17: Distribution of the electric field at the plane (V=22kV, d = 5 cm, a/d = 0%, 2L = 15 cm, e=5mm, e_p=0.1mm).

IV. CONCLUSION

In this paper, electric field distribution in point-barrier-plane air gaps was investigated by using software package of COMSOL Multiphysics based on Finite Element Method (FEM). Comparison between the electric field in both clean and polluted cases was conducted.

The effect of the surface condition of the barrier on the electric field for a point-plane system gives the following results:

- The pollution on the side of the point greatly reduces the insulation quality of the barrier.
- The electric field of the point-barrier-plane configuration increases with increasing conductivity of the pollution layer covering the barrier.
- The influence of the thin pollution layer permittivity on the electric field is remarkable for the small values of the conductivity.
- From our results with different pollution layer thicknesses, we can deduce that this parameter has an important influence on the distribution of the electric field and therefore the dielectric strength of the system.
- There is a limit value of the conductivity from which the polluted barrier gives almost the same result as the conductive barrier. In our study, this value is equal to: 2.25 mS/cm.

REFERENCES

[1] E. Marx, "Der Durchschlag der Luft im unhomogenen elektrischen Felde bei verschiedenen Spannungsarten", E.T.Z., vol. A33, pp. 1161– 1165, 1930 (in German). https://doi.org/10.1007/BF01659576

[2] H. Roser, "Schrime zur Erhorung der Durchschragspannung in Luft", E.T.Z., pp. 411–412, 1932 (in German).

[3] N.F.Wolochtenko, "Problèmes relatifs au mécanisme de l'effet de barrière (en russe)", Elektritchestwo, nr6, p. 61, 1947 (in French).

[4] M.P.Verma, "Electric field lines of rod-barrier-plane in positive impulse voltage", Wiss.Zeit. der TU Dresden H1, pp.111, 1962 (in German).

[5] J. Pilling, "Dielectric barrier in uniform field", Elektrie 23, H11, pp.463, 1969.

[6] F. V. Topalis and I. A. Stathopulos, "Barrier Effect on Electrical Breakdown in Non-uniform Small and Medium Air Gaps", *IEEE 6th Int. Conf. Dielectr. Materials, Measurements and Applications*, 1992, pp. 439–442.

[7] L. Ming, M. Leijon, and T. Bengtsson, "Factors Influencing Barrier Effects in Air Gaps", 9th Int. Symp.High Voltage Engineering, 1995, vol. 2, pp. 2168-1 - 2168-4.

[8] M. Awad, H. Bohme, "Durchlagspannung inhomogener Funkenstrecken mit versmutzten barrieren", Elektrie 31, H1, pp. 35, 1977 (in German).

[9] A. Boubakeur, "Influence des barrières sur la tension de décharge disruptive des moyens intervalles d'air pointe-plan", Thèse de Doctorat, E.P .Varsovie, Pologne, 1979.

[10] A. Beroual and A. Boubakeur, "Influence of Barriers on the Lightning and Switching Impulse Strength of Mean Air Gap in Point/Plane

Arrangements", *IEEE Trans. Dielectr. Electr. Insul*., vol. 26, no. 6, pp. 1130-1139, 1991. https://doi.org/10.1109/14.108150

[11] A. Boubakeur, "Influence des barrières sur l'amorçage des moyens intervalles d'air pointe–plan". Rozprawy Electrotechniczne, vol.27, no.3, pp. 729-744, Pologne, 1981.

[12] A. Boubakeur, "Discharge phenomena in long air gaps with insulation screen", 4th International Symposium on High Voltage Engineering (ISH) , paper 44-05, Athens, Greece, 1983.

[13] S.Mouhoubi, A.Boubakeur, "Partial discharges behaviour in a rod-plane arrangement with an insulating barrier", Archives of Elect Eng. vol. I.VI. no. 3-4, pp. 187-196, 2007.

[14] S. Mouhoubi, "Etude de l'influence d'une barrière dans un intervalle pointe – plan, par la mesure de la tension disruptive, du champ électrique et des décharges partielles", PhD Thesis – Ecole Nationale Polytechnique, Algeria, 2008.

[15] Y. V. Serdyuk, "Numerical simulations of non-thermal electrical discharges in air: Lightning electromagnetics", *IET Power and Energy* Series, pp. 87-138, 2012.

[16] M. A. Benziada, A. Boubakeur, A. Mekhaldi, "Numerical Simulation of the Electric Field Distribution in Point-Barrier-Plane Air Gaps", *IEEE Trans. Dielectr. Electr. Insul*., vol. 25, no. 6, pp. 2093–2102, 2018. https://doi.org/10.1109/TDEI.2018.007160

[17] D.S. Lopes, J.M.B. Bezerra, "Potential Distribution Along a 500kV Polymer Insulator in Presence of a Pollution Layer", Proceedings of the COMSOL Conference in Curitiba, 2015.

[18] M. A. Benziada, "Influence de la charge d'espace sur la distribution du champ dans les intervalles d'air pointe-barrière-plan", PhD Thesis – Ecole Nationale Polytechnique, Algeria, 2020.

[19] M.A. Benziada, A. Boubakeur, A. Mekhaldi, "Investigations of Non-uniform Pollution Impact on Electric Field Distribution in a Point-Barrier-Plane Arrangement under AC Voltage", the International Conference on Advanced Electrical Engineering (ICAEE), Algiers, Algeria, pp. 1-4, 19-21 Nov. 2019. https://doi.org/10.1109/ICAEE47123.2019.9014789

Mohamed Abdelghani Benziada was born in Jijel, Algeria in 1992. He received the degree of Engineer and M.Sc. degree in Power Electrical Engineering in 2015, and Ph.D. in High Voltage Engineering in 2020 from Ecole Nationale Polytechnique (ENP) of Algiers, Algeria. His is currently a voluntary researcher with the Laboratoire de Recherche en Electrotechnique of the ENP. His main research interests are in discharge phenomena, space charge effect, characterization of solid dielectrics, electric field calculation and area of the modeling.

Ahmed Boubakeur was born in Biskra, Algeria in 1952. He received in 1975 the degree of Engineer in Electrical Engineering from Ecole Nationale Polytechnique (ENP) of Algiers, and in 1979 he obtained the Doctorate in Technical Sciences from the Institute of High Voltage Engineering of the Technical University of Warsaw in Poland. He is currently a professor at ENP of Algiers where he is giving lectures and supervising research in the field of High Voltage Engineering since 1982. His principal research areas are discharge phenomena, insulators pollution, lightning, polymeric cables insulation, transformer oil ageing, neural network and fuzzy logic application in HV insulation diagnosis, and electric field calculation and measurement. He is IEEE senior member, member of the CIGRE).

Abdelouahab Mekhaldi was born in Algiers, Algeria in 1958. He received the degree of Engineer in 1984 in Electrical Engineering, a Masters degree in 1990 and a PhD in High Voltage Engineering in 1999 from Ecole Nationale Polytechnique (ENP) of Algiers. He is currently a Professor at ENP of Algiers, His main research areas are in discharge phenomena, outdoor insulators pollution, polymeric cables insulation, lightning, artificial intelligence application in high voltage insulation diagnosis and electric field calculation. He is also IEEE Senior Member.

Analysis and mapping of mining subsidence and underground voids collapse risk using GIS and the weights-of-evidence model for the abandoned Ichmoul mine, Algeria

Nassim Larachi, Abderrahim Bali, Abderrezak Ait Yahiatene and Malek Ould Hamou

Abstract− The present study concerns the assessment of mining subsidence and old underground works collapse hazard of the abandoned Ichmoul mine (Batna, Algeria) using the geographic information system (GIS) and the weight of evidence method (WofE). After the identification of collapse cases on the site and developing a spatial database for old underground works, topography and geology, the weight of evidence model was applied to calculate the weight of each relevant factor. Five main factors controlling or related to subsidence and underground voids collapse were determined from the probability analysis of existing cases; the underground voids depth, the distance between the underground voids, the landforms slope, the lithology and the distance between the fractures. Conditional independence tests were performed for the choice of factors. For the analysis of the subsidence and underground void collapse spatial hazard mapping, the contrast values, W^+ and W^- of the each factor evaluation were analyzed. The analysis results were validated using the curve ROC (AUC) with a past collapse case. For all the factors used, the area under the (ROC) curve showed 92 % accuracy. The results obtained can be used for the prevention of mining subsidence and underground voids collapse risks and the mine site rehabilitation.

***Keywords*−Abandoned mine, Algeria, geographic information system, hazard prediction map, subsidence and collapse hazard, weight of evidence.**

I. Introduction

Abandoned mines are threatened by the ground subsidence and voids collapse risk around old mining works (galleries, pipes, declines, shafts, etc.). This risk with negative environmental impact [1-7] is only a spatio-temporal evolution of the voids physical instability that was once created by the underground exploitation of deposits. Therefore, managing the mining subsidence and voids collapse risk of abandoned mine is urgent and imminent, in order to reduce the impact and so that governments can prevent this risk. So, a systematic prediction of subsidence and voids collapse can be used for sustainable development and future management of the post-mine environment. Although the GIS (geographic information system) has been widely used for geo-risks such as landslides [8-11], floods [12, 13], land subsidence by overexploitation groundwater [14], groundwater vulnerability to pollution [15-18], soil erosion [19-21], soil pollution [22]... etc. and even in the mineral resources potential assessment [23-26], few studies have been carried out for the assessment of GIS-based methods and applications relating to the environmental management of former mining sites [27]. In recent years, there have been probability, statistical, fuzzy logic and artificial neural network methods combined with GIS (Geographic Information System) software that helps predict the subsidence and collapse risk in the mining environment. Indeed, Kim et al., 2006; Blachwski, 2016; Oh et al., 2011 and Lee et al., 2012 predicted the ground subsidence risk using GIS with models based on frequency ratio, logistic regression and an artificial neural network [28-31], Choi et al., 2010 and Park et al., 2012 predicted this risk for an abandoned underground coal mine out of fuzzy logic [32,33]. Oh and Lee, 2011; 2010 also applied the weights of evidence (WofE) method to predict subsidence in an abandoned coal mine [34, 35]. Algeria has old mines, dispersed throughout the country. The various geological risks of old mines, including mine drainage, ground subsidence and voids collapse, contamination, etc. are important in these mines [36]. Very little attention has been paid to the subsidence and collapse risk at these mine sites. Therefore, the Algerian government must initiate research programs on former mining sites in order to carry out data mining for post-mine management. During the sampling campaigns of the mine wastes and geo-mining study on the abandoned Ichmoul mine allowed to identify and observe subsidence and collapse cases around the old galleries (Fig.1). So, a prediction method combined with MapInf software to assess and predict mine subsidence and collapse is applicable. The objective of this study is to analyze and map the land subsidence and underground collapse risk of around the old galleries of the abandoned Ichmoul mine using the weights-of-evidence method and GIS.

II. Methodology

The analysis of the mining subsidence and voids collapse risk of mine sites with underground exploitation requires several steps [30, 32, 33, 35]. The first step involves the collection of mining (mining plans), geological (lithology, faults),

Manuscript received May 16 , 2021; revised September 15, 202.

N. Larachi is with Faculty of Nature and Life Sciences, University of Bejaia, Bejaia, ALGERIA and with Mining Engineering Department, Ecole Nationale Polytechnique Algiers, ALGERIA. (e-mail:nassimlarachi@yahoo.fr).

A. Bali is with Materials of Civil-Engineering and Environment laboratory, Ecole Nationale polytechnique Algiers, ALGERIA. (e-mail:abderrahim.bali@g.enp.edu.dz).

A. Ait Yahiatene and M. Ould Hamou are with Mining Engineering Department, Ecole Nationale Polytechnique Algiers, ALGERIA. (e-mail: abderrezak.aityahiatene@g.enp.edu.dz, malek.ouldhamou@g.enp.edu.dz).

Digital Object Identifier (DOI): 10.53907/enpesj.v1i2.46

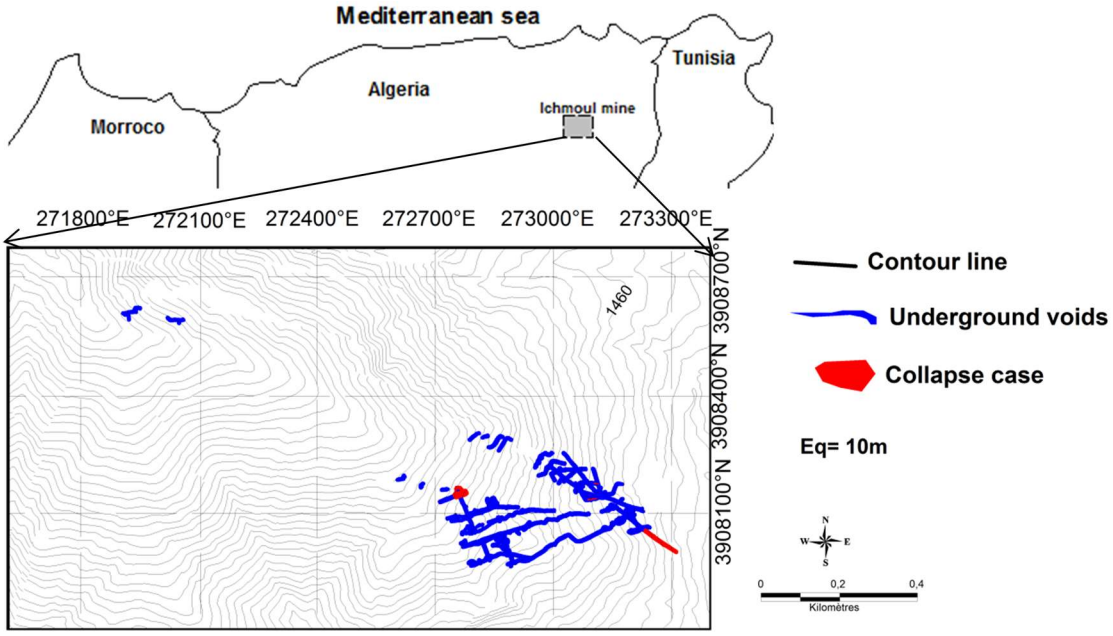

Fig. 1: Old mining galleries and underground collapse location of the abandoned Ichmoul mine site.

hydrogeological, topographic (landform slopes) data as well as an inventory of subsidence and collapse cases on the site. These data will allow selection of the relevant factors. The second step is to assess the spatial hazard using the relationship between this risk and factors related. The third step is to make a risk map of subsidence and underground voids collapses from the factor maps. Finally, the results validation step. Ground subsidence and voids collapse in mine sites are processes of rock mass movement under the influence of various factors. Therefore, it is essential to analyze the conditions of the selected factors to assess this risk. In the literature, the main influencing factors responsible for mining subsidence and voids collapse are the depth and height of underground voids, mining method, degree of voids inclination, mining extent, structural geology, lithology, landforms slope and groundwater [33, 35].In addition, two campaigns carried out on the mine site detected mining subsidence and voids collapse cases (Fig.2), some were used for modeling and others for validation.

Fig. 2: Collapse cases of galleries in the Ichmoul mine site.

A total of 5 cases mapped through field observations. Of the total, a case was mapped to ore masse 3 that caused a land subsidence. A large number of ground breaking phenomena have been observed at high altitudes. It was found that these collapses mainly occurred on the access galleries openings. The escalating feature of collapses has proven to be a major risk for artisanal miners. The study area belongs to the terrain comprising a variety of different dimensions faults. The main one is the tectonic fault located in the ore masse 2 and 4.

The approach to predicting mining subsidence and collapses around voids generated by old mining is based on the spatial correlation of factors and risk. To generate the risk prediction maps for each of the five study factors using WofE , the spatial database was classified into a map by calculating W + and W− from "(1)" and "(2)" [10, 35], which show favorable and unfavorable areas.

$$W^{+} = Log\frac{P\{B/D\}}{P\{B/\bar{D}\}} \quad (1)$$

$$W^{-} = Log\frac{P\{\bar{B}/D\}}{P\{\bar{B}/\bar{D}\}} \quad (2)$$

where P is the probability, B is the presence of a dichotomous pattern,
$\bar{B}$ is the absence of a dichotomous pattern, D is the presence of an event occurrence, and $\bar{D}$ is the absence of an event occurrence. W^{+} and W^{-} are the weights of proof when a factor is present (relevant) and absent (irrelevant), respectively.

A pair of weights, W^{+} and W^{-}, is determined by the degree of overlap between known mining subsidence and collapses and the various classes of factors [11, 34]. If no particular association exists between the collapse occurrences and the factor, then $W^{+} = W^{-} = 0$. A positive value of W^{+} indicates a positive association between known cases and the obvious map. The contrast value C (where $C = [W^{+}] - [W^{-}]$) represents the degree spatial association between the obvious map and known occurrences [11]. The weights significance (S) can be estimated by "(3, 4)" below [10, 11]:

$$s^2(W^{+}) = [1/M\{B \cap D\}] + [1/M\{B \cap \bar{D}\}] \quad (3)$$

$$s^2(W^{-}) = [1/M\{\bar{B} \cap D\}] + [1/M\{\bar{B} \cap \bar{D}\}] \quad (4)$$

Finally, to calculate the standard deviation and the studentized (c/s) of the contrast, "(5)"and "(6)" were used [35, 11, 14].

$$S(C) = \sqrt{s^2(W^{+}) + s^2(W^{-})} \quad (5)$$

$$c/s = \left(C/_{S(C)}\right) \quad (6)$$

III. RESULTS AND DISCUSSION

These past cases of subsidence and voids collapse will help select the relevant factors related to risk. They ensure also that the predicted subsidence and voids collapse will occur under conditions identical to those of the past cases [32].

On the other hand, a laborious work made it possible to develop geographic information system (GIS) using professional MapInfo software while digitizing and calibrating the various maps (paper format) recovered from the National Mining Company of Products Non Ferrous and useful substances (ENOF). This GIS database is made up of the contour lines altitudes generated from a topographic map, lithological information and the faults from the geological map, distances between the old underground voids from the old galleries maps and the old voids depths from geological sections. The thematic data layers are shown in Table I and Figs. 3-7.

Previous studies of ground subsidence in old mine sites have mentioned that void depth factors and the distances between them are important [28, 30, 33], therefore very tight classes were chosen. However, the hydrogeology factor has been eliminated because the Ichmoul mine is above groundwater [37]. The section factors of underground voids and mining method were also eliminated because during the study campaigns on the site, it was observed that the underground voids have small cross-section and the mining is not well developed.

The slope was classified into 10 categories after eliminating certain elevations. Since the distance between fractures factor is relevant, then fractures were included.

The lithology factor has been classified into 6 categories.

Then, using the weight-of-evidence method, the spatial relationships between the location of the detected underground voids collapse and each of the underground voids collapse related factors, such as slope, faults, depth of voids, distance between voids, the depth of voids were analyzed (Table II). Spatial relationships were used as a rating for each factor in the overlay analysis. Subsequently, conditional independence tests were carried out for the selection of factors to be used in the mapping of spatial subsidence and collapse hazard [35].

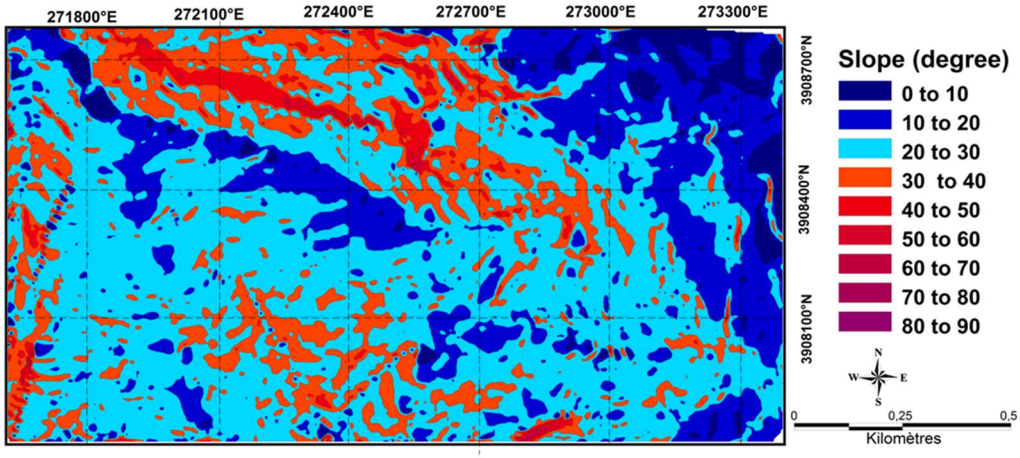

Fig. 3: Class map of the landform slope factor of the Ichmoul mine site.

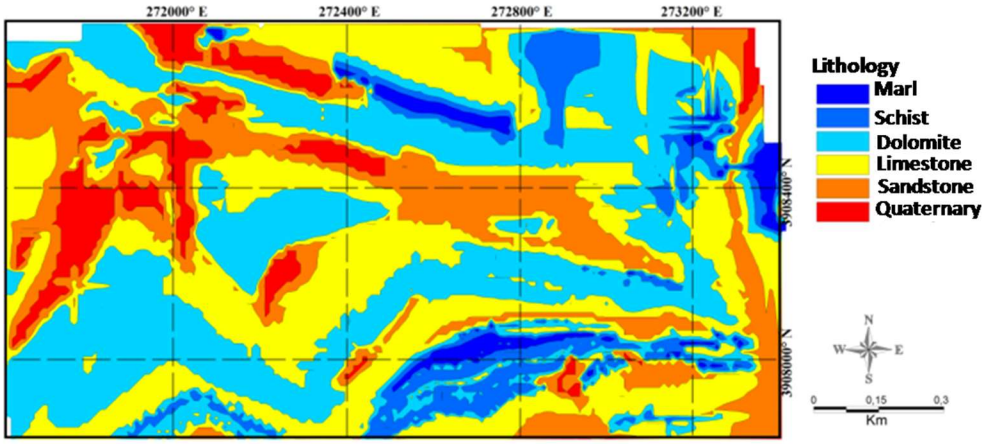

Fig. 4: Class map of the lithology factor of the Ichmoul mine site.

Table. I

CONSTRUCTION OF A GIS DATABASE INCLUDING FACTORS RELATED TO THE MINING SUBSIDENCE AND UNDERGROUND VOIDS COLLAPSE OF THE ABANDONED ICHMOUL MINE.

Category	Factors	Scale
Geology map	Distance between fractures	
	Lithology	1/2000
Topographic map	Slope	1/2000
Galleries maps	Distance between underground voids	1/2000 and 1/500

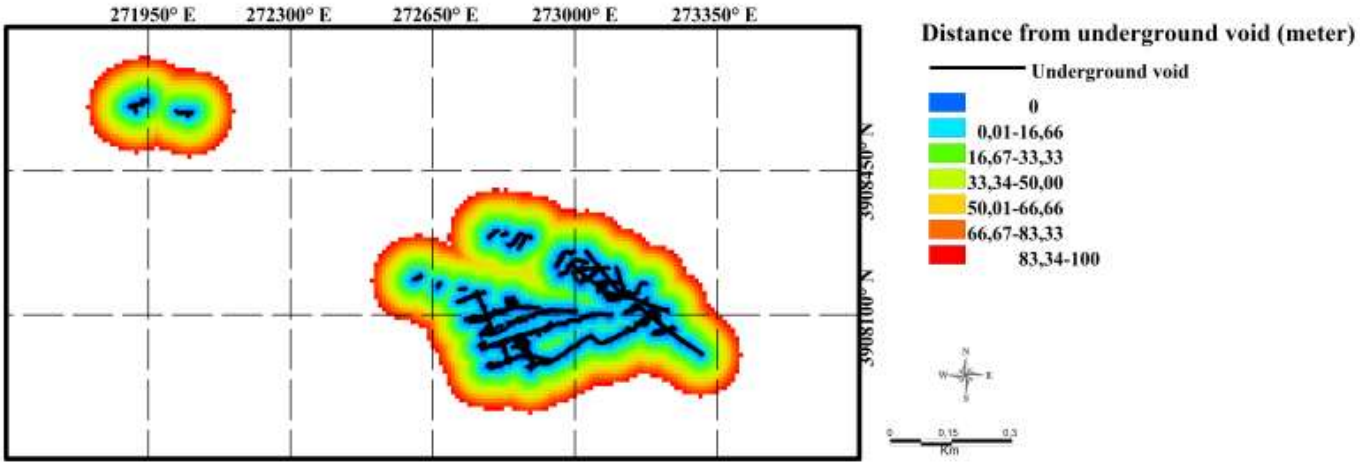

Fig. 5: Class map of distance between underground voids factor of the Ichmoul mine site.

The factors were added to calculate a spatial risk index of subsidence and underground voids collapse hazard was mapped for 5 factors combinations such as a combination using all etc., in one step. The 5 factor maps were submitted to the large WofE tool of the MI-SDM, which resulted in a large table (Table II) containing W^+, W^-, C, S^2 (W^+), S^2 (W^-),S^2 (C) and

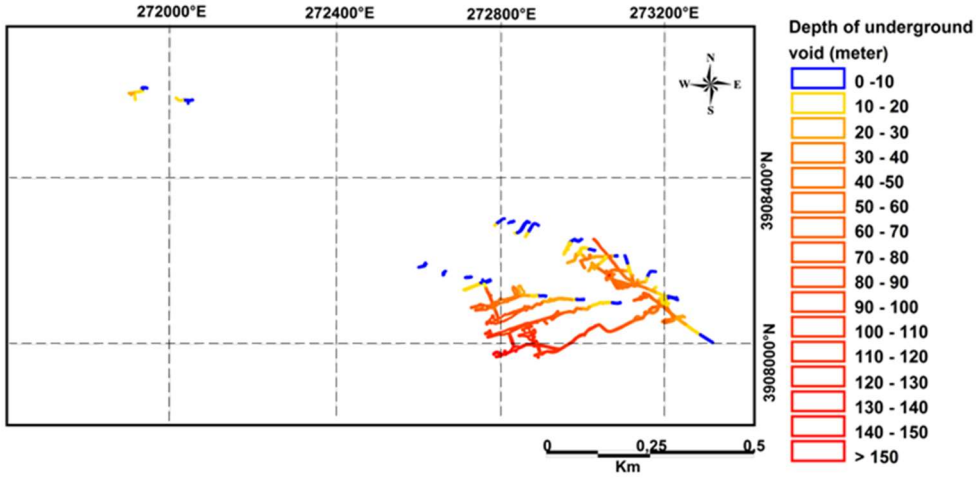

Fig.6: Class map of the underground voids depth factor of the Ichmoul mine site.

variables and 4 others different combinations (without depth of voids, without distance between fracture, without slope, without distance of underground voids). Then, 5 posterior probability maps were generated (Figs.8 and 9). Finally, the results of combining all the factors were validated using the receiver operating characteristic curve (ROC) with previous underground voids collapse cases [30, 35].

C/S (C) information of each the factor classes using "(1-6)".It also resulted in a posterior probability map containing the probability information (in a range of 0 to 1) of the void collapse occurrence, cell by cell. Positive C values are observed in the five selected factors, steep slope category (30 -50), lithology (limestone, dolomite and shale), shallow depth (0–20 m), distance between fractures (0-20,80-90m) and short

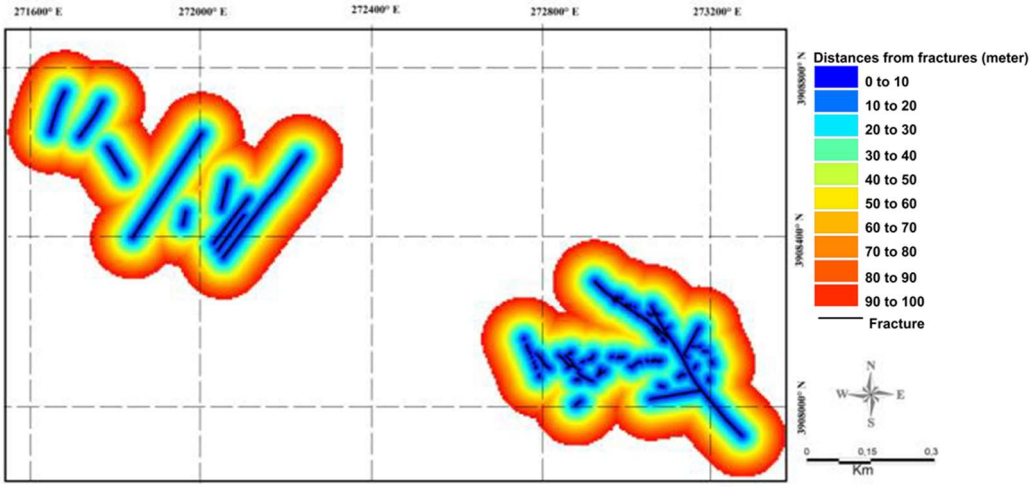

Fig. 7: Class map of the distance between fractures factor of the Ichmoul mine site.

The WofE application in this study, the MI-SDM extension of MapInfo 8 professional software was used. The plugin has several tools to calculate the posterior probability map with a tool that calculates W^+, W^- and the posterior probability map,

distance between voids (0–20m).This indicates that these categories of factors influence the subsidence and underground voids collapse prediction at the former Ichmoul mine.

Table. II
ANALYSIS OF WEIGHTS OF EVIDENCE BETWEEN MINING SUBSIDENCE AND UNDERGROUND VOIDS COLLAPSE AND RELATED FACTORS

Factor	Class	Area (km^2)	point	W^+	$S(W^+)$	W^-	$S(W^-)$	Contrast	S(C)	Stud (C)
.andform	0-10	35	0	-	-	-	-	-	-	-
lope (%)	10-20	177	10	-1.930	0.3256	0.2816	0.0803	-2.2115	0.3553	-6.5955
	20-30	452	132	-0.0001	0.1034	0.0001	0.1094	-0 .0002	0.1506	-0.0014
	30-40	158	98	1.3760	0.1639	-0.3933	0.0917	1.7694	0.1878	9.4199
	40-50	27	10	0.3548	0.3985	-0.0124	0.0766	0.3672	0.4058	0.9047
	50-60	0	0	-	-	-	-	-	-	-
	60-70	0	0	-	-	-	-	-	-	-
	70-80	0	0	-	-	-	-	-	-	-
	80-90	0	0	-	-	-	-	-	-	-
	missing	144	-75	-	-	-	-	-	-	-
	Marl	17	0	-	-	-	-	-	-	-
	Schist	58	21	0.6887	0.27332	-0.0611	0.0874	0.7497	0.2869	2.6126
	Limestone	283	138	1.2056	0.1189	-1.0895	0.1495	2.2951	0.1911	12.0116
	Dolomite	279	28	-0.9382	0.1992	0.3201	0.0936	-1.2583	0.2201	-5.7160
lithology	Sandstone	155	0	-	-	-	-	-	-	-
	Quaternary	48	0	-	-	-	-	-	-	-
	Missing	157	0	-	-	-	-	-	-	-
	0-10	11	6	23224	0.6055	-0.6429	0.4207	2.9653	0.7373	4.0217
Jnderground	10-20	13	4	13291	0.6009	-0.3131	0.3684	1.6422	0.7049	2.3298
oids depth	20-30	12	1	-0.2578	1.0445	0.0271	0.3192	-0.2849	1.0922	-0.2609
m)	30-40	12	0	-	-	-	-	-	-	-
	40-50	12	1	-0.2578	1.0445	0.0271	0.3192	-0.2849	1.0922	-0.2609
	50-60	8	0	-	-	-	-	-	-	-
	60-70	6	0	-	-	-	-	-	-	-
	70-80	8	0	-	-	-	-	-	-	-
	80-90	6	0	-	-	-	-	-	-	-
	90-100	5	0	-	-	-	-	-	-	-
	100-110	7	0	-	-	-	-	-	-	-
	110-120	2	0	-	-	-	-	-	-	-
	120-130	3	0	-	-	-	-	-	-	-
	140-150	1	0	-	-	-	-	-	-	-
	150-160	1	0	-	-	-	-	-	-	-
	0-10	75	12	1.6081	0.3150	-1.7576	0.7094	3.3657	0.7762	4.3360
	10-20	44	2	0.2218	0.7237	-0.0326	0.2940	0.2544	0.7812	0.3257
	20-30	38	0	-	-	-	-	-	-	-
	30-40	34	0	-	-	-	-	-	-	-
Distances	40-50	33	0	-	-	-	-	-	-	-
between	50-60	33	0	-	-	-	-	-	-	-
nderground	60-70	31	0	-	-	-	-	-	-	-
voids (m)	70-80	31	0	-	-	-	-	-	-	-
	80-90	34	0	-	-	-	-	-	-	-
	90-100	25	0	-	-	-	-	-	-	-
	missing	1619	-1	-	-	-	-	-	-	-
	0-10	60	5	1.0521	0.4671	-0.2591	0.3052	1.3112	O.5580	0.3501
	10-20	60	3	0.5055	0.5923	-0.0876	0.2814	0.5932	0.6558	0.9045
Distances	20-30	56	0	-	-	-	-	-	-	-
Between	30-40	56	0	-	-	-	-	-	-	-
ractures (m)	40-50	53	2	0.2113	0.7208	-0.0268	0.2714	0.2382	0.7702	0.3092
	50-60	49	1	-0.4212	1.0104	0.0355	0.2624	-0.4568	1.0439	-0.4376
	60-70	47	1	-0.3787	1.0108	0.0312	0.2624	-0.4098	1.0443	-0.3924
	70-80	47	1	-0.3787	1.0108	0.0312	0.2624	-0.4098	1.0443	-0.3924
	80-90	47	3	0.7644	0.5967	-0.1163	0.2812	0.8807	0.6597	1.3351
	90-100	41	0							
	missing	1480	-3							

A. Mapping of the subsidence and underground voids collapse risk of Ichmoul mine

As mentioned in the previous section, the posterior probabilities should not be considered in absolute terms, but as a relative term of subsidence and underground voids collapse favorability, which can be represented by the relative map of this instead of using the true posterior probability values. MI-SDM's WofE generates a continuous raster, which represents the void collapse probability on a continuous scale from 0 (minimum) to 1 (maximum). In the present study, a minimum probability value of 0.0001 and a maximum of 0.4660 were observed (Fig. 8).

In addition, 4 other combinations of factors were studied and the posterior probability maps were generated (Fig.9).Each map shows different probability values, indicating the effect of each factor on the prediction of the subsidence and underground voids collapse risk in the mine site. Indeed, combination 1 (without depth of voids) and combination 2 (without distance between fractures), show low posterior probability values compared to the other combinations, which suggests that they are the main risk factors for subsidence and underground voids collapse in the Ichmoul mining site.

B. Conditional independence test (CI)

Conditional independence was tested before integrating predictor maps to map the spatial hazard of subsidence and underground voids collapse. All pairs of factors selected for prediction were tested, and a chi-square table X^2 to test conditional independence is shown in Table III.

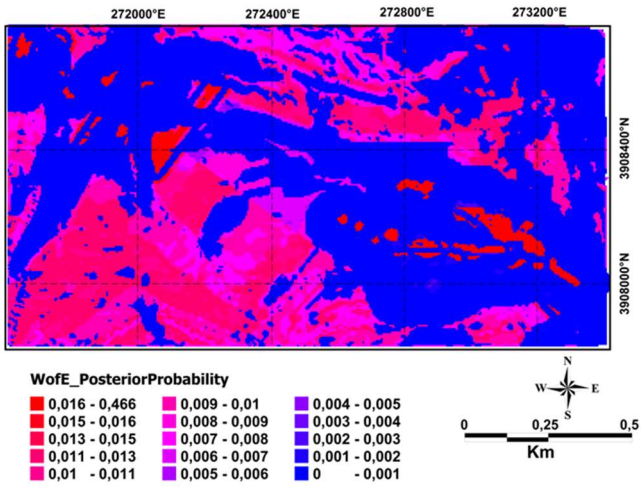

Fig. 8: Posterior probabilities map by combining the all factors.

The theoretical X^2 value of 6.63 to test conditional independence between all pairs of models for each factor was calculated to the significance of 95% and 1 degree of freedom. If the calculated X^2 value is less than 4.84, the pair of prediction factors is independent. For example, using the possibility table to test the conditional independence between the slope factor and the lithology factor is presented in Table III. It can be seen that these two factors show conditional independence, because the calculated X^2 is 0.44 and which is less than theoretical X^2. This implies that these predictors could be used together to map the spatial hazard of subsurface void collapse at the Ichmoul mine site.

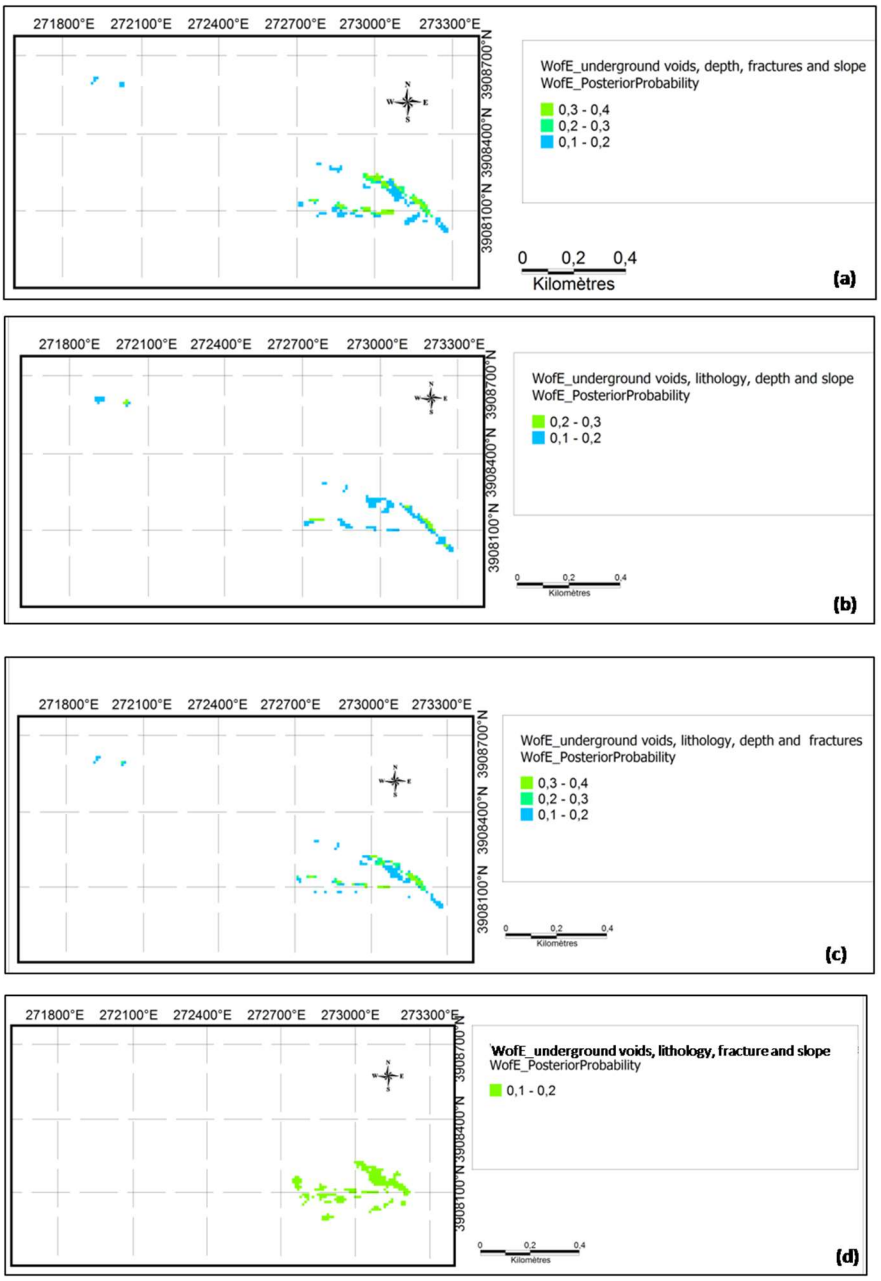

Fig. 9: Class Posterior probability maps for factors combinations (a) without lithology (b) without distance between fractures(c) without landforms slope (d) without underground voids depth

Table. III
CHI-SQUARE VALUES CALCULATED TO TEST THE CONDITIONAL INDEPENDENCE BETWEEN THE FACTORS SELECTED FOR THE ICHMOUL MINE SITE (PROBABILITY OF TEST RELIABILITY OF 5%)

	Underground voids depth	Distances between fractures	Distances between underground voids	lithology	Slope
Underground voids depth	—	**3.329**	**0**	**1.876**	**1.202**
Distances between fractures		—	**0**	**4.179**	**1.977**
Distances between underground voids			—	**0**	**0**
lithology				—	**0.446**
Slope					—

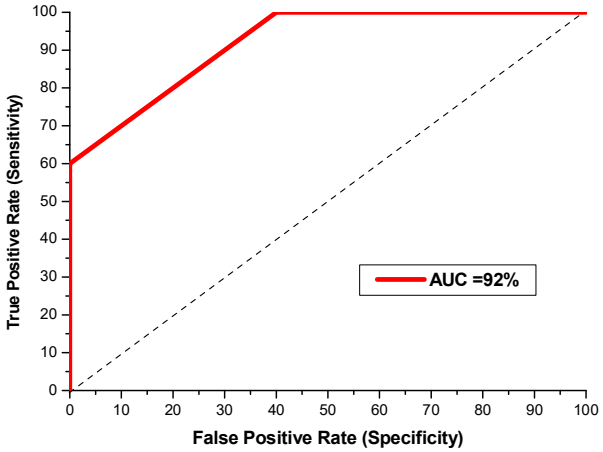

Fig. 11: The ROC (AUC) curve for validation of a prediction map of the underground voids collapse risk in the abandoned Ichmoul mine.

The risk map of mining subsidence and underground voids collapse in the Ichmoul mine site was then produced, using all the factors, and the risk index is shown in Fig.10.
The index was classified into 4 classes depending on the area for visual and easy interpretation: high, medium, low and very low.

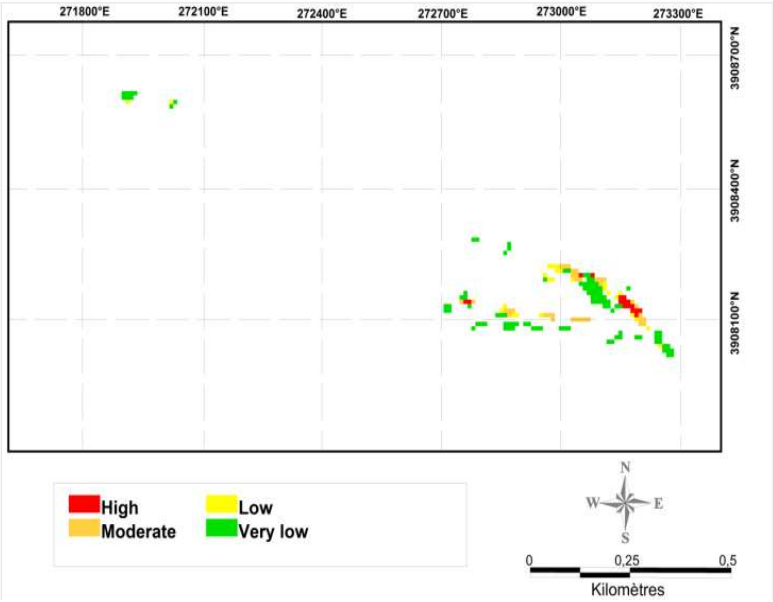

Fig. 10: The risk prediction map of underground voids collapse in the Ichmoul mine site.

C. Validation

The purpose of the validation is to verify the quality and accuracy of the approach applied for the prediction of subsidence and collapse around the old underground voids of the abandoned Ichmoul mine. For this purpose, the generated risk map was validated using the ROC AUC (Area Under the Curve) result. This curve was obtained by comparing the rate of false positives (1-specificity) and the rate of true positives (sensitivity) of the posterior probability map [26]. This curve (Fig.11) was also formed using the underground voids collapse case risk not used for the prediction. The area of this spared case was divided into 30 zones, each of which is approximately 20m^2 and the posterior probability value of each was taken.
The value of the area under the curve is 92%, which shows the precision and perfection of the approach applied for the prediction of mining subsidence and underground voids collapse risk of the Ichmoul mine site.

IV. CONCLUSION

Mapping the risk of subsidence and voids collapse generated by mining is a fundamental tool for the environmental management of former mining sites. This study demonstrates the influence of landforms slope, underground voids depth and their distances, distance between fractures, and lithology factors on mining subsidence and underground voids collapse and their potential distribution in the abandoned Ichmoul mining site. The Subsidence and underground voids collapse risk map produced by the WofE method has been classified into four classes: very low, low, medium and high. The map obtained was validated according to the ROC (AUC) test, the precision was 92%. The results of this study can be used to map the subsidence and underground voids collapse risk at other mine sites. In addition, the risk map of subsidence and underground voids collapse can be used as basic data for the establishment of a risk prevention plan in old mining sites. However, to generalize mine subsidence and underground voids collapse factors, more studies and prediction methods should be performed.

ACKNOWLEDGMENT

The authors are grateful to the management staff of Ain Mimoun mine (Khenchela, Algeria) for their collaboration during outings at the Ichmoul mine site. The authors also thank Dr Asma Boudria, for his help in improving the language of this manuscript. They also

acknowledge Mr Ahmed Belhocine, director of SOMIBAR company (ENOF, Algeria), for facilitating access to the old mine Ichmoul maps.

REFERENCES

[1] F. Bell, T. Stacey, D. Genske, "Mining subsidence and its effect on the environment: some differing examples," Environ. Geol., vol. 40, pp. 135–152, Dec. 2000, 10.1007/s002540000140.

[2] F.G. Bell, S.E.T. Bullock, T.F.J. Halbich, P. Lindsay, "Environmental impacts associated with an abandoned mine in the Witbank Coalfield, South Africa," Inter. J. Coal Geol., vol. 45, no. 2-3, pp. 195–216, Jan. 2001, 10.1016/S0166-5162(00)00033-1.

[3] K.D. Kim, S. Lee, H.J. Oh, et al., "Assessment of ground subsidence hazard near an abandoned underground coal mine using GIS," Environ. Geol., vol. 50, pp. 1183–1191, 2006, 10.1007/s00254-006-0290-5.

[4] C. Loupasakis,V. Angelitsa, D. Rozos,N. Spanou, "Mining geohazards—land subsidence caused by the dewatering of opencast coal mines: The case study of the Amyntaio coal mine, Florina, Greece,". Nat. Hazards, vol.70, pp. 675–691, 2014, 10.1007/s11069-013-0837-1.

[5] K. Ma, Y, Zhang, M. Ruan, J. Guo and T. Chai, "Land Subsidence in a Coal Mining Area Reduced Soil Fertility and Led to Soil Degradation in Arid and Semi-Arid Regions," Int. J. Environ. Res. Public Health, vol. 16:3929, Oct. 2019, 10.3390/ijerph16203929.

[6] X. Wu, XW. Jiang, YF. Chen, et al.,"The influences of mining subsidence on the ecological environment and public infrastructure: a case study at the Haolaigou Iron Ore Mine in Baotou, China," Environ. Earth. Sci., vol. 59:803, Feb. 2009, 10.1007/s12665-009-0076-7.

[7] T. Waltham, H.D. Park, J. Suh, M.H. Yu, H.H. Kwon, K.M. Bang,"Collapses of old mines in Korea,"*Eng. Geol.,* vol.118, no.1-2, pp. 29–36, Feb.2011, 10.1016/j.enggeo.2010.11.007.

[8] A. Akgun, C. Kıncal, and B. Pradhan, "Application of remote sensing data and GIS for landslide risk assessment as an environmental threat to Izmir city (west Turkey)," Environ. Monit. Assess., vol. 184, pp. 5453–5470, Sep. 2012, 10.1007/s10661-011-2352-8.

[9] W., Chen, H.R. Pourghasemi, and S.A. Naghibi, "Prioritization of landslide conditioning factors and its spatial modeling in Shangnan County, China using GIS-based data mining algorithms" Bull. Eng. Geol. Environ., vol. 77, pp. 611–629, May 2018, 10.1007/s10064-017-1004-9.

[10] R. Kumar, and R. Anbalagan,"Landslide susceptibility mapping of the Tehri reservoir rim area using the weights of evidence method," J. Earth Syst. Sci., vol. 128:153, Jun. 2019, 10.1007/s12040-019-1159-9.

[11] Q. Wang, Y. Guo, W. Li, J. He, Z. Wu () "Predictive modeling of landslide hazards in Wen County, northwestern China based on information value, weights-of-evidence, and certainty factor," Geomat. Hazards Risk, vol.10, no.1, pp. 820-835, Jan. 2019, 10.1080/19475705.2018.1549111.

[12] S.A. Mohamed, M.E. El-Raey, "Vulnerability assessment for flash floods using GIS spatial modeling and remotely sensed data in El-Arish City, North Sinai, Egypt," Nat. Hazards, vol.102, pp. 707–728, Jan.2020. 10.1007/s11069-019-03571-x.

[13] X; Wang, H. A. Xie, "Review on Applications of Remote Sensing and Geographic Information Systems (GIS) in Water Resources and Flood Risk Management," Water, vol. 10:608, May 2018, 10.3390/w10050608.

[14] M. Mohammady, H.R. Pourghasemi, and M. Amiri, "Assessment of land subsidence susceptibility in Semnan plain (Iran): a comparison of support vector machine and weights of evidence data mining algorithms," Nat. Hazards, vol. 99, pp. 951–971, 2019, 10.1007/s11069-019-03785-z.

[15] A. Neshat and B. Pradhan,"Evaluation of groundwater vulnerability to pollution using DRASTIC framework and GIS," Arab. J. Geosci., vol.10:501, Nov. 2017, 10.1007/s12517-017-3292-6.

[16] X. WU, B. LI, and C. MA, "Assessment of groundwater vulnerability by applying the modified DRASTIC model in Beihai City, China," Environ. Sci. Pollut. Res., vol. 25, pp. 12713–12727, May 2018, 10.1007/s11356-018-1449-9.

[17] L. Duarte, J. Espinha Marques, A. C. Teodoro, "An Open Source GIS-Based Application for the Assessment of Groundwater Vulnerability to Pollution" *Environments*, vol. 6, no. 7: 86, Jul. 2019, 10.3390/environments6070086. 2019

[18] Singha, S.S., Pasupuleti, S., Singha, S. et al., "A GIS-based modified DRASTIC approach for geospatial modeling of groundwater vulnerability and pollution risk mapping in Korba district, Central India," Environ. Earth Sci., vol. 78:628, Oct. 2019, 10.1007/s12665-019-8640-2.

[19] A., Arabameri, K., Rezaei, H.R. Pourghasemi, et al., " GIS-based gully erosion susceptibility mapping: a comparison among three data-driven models and AHP knowledge-based technique," Environ. Earth Sci., vol. 77:628, Sep. 2018, 10.1007/s12665-018-7808-5.

[20] S.S. Biswas, P. Pani, "Estimation of soil erosion using RUSLE and GIS techniques: a case study of Barakar River basin, Jharkhand, India," Model. Earth Syst. Environ., vol. 1:42, 2015, 10.1007/s40808-015-0040-3.

[21] Y. Farhan, S. Nawaiseh, "Spatial assessment of soil erosion risk using RUSLE and GIS techniques," Environ. Earth Sci., vol. 74, pp. 4649–4669, Sep. 2015, 10.1007/s12665-015-4430-7.

[22] D. Hou, D. O'Connor, P.;Nathanail, L. Tian, Ma, Y. "Integrated GIS and multivariate statistical analysis for regional scale assessment of heavy metal soil contamination: A critical review," Environ. Pollut., vol. 231, no. 1, pp. 1188–1200, Dec. 2017, 10.1016/j.envpol.2017.07.021.

[23] W. Jia, G. Wang, "Multiple level prospectivity mapping based on 3D GIS and multiple geoscience dataset analysis: a case study in LuanchuanPb-Zn district, China," Arab. J. Geosci., vol. 12:332, 2019, 10.1007/s12517-019-4495-9.

[24] N. Li, X. Song, C. Li, et al., "3D Geological Modeling for Mineral System Approach to GIS-Based Prospectivity Analysis: Case Study of an MVT Pb–Zn Deposit," Nat. Resour. Res., vol. 28, pp. 995–1019, Jul. 2019, 10.1007/s11053-018-9429-9.

[25] L., Liu, J., Lu, C. Tao, et al., "GIS-based Mineral Prospectivity Mapping of Seafloor Massive Sulfide on Ultraslow-spreading Ridges: A Case Study of Southwest Indian Ridge 48.7°–50.5° E," Nat. Resour. Res., Jan. 2021, 10.1007/s11053-020-09797-y.

[26] X. Mao, W. Zhang, Z. Liu, J. Ren, R.C. Bayless, H. Deng, " 3D Mineral Prospectivity Modeling for the Low-Sulfidation Epithermal Gold Deposit: A Case Study of the Axi Gold Deposit, Western Tianshan, NW China,". *Minerals,* vol.10, no.3:233, Mar.2020, 10.3390/min1003023.

[27] Y. Choi, J. Baek, S. Park, "Review of GIS-Based Applications for Mining: Planning, Operation, and Environmental Management," *Appl. Sci.,* Apr.2020, vol.10, no. 7:2266, 10.3390/app10072266.

[28] K.D. Kim, S., Lee, H.J. Oh, et al., "Assessment of ground subsidence hazard near an abandoned underground coal mine using GIS," Environ. Geol., vol. 50, pp. 1183–1191, may. 2006, 10.1007/s00254-006-0290-5.

[29] J. Blachowski, "Application of GIS spatial regression methods in assessment of land subsidence in complicated mining conditions: case study of the Walbrzych coal mine (SW Poland)," Nat. Hazards, vol. 84, pp. 997–1014, Jul.2016, 10.1007/s11069-016-2470-2.

[30] H. Oh, S. Ahn, J. Choi, et al., "Sensitivity analysis for the GIS-based mapping of the ground subsidence hazard near abandoned underground coal mines," Environ. Earth. Sci., vol. 64, pp. 347–358, Sep. 2011. 10.1007/s12665-010-0855-1.

[31] S. Lee, I. Park, J.K. Choi,"Spatial Prediction of Ground Subsidence Susceptibility Using an Artificial Neural Network" Environ. Manag., vol. 49, pp. 347–358, Oct. 2012, 10.1007/s00267-011-9766-5.

[32] J.K. Choi, K.D. Kim, S. Lee, et al., "Application of a fuzzy operator to susceptibility estimations of coal mine subsidence in Taebaek City, Korea," Environ. Earth. Sci., vol. 59, pp. 1009–1022, Jan. 2010, 10.1007/s12665-009-0093-6.

[33] I. Park, et al., "Application of an adaptive neuro-fuzzy inference system to ground subsidence hazard mapping," Comput. Geosc., vol.48, pp. 228-238, Nov. 2012, 10.1016/j.cageo.2012.01.005.

[34] . J. Oh, S. Lee, " Integration of ground subsidence hazard maps of abandoned coal mines in Samcheok, Korea," Inter. J. Coal Geol., vol. 86, no.1, pp. 58–72, Apr. 2011, 10.1016/j.coal.2010.11.009.

[35] H. J. Oh, S. Lee, "Assessment of ground subsidence using GIS and the weights-of-evidence model," Eng. Geol., vol. 115, pp. 36–48, Jul. 2010, 10.1016/j.enggeo.2010.06.015.

[36] N. Larachi, A. Bali, M. OuldHamou, S. Bensaadi, " Recovery of lead and barite from the abandoned Ichmoul mine wastes in Algeria," Environ. Earth Sci., vol.78:601, Oct. 2019, 10.1007/s12665-019-8593-5.

[37] M. Daoud " Mise en exploitation du gisement de djebel Ichmoul,". Mémoire de fin d'études, ingéniorat, Dep. Metallurgie, ENP, El-Harrach, 1974.

Nassim LARACHI received a Magister degree from the Ecole Nationale Polytechnique in Mining Engineering, in 2004. He is currently preparing a doctoral thesis on the wastes and the mining voids of mines sites abandoned. He works as an associate professor at Abderrahmane Mira university of Bejaia. His research interests are mining geology, mining exploitation, mine wastes and ores processing, mine-informatics and mining environment.

Abderrahim BALI is Professor and research director in Civil Engineering at Ecole Nationale Polytechnique Algiers, Algeria. He holds a PhD from Aston University in Birmingham (GB). He is involved in research activities and supervisions of Master and Doctorate's theses. He has been a member of the Administration Council of

several national companies**.** He is a member of ACI (Algeria Chapter), and several technical committees for national and international research projects. His field of research and expertise includes microstructure, cementitious additions, recycling, local materials, fire resistance and durability of concrete.

Abderrezak AIT YAHIATENE is born on 05/03/1957, in Tizi-Ouzou (Algeria), is a retired associate Professor from the Mining Engineering Department of Ecole Nationale Polytechnique, Algiers, Algeria. He received the Doctorate degree from AKADEMIA GORNICZO HUTNICZA (AGH) KRAKOW POLAND, in June 1987. He has successfully supervised many engineer, MSc and magister students at Ecole Nationale Polytechnique (ENP, Algiers). His research interests are in the areas of engineering mining, mining economy and mine-informatics.

Malek OULD HAMOU is a professor at Ecole Nationale Polytechnique Algiers, Algeria. He was the head of mining engineering department and the director of the mining engineering laboratory of the same establishment. His research interests are mineralurgy, bio-processing and mining environment.

Numerical investigation on mechanical properties of a nanobiocomposite based on date palm fiber and nanoclays with interphase problem

Khaled Meliani, and Said Rechak

Abstract−The use of biocomposites has been a major concern in recent decades with the emergence of composites as materials that can replace conventional ones. To improve the mechanical properties of these materials, special attention is devoted to nano-reinforcements. Among these nano-reinforcements, NanoClays (NC) are attracting the attention of many researchers. This nanoparticle, in addition to being biobased, has good mechanical properties and its nanometric dimension allows it to be an interesting reinforcement for the composite because of the NC/Matrix surface contact that it develops. In this study, a 4-phase material (Matrix, NC, Palm fiber and interphase) will be studied and the effect of several parameters (Aspect Ratio (AR), distance between NC and loading point, interface thickness and interfacial conditions) will be assessed and discussed. To do this, a 3D FEM model is developed and a mesh convergence study is pre-established.

***Keywords*− nanobiocomposite, nanoclays, nanoparticle, nano-reinforcement, 4-phase material.**

NOMENCLATURE

NC	NanoClays.
AR	Aspect Ratio.
RVE	Representative Volume Element.
FEM	Finite Element Method
BEM	Boundary Element Method
CNT	Carbon Nano Tube
ave	Average
ROM	Rule Of Mixtures
t_i	Thickness of interphase

I. INTRODUCTION

The economic and environmental concerns associated with government initiatives have encouraged the search for more environmentally friendly alternatives to petroleum-derived composites.

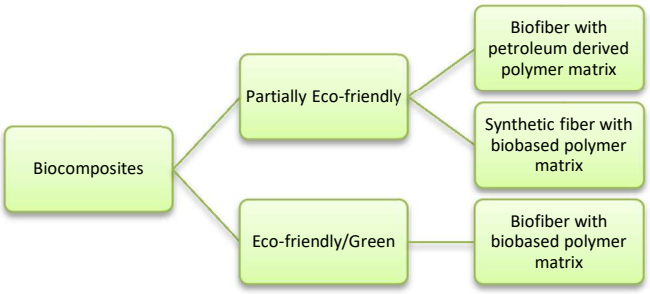

Fig. 1: Classification of biocomposites [1]

Much of this research has focused on the development of biocomposites and other renewable natural materials. Biocomposites can be broadly defined as a composite material that uses one or more environmentally friendly materials such as natural fiber reinforcements or biopolymers. (Fig. 1).

Recently, a large window of opportunity has opened up to overcome the limitations of traditional polymer composites at the micrometer scale by charged polymer composites at the nanoscale - in which the charge is <100 nm in at least one dimension Fig. 2. Researchers have even studied a nano-bio-composite based on a natural fiber (date palm fiber) and carbon nanotubes ‘’CNT’’ [2].

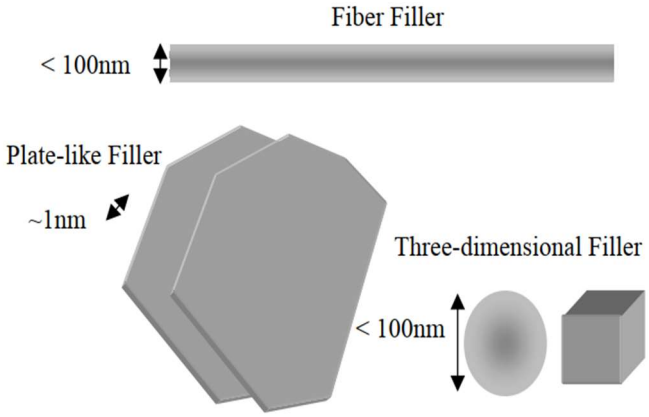

Fig. 2: Schematic of nano-scale filler [1]

Although some nanofilled composites (polymers charged with carbon black [3] and fumed silica [4, 5]) have been in use for more than a century, research and development of polymers has increased considerably in recent years, for several reasons.

Manuscript received May 1, 2021; revised September 22, 2021.
K. Meliani and S. Rechak are with the Mechanical Engineering and Development Laboratory, Department of Mechanical Engineering, Ecole Nationale Polytechnique, Algiers, ALGERIA.
(e-mail: khaled.meliani@g.enp.edu.dz, said.rechak@g.enp.edu.dz)

Digital Object Identifier (DOI): 10.53907/enpesj.v1i2.29

First, unprecedented combinations of properties have been observed in some polymer nanocomposites [6]. For example, the inclusion of equi-centered nanoparticles in thermoplastics, and in particular in semi-crystalline thermoplastics, increases the yield strength, tensile strength and Young's modulus [7] compared to pure polymer . A volume fraction of only 0.04 mica-type silicates (MTS) in the epoxy increases the modulus under the glass transition temperature by 58% and the modulus in the rubbery region by 450% [8]. In addition [9], the permeability of water in poly (e-caprolactone) decreases with the addition of 4.8% silicate. Yano et al. [10] showed a 50% decrease in the permeability of polyimides at a load of 2% MTS.

The "discovery" of carbon nanotubes in the early 1990s [11] is a second reason for the sharp increase in research and development efforts. Although closer examination has shown that nanotubes have been observed since the 1960s [12], it was not until the mid-1990s that they were manufactured in the quantities required for the evaluation of composite's properties. The properties of these carbon nanotubes, in particular resistance and electrical properties, are very different from those of graphite and offer interesting possibilities for new composite materials.

Third, a significant development in the chemical treatment of nanoparticles and in the in situ treatment of nanocomposites has led to unprecedented control of the morphology of these composites. It also created an almost unlimited ability to control the interface between the matrix and the filler.

Nanoclays are the good example of natural nanomaterials and are generally used for a clay mineral having a phyllosilicate or foil structure with a thickness of about 1 nm and areas of about 50 to 150 nm in one dimension [13, 14]. Nanoclays are therefore the general term for the layered mineral silicate nanoparticles having a high aspect ratio. Depending on the morphology of the nanoparticles and the chemical composition of the nanoclays are organized into various classes such as illite, halloysite, bentonite, kaolinite, montmorillonite, hectorite and chlorite [14]. Researchers explored that nanoclays can be obtained from raw clay minerals in fewer steps [15], instead of several general nanoparticle synthesis techniques [15].

The layered structure allows the material to swell or shrink depending on its tendency to absorb water. In addition, the purity and cation exchange capacity of nanoclay is one of the critical properties, as it provides the surface activity required for inclusion of modifiers and for surface treatments [16].

Nanoclays products are typically modified with ammonium salts and are often referred to as "organically modified nanoclays or organoclays" [17].

Organoclays are one of the attractive and promising inorganic organic hybrids of nanomaterials typically used for the modification of polymers and polymer-based composites. The modification of clay surfaces makes them organophilic to make them compatible with the hydrophobic properties of organic polymers [18].

The researchers stated that the structure of nanoclays or its dispersion in resins are of different types and can be characterized as separate, intercalated or exfoliated phases shown in Fig. 3 [19].

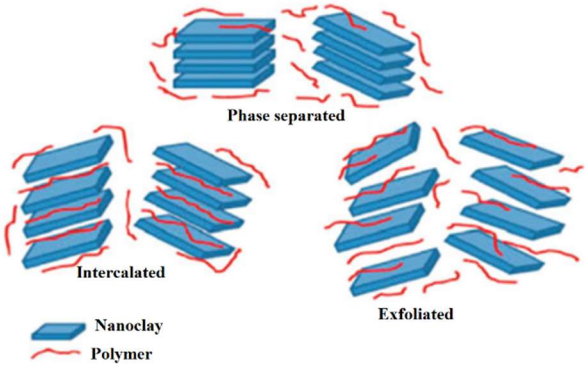

Fig. 3: Dispersion mechanism of nanoclay in resin.

In order to predict effective elastic properties, analytical methods (such as Mori and Tanaka, Halpin and Tsai, self-consistent techniques) and numerical (homogenization technique based on representative volume element and finite element method) are often preferred to experimental approaches. During the last decade, several works have used various techniques to model nano-clay / polymer composites. Fornes and Paul [20] obtained the properties of the nylon - clay composite using the theory of composites. Luo and Daniel [21] characterize the mechanical behavior of the polymer / clay nanocomposite using the Mori-Tanaka Method for a three-phase material. Odegard et al. [22] have also obtained the mechanical properties of nanoparticle polymer composites using a continuum-based micromechanics model. Hbaieb et al. [23] obtained the stiffness of the polymer / clay nanocomposite, they show prove that the Mori-Tanaka method is more accurate for aligned particles volume fractions less than 5%. More recently, Wang et al. [24] presented the prediction and improvement of the tensile and breaking strength of epoxy / nanocomposite clay using a double interpenetrating network. Wang et al. [25] used a 3-D finite element model to obtain the elastic properties of a nano-reinforced polymer composite. Chia et al. [26] presented a 3-D finite element method to understand the effect of nanoparticles on the mechanical properties of epoxy clay nanocomposite using representative volume element (RVE). Zhu and Narh [27] used a numerical simulation to obtain the tensile modulus of a nano clay / polymer composite. Dong and Bhattacharyya [28] proposed a representative volume element (RVE) to find the mechanical behavior of a polymer / clay composite.

In the present study, a 3D FEM model is developed for the analysis of the bionanocomposite. The 'nanocomposite' is modeled with 3 and 4 phases (Matrix, palm fiber, NC and interphase) material. A first study on the convergence of the mesh as a function of the number of elements will be established. Then the effects of Aspect Ration ''AR'', distance between NC itself, distance between NC and loading point, thickness of the interface, and the interfacial conditions will be evaluated and discussed.

II. CONTINUUM MODELING APPROACH

To predict the mechanical behavior of polymer nanocomposites, many modeling techniques are proposed, these modeling methods span a wide range of length and time scales. Computational chemistry are used for small length and time scales. However, computational mechanics is used to predict mechanical behavior of materials for largest length and time scales [29].

Continuum models are used for the analysis of a bio composite reinforced with date palm fiber and Nano Clay. The continuum based methods include, for computational micromechanics, the Finite Element Method (FEM) and the Boundary Element Method (BEM), and for analytical micromechanics it includes the Eshelby, Halpin-Tsai and Rule of mixtures approaches.

To extract the effective material properties of nanocomposites, both the analytical and computational approaches are used. It should be noticed that both methods assume the existence of continuum for all calculations.

Recent studies use continuous mechanical approaches for the modeling of nanocomposites and this because modeling at the molecular scale is limited to small time and dimensional scales which limit their uses, especially for engineering applications. Regarding continuous mechanics approaches, the reinforcements are considered homogeneous and isotropic.

2.1. Analytical formulation

The overall properties of nanocomposites can be evaluated by a volume average stress and strain fields of the individual constituents.

The rule of mixtures is one of the simplest analytical approaches to predict the elastic properties of the nanocomposites. For a four phase composite material the mathematical expression for composite modulus can be written as :

$$E = (1 - V_f - V_{NC} - V_i)E_m + V_f \cdot E_f + V_i \cdot E_i + V_{NC} \cdot E_{NC} \quad (1)$$

Where E, E_m, E_f, E_i and E_{NC} are the young moduli of the nanocomposite, the matrix, the fiber, the interphase and the NC respectively and V_f, V_i and V_{NC} are the volume fractions of the fiber, the interphase and the NC respectively. The volume fractions of fiber, NC and interphase can be calculated, for a square RVE or "representative volume element", as:

$$V_f = \frac{\pi {r_f}^2}{a^2} \quad (2)$$

$$V_{NC} = \frac{N_{NC} W_{NC} Th_{NC} L_{NC}}{La^2} \quad (3)$$

$$V_i = V_{NC} - \frac{N_{NC}.W_i.Th_i.L_i}{L.a^2} \quad (4)$$

Where N_{NC}, L_{NC}, W_{NC} and Th_{NC} are respectively the number, length, width and thickness of NC and r_f, W_i, L and a are respectively the radius of fiber, the width of the interphase, the length of the RVE .

The modulus of the interphase differs from that of the matrix and the NCs. It has an intermediate value between E_m and E_{NC} and varies punctually, the equation which gives its punctual value was found by establishing a mathematical model with the following conditions:

$E_i = E_m$ on the Matrix/Interphase contact surface

$E_i = E_{NC}$ on the Interphase/NC contact surface

One of the methods proposed and gives good agreement with the experimental results [30, 31, 32] for the calculation of the modulus of elasticity of the interphase is given as follows:

$$E_i(r) = E_m \times \frac{r_i}{r} + \left[\frac{r_i - r}{r_i - r_{NC}}\right]^{n/2} \times \left[E_{NC} - E_m \times \frac{r_i}{r_{NC}}\right] \quad (5)$$

Where, r = W / 2 is a radial coordinate in the interphase region, n is the interfacial enhancement factor, it depends on the properties of the matrix, NCs and on the interfacial conditions (treatment, additives, etc.).

From eq. 5, we can find the average modulus of elasticity of the interphase as follows:

$$E_i = \frac{1}{r_i - r_{NC}} \times \int_{r_{NC}}^{r_i} E_i(r)dr \quad (6)$$

The properties of matrix (Epoxy matrix with 10% of alumina) and fiber are listed in Table1, and those of NC are listed in table 2.

TABLE. I
Fiber and matrix material properties

	E (GPa)	ν
Matrix	**6**	**0.3**
Palm date fiber [33]	**5**	**0.3**

TABLE. II
NanoClay properties [34]

Density (Kg/m^3)	1800
E_3 (Gpa)	178
υ_{13}	0,25
G_{31} (Gpa)	70,4
E_1=E_2 (Gpa)	55
υ_{12}	0,25

2.2. Numerical formulation

Finite Element Method 'FEM' can be used for numerical computation. It also has been used for the prediction of mechanical properties of nanostructured composites.

FEM involves discretization of a RVE for which the elastic solutions lead to determination of stress field. Fig. 4 shows the three possible RVEs for the analysis of NC-based nanocomposites. Cylindrical RVEs are easy to use but they can lead to errors due to ignoring materials not covered by the cylindrical cells. For the present study the square RVE is adopted in both the analytical and numerical computations.

(a) (b) (c)

Fig. 4: Three possible RVEs for the analysis of NC-based nanocomposites, (a) Cylindrical RVE; (b) square RVE; and (c) hexagonal RVE.

As represented in Fig. 4 the palm date fiber is kept in the central part of the representative element while the matrix is reinforced with the nanoclay surrounded by an interphase.

The nanocomposite analysis is conducted using the Ansys software that is one of the few codes that have special capacities to analyze nanocomposite materials. The first step is to define the geometry then the material properties given in Tables 1 and 2. The diameter of the Palm date fiber is 300 nm and has a length of 500 nm. The matrix has width equal to 400 nm and a depth equal to 500 nm.

The physical properties of nanoclay are:

- Width : varies from 102 to 353nm
- Thickness : varies from 0.59 to 2.04 nm
- Length = 480 nm

The physical properties of interphase are:

- Width : varies from 105 to 356 nm
- Thickness =1.5 nm
- Length = 483 nm

The volume fraction of NC is set to be 1% for all calculations.

The mesh is established using the brick elements with refinement for the NC and the parts of the matrix that surround them Fig. 5. The choice of a brick element is motivated by: on one side brick element is more suitable in a finite element analysis leading to better accuracy, on the other hand the 8 nodes 24 degrees of freedom brick elements leads us to a significant reduction in the number of elements.

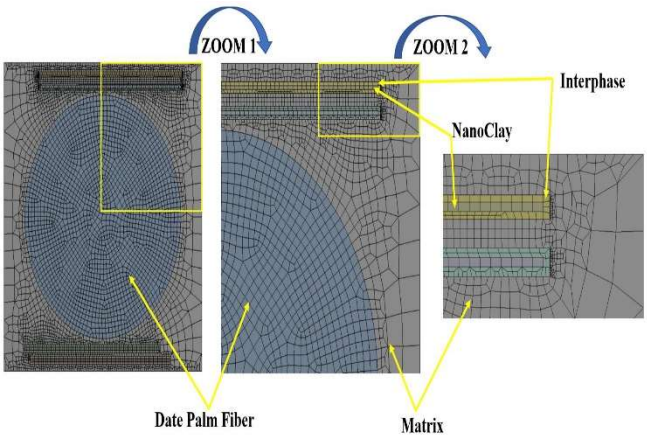

Fig. 5: Meshing of the square RVE containing four NC using brick elements with a zoom on the refined parts.

Depending on nanoclay's thickness, the number of elements varies from 2E+05 to 4E+05 corresponding respectively to 7E+05 to 14.6E+05 nodes. The calculation time varies from 500 s to up to 3000 s.

To extract the equivalent material constants, a homogenized elasticity model is considered. Solutions can be obtained under axial stretch Fig. 6. The material considered in this study is transversely isotropic and have five independent material constants. The effective material constants are Young's moduli E_x and E_Z, Poisson's ratios ν_{xy} and ν_{zx} and shear modulus G_{zx}. It is to be noticed that the computations were made on the whole of the RVE.

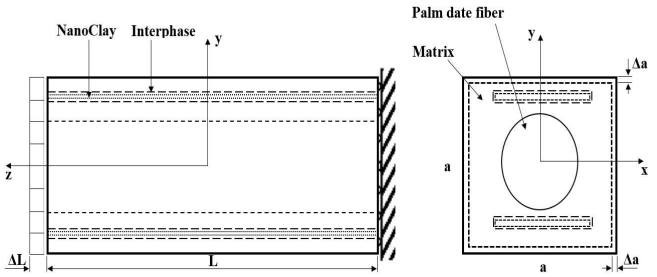

Fig. 6: Square RVE under axial stretch ΔL

The strain-stress relation relating the normal stresses (σ_x, σ_y, σ_z) and strains (ε_x,ε_y,ε_z) for a transversally isotropic material can be written as:

$$\begin{bmatrix}\varepsilon_{xx}\\ \varepsilon_{yy}\\ \varepsilon_{zz}\\ \varepsilon_{yz}\\ \varepsilon_{zx}\\ \varepsilon_{xy}\end{bmatrix} = \begin{bmatrix} \frac{1}{E_x} & -\frac{\nu_{xy}}{E_x} & -\frac{\nu_{zx}}{E_z} & 0 & 0 & 0 \\ -\frac{\nu_{xy}}{E_x} & \frac{1}{E_x} & -\frac{\nu_{zx}}{E_z} & 0 & 0 & 0 \\ -\frac{\nu_{zx}}{E_z} & -\frac{\nu_{zx}}{E_z} & \frac{1}{E_z} & 0 & 0 & 0 \\ 0 & 0 & 0 & \frac{1}{2G_{zy}} & 0 & 0 \\ 0 & 0 & 0 & 0 & \frac{1}{2G_{zy}} & 0 \\ 0 & 0 & 0 & 0 & 0 & \frac{1+\nu_{xy}}{E_x} \end{bmatrix} \begin{bmatrix}\sigma_{xx}\\ \sigma_{yy}\\ \sigma_{zz}\\ \sigma_{yz}\\ \sigma_{zx}\\ \sigma_{xy}\end{bmatrix} \quad (7)$$

2.2.1 Square RVE under axial stretch

The square RVE is embedded on one side and subjected to a displacement ΔL on the other side along the Z axis (Fig. 6).

The stresses and strains are given by: $\sigma_x=\sigma_y=0$, $\varepsilon_z=\Delta L/L$,

$\varepsilon_x=2\Delta a/a$ along $x=\pm a/2$

and $\varepsilon_y=2\Delta a/a$ along $y=\pm a/2$

The young's modulus E_z is then given by :

$$E_z = \frac{\sigma_{ave}}{\varepsilon_z} = \frac{L}{\Delta_L}\sigma_{ave} \quad (8)$$

where the average value of stress σ_z is given by:

$$\boldsymbol{\sigma_{ave}} = \frac{1}{A}\int_A \boldsymbol{\sigma_z}\left(\boldsymbol{x},\boldsymbol{y},\frac{\boldsymbol{L}}{\boldsymbol{2}}\right)\boldsymbol{dxdy}$$

where A is the area of the end surface and σ_ave is calculated from the numerical results.

III. RESULTS AND DISCUSSIONS

3.1- Convergence of the mesh

The mesh of the nanocomposite is an important step in the digital resolution process. Indeed, for a multiscale material, it is necessary to find an optimal mesh to both have precise results but also to reduce the calculation time. To do this, for each model, a mesh convergence study is necessary in order to obtain the number of elements that allows having an optimal solution.

Fig. 7 shows that for the nanocomposite based on clay nanoparticles and palm fibers, the modulus of elasticity stabilizes for a number of elements greater than 2E+05.

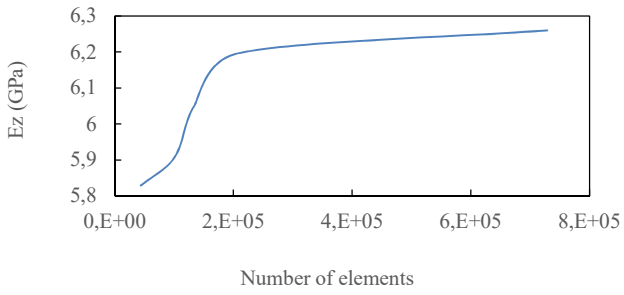

Fig. 7: Meshing convergence with RVE element's number

3.2- Validation of the 3D FEM Model and Effect of the aspect ratio

The results obtained from the 3D MEF model containing NCs are compared to the "ROM" mixture rule which is one of several theoretical models for computing elastic modulus of multi-phase materials. Numerical results are obtained by solving the 3D FEM system using the "ANSYS" simulation software and the equation (8). The analytical results are obtained by the Rule of mixtures ROM Eq. (1).

We see from the results presented in Figure 8 that the 3D FEM model predicts the modulus of elasticity in a similar way to that obtained by ROM with a difference not exceeding 12% for AR = 50. This difference decreases for aspect ratio values greater than 50.

Fig. 8 depicts the effect of AR on the modulus of the composite. The modulus of elasticity can be seen to increase with increasing AR. This is explained by the increase in the Matrix / Nano-reinforcement contact surface (Fig. 9), because the increase in the contact surface generates an increase in the matrix / Nano-reinforcement charge transfer as can be seen from the distribution of constraint in Fig. 10.

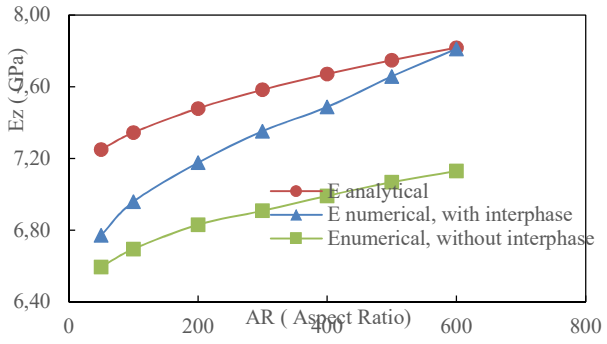

Fig. 8: Evolution of E_z with AR

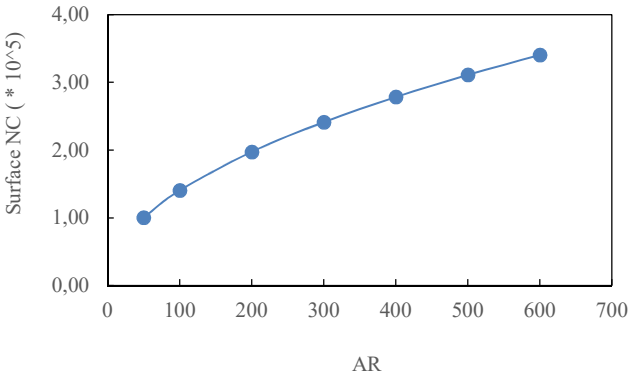

Fig. 9: Evolution of NC's surface with AR

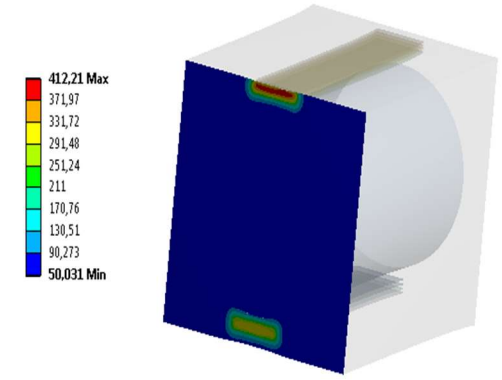

(a)

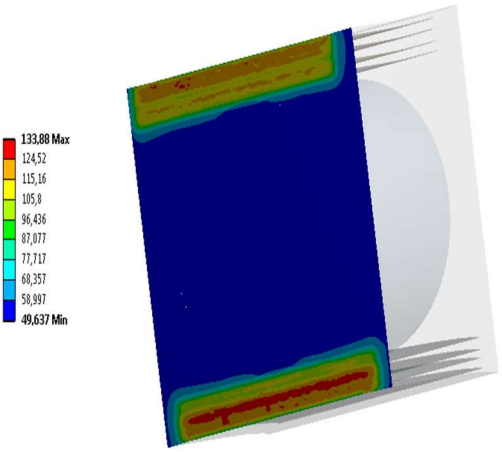

(b)

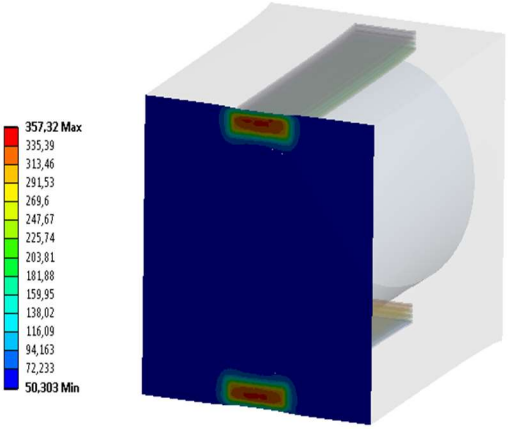

(c)

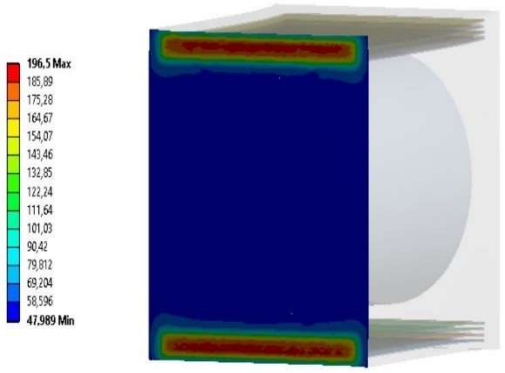

(d)

Fig. 10: Stress plot (MPa) for the surface Z=500 nm (a) AR=50 without interphase, (b) AR=600 without interphase, (c) AR=50 with interphase, (d) AR=600 with interphase

3.3 effect of t_i and n on E_i

Fig. 11 depicts the effect of t_i and n on the elastic modulus of the interphase. It can be seen that for perfect interfacial conditions characterized by n = 2, the interphase modulus decreases with increasing t_i (Fig. 11(a)). For imperfect interfacial conditions characterized by n> 2, the modulus of elasticity of the interphase increases with increasing t_i (Fig. 11(c), Fig. 11(d)).

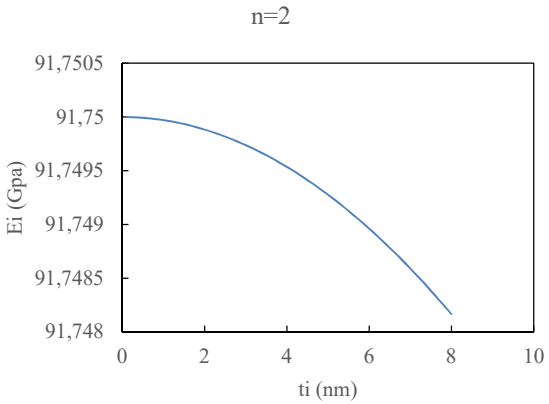

(a)

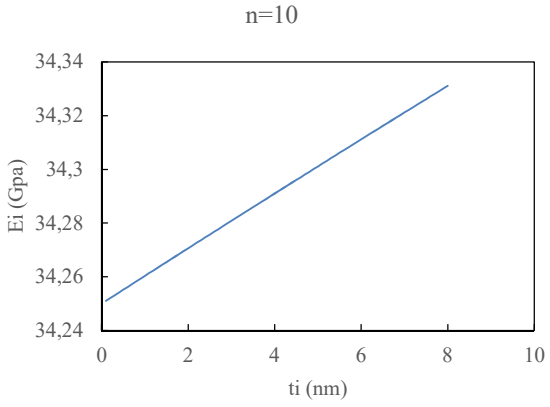

(b

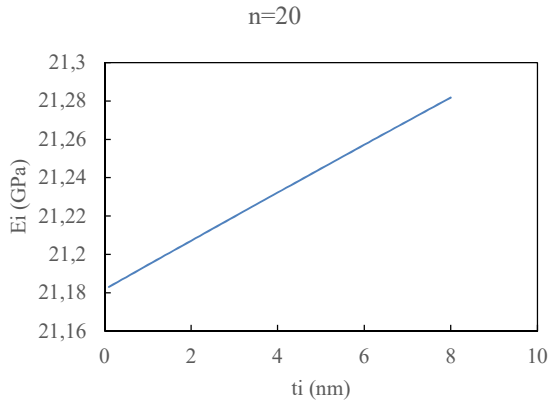

(c)

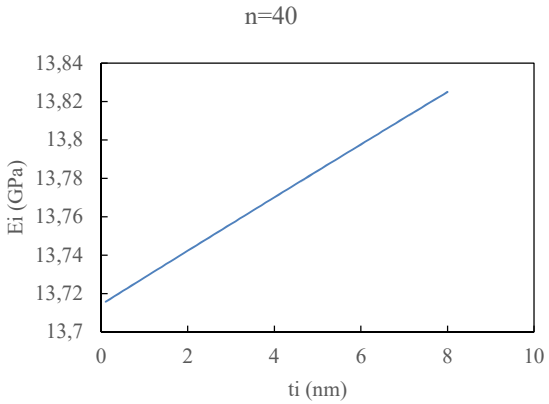

(d)

Fig. 11: Variation of the elastic modulus of the interphase with n and ti (a) n=2, (b) n=10, (c) n=20, (d) n=40.

3.4 Effect of the distance between NC "d"

Fig. 12 shows the effect of the distance between nano clay particles on the modulus of elasticity of the composite. It can be seen that the greater this inter-particle distance, the greater the modulus of the composite. For d = 0nm there is an agglomeration of the nanoparticles and the contact surface decreases considerably and therefore the charge transfer decreases which leads to a low modulus of elasticity. For a large enough d we have totally exfoliated nanoparticles and give a maximum matrix / nano-reinforcement charge transfer which can be visualized on the stress distribution Fig. 13.

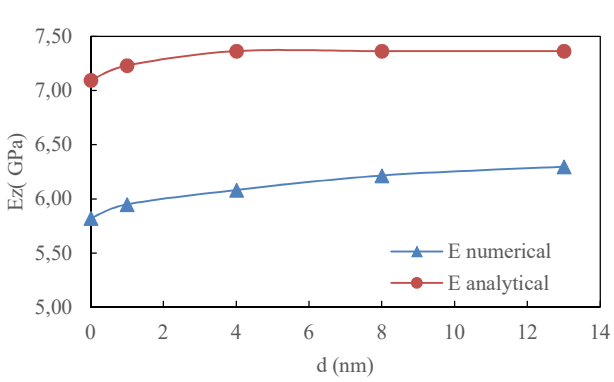

Fig. 12: Evolution of Ez with d

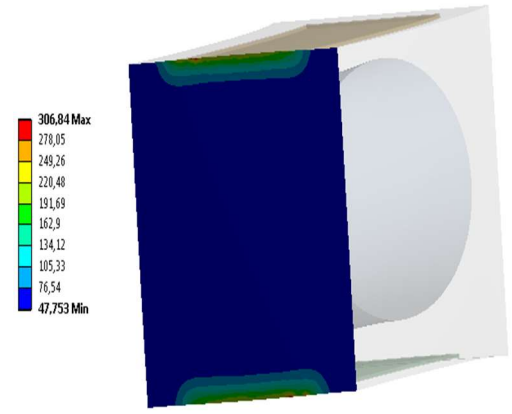

(a)

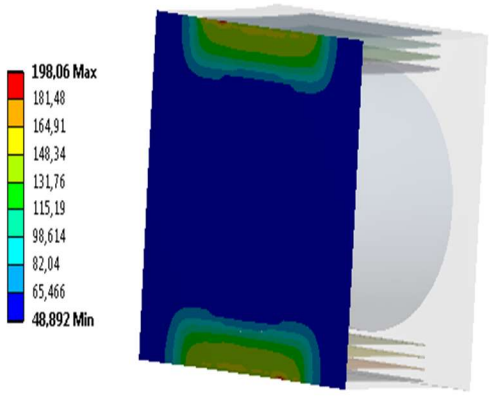

(b)

Fig. 13: Stress plot (MPa) for the surface z=500 nm (a) d=0 nm, (b) d= 13 nm.

3.5 Effect of the distance from charging point "D"

Fig. 14 depicts the effect of the distance D between the applied load and the nanosheets on the elastic modulus of the composite. We see a decrease in modulus with increasing distance D. This is explained by the existence of losses with respect to the matrix / nano-reinforcement load transfer that can be visualized on the stress distribution in Fig. 15.

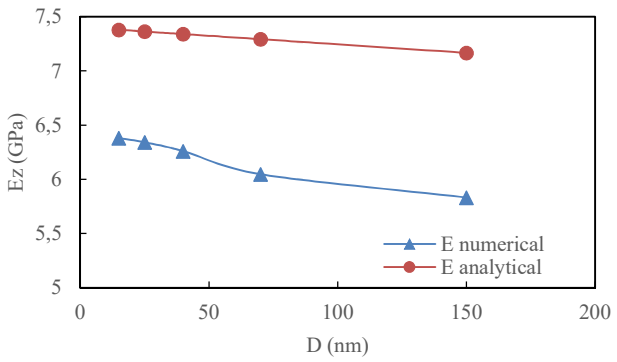

Fig. 14: Evolution of elastic modulus with D

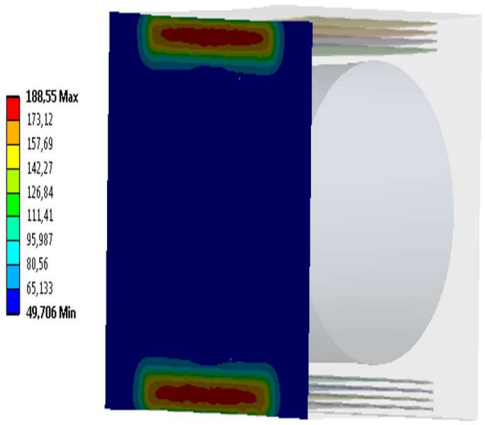

(a)

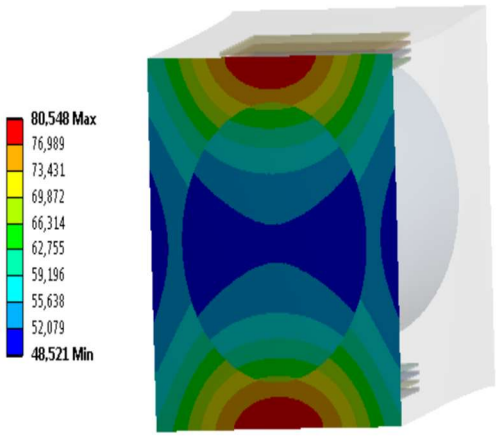

(b)

Fig. 15: Stress plot for the surface z=500 nm (a) D=15 nm, (b) D= 150 nm.

IV. Conclusion

In this work, a three and four phase materials were considered and a 3 D FEM model was developed to extract the nanocomposite's elastic properties. Firstly, a study on meshing convergence was conducted. It was found that the mesh converged from a number of element greater than 2E+05. Various processing parameters were set (including the Aspect Ration ''AR'', distance between NC, distance from charging point, interphase thickness and interfacial characteristics represented by the intra gallery enhancement factor ''n'') and there effects on composite's modulus Ec was evaluated and discussed. It was found that an increase in AR leads to an increase in the elastic modulus Ec. In addition, Ec was found greater when the interphase is considered. From various parameters studied, one can conclude that fully exfoliated NC and good interfacial carachteristics allow the improvement of mechanical properties of the nanocomposite.

References

[1] A. G. CUTTER, *Development and Characterization of Renewable Resource-based Structural Composite Materials,* University of California, San Diego, 2008.

[2] K. MELIANI and S. RECHAK, «Comparative study of biocomposite reinforced with vegetable fiber and based on carbon nanotubes of different corrugated shapes with interphase problem,» *COMPOSITE INTERFACES,* vol. 27, pp. 161-175, 2019, 10.1080/09276440.2019.1604049.

[3] A. M. Bueche, «Filler reinforcement of silicone rubber,» *Journal of Polymer Science,* vol. 25, no. 1109, pp. 139-149, 1957, 10.1002/pol.1957.1202510902.

[4] B. Kuriakose, S. K. De, S. S. Bhagawan, R. Sivaramkrishnan et S. K. Athithan, «Dynamic mechanical properties of thermoplastic elastomers from polypropylene–natural rubber blend,» *Journal of Applied Polymer Science,* vol. 32, no. 16, pp. 5509-5521, 1986, 10.1002/app.1986.070320619 .

[5] M. Sumita, T. Shizuma, K. Miyasaka et K. Ishikawa, «Effect of reducible properties of temperature, rate of strain, and filler content on the tensile yield stress of nylon 6 composites filled with ultrafine particles,» *Journal of Macromolecular Science, Part B,* vol. 22, no.14, pp. 601-618, 1983, 10.1080/00222348308224779.

[6] P. C LeBaron, Z. Wang et T. J Pinnavaia, «Polymer-layered silicate nanocomposites: an overview,» *Applied Clay Science,* vol. 15, no. 11, pp. 11-29, 1999, 10.1016/S0169-1317(99)00017-4.

[7] M. Sumita, Y. Tsukumo, K. Miyasaka et K. Ishikawa , «Tensile yield stress of polypropylene composites filled with ultrafine particles,» *Journal of Materials Science,* vol. 18, pp. 1758-1764, 1983, 10.1007/BF00542072.

[8] P. B. Messersmith et E. P. Giannelis, «Synthesis and Characterization of Layered Silicate-Epoxy Nanocomposites,» *Chemistry of Materials,* vol. 6, pp. 1719-1725, 1994, 10.1021/cm00046a026.

[9] P. B. Messersmith et E. P. Giannelis, «Synthesis and barrier properties of poly(ε-caprolactone)-layered silicate nanocomposites,» *Journal of Polymer Science Part A: Polymer Chemistry,* vol. 33, no. 17, pp. 1047-1057, 1995, 10.1002/pola.1995.080330707.

[10] K. Yano, A. Usuki, A. Okada, T. Kurauchi et O. Kamigaito, «Synthesis and properties of polyimide–clay hybrid,» *Journal of Polymer Science Part A: Polymer Chemistry,* vol. 31, no. 110, pp. 2493-2498, 1993, 10.1002/pola.1993.080311009.

[11] S. Iijima, «Helical microtubules of graphitic carbon,» *Nature,* vol. 354, pp. 56-58, 1991, 10.1038/354056a0.

[12] D. T. Colbert et R. E. Smalley, «Past, Present and Future of Fullerene Nanotubes: Buckytubes,» *Ōsawa E. (eds) Perspectives of Fullerene Nanotechnology,* pp. 3-10, 2002, 10.1007/978-94-010-9598-3_1 .

[13] S. Sedaghat, «Synthesis of clay-CNTs nanocomposite,» *Journal of Nanostructure in Chemistry,* vol. 3, no. 124, 2013, 10.1186/2193-8865-3-24 .

[14] S.Pavlidou et C.D.Papaspyrides, «A review on polymer–layered silicate nanocomposites,» *Progress in Polymer Science,* vol. 33, no. 112, pp. 1119-1198, 2008, 10.1016/j.progpolymsci.2008.07.008.

[15] F. Uddin, «Studies in Finishing Effects of Clay Mineral in Polymers and Synthetic Fibers,» *Advances in Materials Science and Engineering,* vol. 2013, p. 13, 2013, 10.1155/2013/243515.

[16] G. Xu et F. D.Blum, «Surfactant-enhanced free radical polymerization of styrene in emulsion gels,» *Polymer,* vol. 49, no. 115, pp. 3233-3238, 2008, 10.1016/j.polymer.2008.05.019.

[17] Y. Zhang, A. Tang, H. Yang et J. Ouyang, «Applications and interfaces of halloysite nanocomposites,» *Applied Clay Science,* vol. 119, no. 11, pp. 8-17, 2016, 10.1016/j.clay.2015.06.034.

[18] R. Jahanmardi, B. Kangarlou et A. R. Dibazar , «Effects of organically modified nanoclay on cellular morphology, tensile properties, and dimensional stability of flexible polyurethane foams,» vol. 3, no. 182, 2013, 10.1186/2193-8865-3-82 .

[19] F.L.Nabil, A.Zaidon, M.Jawaid, U.M.K.Anwar, E.S.Bakar, M.T.Paridah, S.M.A.Ridzuan et G.M.Aizat, «Physical and morphological properties of nanoclay in low molecular weight phenol formaldehyde resin by ultrasonication,» *International Journal of Adhesion and Adhesives,* vol. 62, pp. 124-129, 2015, 10.1016/j.ijadhadh.2015.07.012.

[20] T.D.Fornes et D.R.Paul, «Modeling properties of nylon 6/clay nanocomposites using composite theories,» *Polymer,* vol. 44, no. 117, pp. 4993-5013, 2003, 10.1016/S0032-3861(03)00471-3.

[21] J. Luo et I. M.Daniel, «Characterization and modeling of mechanical behavior of polymer/clay nanocomposites,» *Composites Science and Technology,* vol. 63, no. 111, pp. 1607-1616, 2003, 10.1016/S0266-3538(03)00060-5.

[22] G.M. Odegard, T.C. Clancy et T.S.Gates, «Modeling of the mechanical properties of nanoparticle/polymer composites,» *Polymer,* vol. 46, no. 12, pp. 553-562, 2005, 10.1016/j.polymer.2004.11.022.

[23] K. Hbaieb, Q.X. Wang, Y.H.J. Chia et B. Cotterell, «Modelling stiffness of polymer/clay nanocomposites,» *Polymer,* vol. 48, no. 13, pp. 901-909, 2007, 10.1016/j.polymer.2006.11.062.

[24] M. Wang, X. Fan, W. Thitsartarn et C. He, «Rheological and mechanical properties of epoxy/clay nanocomposites with enhanced tensile and fracture toughnesses,» *Polymer,* vol. 58, no. 110, pp. 43-52, 2015, 10.1016/j.polymer.2014.12.042.

[25] H.W. Wang, H.W. Zhou, R.D. Peng et L. Mishnaevsky, «Nanoreinforced polymer composites: 3D FEM modeling with effective interface concept,» *Composites Science and Technology,* vol. 71, no. 17, pp. 980-988, 2011, 10.1016/j.compscitech.2011.03.003.

[26] J.K. Kim, D.Z. Wo, L.M. Zhou, H.T. Huang, K.T. Lau et M. Wang, «Finite Element Modelling Epoxy/Clay Nanocomposites,» *Key Engineering Materials,* vol. 334, pp. 785-788, 2007, 10.4028/www.scientific.net/KEM.334-335.785.

[27] L. Zhu et K.A. Narh, «Numerical simulation of the tensile modulus of nanoclay-filled polymer composites,» *Journal of Polymer Science Part B: Polymer Physics,* vol. 42, no. 112, pp. 2391-2406, 2004, 10.1002/polb.20112.

[28] Y. Dong et D. Bhattacharyya, «A simple micromechanical approach to predict mechanical behaviour of polypropylene/organoclay nanocomposites based on representative volume element (RVE),» *Computational Materials Science,* vol. 49, no. 11, pp. 1-8, 2016, 10.1016/j.commatsci.2010.03.049 .

[29] P. Valavala et G. Odegard, «Modeling techniques For determination of mechanical properties,» *Rev.Adv.Mater.Sc,* vol. 9, pp. 34-44, 2005.

[30] M. H. Meybodi, S. S. Samandari et M. Sadighi, «A new approach for prediction of elastic modulus of polymer/nanoclay composites by considering interfacial debonding: Experimental and numerical investigations,» *Composites Science and Technology,* vol. 117, no. 129, pp. 379-385, 2015, 10.1016/j.compscitech.2015.07.014 .

[31] S. S. Samandari et A. A. Khatibi, «The Effect of Interphase on the Elastic Modulus of Polymer Based Nanocomposites,» *Key Engineering Materials,* vol. 312, pp. 199-204, 2006, 10.4028/www.scientific.net/KEM.312.199.

[32] S. S. Samandari et A. A. Khatibi, «Evaluation of elastic modulus of polymer matrix nanocomposites,» *Polymer Composites,* vol. 28, no. 13, pp. 405-411, 2007, 10.1002/pc.20322 .

[33] S.Abani, F.Hafsi, A.Kriker et A.Bali, «Valorisation of Date Palm Fibres in Sahara Constructions,» *Energy Procedia,* vol. 74, pp. 289-293, 2015, 10.1016/j.egypro.2015.07.608.

[34] M. H. Meybodi, S. S. SAMANDARI et M. SADIGHI, «3D multiscale modeling to predict the elastic modulus of polymer/nanoclay composites considering realistic interphase property,» *Composite Interfaces,* vol. 23, no. 17, pp. 641-661, 2016, 10.1080/09276440.2016.1166742 .

Khaled MELIANI received his mechanical engineering diploma from Ecole Nationale Polytechnique, Algiers and Master's degree in solid mechanics from the same school. He is currently Ph.D student in Ecole Nationale Polytechnique of Algiers. His research fields are biocomposites, nanocomposites, numerical analysis, carbon nanotubes and nanoclays.

Said RECHAK is a professor at the Ecole Nationale Polytechnique, Algiers. He obtained his degree in Mechanical Engineering from Ecole Nationale Polytechnique in 1980. He obtained his Master of Science and Ph.D. degrees from the School of Aeronautics and Astronautics at Purdue University, Indiana, USA in 1982 and 1986, respectively. His main research areas are composite materials, numerical modeling by standard, and extended finite element. He opened a new research topic in nonlinear vibration and diagnosis in rotating machinery. He is the author of several scientific papers.

Near Real-Time Low Frequency Load Disaggregation

Selim Sahrane, Mourad Haddadi

Abstract—Device-level power consumption information can lead to considerable energy savings. Smart meters are being adopted in several countries, but they are only capable of measuring the total power consumption. NonIntrusive Load Monitoring (NILM) aims to infer the power consumption of individual electrical loads by analyzing the aggregate power signal taken from a single-point measurement. Most existing NILM solutions are offline methods that do not allow the end-user to get real-time feedback on his energy consumption. In this paper, we present a near real-time NILM solution based on multi-label classification and multi-output regression. We use the multi-label classifier to predict the state of each load and use the multi-output regressor to estimate the disaggregated active power consumptions. We test our method using a publically available dataset of real power measurements. Performance results show that the proposed near real-time method can accurately estimate the energy consumption of the targeted loads with an average relative energy error of 1.55%

***Keywords*—NILM, Load Disaggregation, Multi-label Classification, Multi-output Regression, Energy Estimation, Smart Meters.**

I. Introduction

The worldwide increase in energy demand and climate change has resulted in new technologies which aim to reduce the use of fossil fuels as well as reducing the overall energy consumption. If actions are not undertaken, the CO2 emissions will double by 2050 [1]. Residential buildings consume up to 40% of total energy [1]. Studies show that consumers don't know the necessary actions which will reduce their energy bill [2]. Furthermore, 55.2% of people do prefer reducing the usage of inefficient appliances while only 11.7% prefer replacing their old appliances. This highlights the importance of providing relevant feedback information to the consumer on his energy consumption. The most common type of feedback is provided through energy bills (e.g., KWatt/hour) [2] which does not provide detailed information to the user. The effect of energy feedback on household consumption is covered in detail in [3]. Furthermore, providing appliance-level consumption information can result in more than 12% of energy savings [4] [5] [6].

Non-intrusive load monitoring (NILM) also called load or energy disaggregation aims to infer the energy consumption of single appliances from the aggregate energy use measured at the power source interface [7]. One instrumented point is sufficient to get the energy consumption of each appliance. Intrusive load monitoring (ILM) on the other hand uses one measuring system for each appliance which has the advantage to be more accurate but is more expensive and difficult to deploy at a large scale. This is why NILM is preferred when it comes to load disaggregation [8]. Each type of appliance or electrical load is different in the way it consumes electricity due to its internal circuitry and therefore has what is called "an appliance signature" [7]. A NILM system will typically rely on machine learning and signal processing techniques in order to extract features from each appliance's signature and to disaggregate the total energy signal by identifying different signatures. Most of the existing disaggregation approaches are offline methods [9], meaning that they use the entire dataset or day measurements before inferring the consumption of each appliance. This translates into a very low frequency of feedback that does not allow the consumer to take actions in real or near-real time. Real-time or near real-time disaggregation information is needed for the consumer in order to reduce his consumption for more than 9.2% [4] [5]. Zeifman [10] proposed six requirements for a load disaggregation system to be practical with the existing smart meter technology:

1. A sampling rate of 1 Hz: most smart meters use a 1 Hz sampling rate. The sampling frequency affects the feature extraction process and hence the NILM should be designed to work with 1 Hz data.
2. Accuracy: for an acceptable user experience the system should have a minimum accuracy of 80-90%.
3. Easy configuration: minimum training or no training (i.e., unsupervised) and capability to adapt to new appliances and discard old ones.
4. Near real-time feedback: the system is able to give feedback on the energy use of each appliance in a minimum time interval.
5. Robustness: the ability to detect a large number of appliances (e.g., more than 20 devices).
6. Multi-type appliance recognition: some types of appliances are trickier to detect than others, light dimmers which do not have a finite sate of consumption are more

Manuscript received March 23, 2021; revised September 29, 2021.

S. Sahrane and M. Haddadi are with the Ecole Nationale Polytechnique (e-mail: selim.sahrane@g.enp.edu.dz, mourad.haddadi@g.enp.edu.dz).

Digital Object Identifier (DOI): 10.53907/enpesj.v1i1.15

difficult to identify than multi-sate appliances like dishwashers. A practical NILM should be able to detect all types of appliances.

These requirements are extensively used among the NILM community and are used as a reference to evaluate load disaggregation methods and there is still no complete solution that satisfies all the six requirements. The fourth requirement (i.e., near real-time capability) is not largely addressed in the NILM literature and this is what motivated us to work on this issue.

In [11] an unsupervised near real-time solution is proposed. This solution is based on the use of low-frequency features (i.e., reactive and active power) as well as high-frequency features (i.e., transients). A clustering algorithm and a manual labeling procedure are used to construct an appliance signature database. The advantage of this solution is that it is unsupervised. However, some features like transients cannot be obtained with existing smart meters. In [12] a practical implementation of a spectral decomposition-based real-time NILM solution is proposed. The authors use active power and voltage measurements obtained at a frequency of 1 Hz. This method shows good results but has a high implementation cost due to the complexity of the used method. In [13], the author describes a NILM system able to perform disaggregation on a low-cost embedded processor in real-time using low-frequency sampling data. The method uses a super-state hidden Markov model and a Viterbi algorithm variant which preserves dependencies between loads. This approach is not scalable to a large number of appliances. In [14], a particle-based distribution truncation method is proposed. This solution uses 1 Hz measurements and has the ability to run in real-time. This approach presents good performance but has a high implementation cost. In fact, the authors implemented their solution on an Intel Core i7-2600 with 8GB of random access memory. In [15], a method based on particle filtering is proposed. This method uses 1 Hz measurements and is capable of running in real-time. For the implementation, it is reported that the algorithm can work in real-world applications on low-cost hardware such as a Raspberry Pi. In this work, we explore if the power consumptions of a given household's electrical loads can be accurately estimated in near real-time. Meaning that our NILM method should predict the current disaggregated power of each load for each aggregate power sample input.

The remaining of this paper is organized as follows: in section II., we formulate the load disaggregation problem, in section III., the proposed method is described in detail. In section IV., results are presented and a discussion is made. Finally, a conclusion is given in section V..

II. Problem formulation

The aim of NILM is to separate each load's signal $S_j(t)$ from the aggregate signal $S_{agg}(t)$ to then find the energy consumption of each load. The aggregate signal $S_{agg}(t)$ is expressed as:

$$S_{agg}(t) = \sum_{j=1}^{M} S_j(t) + e(t) \quad (1)$$

With M representing the number of loads and $e(t)$ a error term that accounts for unwanted noise. Fig. 1 shows how each appliance's Signal $S_j(t)$ contributes to form the aggregate signal $S_{agg}(t)$.

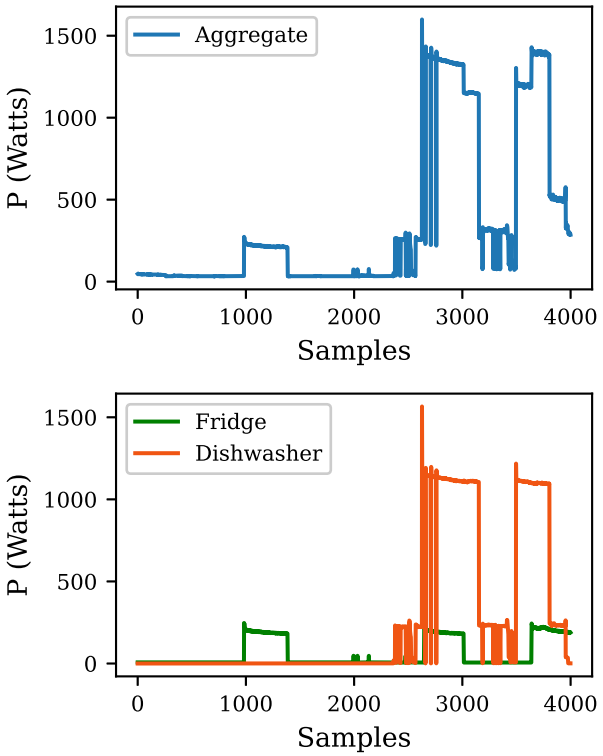

Fig. 1: Top figure shows the aggregate power signal and down figure shows the ground truth of each load.

III. Proposed method

Our disaggregation method combines a multi-label classification algorithm with a multi-output regression algorithm as shown in Fig. 2. The classification step serves to predict the state of each load (ON/OFF), and the regression method returns the power consumption of each load in a near real-time fashion. More specifically, for each single aggregate power measurement, our method predicts the corresponding disaggregated power values for each load.

A. *Multi-label Classification*

We choose a multi-label classification approach because it is more appropriate for the load disaggregation problem. In general, multiple loads can be operating concurrently in a household, which makes their identification challenging. In a classification context, each load is represented by a unique class/label. A multi-label classification approach allows the association of multiple labels to one data instance thus, permitting to account for cases where more than one load is operating. Formally, given a set of labels Y, each data instance x is associated with a subset $l \subset L$, with L the power set of Y. Two types of multi-label classification methods exist, namely, problem transformation methods and algorithm adaptation methods [16]. Problem transformation methods transform the multi-label classification problem into multiple binary classification problems. Algorithm adaptations modify an existing multi-class algorithm to support multi-label classification. In this work, we use a random forest classifier algorithm implementation adapted to support multi-label classification. The random forest algorithm [17] is an

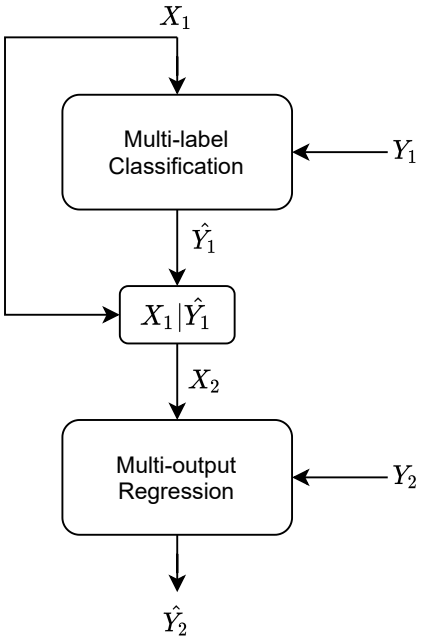

Fig. 2: Block diagram of the proposed method.

ensemble method that grows multiple decision trees on various sub-samples of the dataset and then averages the predictions to improve the predictive accuracy and control over-fitting. We use the multi-label classification to map each aggregate power sample $x_{1i} \in X_1$ to a label subset l, with X_1 representing a vector of N active power measurements. The ground truth label subset corresponding to each x_{1i} is found in the labels matrix $Y_1 = [y_{1i}, ..., y_{1N}]^T$ with y_{1i} an M-binary vector containing the ON/OFF state of the M loads. $\hat{Y}_1$ represents the predicted states of the M loads given X_1 as input to the classifier, as shown in Fig. 2.

B. Multi-output Regression

The goal of multi-output regression is to predict more than two numerical values given an input instance. As for multi-label classification, we find problem transformation methods and algorithm adaptation methods for solving the multi-output problem. An in-depth review of multi-output regression approaches is found in [18]. In this work, we use a problem transformation approach that consists of performing a separate regression for each target. Treating each target load independently is possible because the power consumptions of each load are mutually independent. The feature matrix X_2 is built using the predictions $\hat{Y}_1$ and the aggregate power values X_1 as shown in Fig. 2. The ground truth power trace of each load $P_j = [p_1, ..., p_N]^T$ is contained in the matrix $Y_2 = [P_1, ..., P_M]$. To find the coefficients of our model, we use Ridge regression [19]. Unlike linear regression, which estimates the model's coefficients by minimizing the residual sum of squares between the observed targets in the data and the targets predicted by linear approximation, Ridge regression minimizes a penalized residual sum of squares. We choose to use Ridge regression because, as mentioned in [19], when using multiple independent variables, and if these variables are not perfectly uncorrelated, the residual sum of squares method has a high probability of giving unsatisfactory results. In our case, the aggregate power samples X_1 and the predicted states of each load $\hat{Y}_1$ are more or less correlated depending on the average consumption of each load. Because switching a load ON/OFF translates into a high/low state which increases/decreases the aggregate power.

C. Data

We used The REDD dataset [20]. This dataset is largely used by NILM researchers, it contains sensor measurements collected from 10 households. Also, it provides low frequency aggregate measurements as well as ground truth measurements. We considered Household 1 which contains active power of ground truth and aggregate data measured over a period of 8 days. We used 80% of the signal for training and 20% for testing. To compare our results with [15], we targeted the same appliances which are, fridge, oven, washing dryer, dishwasher, kitchen outlet, and microwave.

IV. Results and Discussion

The field of NILM lacks standard (or commonly adopted) metrics for the evaluation of the algorithms, making fair comparison difficult [8]. To evaluate the results of our approach, we use the F1-score (3) and the relative energy error (8). To compare our results with [15], we use the accuracy Acc (2) and the normalized mean square error $NRMSE$ (6).

$$Acc = \frac{TP + TN}{TP + FN + TN + FP} \tag{2}$$

$$\text{F1-score} = \frac{2 \times Pr \times R}{Pr + R} \tag{3}$$

$$Pr = \frac{TP}{TP + FP} \tag{4}$$

$$R = \frac{TP}{TP + FN} \tag{5}$$

The true positive parameter TP represents the number of samples that have been correctly classified or, more precisely, the power quantity correctly assigned to that device. The false-positive parameter FP represents the number of samples that have been incorrectly classified or, more precisely, the power quantity incorrectly assigned to that device. The false-negative parameter FN represents the number of samples that should be but have not been classified or, more precisely, the power quantity that should have been assigned to that device but has been assigned to another or has not been assigned at all. The precision parameter (Pr) measures the portion of power samples that have been correctly classified among the power samples assigned to a given device. The recall parameter (R) measures what power portion of a given device is correctly classified in general, also considering the samples that would belong to that device but have been wrongly assigned to another or not assigned at all. Therefore, the accuracy Acc measures how well each appliance is detected and the F1-score combines the results obtained through the precision and recall analysis.

$$NRMSE = \frac{RMSE}{\overline{X}_1} \tag{6}$$

Table. I
PERFORMANCE RESULTS FOR EACH LOAD.

Load	F1-score (%)	Energy error (%)
Fridge	96.95	3.93
Oven	84.71	0.17
Dishwasher	77.38	3.24
Kitchen Outlet	85.62	0.39
Washing Dryer	78.34	1.26
Microwave	89.87	0.33

Table. II
OVERALL PERFORMANCE RESULTS OF THE PROPOSED NILM METHOD.

Macro-F1 (%)	Micro-F1 (%)	Average Error (%)
85.48	91.88	1.55

$$RMSE = \sqrt{\frac{\sum_{i=1}^{N} (\hat{x}_{1i} - x_{1i})^2}{N}} \tag{7}$$

$$\text{Energy-Error}_j = \frac{\mid \hat{E}_j - E_j \mid}{E_j} \tag{8}$$

With $\hat{E}_j$, the estimated energy consumption for the j^{th} load and E_j is the actual energy consumed by the load.

Table. I shows the evaluation results of our method. We obtain the best classification performance for the fridge with an F1-score = 96.95%. This is because the refrigerator has a less complexe load signature in comparison to other loads. Also, the refrigerator has the highest number of working cycles, thus, allowing the classifier to learn to detect it in different loads combinations scenarios. The worst classification performance is obtained for the dishwasher with an F1-score = 77.38%. We found that the "wash and drain" cycle of the dishwasher consumes almost the same power as the refrigerator and, because we only use the power as a feature, the classifier can't discriminate between them. In this case, the classifier will often predict the refrigerator as it is the most populated class compared to the dishwasher. The proposed near real-time method can detect loads that work simultaneously as shown in Fig. 3. We found in our data thirty-nine different load combinations and up to four loads working simultaneously.

Table. III
PERFORMANCE COMPARISON BETWEEN OUR METHOD AND THE PALDI METHOD [15].

Load	Accuracy (%)	
	Our method	PALDi
Fridge	98.4	78.86
Oven	99.91	99.09
Dishwasher	98.57	77.12
Kitchen Outlet	96.72	98.32
Washing Dryer	99.63	99.53
Microwave	99.76	88.33
Total	98.83	90.21
NRMSE	0.65	2.96

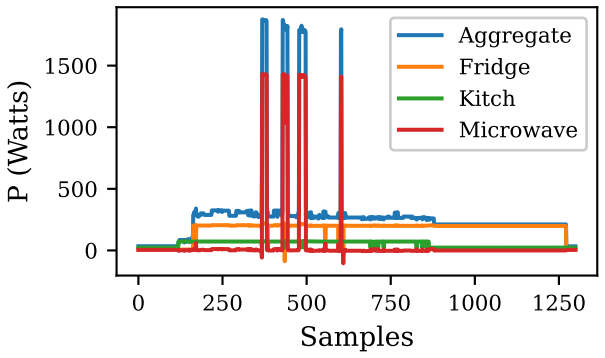

Fig. 3: Figure showing the disaggregation result obtained using our method. The power signals of the fridge, kitchen outlet, and microwave are disaggregated from the aggregate power signal.

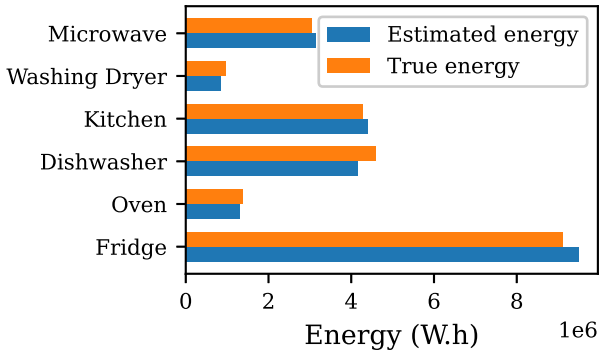

Fig. 4: Comparison between the estimated energy by our method for each load, and the corresponding actual energy consumption.

Concerning the energy estimation performance, we found that, in our case, good classification performance doesn't always result in good power/energy estimation performance. For instance, the refrigerator which is the most accurately classified load has the highest energy estimation error as shown in Table. I. High power spikes which occur when the refrigerator's compressor starts working can attain up to ten times its average power consumption. These values are difficult to predict because they don't have consistent measurement values in the dataset due to the low temporal resolution of the data. Fig. 4 shows a bar plot of the estimated energy and the actual consumed energy. Table. II gives the overall performance of the proposed method. Table III shows the comparison of the results of our method with the PALDi method [15]. We observe that the accuracy is higher for all loads except for the kitchen outlet. We also obtained a lower energy estimation error as measured with the NRMSE.

V. CONCLUSION

In this paper, we presented a near real-time load disaggregation method based on multi-label classification and multi-output regression. We used a multi-label classifier to predict the ON/OFF state of each load from the aggregate active power signal and a multi-output regression to estimate the power consumption of each load. The obtained results showed that our method disaggregates loads' energy consumption with low relative energy error. Using only the active power as a feature doesn't allow to differentiate between loads that consume the same power. A compromise exists between NILM feedback frequency and

disaggregation performance. Increasing NILM feedback frequency translates into decreasing the amount of available data for NILM prediction, thus, reducing the discriminative capability of extracted features. Also, using high-frequency data may be more adapted for the near real-time NILM problem but at the expense of higher implementation costs.In the future, we will work on the hardware implementation of our method and test it on several households.

References

[1] U. Berardi, "A cross-country comparison of the building energy consumptions and their trends," *Resources, Conservation and Recycling*, vol. 123, pp. 230–241, 2017. https://doi.org/10.1016/j.resconrec.2016.03.014

[2] N. J. Nunes, L. Pereira, F. Quintal, and M. Berges, "Deploying and evaluating the effectiveness of energy eco-feedback through a low-cost nilm solution," in *Proceedings of the 6th International Conference on Persuasive Technology*, 2011, pp. 2–5.

[3] C. Fischer, "Feedback on household electricity consumption: a tool for saving energy?" *Energy efficiency*, vol. 1, no. 1, pp. 79–104, 2008. https://doi.org/10.1007/s12053-008-9009-7

[4] K. C. Armel, A. Gupta, G. Shrimali, and A. Albert, "Is disaggregation the holy grail of energy efficiency? the case of electricity," *Energy Policy*, vol. 52, pp. 213–234, 2013. https://doi.org/10.1016/j.enpol.2012.08.062

[5] K. Ehrhardt-Martinez, K. A. Donnelly, S. Laitner *et al.*, "Advanced metering initiatives and residential feedback programs: a meta-review for household electricity-saving opportunities." American Council for an Energy-Efficient Economy Washington, DC, 2010.

[6] S. Ahmadi-Karvigh, B. Becerik-Gerber, and L. Soibelman, "A framework for allocating personalized appliance-level disaggregated electricity consumption to daily activities," *Energy and Buildings*, vol. 111, pp. 337–350, 2016. https://doi.org/10.1016/j.enbuild.2015.11.029

[7] G. W. Hart, "Nonintrusive appliance load monitoring," *Proceedings of the IEEE*, vol. 80, no. 12, pp. 1870–1891, 1992. https://doi.org/10.1109/5.192069

[8] C. Nalmpantis and D. Vrakas, "Machine learning approaches for non-intrusive load monitoring: from qualitative to quantitative comparation," *Artificial Intelligence Review*, pp. 1–27, 2018. https://doi.org/10.1007/s10462-018-9613-7

[9] S. Barker, S. Kalra, D. Irwin, and P. Shenoy, "Nilm redux: The case for emphasizing applications over accuracy," in *NILM-2014 workshop*. Citeseer, 2014.

[10] M. Zeifman, "Disaggregation of home energy display data using probabilistic approach," *IEEE Transactions on Consumer Electronics*, vol. 58, no. 1, pp. 23–31, 2012. https://doi.org/10.1109/TCE.2012.6170051

[11] T. Bernard and M. Marx, "Unsupervised learning algorithm using multiple electrical low and high frequency features for the task of load disaggregation," in *Proceedings of the 3rd International Workshop on NILM, Vancouver, BC, Canada*, 2016, pp. 14–15.

[12] S. Welikala, N. Thelasingha, M. Akram, P. B. Ekanayake, R. I. Godaliyadda, and J. B. Ekanayake, "Implementation of a robust real-time non-intrusive load monitoring solution," *Applied Energy*, vol. 238, pp. 1519–1529, 2019. Implementation of a robust real-time non-intrusive load monitoring solution

[13] S. W. Makonin, "Real-time embedded low-frequency load disaggregation," Ph.D. dissertation, Applied Sciences: School of Computing Science, 2014.

[14] Y. F. Wong, T. Drummond, and Y. Şekercioğlu, "Real-time load disaggregation algorithm using particle-based distribution truncation with state occupancy model," *Electronics Letters*, vol. 50, no. 9, pp. 697–699, 2014. https://doi.org/10.1049/el.2013.3967

[15] D. Egarter, V. P. Bhuvana, and W. Elmenreich, "Paldi: Online load disaggregation via particle filtering," *IEEE Transactions on Instrumentation and Measurement*, vol. 64, no. 2, pp. 467–477, 2015. https://doi.org/10.1109/TIM.2014.2344373

[16] B. Buddhahai, W. Wongseree, and P. Rakkwamsuk, "A non-intrusive load monitoring system using multi-label classification approach," *Sustainable cities and society*, vol. 39, pp. 621–630, 2018. https://doi.org/10.1016/j.scs.2018.02.002

[17] T. K. Ho, "Random decision forests," in *Proceedings of 3rd international conference on document analysis and recognition*, vol. 1. IEEE, 1995, pp. 278–282. https://doi.org/10.1109/ICDAR.1995.598994

[18] H. Borchani, G. Varando, C. Bielza, and P. Larranaga, "A survey on multi-output regression," *Wiley Interdisciplinary Reviews: Data Mining and Knowledge Discovery*, vol. 5, no. 5, pp. 216–233, 2015. https://doi.org/10.1002/widm.1157

[19] A. E. Hoerl and R. W. Kennard, "Ridge regression: Biased estimation for nonorthogonal problems," *Technometrics*, vol. 12, no. 1, pp. 55–67, 1970. https://doi.org/10.2307/1271436

[20] J. Z. Kolter and M. J. Johnson, "Redd: A public data set for energy disaggregation research," in *Workshop on Data Mining Applications in Sustainability (SIGKDD), San Diego, CA*, vol. 25, no. Citeseer, 2011, pp. 59–62.

Selim Sahrane was born in Algiers, Algeria, in 1989. He received the M.Sc. degree in electronics instrumentation engineering from the USTHB, Algiers, Algeria, in 2013. Currently, he is a Ph.D. student at the Ecole Nationale Polytechnique, Algiers, Algeria. His research interests include intelligent monitoring systems, applied machine learning, and energy management systems.

Mourad Haddadi received a Ph.D. degree in electronics from the Ecole Nationale Polytechnique in Algiers, Algeria. He is currently a Senior Researcher and Head of the Electronics Department at the Ecole Nationale Polytechnique. He was engaged in renewable energies and solar electricity for more than 30 years. His research and development tasks mainly relate to photovoltaic applications, solar energy, photovoltaic systems and devices, and the most promising applications in renewable energies. He is an expert and reviewer in many journals. He is the author or co-author of more than 60 publications.

Investigation of Diethyl Hexyl Phthalate Migration from Poly(Vinyl Chloride) Serum Bags

Dalila Ikermoud, Naima Belhaneche-Bensemra, and Hicham Benaissa

Abstract−Plasticizers are used to make Poly (Vinyl Chloride) (PVC) flexible so it can be used in different areas such as intravenous solution containers. Plasticizers can migrate from PVC over time because of contact with these solutions; this phenomenon creates gaps in the polymer structure and causes the migration of other additives. This paper discusses the specific migration of di-2-ethyl hexyl phthalate (DEHP) from plasticized poly (vinyl chloride) (PVC) into 5% glucose solution, although studying the possibility of migration of other components. For this purpose, the bags were stored in real conditions by respecting temperatures (20 ± 2°C) and time of conservation (18 months). Samples were taken off every 3 months to be analyzed. The Fourier transform infrared spectroscopy was used to investigate the migration phenomena, the atomic absorption spectrometry was used to follow the migration's evolution of metals from plastic bags and the gas chromatography coupled with mass spectrometry was used for the determination of DEHP migration. The results obtained by the three techniques showed the migration of the serum bags additives such as DEHP in the glucose solution. This migration depends on time of contact.

***Keywords*−DEHP, migration, plasticizer, PVC, serum bag.**

I. Introduction

Polyvinylchloride is an inexpensive commodity plastic material that is used in a wide variety of domestic and industrial applications. Knowing that practically all plastics are composed of polymerized organic substance, PVC is made up of polymerized vinyl chloride, together with one or more additives that modify the characteristics of the polymer in order to optimize its suitability for a given application or process. PVC is used in some situations with minimal additives; in this case, it is used as rigid and hard material. However, the best performance can be achieved when the material is made more flexible and softer. For this purpose, an additive described as a plasticizer is used, and the resulting plasticized PVC finds extensive applications because of its excellent and varied properties.

The flexible PVC is used as pharmaceutical packaging materials witch offer several advantages: extended storage time, efficient transportation for product freshness and low price, but the interaction between the package and the product can affect the quality of the content. This interaction can be caused by the migration of the plasticizer into liquid, which is attributed to two mechanisms. The extraction of the plasticizer can occur in the first case when the molecular size of the extractant is too large to enter the PVC polymer structure; therefore, the migration can occur only by the plasticizer molecules diffusing to the surface of the PVC and then dissolving into the liquid. The second case, when the molecular size of the extractant liquid is sufficiently small to enter into the PVC polymer structure; the major mechanism for this extraction is that the extractant diffuses into the plasticized PVC, dissolves the plasticizers then diffuses together with the dissolved plasticizers out to the surface of the PVC [1].

Di (2-ethylhexyl) phthalate, also known as di-octyl phthalate (DOP), universally referred to as DEHP is a colorless with almost no odors, oily liquid used to increase flexibility of PVC. DEHP was first produced in commercial quantities in Japan around 1933 and in the United States of America in 1939; it is found in a wide array of products including medical devices. Virtually all glucose bags made from PVC use this plasticizer, which is the long chain phthalate ester examined most extensively. There are a large number of reviews of the toxicological profile of DEHP; since February 2015 di(2-ethylhexyl) phthalate may only be sold and used in the European Union after authorization for a particular use [2-4].

People as well as animals can be exposed to the phthalate compounds through ingestion, inhalation or dermal exposure and it has a harmful effect on their health. The effects of di-(2-ethylhexyl) phthalate and its metabolites on fatty acid homeostasis regulating proteins in cells were proved in many investigations. To study the effect of DEHP on testicular mitochondrial viability: male albino rats were received di-ethyl hexyl phthalate (DEHP) (500 mg/kg/day orally). The administration of DEHP increases the lipid peroxidation and decreases considerably the testicular mitochondrial viability. DEHP induces a severe testicular oxidative damage and DNA (Deoxyribonucleic acid) fragmentation. Other studies examined the metabolite profile in plasma and liver of rats exposed to DEHP and showed induction of cyanide-insensitive palmitoyl-coenzyme an oxidation per gram of liver was greater in males than in females. Liver weight was significantly increased in the DEHP-treated groups compared to that of controls. Immunohistochemical analysis demonstrated that DEHP caused strong staining of proliferating cell nuclear

Manuscript received May 20, 2021; revised November 27, 202.

D. Ikermoud is with the Centre de Recherche en Technologie des Semi-conducteurs pour l'Energétique (CRTSE), Algiers, ALGERIA. (e-mail: ikermoud.dalila@gmail.com).

N. Belhaneche-Bensemra is with Laboratoire des Sciences et Techniques de l'Environnement, Ecole Nationale Polytechnique (ENP), Algiers, ALGERIA. (e-mail: naima.belhaneche@g.enp.edu.dz).

H. Benaissa is with the Central Forensic Laboratory of Algiers, Algiers, ALGERIA. (e-mail: hbenaissa66@gmail.com)

Digital Object Identifier (DOI): 10.53907/enpesj.v1i2.48

antigen after exposure, suggestive of hepatocyte proliferation [5-8].

In rats, after 10 days systemic administration of DEHP, a study conducted to investigate the hepatic toxicity of sub-acute DEHP exposure at different selenium (Se) status demonstrated that DEHP exposure increased oxidative stress by disturbing the antioxidant balance in the hepatocytes [9]. The male reproductive toxicity of DEHP is well established and has been studied in many species including mice, rats, hamsters, ferrets, and non-human primates. This toxicity is depending on the age of animals, the doses, dosing duration and endpoints included. It has been shown that oral treatment with DEHP causes decreased weights of male, reduced fertility, reproductive organs, and histopathological changes in the testis of juvenile and adult rats. Testes of the Big Blue® transgenic mice were treated every day for a month with DEHP indicated an approximately 3-fold increase in genomic DNA mutation frequency compared with controls. These results unveiled the hazardous effects of direct low-level exposure of DEHP on ability of spermatozoa fertilization as well as embryonic development, and proved that *in vivo* DEHP exposure posed mutagenic hazards in the reproductive organ, which are of great concern to human male reproductive health [10, 11].

For the general adult human population, exposures to DEHP are estimated to be 3-30 µg/kg/day. This plasticizer is suspected to induce anti-androgenic effects in men via its metabolite mono (2-ethylhexyl) phthalate (MEHP). However, there isn't enough information on the kinetic behavior of DEHP and its metabolites in humans. A comparative human intravenous and oral administration of DEHP in recent study likewise yielded a high proportion of glucuronized metabolites of between 77% and 84%, after oral administration; this value was 80% in intravenous administration [4, 12, 13].

The noticed toxicity of DEHP and existence of alternatives to many DEHP-containing PVC medical devices presents a compelling argument for moving assertively, but carefully, to the substitution of other materials for PVC in medical devices. The substitution of other materials for PVC or phthalate plasticizer would have an added people and community health benefit of reducing population exposures to DEHP [14-17].

The aim of the present work is to investigate the specific migration of DEHP from plasticized PVC into 5% glucose solution and to estimate this rate of loss, although studying the possibility of other component's migration by using various analytical methods such as Fourier transform infrared spectroscopy, atomic absorption spectrometry and gas chromatography coupled with mass spectrometry.

II. EXPERIMENTAL

A. Materials

The glucose solution bags used in this study are transparent. These bags are used in hospitals. They were produced by an Italian company which is specialized in the production of flexible containers in PVC. Nitric acid used in the mineralization (purity of 65%) is purchased from the Spanish company Panreac Quimica Slu and used as received. The di-octyl phthalate (DOP) used in the identification and quantification of the plasticizer in the composition of glucose solution bags formulation is a low volatile substance produced by Société Générale of Tunisia Plasticizers. Tetrahydrofuran and chloroform of high purity HPLC grade were purchased from Panreac Quimica Slu. Sigma Aldrich from Germany produces the methanol used in GC/MS (purity of 99.99%).

B. Migration Testing and Sample Preparation

Migration tests were conducted using glucose solution bags, stored in real conditions by respecting the temperatures and the time of conservation. The bags were stored for 18 months (the shelf life of the glucose solution) at temperature between 18 and 22°C in the central pharmacy of the hospital which is the usual area for their conservation before their use by different services. To carry out the various analyzes, samples were collected from the bags taken off every three months; they were washed with deionised water and dried at 40°C. A new bag without contact with glucose solution was taken as a control bag.

C. Fourier Transform Infrared (FTIR) Spectroscopy Analysis

The technique applied is Universal Attenuated Total Reflexion (U.A.T.R). Infrared solution software was used for spectra processing data. All spectra were obtained using an ATR-FTIR Spectrum One model infrared spectrometer of PerkinElmer®. The spectra were collected at a resolution of 2 cm^{-1} in the range of 4000–650 cm^{-1}. Each spectrum was rationed against a fresh background spectrum recorded from the bare ATR crystal. Before collection of each background spectrum, the ATR crystal was cleaned with absolute ethanol to remove any residual. Each sample was scanned in triplicate.

D. Atomic Absorption Spectrometry Analysis

Before analysis, a mineralization of the samples was performed according to Vandeburg and Clifford [18]. The analysis was carried out with an AAnalyst 800-PerkinElmer® with Zeeman effect for graphite furnace system and on AAnalyst 300-PerkinElemer® with deuterium lamp for flame system.

E. Gas Chromatography - Mass Spectrometry (GC/MS) Analysis

For the gas chromatography analysis, the separation of plasticizers from PVC was done by the dissolution/precipitation process [19, 20]. The dried extract was dissolved in chloroform and analyzed on a Perkin Elmer® GC/MS system, with a medium polarity capillary column (*PE-5MS* column (30 m × 0.25 mm), with film thickness of 0.25 µm). Carrier gas was helium with a flow of 1.2 ml/min and 31 kPa of pressure. One microliter of the sample was injected using splitless injection with injector temperature 300°C according to the following conditions: 90°C for 3 min with 6°C/min up to 280°C, the final temperature was held for 13 min. The total run time for each sample was 48 min.

For mass spectrometry detection, electron ionization with 70 eV was applied and mass fragments were detected between 50 and 450 *m/z*. Both the ion source temperature and transfer line temperature were at 280°C. Note that the detector was activated after 5 min on mode electronic impact.

The dosage of DEHP in the control bag and in the bags that have undergone the migration test was performed by establishing a calibration curve produced by mixing DOP standard in chloroform at concentrations that covered the concentration range found in the polymer extracts; the resulting

line was linear with correlation coefficient of 0.998. Three analytical replicates were analysed for each concentration.

III. RESULTS AND DISCUSSION

A. FTIR Investigation of the PVC Films Before and After Migration Testing

The comparison of the three spectra in Fig. 1 allowed the identification of some characteristic bands which are present in serum bag spectra but don't exist in PVC spectrum; these bands refer to the additives present in the formulation of serum container.

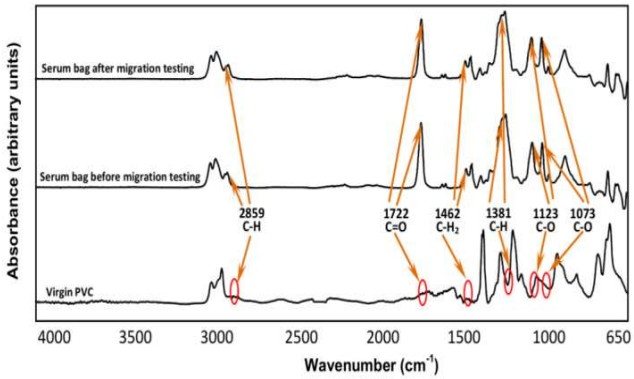

Fig. 1: Infrared spectra of PVC and serum bag before and after migration testing.

The spectra in Fig. 1 show C=O (ester) group stretching vibration at 1722 cm^{-1} and –CH stretching vibrations at 2859 and 1381 cm^{-1} [21-24]. The –C–O group absorbs at 1123 and 1073 cm^{-1} while the $–CH_2$ group absorbs at 1462 cm^{-1}, which permits to expect a possible presence of additives such as dioctyl phthalate (DOP) as plasticizer (Fig. 2), zinc stearate as heat stabilizer and a phenol derivative as an antioxidant [25, 26].

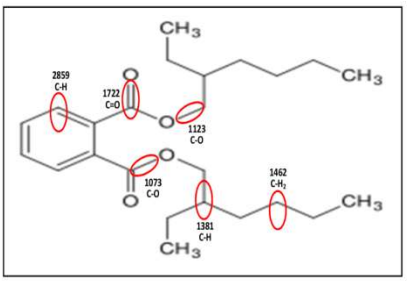

Fig. 2: Molecular structure of di(2-ethylhexyl) phthalate (DEHP).

The study of FTIR spectra of the control bag and bags contacted the glucose solution for various times in months were performed in order to follow the evolution of characteristic additives bands in the formulation of the polymer constituting these bags. The comparison of PVC films spectra (Fig. 3) shows a decrease in all additives bands, especially of the carbonyl band at 1722 cm^{-1}. The ester band at 1722 cm^{-1} would be associated with the presence of plasticizer from the phthalates family as shown in Fig. 2 -whose presence was confirmed by GC/MS analysis- and thermal stabilizer of the family of epoxidized oils or metallic stearates. Generally, dioctyl phthalate, epoxidized soybean oil and zinc stearate are the most used additives [25, 26].

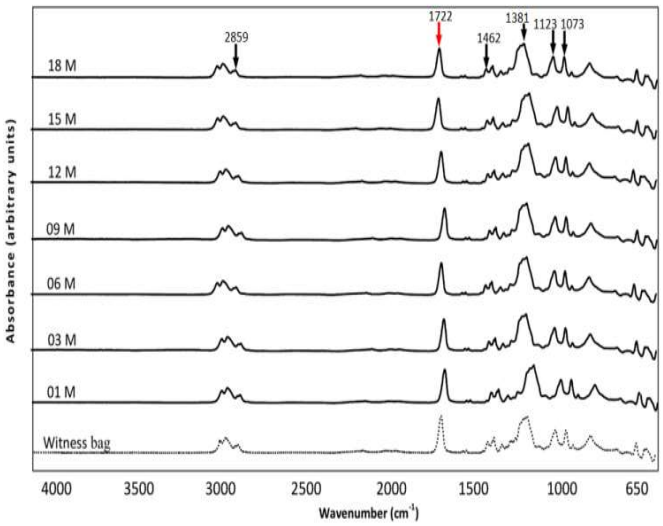

Fig. 3: FTIR spectra of serum bags at different contact time (months).

To study the changes undergone by each band, a semi-quantitative estimation was carried out by calculating the following absorbance ratios (Fig. 4): A2859/A1428, A1722/A1428, A1462/A1428, A1381/A1428, A1123/A1428 and A1073/A1428. The band at 1428 cm^{-1} corresponding to the CH_2 bond in PVC is used as a reference band [27].

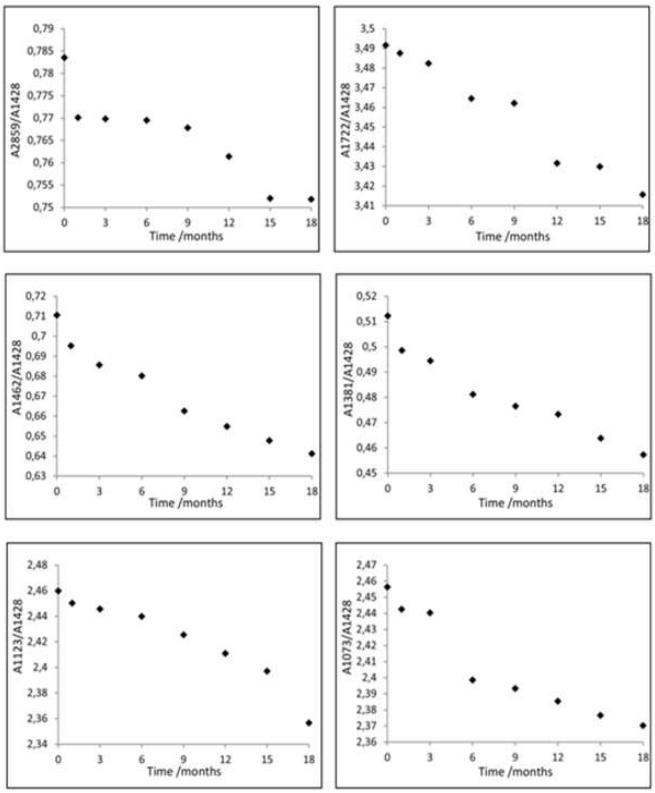

Fig. 4: Absorbance ratio's variation as a function of contact time of serum bags.

According to Fig. 4 gathering the variation of these ratios depending on the contact time, a decrease of all the ratios is observed on all the curves. This indicates that the migration of a certain amount of additives (dioctyl phthalate, zinc stearate, epoxidized soybean oil) present in the poly(vinyl chloride) bag's towards the glucose solution occurred; this phenomenon was already observed in other studies [28-30].

The decrease shown in all the curves without the appearance of any increase of the studied bands absorbance ratios (Fig. 4). More precisely at the wave numbers 1123 cm^{-1} and 1073 cm^{-1}, relative to the vibration of the –CO band, also found in the infrared spectrum of glucose according to the literature, it can indicate that there is no penetration of glucose molecules because of their large size. This result is also confirmed by the non-appearance of the –OH band which can be between 3600-3643 cm^{-1} in the infrared spectrum of the bag which contained glucose under the migration tests (Fig.1 and Fig. 2) [31].

B. AAS Investigation of the PVC Films Before and After Migration Testing

The atomic absorption spectrometry was applied to the determination of the metal content in the control bag and in those that have been in contact with the glucose solution for different contact times.

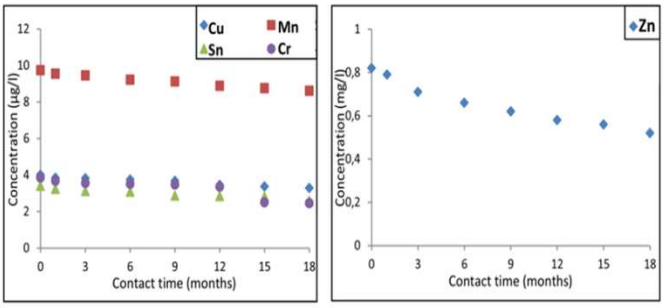

Fig. 5: Variation of the residual content of metals in bags conditioning the glucose solution.

The results obtained show the presence of copper (Cu), chromium (Cr), manganese (Mn), tin (Sn) and zinc (Zn). The presence of the latter is probably due to the zinc stearates, its characteristic bands have also been detected by infrared spectroscopy. The presence of the other elements would be related to the other additives present in the formulation and to the possible impurities they contain.

According to Fig. 5, a decrease in all residual metal's concentration in bags containing the glucose solution through storage time can be observed. This decrease is related to the migration of DEHP, so that creates gaps in the structure of the bags' polymer which involve the migration of other additives like Zn stearate. The results of atomic absorption spectrometry are in accordance with the results obtained by FTIR spectroscopy.

C. GC/MS Investigation of the PVC Films Before and After Migration Testing

Identification of serum bag's plasticizer

To identify the serum bag's plasticizer, the control bag was analysed by GC/MS method. The identification of the peak was deduced by searching in the MS libraries (NIST) and further confirmed by running the known chemicals for DOP. The identification and quantification of DOP in glucose solution bags were performed using m/z 149 [27].

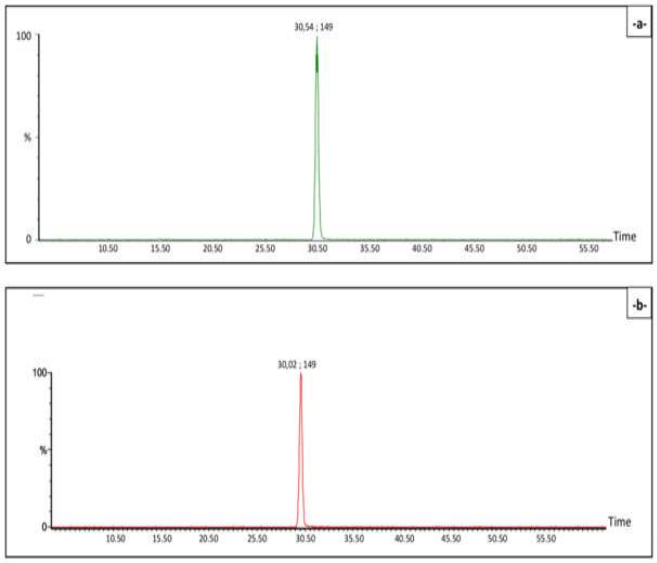

Fig. 6: Chromatogram of: **-a-** the extract from the serum bag.
-b- the DOP standard.

From the chromatogram of the extract of the reference serum bag and of the DOP standard (Fig. 6) analysed by GC/MS in the same operating conditions, the presence of one major peak can be noted. It has a retention time of 30.54 minutes with m/z 149 which is practically the same retention time of DOP (30.02 min) and which confirms that the plasticizer used in the manufacture of these bags is dioctyl phthalate. It is to be noted that all phthalate plasticizers have a basic characteristic peak at m/z = 149.

These results were confirmed in Fig. 7 which shows the mass spectra of the control bag extract, the DOP standard and of the DEHP spectrum according to the literature. Through these spectra, it can be confirmed that the plasticizer used in the serum bags formulation is the di-2 ethyl hexyl phtalate (DEHP) which is also a ramified dioctyl phthalate.

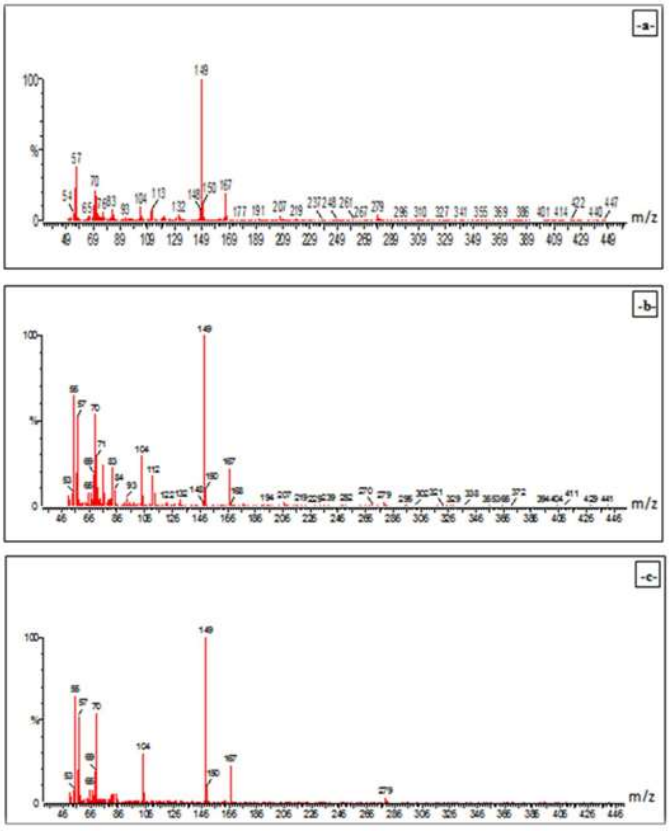

Fig. 7: Mass spectrum of: **-a-** the extract from control serum bag.
-b- the DOP standard.
-c- DEHP according to the literature.

Using the SM peaks of Fig. 7, we can propose the different steps of di (2-ethylhexyl) phthalate defragmentation, which are presented in Fig. 8 [32].

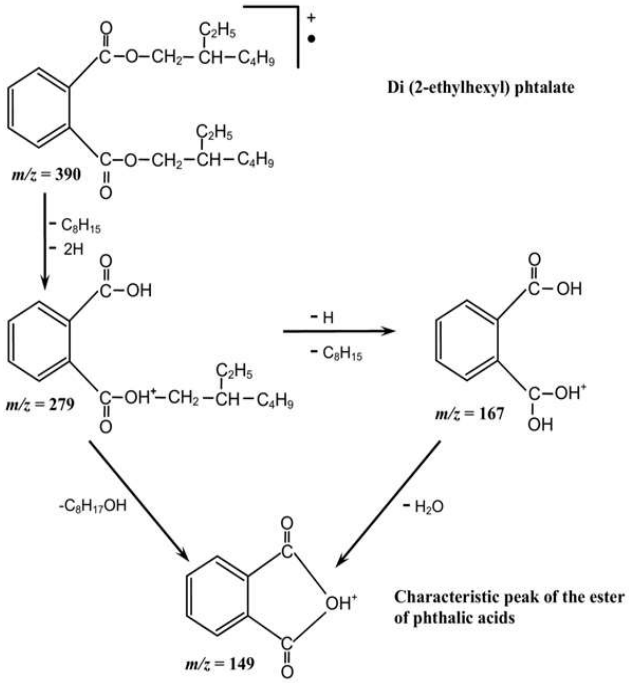

Fig. 8: Defragmentation scheme of DEHP.

Quantification of DEHP in serum bags

Table. I represents the results of the quantitative gas chromatography analyzes of the control bag and the bags which have undergone the migration tests at the 3rd, 9th and 18th month of contact.

Table. I
GAS CHROMATOGRAPHY ANALYSIS RESULTS.

-	Control bag	Bag stored for 3 months	Bag stored for 9 months	Bag stored for 18 months
Peak area (µv/s)	3256553	3254456	3251739	3250261
Residual [DEHP] (ppm)	2.391	2.389	2.387	2.386
[DEHP] migrated (ppm)	/	0.002	0.004	0.005
% of leaching	/	0.084	0.167	0.209

According to Table. I, it appears that the decrease in specific surface DEHP peaks corresponds to the reduction of residual concentrations of this plasticizer in any bag having undergone migration testing, which means the leaching of DEHP in the solution due to the presence of glucose molecule and time contact. The ratio of leaching was about 0.209% after 18 months of contact.

Several works having studied the influence of time on diffusion of di(2-ethylhexyl) phthalate from PVC into infused drug solutions and human biological fluids were reported [33-37]. Some studies showed a greater concentration of the plasticizer at the surface, resulting in the formation of a more plasticized layer near the interface. In this case the plasticizer can be transferred from the plasticized polyvinyl chloride into the liquid phase by a three steps: **(1)** plasticizer transport into solid PVC itself, **(2)** transport phenomena at the interface of PVC and solution, **(3)** plasticizer transport onto the liquid [38,39]. Fig. 9 shows the evolution of the residual concentration of DEHP in control bag and in those conditioning glucose solutions at various contact times. A low decrease can be observed.

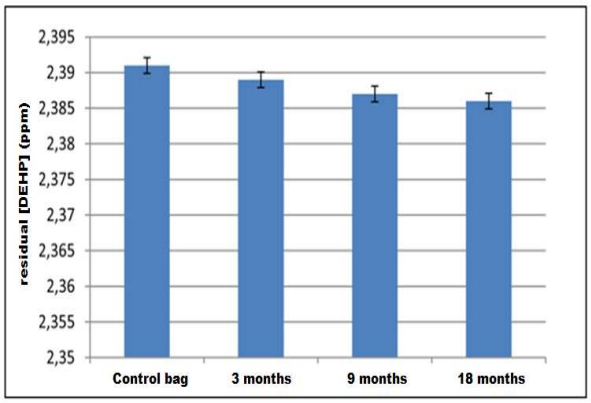

Fig. 9: Comparison of the residual rates of the DEHP in control bag and in those conditioning the glucose solution at different time contact.

IV. CONCLUSION

Based on the results of this study, the issues to be noted are the following:

The application of the FTIR spectroscopy allowed to confirm that PVC is the constitutive polymer of the glucose bags. This technique allows expecting the presence of plasticizer from the phthalates family, thermal stabilizer of the family of epoxidized oils or metallic stearates. The follow-up of the variation of the characteristic bands of the additives according to the time of contact between the bags and the glucose solution showed that a phenomenon of migration of these additives took place.

The AAS results showed that the PVC bags formulation contains copper, manganese, tin, chromium and zinc. The presence of the latest element is related to the zinc stearate stabiliser. The follow-up of the variation of the residual contents of metals in bags conditioning the glucose solution showed the loss of additives during storage time.

The GC/MS analysis of the control bag and of the bags which were submitted to the tests of migration allowed to confirm that the di(2-ethylhexyl) phthalate (DEHP) is the plasticizer used in the formulation of the serum bag and showed that its migration occurred in glucose solution. The phenomenon is influenced by the time of contact.

ACKNOWLEDGMENT

Special thanks to Dr. B. Aloui and his team from CRNA (Centre de Recherche Nucléaire d'Alger, Algeria) for performing GC/MS analysis. Also thanks to Dr. N. Larjane (Université Mouloud Mammeri de Tizi Ouzou, Algeria) and Dr R. Mihoub (Centre National de Toxicologie d'Alger, Algeria) for their help in this work.

REFERENCES

[1] T. D. Stark, H. Choi and P. W. Diebel, "Influence of plasticizer molecular weight on plasticizer retention in PVC geomembranes", *Geosynth. Int.*, vol. 12, no. 2, pp. 99-110, 2005, 10.1680/gein.2005.12.2.99.

[2] E. Testai, P. Hartmann, S. C. Rastogi, U. Bernauer, A. Piersma, W. De Jong and T. Vermeire, "The safety of medical devices containing DEHP plasticized PVC or other plasticizers on neonates and other groups possibly at risk", *Regul. Toxicol. Pharmacol*., vol. 76, pp. 209-210, 2016, 10.1016/j.yrtph.2016.01.013.

[3] A. Arthur and M. D. Strauss, "Di(2-ethylhexyl)phthalate (DEHP)", *J. Pediatr. Pharmacol. Ther.*, vol. 9, no. 2, pp. 89-95, Apr. 2004, 10.5863/1551-6776-9.2.89.

[4] H. Y. Kim, "Risk assessment of di(2-ethylhexyl) phthalate in the workplace", *Environ. Health. Toxicol*., vol. 31, May. 2016, 10.5620/eht.e2016011.

[5] Y. Xu, T. J. Cook and G. T. Knipp, "Effects of di-(2-ethylhexyl)-phthalate and its metabolites on fatty acid homeostasis regulating proteins in rat placental HRP-1 trophoblast cells", *Toxicol. Sci*., vol. 84, pp. 287-300, Jan. 2005, 10.1093/toxsci/kfi083.

[6] S. H. Abdel-Kawi, K. S. Hashem and S. Abd-Allah, "Mechanism of diethylhexyl phthalate (DEHP) induced testicular damage and of grape seed extract-induced protection in the rat", *Food. Chem. Toxicol*., vol. 90, pp. 64-75, Apr. 2016, 10.1016/j.fct.2016.02.003.

[7] B. Van Ravenzwaay, G. Coelho-Palermo Cunha, V. Strauss, J. Wiemer, E. Leibold, H. Kamp, T. Walk, W. Mellert, R. Looser, A. Prokoudine, E. Fabian, G. Krennrich and M. Herold, "The individual and combined metabolite profiles (metabolomics) of dibutylphthalate and di(2-ethylhexyl)phthalate following a 28-day dietary exposure in rats", *Toxicol. Lett*., vol. 198, no. 2, pp. 159-170, Oct. 2010, 10.1016/j.toxlet.2010.06.009.

[8] N. Y. Kim, T. H. Kim, E. Lee, N. Patra, J. Lee, M. O. Shin, S. J. Kwack, K. L. Park, S. Y. Han, T. S. Kang, S. H. Kim, B. M. Lee and H. S. Kim, "Functional role of phospholipase D (PLD) in di(2-ethylhexyl) phthalate-induced hepatotoxicity in sprague-dawley rats", *J. Toxicol. Environ. Health.*, vol. 73, pp. 1560-1569, Oct. 2010, 10.1080/15287394.2010.511582.

[9] P. Erkekoglu, N. D. Zeybek, B. K. Giray, W. Rachidi, M. Kizilgün, I. Hininger-Favier, A. Favier, E. Asan and F. Hincal, "The effects of di(2-ethylhexyl) phthalate on rat liver in relation to selenium status", *Int. J. Exp. Pathol.*, vol. 95, no. 1, pp. 64-77, Nov. 2014, 10.1111/iep.12059.

[10] X. F. Huang, Y. Li, Y. H. Gu, M. Liu, Y. Xu, Y. Yuan, F. Sun, H. Q. Zhang and H. J. Shi, "The effects of di-(2-ethylhexyl)-phthalate exposure on fertilization and embryonic development *in vitro* and testicular genomic mutation *in vivo*", *PLoS ONE*, vol. 7, no. 11, Nov. 2012, 10.1371/journal.pone.0050465.

[11] E. G. Radke, J. M. Braun, J. D. Meeker and G. S. Cooper, "Phthalate exposure and male reproductive outcomes: A systematic review of the human epidemiological evidence", *Environ. Int.*, vol. 121, pp. 764-793, Oct. 2018, 10.1016/j.envint.2018.07.029.

[12] W. Kessler, W. Numtip, W. Völkel, E. Seckin, G, A. Csanády, C. Pütz, D. Klein, H. Fromme and J. G. Filser, "Kinetics of di(2-ethylhexyl) phthalate (DEHP) and mono (2-ethylhexyl) phthalate in blood and of DEHP metabolites in urine of male volunteers after single ingestion of ring-deuterated DEHP". *Toxicol. Appl. Pharmacol*., vol. 264, no. 2, pp. 284-291, Aug. 2012, 10.1016/j.taap.2012.08.009.

[13] A. Hartwig and MAK Commission, "Di(2-ethylhexyl) phthalate (DEHP) [MAK Value Documentation, 2015]", vol. 1, no. 3, pp. 1743-1791, Jul. 2016, 10.1002/3527600418.mb11781e5916.

[14] J. A. Tickner, T. Schettler, T. Guidotti, M. McCally and M. Rossi, "Health risks posed by use of di-2-ethylhexyl phthalate (DEHP) in PVC medical devices: a critical review", *Am. J. Ind. Med.*, vol. 39, no. 1, pp. 100-111, Jan. 2001, 10.1002/1097-0274(200101)39:1<100::aid-ajim10>3.0.co;2-q.

[15] Y. Haishima, T. Kawakami, C. Fukui, A. Tanoue, T. Yuba, S. Ozono, H. Kumada, K. Inoue, T. Morikawa, M. Takahashi, A. Fujisawa, K. Yamasaki, Y. Nomura, K. Isama, U. Chung, K. Ogawa, Shingo Niimi and M. Yoshida, "Characterization of alternative plasticizers in poly(vinyl chloride) sheets for blood containers", *J. Vinyl. Addit. Technol.*, vol. 22, no. 4, pp. 520-528, Dec. 2016, 10.1002/vnl.21472.

[16] H. Miao, H. Zhao and P. Jiang, "Poly(vinyl chloride) films plasticized with novel poly-nadic-anhydride polyester plasticizers", *J. Vinyl. Addit. Technol*., vol. 23, no. 4, pp. 321-328, Aug. 2015, 10.1002/vnl.21510.

[17] H. M. Koch, H. Drexler and J. Angerer, "An estimation of the daily intake of di(2-ethylhexyl)phthalate (DEHP) and other phthalates in the general population", *Int. J. of Hyg. Environ. Health*, vol. 206, no. 2, pp. 77-83, 2003, 10.1078/1438-4639-00205.

[18] H. J. Vandeburg, A. A. Clifford, K. D. Bartle, J. Carroll, I. Newton, L. M. Garden, J. R. Dean and C. T. Costley, "Analytical extraction of addives from polymers", *Analyst*, vol. 122, no. 9, pp. 101R-115R, Sept. 1997, 10.1039/A704052K.

[19] H. J. Vandeburg, A. A. Clifford, K. D. Bartle, J. Carroll, I. Newton, L. M. Garden, J. R. Dean and C. T. Costley, "Analytical extraction of addives from polymers", *Analyst*, vol. 122, no. 9, pp. 101R-115R, Sept. 1997, 10.1039/A704052K.

[20] Q. Wang and B. K. Storm, "Separation and analysis of low molecular weight plasticizers in poly(vinyl chloride) tubes", *Polym. Test*., vol. 24, no. 3, pp. 290-300, Jan. 2005, 10.1016/j.polymertesting.2004.12.002.

[21] L. Fantoni and C. Simoneau, "European survey of contamination of homogenized baby food by epoxidized soybean oil migration from plasticized PVC gaskets", *Food. Addit. Contam*., vol. 20, no. 11, pp. 1087-1096, Nov. 2003, 10.1080/02652030310001615186.

[22] F. N. Ajjan, M. J. Jafari, T. Rębis, T. Ederth and O. Inganãs, "Spectroelectrochemical investigation of redox states in a polypyrrole/lignin composite electrode material", *J. Mater. Chem. A*, vol. 3, no. 24, pp. 12927-12937, May. 2015, 10.1039/c5ta00788g.

[23] M. D Guillén and N. Cabo, "Infrared spectoscopy in the study of edible ails and fats", *J. Sci. Food. Agric*., vol. 75, no. 1, pp.1-11, 1997, 10.1002/(SICI)1097-0010(199709)75:1<1::AID-JSFA842>3.0.CO;2-R.

[24] M. Beltrán, and A. Marcilla, "PVC plastisols de composition by FT-IR spectroscopy", *Eur. Polym. J.*, vol. 33, no. 8, pp. 1271-1280, Aug. 1997, 10.1016/S0014-3057(97)00004-9.

[25] H. Baltacioğlu and D. Balköse, "Effect of zinc stearate and/ epoxidized soybean oil on gelation and thermal stability of PVC-DOP plastigels", *J. Appl. Polym. Sci*., vol. 74, no. 10, pp. 2488-2498, Sept. 1999, 10.1002/(SICI)1097-4628(19991205)74:10<2488::AID-APP18>3.0.CO;2-B.

[26] M. A. Semsarzadeh, M. Mehrabadeh and S. S. Arabshahi, " Dynamic mechanical behavior of the diocty phthalate plasticized polyvinyl chloride-epoxidized soya bean oil", *Eur. Polym. J.,* vol. 38, no. 2, pp. 351-358, Oct. 2002, 10.1016/S0014-3057(01)00168-9.

[27] M. O. Boussoum and N. Belhaneche-Bensemra, "Study and optimization of soaking treatment to reduce migration from plasticized polyvinyl chloride", *J. Appl. Polym. Sci.*, vo.124, no. 2, pp. 1241-1248, Oct. 2011, 10.1002/app.35141.

[28] D. Atek and N. Belhaneche-Bensemra, "FTIR investigation of the specific migartion of addives from rigid poly(vinyl chloride) ", *Eur. Polym. J.*, vol. 41, no. 4, pp. 707-714, Jan. 2005, 10.1016/j.eurpolymj.2004.10.043.

[29] T. J. Suhrhoff and B. M. Scholz-Böttcher, "Qualitative impact of salinity, UV radiation and turbulence on leaching of organic plastic additives from four common plastics- A lab experiment", *Mar. pollut. bull.*, vol. 102, no. 1, pp. 84-94, Jan. 2016, 10.1016/j.marpolbul.2015.11.054.

[30] D. Ikermoud, H. Benaissa, W. Kherfane and N. Belhaneche-Bensemra, "Investigation of additives migration from salted serum bags", *Polym. Test*., vol. 80, 106118, Oct. 2019, 10.1016/j.polymertesting.2019.106118.

[31] L. J. Bellamy, "Alcohols and phenols" in *The infra-red spectra of complex molecules*, 3rd ed. Ed. Chapman and Hall, London, UK, 1975, pp. 107-128, 10.1007/978-94-011-6017-9.

[32] A. O. Earls, I. P. Axford and J. H. Braybrook, "Gas chromatography-mass spectrometry determination of the migration of phthalate plasticisers from polyvinyl chloride toys and childcare articles", *J. chrom. A*, vol. 983, pp. 237-246, Jan. 2003, 10.1016/s0021-9673(02)01736-3.

[33] J. Kastner, D. G. Cooper, M. Marić, P. Dodd and V. Yargeau, "Aqueous leaching of di-2-ethyl phthalate and green plasticizers from poly(vinyl chloride)", *Sci. Total. Environ.*, vol. 432, pp. 357-364, 2012, 10.1016/j.scitotenv.2012.06.014.

[34] L. Bernard, B. Décaudin, M. Lecoeur, D. Richard, D. Bourdeaux, R. Cueff, V. Sautou, "Analytical methods for the determination of DEHP plasticizer alternatives present in medical devices: A review", *Talanta.*, vol. 129, pp. 39-54, 2014, 10.1016/j.talanta.2014.04.069.

[35] J. R. Snell, C. R. Monticello, C. Her, E. L. Ross, A. A. Frazer-Abel, J. F. Carpenter and T. W. Randolph, "DEHP nanodroplets leached from polyvinyl chloride IV bags promote aggregation of IVIG and activate complement in human serum", *J. Pharm. Sci.*, vol. xxx, pp. 1-14, 2019, 10.1016/j.xphs.2019.06.015.

[36] J. L.Taverdet and J. M. Vergnaud, "Modelisation of matter transfers between plasticized PVC and liquids in case of a maximum for liquid-time curves", *J. Appl. Polym. Sci.*, vol. 31, pp. 111-122, 1986, 10.1002/app.1986.070310111.

[37] E. Testai, P. Hartemann, S. C. Rastogi, U. Bernauer, A. Piersma, W. De Jong, H. Gulliksson, R. Sharpe, D. Schubert, E. Rodriguez-Farre and Ms Scientific Committee SCENIHR, "The safety of medical devices containing DEHP plasticized PVC or other plasticizers on neonates and other groups possibly at risk (2015 up date)", *Regul. Toxicol. Pharmacol*., vol. 76, pp. 209-210, 2016, 10.1016/j.yrtph.2016.01.013.

[38] H. Al Salloum, J. Saunier, A. Tfayli and N. Yagoubi, "Studying DEHP migration in plasticized PVC used for blood bags by coupling Raman confocal microscopy to UV spectroscopy", *Mat. Sci. Eng*., vol. 61, pp.56-62, 2016, 10.1016/j.msec.2015.12.008.

[39] D. Messadi, J. M. Vergnaud and M. Hivert, "A new approach to the study of plasticizer migration from PVC into methanol", *J. Appl. Polym. Sci*., vol. 26, pp. 667-677, 1981, 10.1002/app.1981.070260225.

Dalila Ikermoud has received her State Engineer degree in Industrial Chemistry with "Environment" option from Saâd Dahlab University (Blida-Algeria) in 1999, her Magister degree and PhD degree in Environmental Engineering both from Ecole Nationale Polytechnique (Algiers-Algeria) in 2010 and 2020, respectively. From 2003 until 2016, she was with the Centre National de Toxicologie (Algiers-Algeria) as a Chemical Engineer. Since 2016, she is with the Centre de Recherche en Technologie des Semi-Conducteur (CRTSE) (Algiers-Algeria).

Naima Belhaneche-Bensemra is professor at the Environmental Engineering Department of the Ecole Nationale Polytechnque, Algiers. She is Head of the Materials and Environment Interactions Team at the Laboratory of Sciences and Techniques of the Environment since 2000. She received the Engineering Degree in Chemical Engineering in 1985 from university Ferhat Abbas of Sétif (Algeria) and the PhD Degree in Polymeric Materials and Composites from university Claude Bernard-Lyon I (France) in 1989. She is author and co-author of about 110 publications in peer reviewed high impact factor journals as well as 11 invited book chapters. She is in the editorial boards of several journals and referee of about 40 journals. Her research interests focus on oil based and bio derived polymers and composites; polymer blends; ageing, degradation, stabilization and recycling of polymers; valorization of renewable resources; interactions in plastics food packaging.

Hicham Benaissa is a Chief engineer at the Central Forensic Laboratory of Algiers, where he is in charge of analytical instrumentation using optical and chromatographic techniques with analysis covering a wide range of crime clues like drugs, toxics, explosives, hazardous materials. He has cooperated several times with universities in both technical assistance and supervision of students preparing Master and PhD degrees. Prior to joining Central Forensic Lab-Algiers, Hicham Benaissa has teached chemistry in high school from 1990 to 1996 in full time and at USTHB university as an analytic Lab teacher-assistant by time. Hicham Benaissa was born in 1966 and raised in Algiers city. He obtained in 1990 his State Engineer Degree in Chemical Engineering from Ecole Nationale Polytechnique and the Post Graduate Diploma in instrumental Methods of identification and characterization in 2008 from USTHB. In addition he obtained the advanced level in English in 2017 at the Intensive Language Learning Centre of Algiers University and recently he received a Master degree in Nuclear Security from USTHB in 2020.

Modal identification and dynamic analysis of a 1000 years old historic minaret of Kalaa Beni-Hammad

Nouredine Bourahla, Zakaria Assameur, Mohamed Abed, and Ahmed Mébarki.

Abstract− From structural and material point of view each historic monument is a textbook case, as it differs in shape, age, material characteristics and level of preservation. New means and approaches are used for geometric and shape survey, material and modal characterization, which helps restitute detailed information regarding the structural elements of the edifices. This paper investigates a 1000 years old historic minaret having a square base of 6.50 m of side and 24.70 m height. An ambient vibration survey has been carried out and the results were used to update a Finite Element (FE) model of the minaret in two stages. First, the elastic modulus of the rubble stone masonry has been determined by matching the experimental and numerical fundamental frequency. In a second phase, a frequency response function (FRF) correlation is carried out iteratively by adjusting the damping ratios to minimize the FRF error. The elastic modulus of the rubble stone masonry is found to be in the lowest range of values given in the literature, which confirms a deteriorated quality of the material. A seismic performance of the structure has been carried out using the updated FE model subjected to a set of acceleration time histories having the mean spectrum matching a compatible site spectrum. The stress concentration zones have been determined and a steel tie system to retrofit the structure is proposed. Beside the proposed investigation framework, the characterization results are valuable facts that can be added to the available database of historic monuments.

***Keywords*− Historic monument, Kalaa Beni-Hammad, قلعة بني حماد, Model updating, Ambient vibration testing, Structural strengthening, Finite element method model calibration.**

NOMENCLATURE

The main abbreviations used in this article are listed below:

AVT	Ambient Vibration Testing.
FDAC	Frequency Domain Assurance Criteria.
FE	Finite Element.
FRF	Frequency Response Function.
MAC	Modal Assurance Criteria.
PPM	Pick-Picking Method

I. INTRODUCTION

The historic heritage is a universal valuable asset that requires more attention to preserve. Those edifices, located in seismic prone regions, have survived several earthquakes and are still standing. They can be of particular interest from a structural engineering point of view. The research activity for structural assessment [5], material properties evaluation [4] and retrofitting of historic buildings all over the world continues to be very attractive and energetic [2, 9, 17, 19]. This has led to development of a variety of methods and practices for diagnosis and seismic strengthening of ancient monuments where advanced technological means are used to scan, test and model the edifices [11, 15]. The use of such innovative methods enhances the precision of the analyses, but uncertainties in the material properties are still a challenge and vary significantly from case to case. More data on different types of historic monuments with different materials and different ages is still needed to understand better their structural behaviors. In this paper, a 1000 years old minaret of about 24 m height made of rubble stone masonry is experimentally and numerically investigated. The measured and the numerical FRF curves were used to match the natural frequencies of the structure and their corresponding damping ratios. A conceptual strengthening solution is proposed and the performance is assessed.

Manuscript received August 12, 2021; revised December 15, 2021.
N. Bourahla is with LGSD laboratory, Civil Engineering Department, Ecole Nationale Polytechnique, Algiers, Algeria. (email: nouredine.bourahla@g.enp.edu.dz)
Z. Assameur and M. Abed are with LGMGC laboratory, Civil Engineering Department, University Saad Dahlab, Blida, Algeria. (e-mail: zakassam@hotmail.com, abedmed@yahoo.fr)
Ahmed Mébarki is with University Gustave Eiffel, UPEC, CNRS, Laboratory Modelling and Multi Scale Simulation (MSME 8208 UMR), Marne-la-Vallée, France. (e-mail: Ahmed.Mebarki@univ-eiffel.fr)

Digital Object Identifier (DOI): 10.53907/enpesj.v1i2.56

II. HISTORICAL BACKGROUND AND STRUCTURAL IDENTIFICATION AND MODELING OF THE MINARET

Founded in 1007 by Hammad ibn Bologhine [10], the fortress (Kalaa) of Beni-Hammad has played an important role as a capital of North Africa during the eleventh century. In 1980, UNESCO inscribed the site as a World Heritage Site. The archeological site is located on the Hodna plain at 36 km to the northeast of the town of M'Sila (Algeria). The region is classified as moderate seismic zone IIa by the Algerian code RPA99 v2003 [20].

The historic monument object of this study is a remaining minaret of a great mosque in ruin, having a square base of 6.50 m of side and 24.70 m height. Structurally, the edifice is made of a 1.80 m x 1.80 m square core surrounded by a 1.20 m thick walls both supporting the stairs and the barrel-vaulted ceilings creating a monolithic ensemble (Fig. 1). All the structural elements are made of local sandstone ruble, which has suffered severe ageing and environmental actions. The upper part and the ornament of the minaret tumbled down long time ago at an

undefined age [1]. The edifice has been restored according to a plan of protection and restoration of the site set up by UNESCO in the period of 1976-82 [20].

For the purpose of the present study, a simple Finite Element (FE) model is elaborated. The core of the minaret is modeled using solid elements. The outer walls, the stairs and ceilings are modeled using thick shell elements. An adequate meshing is adopted to meet the required precision without oversizing the model. The structure is assumed to be fixed at its base. The specific weight of the material is obtained from the literature for similar type of masonry and is taken equal to 18 kN/m^3 with a Poisson ratio equal to 0.24 [18].

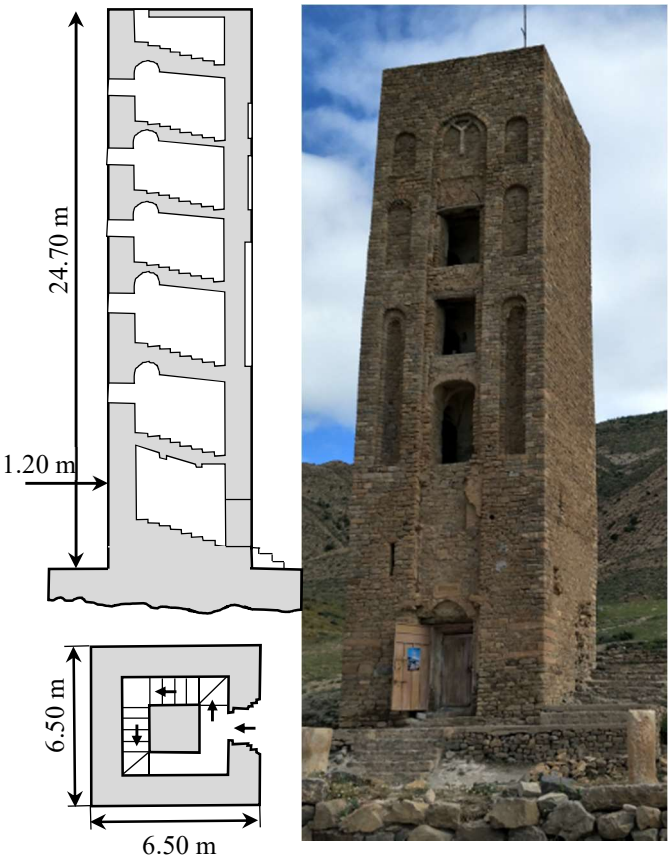

Fig. 1: Global view, layout and elevation sections of Kalaa beni-Hammad.

III. Ambient Vibration Testing (AVT) and Model Updating

Ambient vibration method has been used for more than five decades for full scale testing of civil engineering structures [13]. Its simplicity, cost effectiveness and wide range of applicability made of it a powerful tool for in-situ identification testing. One of the most frequent uses of AVT involves identification of natural frequencies, mode shapes of vibration and equivalent viscous damping ratio of full-scale structures [6, 21, 24]. These results are used to update the FE model by matching the experimental and numerical modal properties [7, 14, 22]. First, a careful selection of the model parameters to be modified by the updating procedure is to be made in order to ensure that the necessary changes to the model are realistic and physically realizable and meaningful [14]. In this instance, the material properties, which are uncertain, are chosen as matching parameters as the geometric characteristics and masses are precisely determined.

A. Test set-up and procedure

The tests were performed using three degrees of freedom seismometer type Lennartz electronic (Le3Dlite) and a data acquisition system type City Shark II. The measured signals were processed using the GEOPSY program [25] capable to perform most of the signal processing operations for the analysis of ambient vibration data. Seven measurement points were located along the height of the minaret at the façade side to record the vibration along two horizontal and one vertical axes (Fig. 2). Two other recording points were used; one point was positioned at the corner of the roof and the other one at a free field. The recording time for each sequence was set to 6 mn and found to be largely sufficient to obtain smooth frequency response function (FRF) curves. Measurement locations were chosen to capture the fundamental and second lateral and torsional modes.

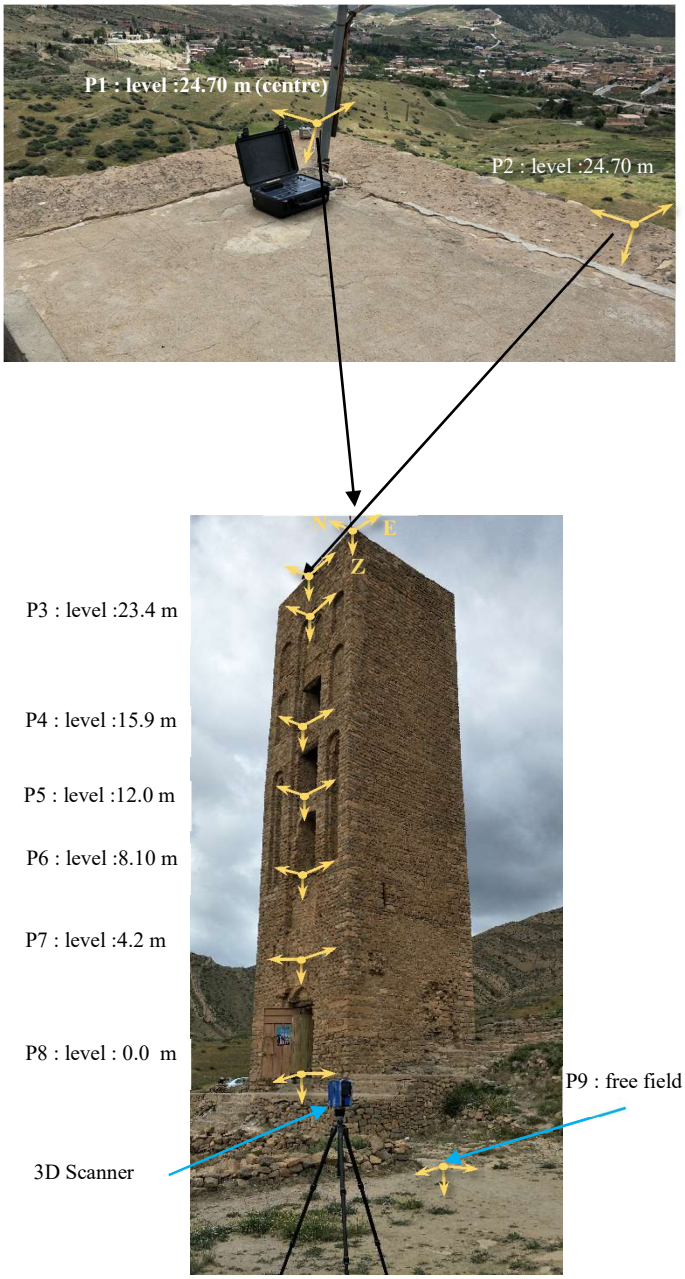

Fig. 2: Global view of the minaret with the positions of the measurement points.

B. Frequencies identification

The natural frequencies of Kalaa Beni-Hammad minaret were identified by applying the peak-picking method (PPM) on the FRFs. The curve in Fig. 3 shows the FRF of the vibrations measured along the two horizontal axes denoted as E-axis and

N-axis at the edge of the floor corresponding to point 1. The clearly distinct first peaks at 1.88 Hz and 1.90 Hz correspond to the fundamental lateral mode along N and E directions respectively (Fig 4). It should be noted that the peak corresponding to the torsional mode is missing on the FRF curve of record point 2, which is located at mid-façade on the N-axis where only lateral modes in N-direction are detectable.

The amplitudes of fundamental modes dominate those of the higher modes. The latter are more apparent at lower heights. As shown in Fig. 5, the peaks of the second lateral modes are comparable to those of the fundamental modes. A peak at frequency of 10.83 Hz corresponds to the pure vertical mode (Fig. 6).

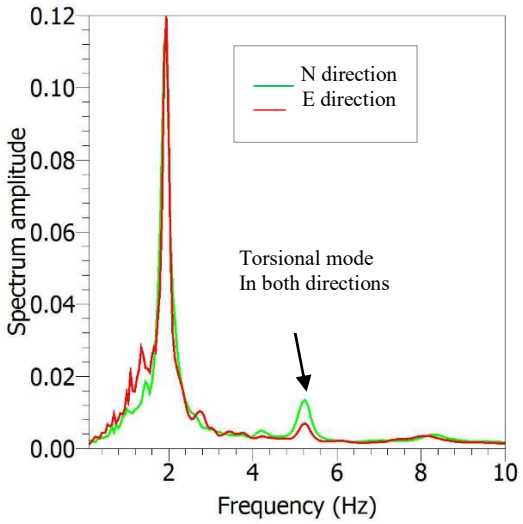

Fig. 3: FRF curves of record points 1

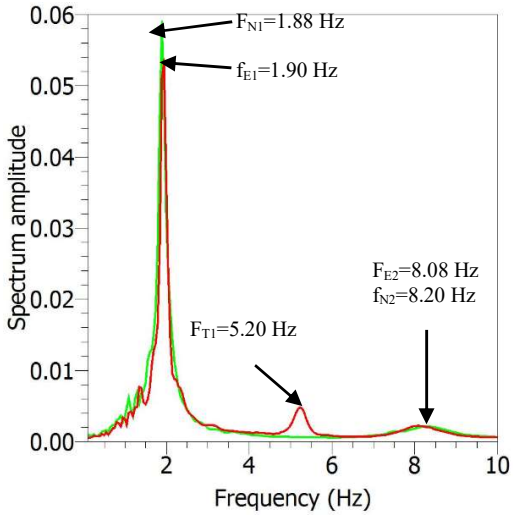

Fig. 4: FRF curves of record points 2.

C. *Identification of the modal damping ratios*

For each identified frequency, a damping ratio has been determined using the random decrement technique (Table 1). Figure 7 shows typical free decay fitting using GEOPSY software [25] where f is the natural frequency, z is the damping ratio and N is the number of windows used in the calculation. The values of the damping ratios are low compared to ratios used in analysis for such type of structure. These values are common for very low excitations (ambient vibrations).

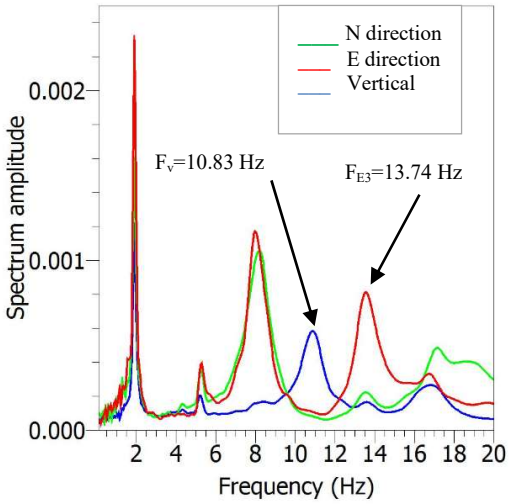

Fig. 5: FRF curves of record points 7.

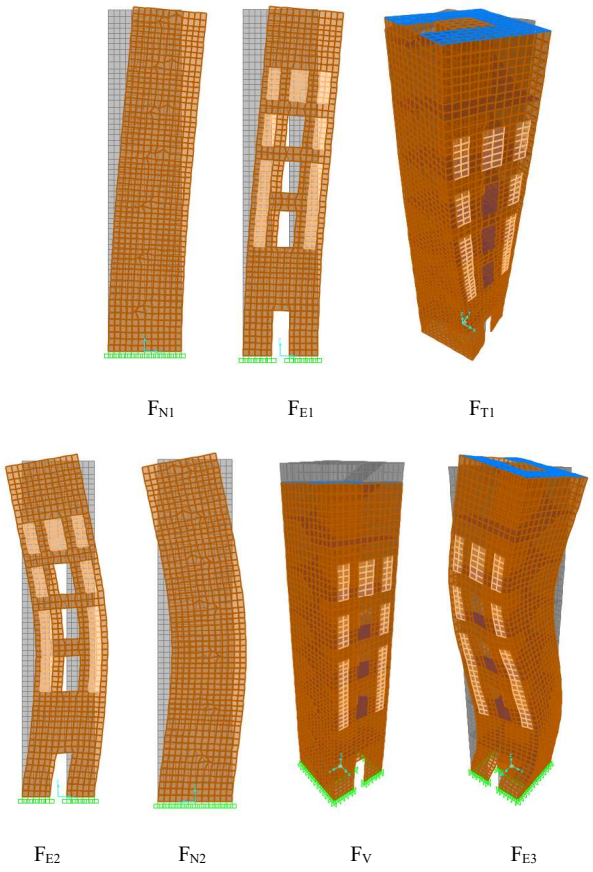

Fig. 6: Numerical mode shapes.

F_{Ei}, F_{Ni}, FV and F_{Ti} denote the ith frequency in the east, north, vertical direction and the torsional mode respectively.

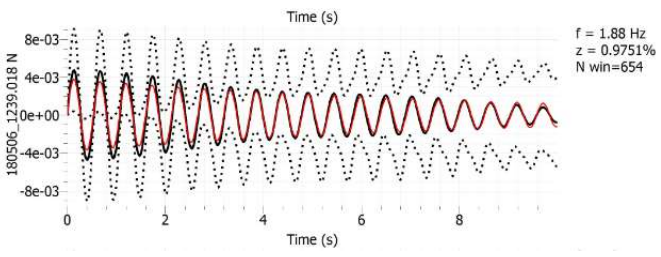

Fig 7: Typical free decay fitting of the fundamental frequency.

IV. EXPERIMENTAL AND NUMERICAL MODAL CORRELATION

A finite element model updating is performed in the frequency domain in two stages. First, the uncertain data of the numerical model is defined. In this instance, the geometry of the structure is simple; it has been precisely defined using the 3-D scan and introduced with high accuracy into the FE model. The mass distribution is also well known; however, the material properties of the old non-homogeneous masonry are uncertain. Therefore, as an inverse problem, the elastic modulus is used as a variable parameter to be identified and the fundamental frequency as an objective function to update iteratively the numerical model with the experimental results. Several iterations are made for changing values of the elastic modulus for which the modal analysis is carried out in each iteration. The best fit for the fundamental frequency is obtained for E = 2.88 GPa. This value is in the range of the elastic modulus of historic stone masonry as reported in many experimental investigations [3, 16, 23]. The numerical frequencies of the model are compared to those determined experimentally in Table1. The fundamental frequencies match closely and remain within 5 % error for second higher modes. The largest error of 17% corresponds to the torsional mode.

Table. I
EXPERIMENTAL AND NUMERICAL FREQUENCIES

No	Direction	Measured (HZ)	Computed (Hz)	Error (%)
Mode 1	Lateral X	1.88	1.89	0.5
Mode 2	Lateral Y	1.90	1.90	0
Mode 3	Torsional	5.20	6.28	17.2
Mode 4	Lateral X	8.08	8.24	2.0
Mode 5	Lateral Y	8.20	8.56	4.2
Mode 6	Vertical	10.83	11.42	5.2
Mode 7	Lateral Y	13.74	16.18	15.1

In a second phase, a frequency correlation function is used. The variable parameter is the modal damping ratios. The numerical FRF is obtained by subjecting the numerical model to a signal with a uniform band limited spectrum. The damping ratios determined using the random decrement technique from the ambient vibration records have been first introduced in the numerical model to compute the initial numerical FRF curve. Then the FRF curve is normalized with respect to the experimental amplitude of the first peak related to the fundamental frequency. The updating procedure is carried out iteratively by adjusting the damping ratios to minimize the FRF error expressed by:

$$\varepsilon H_{ij} \frac{|(H_E)_{ij}-(H_N)_{ij}|}{|(H_E)_{ij}|} \times 100 \qquad (1)$$

Where:

$(H_E)_{ij}$: ith value of the measured FRF curve at point j

$(H_N)_{ij}$: ith value of the numerical FRF curve at point j

The closeness of the measured and numerically calculated FRF is assessed using the Frequency Domain Modal Assurance Criteria (FDAC) technique applied to the FRF as given by the following criterion:

$$FDAC(\omega_E, \omega_N, j) = \frac{\left(\{H_E(\omega_E)\}_j^T \{H_N(\omega_N)\}_j\right)^2}{\left(\{H_E(\omega_E)\}_j^T \{H_E(\omega_E)\}_j\right)\left(\{H_N(\omega_N)\}_j^T \{H_N(\omega_N)\}_j\right)} \qquad (2)$$

Where:

$\{H_E(\omega_E)\}_j$ is the measured FRF curve (column or vector) at point j

$\{H_N(\omega_N)\}_j$ is the calculated FRF curve (column or vector) at point j

ω_E and ω_N correspond to the frequencies at which the FRF amplitudes H_E and H_N are measured and calculated respectively.

Values of the FDAC vary between 0 and 1. When FDAC = 1, it means a perfect matching whereas 0 indicate no correlation at all. After few iterations on the FRF curve of point 2 along the N axis, the best fit is obtained for a damping value $\xi_1 =$ 1.0 % for the fundamental frequency at 1.88 Hz and $\xi_2 =$ 6.0 % for the second mode at 8.20 Hz. The FRF error corresponding to the best fit is εH_{ij} = 0.23 and the FDAC = 0.96. Fig. 8 shows the experimental and the matched numerical FRF curves.

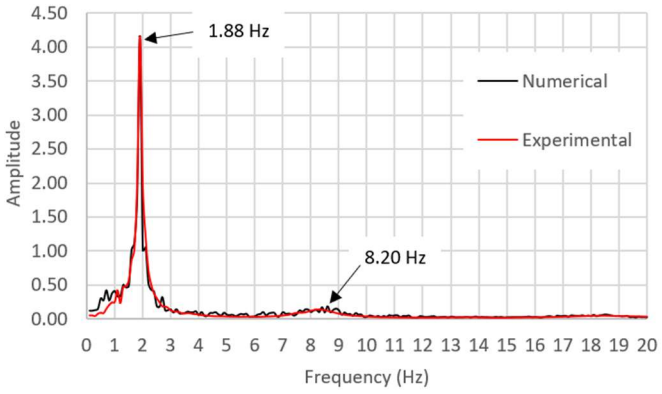

Fig. 8: Experimental and numerical (matched) FRF curve at point 2 along the N axis.

V. SEISMIC PERFORMANCE UNDER EARTHQUAKE GROUND MOTIONS

The seismicity of the region of M'sila, where the site of Kalaa Beni-Hammad is implemented (Maadid), is considered as moderate. It is classified as zone IIa by the Algerian seismic code RPA99v2003 [20]. The CRAAG database [12] reports five seismic events in the region of Msila in the period from1885 to 1965. The last three events of 1946, 1960 and 1965 have similar intensity of VIII and a magnitude of 5.5. The largest most recent earthquake of magnitude 5.2 occurred on 14-05-2010 in the region of Béni-Ilmane at about 70 km from the Kalaa Beni-Hammad site. An elastic spectrum for the site is derived in accordance with the RPA99v2003. This is used to adjust a set of real earthquake records and generate two artificial acceleration ground motions. A set of six acceleration time histories are defined and are used for linear dynamic analyses. The mean spectrum of all ground motions is plotted against the code elastic spectrum in Fig. 9.

Linear time history analyses are carried out to determine the

lateral drift and the most stressed zones in the structure. It is worth noting that the results from the linear analysis are limited to portray the stress distribution at an early elastic stage.

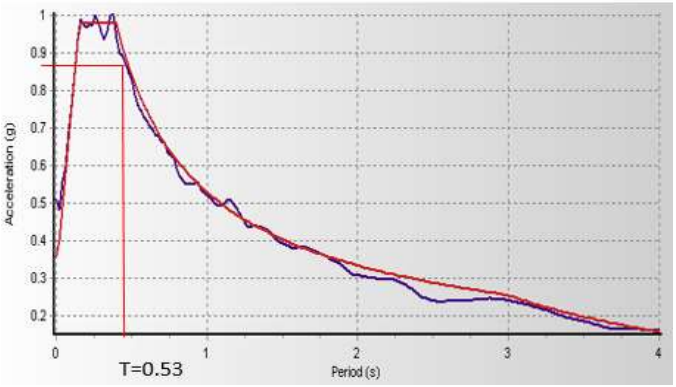

Fig. 9: Code elastic spectrum and mean spectrum of the normalized acceleration ground motions.

The maximum lateral drift at the top, which reaches 9.19 cm (Fig. 10), is very low compared to 1% of the height (25 cm). This is common for this very type of stiff structures with thick exterior walls and a massive masonry core.

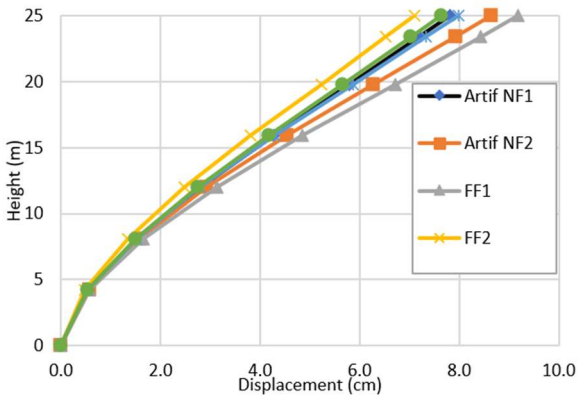

Fig. 10: Lateral drift caused by different acceleration ground motions.

The tensile overstressed zone outspread from the bottom to mid-height of the tower. The shear-overstressed zones, however, are mainly observed near lintels of some openings as shown in Fig. 11 and 12.

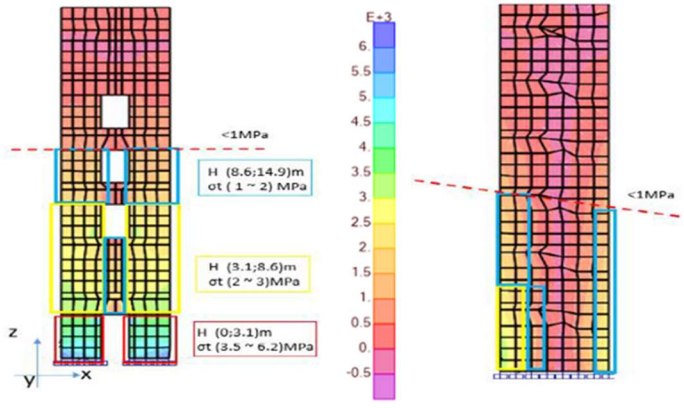

Fig. 11: Tensile stress distribution and locations of overstressed zones.

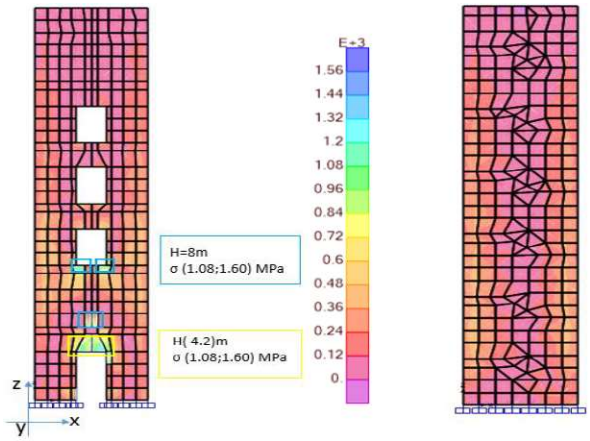

Fig. 12: Shear stress distribution and locations of overstressed zones.

VI. CONCEPTUAL RETROFITTING PROPOSAL

Any strengthening scheme ought to be based on thorough assessment of the edifice, which is out of the scope of the present research work. Nevertheless, a feasibility study of a strengthening solution is proposed. First, to relief the local shear overstressing in some locations of the lower openings, steel or reinforced concrete framing can be incrusted around the openings. This solution has not been developed in this article as the latter is investigating only the steel tie system.

In order to absorb the tensile stresses that would develop in several locations in the ruble stone masonry of the structure as shown above, a lightly post-tensioned steel tie system (Fig. 13) is proposed to bind horizontally and vertically the structure. This is done in such a way that any overstress that may happen in the masonry will be transferred passively to the steel rods. For the purpose of the present study, a simple model based on predefined failure mechanism is used to design the elements of the steel tie system. As shown on Fig. 14, the walls are supposed to be completely maintained by the steel rods and a spectrum analysis is used to determine the tensions in the rods. It has been found that a diameter of 22 mm for all the rods is sufficient to withstand the resulting tensions. Such a system was successfully employed to strengthen an ancient masonry building [8].

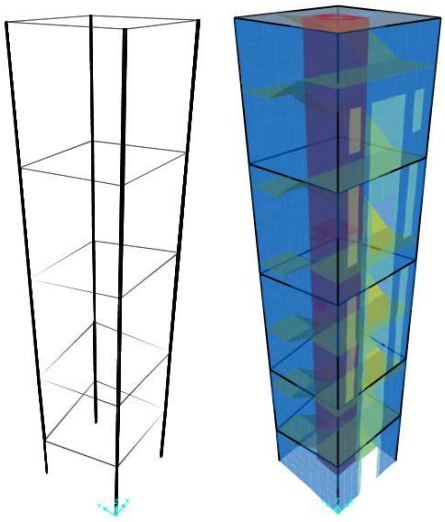

Fig. 13: Steel tie system position in the minaret model

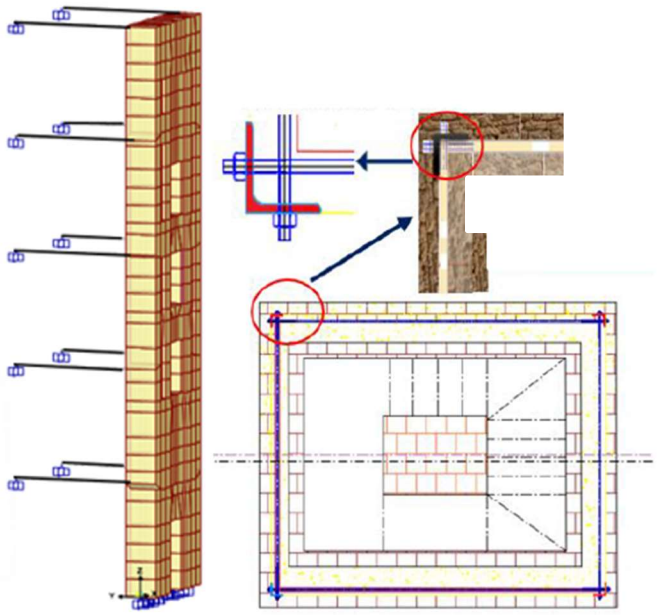

Fig. 14: Strengthening details of the steel tie elements

VII. CONCLUSION

The 24.7 m height minaret of the Kalaa Beni-Hammad is 1000 years old historic monument that has been investigated in this paper in order to assess its structural integrity. An ambient vibration survey has been carried out to update a FE model and identify the material characteristics. For this purpose, a two phases FRF matching procedure has been applied in which the closeness of the measured and numerically calculated FRF is assessed using the Frequency Domain Modal Assurance Criteria with varying modal damping ratios. The results show that the elastic modulus of the material lays within the range of Young's modulus of historic rubble stone masonry. The updated model is subjected to site spectrum compatible set of acceleration ground motions. Tensile and shear stresses concentration zones are identified and a post-tensioned steel tie system is proposed as a strengthening measure to absorb the tensile stresses that develop in several locations.

ACKNOWLEDGMENT

Research for this paper was conducted with partial MERS (Ministry of higher education in Algeria) support under Grant PRFU A01L02ES160220190001. It also benefited from ANTiNEA project, the bilateral cooperation research project between University Saad Dahlab (Blida, Algeria) and University Paris-Est Marne-la-Vallée, (France) with partial support of the IFA in Algeria.

REFERENCES

[1] Al Qal'a of BaniHammad (Kalaa Beni-Hammad), https://whc.unesco.org/en/list/102/, accessed 11/05/2021.

[2] A. Al-Sibahy and R. Edwards, "Structural evaluation for the historic Palace of King Ghazi and mechanism of its rehabilitation. *Case Studies in Construction Materials,*" Volume (13)2020, 10.1016/j.cscm.2020.e00371.

[3] F. Aras and G. Altay, "Investigation of mechanical properties of masonry in historic buildings," *GRAĐEVINAR* 67 (2015) 5, 461-46. 10.14256/JCE.1145.201.

[4] M. Barnaure and M. Cincu, "Testing methods for the assessment of material properties in historical masonry structures: a review," *2020 IOP Conf. Ser.: Mater. Sci. Eng.*789 012003, https://doi.org/10.1088/1757-899X/789/1/012003

[5] R. Bento, "An Interdisciplinary Approach to the Seismic Assessment of Built Cultural Heritage: Case Studies in Lisbon and Outskirts," *In: Aguilar R., Torrealva D., Moreira S., Pando M.A., Ramos L.F. (eds) Structural Analysis of Historical Constructions. RILEM Bookseries,* vol 18. Springer, Cham. 10.1007/978-3-319-99441-3_1.

[6] N. Bourahla, F. Bouriche, M. Benredouane and M. Ould-Amara, "Structural Assessment by Modal Analysis: Case Study of the New Algiers Airport", *in B.H.V. Topping, Z. Bittnar, (Editors), Proc. of the Sixth International Conference on Computational Structures Technology,* Civil-Comp Press, Stirlingshire, UK, Paper 53, 2002. Doi:10.4203/ccp.75.53

[7] N. Bourahla, A. Si-Chaib, Y. Basta, F. Z. Sahraoui and H. Djabali, "Calibration of a reference numerical model of an embankment dam using ambient vibration testing and genetic algorithm". *In French, Proceedings of 10th AFPS Colloquium*, Strasbourg, France 2019.

[8] N. Bourahla, S. Tafraout and N. Allal, "Seismic strengthening of old masonry building using steel ties system – case study", *Proc. of the 8th colloquium AFPS 11*, Paris, France, 2011.

[9] D. D'Ayala and S. Paganoni, "Seismic Strengthening Strategies for Heritage Structures," *In: Beer M., Kougioumtzoglou I.A., Patelli E., Au SK. (eds) Encyclopedia of Earthquake Engineering.* Springer, Berlin, Heidelberg. 0.1007/978-3-642-35344-4_199

[10] L. De Beylie, "La Kalaa des Béni Hammad. Une capitale Berbère de l'Afrique du Nord du XI siècle (Qal'a BeniHammad, A Berber capital of North Africa in the XI century)", Ernest Leroux, Paris, 1909

[11] S. Fais, G. Casula, F. Cuccuru et al., "An innovative methodology for the non-destructive diagnosis of architectural elements of ancient historical buildings," *Sci Rep* 8, 4334 (2018). 10.1038/s41598-018-22601-5

[12] A. Harbi, A. Peresan and G. F. Panza, "Seismicity of Eastern Algeria: A revised and extended earthquake catalogue," *Nat Hazards* (2010) 54:725–747. 10.1007/s11069-009-9497-6

[13] D. E. Hudson, W. O. Keightley and N. N. Nielson, A new method for the measurement of natural periods of buildings, Bulletin of the Seismological Society of America. Vol. 54, No. 1, pp. 233-241, Feb. 1964.

[14] B. Jaishi and W. Ren, "Structural Finite Element Model Updating Using Ambient Vibration Test Results," Journal of Structural Engineering, 131 (2005) 4. doi.org/10.1061/(ASCE)0733-9445(2005)131:4(617)

[15] A. Manzo and C. Chesi, "Building Techniques and Structural Damage of Historical Constructions Detected Through the Point Cloud Survey," *In: Aguilar R., Torrealva D., Moreira S., Pando M.A., Ramos L.F. (eds) Structural Analysis of Historical Constructions. RILEM Book series,* vol 18. Springer, Cham. 10.1007/978-3-319-99441-3_13

[16] O. Onat and B. Yön, "Adopted Material Properties of Historical Masonry Structures for Finite Element Models: Mosques and Bridges," *Turkish Journal of Science & Technology*, Volume 13(1), 69-75, 2018.

[17] S. Petrovčič, and V. Kilar, "Design Considerations for Retrofitting of Historic Masonry *Structures with Externally Bonded FRP Systems," International Journal of Architectural Heritage, 10.1080/15583058.2020.1853278*

[18] *F. Pinho, V. Lúcio, "Rubble stone masonry walls in portugal: material properties, carbonation depth and mechanical characterization," International Journal of Architectural Heritage, 11:5, 685-702, DOI: 10.1080/15583058.2017.1289424*

[19] *J. Radnić, D. Matešan, and A. Abaza, "Restoration and Strengthening of Historical Buildings: The Example of Minceta Fortress in Dubrovnik," Advances in Civil Engineering, vol. 2020, Article ID 8854397, 17 pages, 2020. 10.1155/2020/8854397*

[20] *Algerian Seismic Regulations RPA99* version 2003 – DTR BC 2.48, Earthquake engineering national research centre (CGS), Algiers, 2004.

[21] A. Si-Chaib, N. Bourahla and M. K. Abidi, "As built modal characteristics identification of an RCC gravity dam using ambient vibration testing," *Second European Conference on Earthquake and Seismology Engineering*, Istanbul, Turkey, 2014.

[22] J. Snoj, M. Österreicher and M. Dolšek, "The importance of ambient and forced vibration measurements for the results of seismic performance assessment of buildings obtained by using a simplified non-linear procedure: case study of an old masonry building", *Bull Earthquake Eng 11, 2105–2132 (2013)*. doi.org/10.1007/s10518-013-9494-8

[23] M. M. Sorour, G. A. Parsekian, D. Duchesne, J. Paquette, A. Mufti, L. Jaeger and N. G. Shrive, "Evaluation of Young's Modulus for stone masonry walls under compression," *Proc. 11th Canadian Masonry Symposium,* Toronto, Ontario, May 31- June 3, 2009.

[24] M. Ta, J. Lardies and B. Marc, "Natural frequencies and modal damping ratios identification of civil structures from ambient vibration data", *Shock and Vibration 13 (2006) 429–444, doi.org/10.1155/2006/625927*

[25] M. Wathelet, GEOPSY geophysical Signal Database for Noise Array Processing, Software, LGIT, 2005, Grenoble, France.

Nouredine Bourahla is a professor of structural dynamics and earthquake engineering, LGSD laboratory, Civil Engineering Department at Ecole Nationale Polytechnique, Algiers, Algeria.

Zakaria Assameur is a graduate Engineer, Civil Engineering Department at University Saad Dahlab, Blida, Algeria.

Mohamed Abed is a professor in civil engineering, LGMGC laboratory, Civil Engineering Department, at University Saad Dahlab, Blida Algeria.

Ahmed Mébarki is a professor in civil engineering, natural and technological risks and resilience at University Gustave Eiffel, UPEC, CNRS, Laboratory Modelling and Multi Scale Simulation (MSME 8208 UMR), Marne-la-Vallée, France.

A Differential Pressure Technique for Void Fraction Measurement in Gas-Liquid Flow

Ammar ZEGHLOUL, Abdelwahid AZZI, Nabil GHENDOUR, and Abdallah S. BERROUK

Abstract− Two-phase Gas-liquid flows have many industrial uses, such as hydrocarbon transportation and energy production. The knowledge and an accurate determination of the gas phase's proportion rate in the two-phase mixture known as the gas void fraction is necessary for optimal and secure sizing of the installations where this kind of flow takes place. This paper focuses on the possibility of using a cost-effective differential pressure transmitter to measure the void fraction parameter. It is obtained using a mathematical model derived from the energy balance equation and the measured pressure drop from the vertical upward gas-liquid flow. Results on flow void fraction obtained through the use of the conductance probe method, are used to validate those derived from the pressure drop that is evaluated by employing the differential pressure transmitter. The measurement accuracy of the void fraction measured using the pressure drop technique, is found to be principally affected by the flow pattern. Moreover, the slip ratio between the phases was the primary factor influencing the void fraction measurement by the differential pressure technique.

***Keywords*− Two-phase flow, Void fraction, Flow pattern, Differential pressure, Transmitter.**

NOMENCLATURE

D	Diameter of the pipe, m
f	Single-phase friction factor
g	Acceleration of gravity, m/s^2
h	Pressure tapping vertical distance, m
P	Pressure at the taping, Pa
Re	Reynolds numbers
S	Slip ratio
U_m	Mixture velocity, m/s
U_G	Gas velocity, m/s
U_{GS}	Gas superficial velocity, m/s
U_L	Liquid velocity, m/s
U_{LS}	Liquid superficial velocity, m/s
x	Mass flow quality
ε_G	Gas void fraction
ΔP	Pressure drop, Pa
ρ_L	Liquid density, kg/m^3
ρ_G	Gas density, kg/m^3
ρ_{TP}	Two-phase mixture density, kg/m^3
G	Gas
L	liquid
m	mixture
TP	two-phase flow

Manuscript received October 4, 2021; revised December 26, 2021.

A. Zeghloul is with the University of Sciences and Technology Houari Boumediene and the Ecole Nationale Polytechnique, Algiers, Algeria. (e-mail: ammar.zeghloul@g.enp.edu.dz)

A. Azzi is with the University of Sciences and Technology Houari Boumediene, Algiers, ALGERIA. (e-mail: azzi.1963@yahoo.fr)

N. GHENDOUR is with the University of Sciences and Technology Houari Boumediene, Algiers, ALGERIA (e-mail: ghendour.nabil@gmail.com)

A. S. BERROUK is with Khalifa University of Science and Technology, Abu Dhabi, United Arab Emirates. (e-mail: abdallah.berrouk@ku.ac.ae)

Digital Object Identifier (DOI): 10.53907/enpesj.v1i2.21.61

I. INTRODUCTION

In two-phase or three-phase flow hydrodynamics, the void fraction represents one of the most critical parameters. It gives information about the fraction of the gas in the pipe's total surface or volume. Moreover, the void fraction is a crucial parameter in predicting the interfacial section and the masse transfer between different phases [1].

Several invasive or non-invasive techniques have been proposed in the literature to predict the void fraction parameter. Among these techniques, one can cite the estimation of void fraction via the time-averaged two-phase pressure drop measurement. This technique is widely used because of its simplicity, high safety, low-cost, and for being non-intrusive. Additionally, the two-phase pressure acquisition signals can be used in two-phase flow pattern recognition [2][3].

Many works have been done in order to establish a correlation between the void fraction and the measured two-phase pressure drop. However, these correlations were not reliable for all flow patterns. In the earlier work, Wallis [4] correlates the liquid holdup ($1-\varepsilon_g$) as a function of Lockhart and Martinelli's parameter, which depends on the two-phase pressure drop. Tang and Heindel [5] proposed a new method to estimate the void fraction from the differential pressure measurement in bubble columns. The proposed method highlighted the pressure drop's influence due to friction on the void fraction measurement. Their experimental data analysis showed that the proposed method gives more accurate void fraction results than the model proposed by Wallis. As Gharat and Joshi [2] stated, the frictional two-phase pressure drop depends mainly on two factors. One of them depends on the shear stress between the liquid and the conduit wall, and the second is the friction between the liquid and the gas phases. On the other hand, the experimental work presented by Shafquet et al. [6] considered the frictional parameter negligible . In their study, the tested flow condition covered the bubbly flow pattern with the range of the void fraction [0.17 to 0.33]. They used Electrical Capacitance Tomography technique, ECT, as another technique to validate the void fraction predicted results. Abbas [7] performed a theoretical and experimental study for the bubbly flow regime, considering the value of the void fraction

less than 0.1748. They proposed a mathematical model derived from the two-phase pressure drop measurement to estimate the gas proportion. However, the experimental results showed that the proposed model is not suitable when the void fraction increases beyond 17.48%. Jia et al. [8] conducted an experimental study in vertical upward bubbly and slug flows. To obtain the void fraction, two-phase pressure drop measurement data were introduced into a mathematical model that was based on the energy conservation. The latter was compared to the ones obtained from Electrical Resistance Tomography, ERT, device and Wire Mesh Sensor, WMS. The experimental investigations showed that the frictional pressure drop could not be neglected mostly for a gas volume fraction less than 0.2. Kara et al. [9] performed a comparison of the void fraction values derived from the pressure drop experimental data and those by measuring the difference in the level between the two-phase mixture and the one of the static liquid in a bubble column. They found that both measurement technics matched well with an accuracy of 3%.

The present experimental study consists in investigating the derivation of the void fraction using differential pressure measurement. Moreover, the effect of the flow pattern on the void fraction measurement accuracy is discussed.

II. Theoretical Background

The mathematical correlation relying the void fraction and differential pressure measurement is based on Bernoulli's energy conservation principle. According to the diagram in Figure 1. One can write;

$$P_1 = P_2 + \rho_{TP} g\, h + \Delta P_{friction} \quad (1)$$

where P_1 and P_2 are the measured pressures at two selected positions along the pipe, ρ_{TP} is the two-phase density, g is the gravitational acceleration, h is the distance between the two measurement points and $\Delta P_{friction}$ the frictional pressure drop.

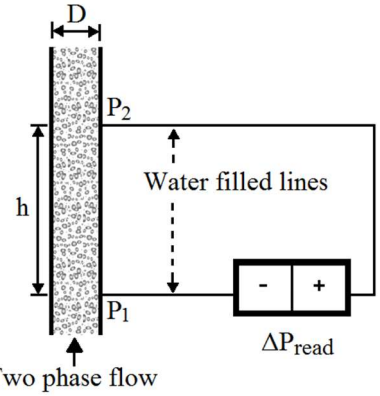

Fig. 1: Void fraction measurement

Measured pressure drop (read) between the two tappings, ΔP_{read}, can be expressed from the hydrodynamic balance as;

$$\Delta P_{read} = P_2 + \rho_L g\, h - P_1 \quad (2)$$

Eq. 1 and Eq. 2 lead to;

$$\Delta P_{read} + \Delta P_{friction} = g\, h\, (\rho_L - \rho_{TP}) \quad (3)$$

The two-phase density ρ_{TP} is expressed as follow:

$$\rho_{TP} = \varepsilon_G \rho_G + (1-\varepsilon_G)\, \rho_L \approx (1-\varepsilon_G)\, \rho_L \quad (4)$$

where ε_G is the void fraction.

Replace Eq. 4 into Eq. 3 and solving for void fraction ε_G reads:

$$\varepsilon_G = \frac{(\Delta P_{read} + \Delta P_{friction})}{(\rho_L - \rho_G) g\, h} \quad (5)$$

According to [7], the pressure drop due to friction is:

$$\Delta P_{friction} = \frac{2\, \rho_L\, h\, f\, U_m^2}{D} \quad (6)$$

Where U_m represents the mixture velocity, D is the internal pipe diameter, and *f* the single-phase friction factor, also known as the Fanning friction factor, which depends on flow conditions and the pipe wall roughness. In our experiment, the pipe material is Perspex, which can be considered a smooth surface.

The friction factor, *f*, can be obtained experimentally by employing the following expression [7];

$$f = \frac{\Delta P_L\, D}{2\, \rho_L\, h\, U_L^2} \quad (7)$$

Where ΔP_L is the measured liquid pressure drop, and U_L is the liquid velocity.

A different form of Fanning friction factor can be found in the literature, which depends on Reynolds numbers, Re. In the present work, the Reynolds numbers test conditions were ranged from 3500 to 30600. The corresponding Fanning friction factor *f* is expressed as;

$$f = 0.079\, Re^{-0.25} \quad (8)$$

III. Experimental Facility

The test facility performed to carried out measurements of the pressure drop and the void fraction simultaneously is presented in Figure 2. This test facility has been used earlier by Zeghloul et al.[10][11]. The test section, which is transparent for visual observation of the flow regime is positioned vertically. Its length is about 6m with an inner diameter of 34mm. A centrifugal pump (9), which can reach a maximal masse flow rate of 40 m^3/s, draws tap water from the tank (10) to the mixing section through calibrated water rotameters (4). A pressure regulator (2) was used to adjust the air supplied from a compressor (1) to the operating pressure before it passes through the air rotameters (5). Both air and water flow-meters have a maximum uncertainty of 2%. The two-phases are blended in the mixer (8) to create the air-water mixture. Further information on the mixer geometry is given in Zeghloul et al. [12], [13]. After the mixer, the gas and liquid phases flow through the test section then continues up to the separator (10). The liquid flowed down to the separator's bottom due to gravity, and the gas (air) flows into the ambient.

Two conductance probes have been installed in the vertical test section to provide the gas volume fraction, ε_G. The first conductance probe, CP1, was placed at 4760 mm (140D) downstream of the mixer, and the second probe, CP2, at a distance of 790 mm after the first probe. These two positions were chosen carefully to ensure enough distance to allow the flow to be fully developed Saidj et al. [14].

To increase the measurement accuracy, two selected differential pressure transmitters have been used to measure the difference in pressure between the two tappings. The latter has the exact locations as the two conductance probes CP1 et CP2. The two transmitters were provided from FOXBORO company with 0.2% accuracy corresponding to their full scale with ranges of [0-7.2] kPa and [0-36] kPa, respectively. Using an appropriate pressure calibrator (Fluke 725) with an error of 0.02%, the two transmitters were further re-calibrated.

Before starting the pressure measurements, it is necessary to ensure that the pressure sampling lines have a constant fluid density, i.e., the pressure lines contain only liquid without any air bubbles inside. Therefore, a purging arrangement has been used to evacuate air bubbles from the pressure sampling lines, as shown in Figure 3.

A data acquisition card (6092E) and the corresponding LabVIEW software from National Instruments Company, was used to acquire all the necessary data from the different experiments. 200 Hz was the sampling frequency of the data acquisition for a duration of 60 seconds for each test, i.e., total data samples of 12000 for each run.

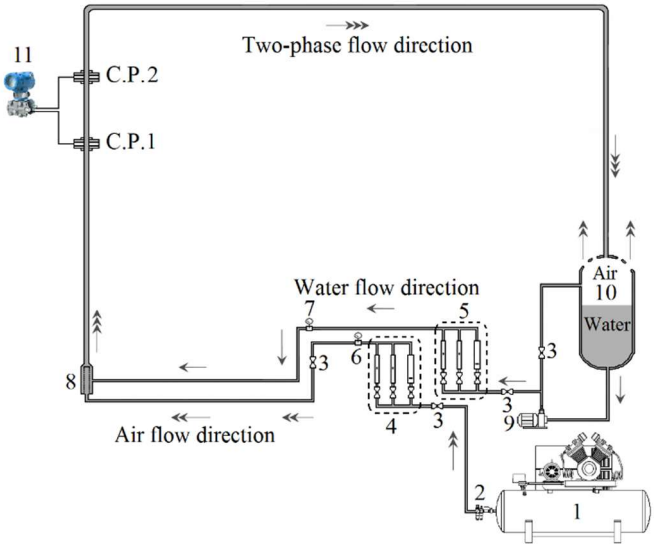

1: Compressor, 2: regulator, 3: Valve, 4: Air Flow-meters, 5: Water flow-meters, 6: Manometer, 7: Thermometer, 8: Mixer, 9: Pump, 10: Tank/Separator, 11: Differential pressure transmitter, CP1-CP2: Conductance probes

Fig. 1: Test facility.

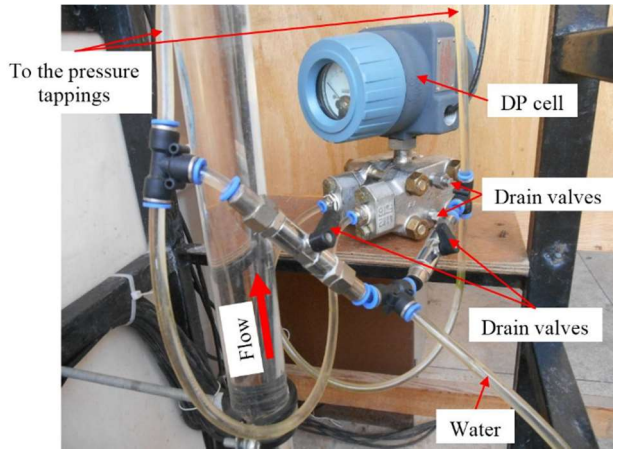

Fig. 2: Purging system arrangement [15].

IV. Experimental Results

A. Flow Pattern Map

The test experimental conditions of the gas and liquid superficial velocities varied from 0 to 3.5 ms^{-1} and from 0.1 to 0.92 ms^{-1}, respectively, which cover a wide flow pattern range from bubbly to churn flows. The two-phase flow configuration was first visually observed through the Plexiglas pipes near the pressure tapings. At these locations, the flow regime is considered to be entirely developed. These flow observations were confirmed by analyzing the signature shape of the Probability Density Function (PDF) and the temporal variation of the acquired gas volume fraction signals (Bouyahiaoui et al. [16], Costigan and Whalley[17]).

The test experimental conditions of the gas and liquid superficial velocities varied from 0 to 3.5 ms^{-1} and from 0.1 to 0.92 ms^{-1}, respectively, which cover a wide flow pattern range from bubbly to churn flows. The two-phase flow configuration was first visually observed through the Plexiglas pipes near the pressure tapings. At these locations, the flow regime is considered to be entirely developed. These flow observations were confirmed by analyzing the signature shape of the Probability Density Function (PDF) and the temporal variation of the acquired gas volume fraction signals (Bouyahiaoui et al. [16], Costigan and Whalley[17]).

From Figure 4, A total number of 121 experimental test conditions were plotted over the flow pattern map of Shoham [18]. From this figure, one can note that the slug flow test conditions have taken a large area in Shoham's map. Furthermore, the transition line between the bubbly and the slug flow shows a good prediction of the experimental test conditions. However, the slug/churn line transition poorly predicts the experimental data. This overprediction may be due to the difference in the experimental conditions used in predicting the slug/churn line transition.

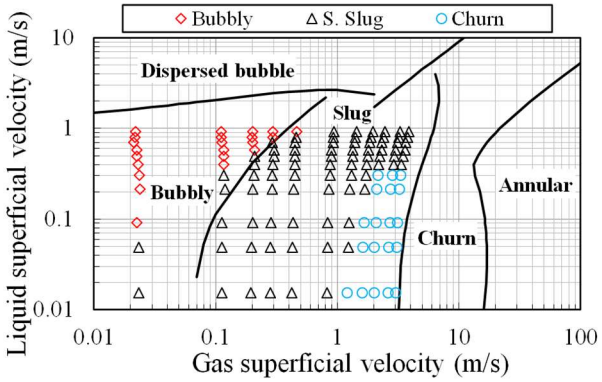

Fig. 3: Shoham's flow pattern map [18] including the experimental test conditions studied in the present work.

B. Void Fraction Temporal Variation

Figure 5 illustrates example plots of the void fraction temporal variation obtained from the two conductance probes (CP1 and CP2). Three different velocities combination of liquid and gas has been chosen to exhibit the various flow patterns studied in this work. It can be observed from the void fraction temporal variation that the two conductance probe signals are very close to each other, which confirms that the flow pattern is thoroughly

developed [14]. Figure 5 (a) shows the typical void fraction signal of bubbly flow. The latter is often characterized by stable fluctuations with some small peaks that indicate both agglomerated and dispersed bubbles. The mean void fraction of the corresponding bubbly flow is about 0.19. Figure 5 (b) depicts the slug flow void fraction temporal variation that was represented by an alternative value of the void fraction. The void fraction values of the threshold corresponding to the passage of Taylor bubbles, and the low void fraction values representing the liquid plug, which contain tiny bubbles. The mean void fraction value of the corresponding slug flow is found to be 0.45. Figure 5 (c) represents a typical void fraction temporal variation of the churn flow. This flow pattern signals and appearance show a chaotic behavior with a mean void fraction of 0.81.

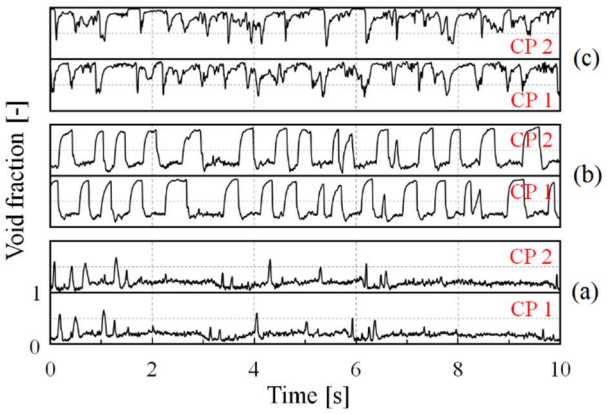

Figure 4: Temporal variation of the void fraction, (a), bubbly flow [Uls=0.80 m.s^{-1}, Ugs=0.10 m.s^{-1}], (b), slug flow [Uls=0.40 m.s^{-1}, Ugs=0.43 m.s^{-1}], (c), churn flow [Uls=0.21 m.s^{-1}, Ugs=3.01 m.s^{-1}],

C. Single and Two-Phase Flow Pressure Drop

The measured two-phase gas-liquid pressure drop, ΔP_{read}, from the differential pressure transmitter was fed into the equation (2) to obtain the total pressure difference (P_1 - P_2). Figure 6 represents the gas-liquid total pressure drop variation depending on the gas superficial velocity by keeping the liquid superficial velocity constant. From this figure, one can see for a particular gas superficial velocity that the gas-liquid total pressure drop increases with the liquid superficial velocity's augmentation. Furthermore, and by keeping the liquid superficial velocity constant, the two-phase total pressure drop decreases with the increase of the gas superficial velocity.

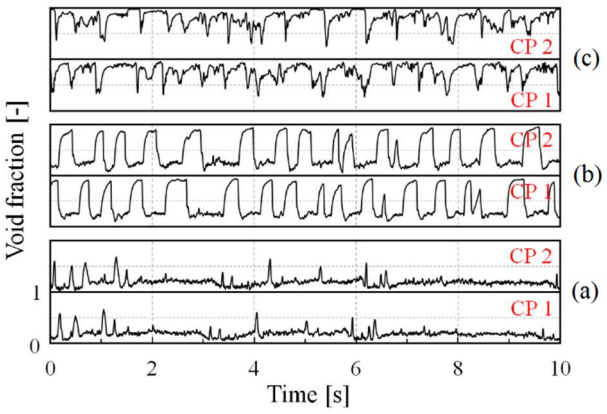

Figure 5: Temporal variation of the void fraction, (a), bubbly flow [Uls=0.80 m.s^{-1}, Ugs=0.10 m.s^{-1}], (b), slug flow [Uls=0.40 m.s^{-1}, Ugs=0.43 m.s^{-1}], (c), churn flow [Uls=0.21 m.s^{-1}, Ugs=3.01 m.s^{-1}].

This finding can be clarified by the expansion of the gas in the gas-liquid flow due to gas superficial velocity increasing, which required less energy for the gas-liquid mixture to flow inside the pipe [14][19]. Besides the effect of the gas and liquid velocities, the way that the gas-liquid total pressure drop evolves in each flow pattern is not the same; the latter is very important for the bubbly flow and less when passing to the slug flow. The gas-liquid total pressure drop is nearly constant for the churn flow.

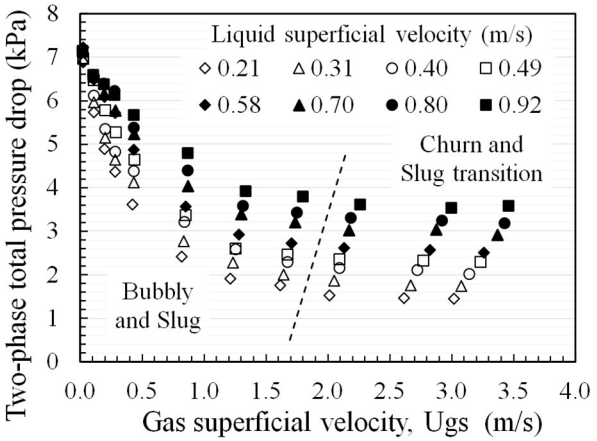

Figure 6: Total gas-liquid differential pressure vs. gas superficial velocity.

Figure 7 represents the calculated two-phase frictional pressure drop for different velocity combinations of the gas and the liquid. The corresponding data of the frictional pressure drop was derived from equation (3). From this figure and by maintaining a liquid superficial velocity constant, one can remark that the two-phase frictional pressure drop increases with the increase of the gas superficial velocity. The same behavior of the frictional pressure drop was noticed for a constant gas and variable liquid velocity. Besides the gas and liquid velocities' impact, the flow pattern was also found to affect the frictional two-phase pressure drop. The latter can be noticed from the different slopes of the frictional pressure drop, which characterizing each liquid superficial velocity. The sharpest slope was found in the churn flow. This may be caused by the turbulent effect of this kind of chaotic flow pattern, which enhances friction between phases and between the gas-liquid mixture and the pipe inside wall.

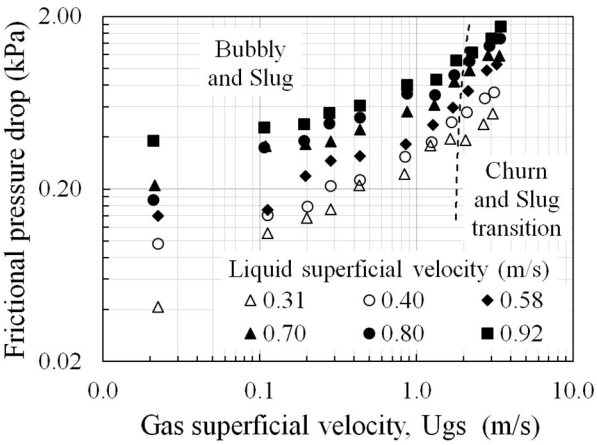

Figure 7: Gas-liquid frictional pressure drop vs. gas superficial velocity.

The measured single-phase (liquid) pressure drop was injected into equation (7) to find the experimental friction factor, *f*.

The actual friction factor data and those calculated from Fanning correlation (Eq. (8)) and the experimental data of Abbas [7] are represented in Figure 8. From this figure, one can notice a good fit of the actual data to the experimental data of Abbas and fanning correlation for the conditions of liquid superficial velocity, Uls, over 0.4 ms^{-1}. For Uls, less than 0.4 ms^{-1}, we found some difference between the represented data with a relatively good approach between the actual data and the Fanning correlation. This may be due to the accuracy of the differential pressure device when it is used in the low gas and liquid velocity conditions.

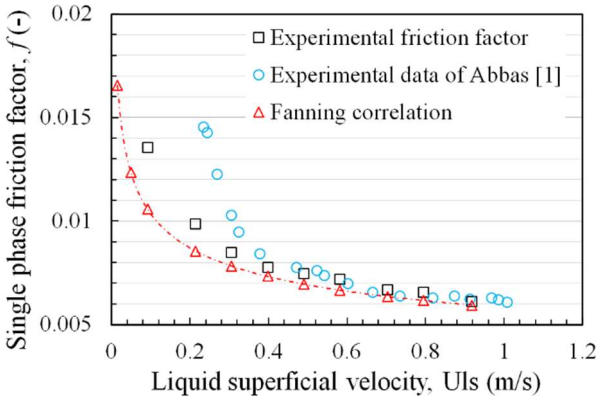

Fig. 8: Friction factor variation with water superficial velocity.

Figure 9 shows the variation of the measured gas-liquid pressure drop with the mean void fraction obtained from the conductance probes. One can see that the experimental data present a linear curve with a negligible effect of the various flow regimes. This finding confirms the linear relationship expressed in equation (5) between the measured two-phase pressure drop and the void fraction. In addition, the experimental data of the two-phase pressure drop increase with the increase of the void fraction. The latter can be obtained by increasing the gas's mass flow rate, i.e., the total two-phase flow rate, which induces in augmentation of both void fraction and the gas-liquid measured pressure drop.

D. Calculated vs. Experimental Void Fraction

Figure 10 exhibit the comparison between the calculated void fraction from the differential pressure transmitter (predicted void fraction) and the measured data using conductance probes.

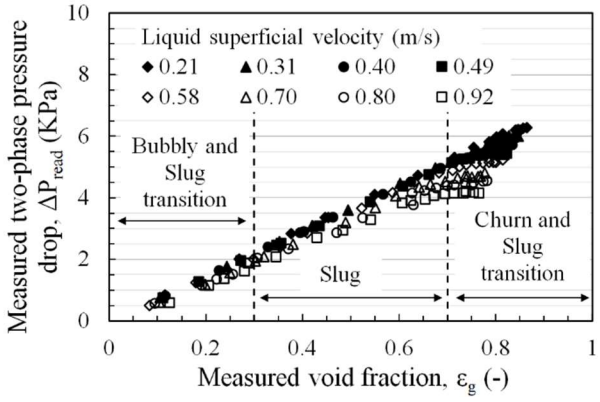

Figure 9: Experimental gas-liquid pressure drop vs. void fraction.

It can be inferred from Figure 9 that, for $\varepsilon_g < 0.30$, the void fraction predicted from differential pressure measurement agrees well with the measured one. For $\varepsilon_g > 0.30$, the deviation from the diagonal line increases with the void fraction. The deviation can reach 30% as the flow pattern approaches the slug/churn transition, which corresponding to the void fraction of about 0.7.

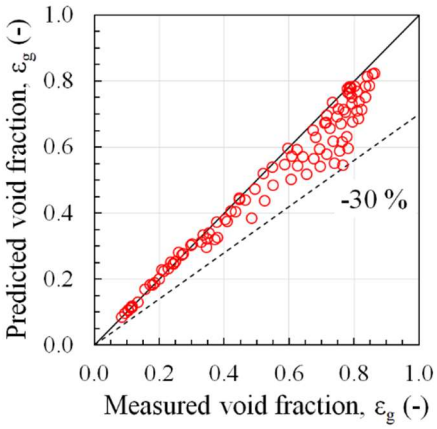

Figure 10: Comparison between Measured and predicted void fraction.

To quantify the deviation between the calculated void fraction from the gas-liquid pressure drop measurement and the measured void fraction from the conductance probes, two statistical parameters have been used. The first parameter is the root mean square deviation, RMS, and the second one is the mean relative absolute error, ABE, expressed in equations (9) to (11).

$$RMS=\sqrt{\frac{1}{n}\sum_{i=0}^{n}\left[\frac{\varepsilon_{g_{i,calculated}}-\varepsilon_{g_{i,measured}}}{\varepsilon_{g_{i,measured}}}\right]^2} \quad (9)$$

$$x_i=\frac{\left|\varepsilon_{g_{i,calculated}}-\varepsilon_{g_{i,measured}}\right|}{\varepsilon_{g_{i,measured}}} \quad (10)$$

$$ABE=\frac{1}{n}\sum_{i=0}^{n}x_i \quad (11)$$

where $\varepsilon_{g_{i,calculated}}$ is the predicted void fraction from the two-phase pressure measurement and $\varepsilon_{g_{i,measured}}$ is the measured void fraction from the conductance probes.

Table I, summarizes the two statistical parameters RMS and ABE obtained from the 121 experimental tests. From this table, one can see that the most accurate predicted data of the void fraction are those of the bubbly flow with an RMS and ABE of 3.63% and 2.57%, respectively. As expected from figure 8, The RMS and ABE increase considerably when passing from the bubbly to the slug flow with an RMS and ABE of 10.75% and 8.55%, respectively, which are three times less accurate compared to the bubbly flow. For the churn flow, the results show the most deviated results with an RMS and ABE of 12.01% and 9.39%, respectively.

Table. I
RMS AND ABE (%) OF VOID FRACTION FOR DIFFERENT FLOW REGIMES

	RMS	ABE
Bubbly	3.63%	2.57%
Slug	10.75%	8.55%
Churn	12.01%	9.39%

E. Slip Ratio and Flow Pattern Effects

Figure 11 illustrates the impact of the flow pattern on the relative difference between the calculated and the experimental void fraction. Equally, in order to exhibit the slippage between the phases, the slip ratio has been added in the second axes. The latter can be calculated using the following expression.

$$S = \frac{U_G}{U_L} = \frac{U_{GS}(1-\varepsilon_G)}{U_{LS}\,\varepsilon_G} \qquad (12)$$

From this figure, the impact of the flow pattern is evident. For the bubbly flow ($\varepsilon_g < 0.30$), the slip ratio between phases is around the unity indicating that the flow can be considered as homogeneous. The slip ratio increases beyond the unity when passing from bubbly to slug and considerably increases when reaching churn flow. A similar behavior of the slip ratio has been noticed for the relative difference error. The relation between these two parameters can be explained by the slip ratio's effect between the phases, which increases the frictional pressure drop between gas and liquid phases, i.e., the total frictional pressure drop [7]. The latter was not taken in the void fraction prediction, which in turn increases the error between the predicted and the measured void fraction.

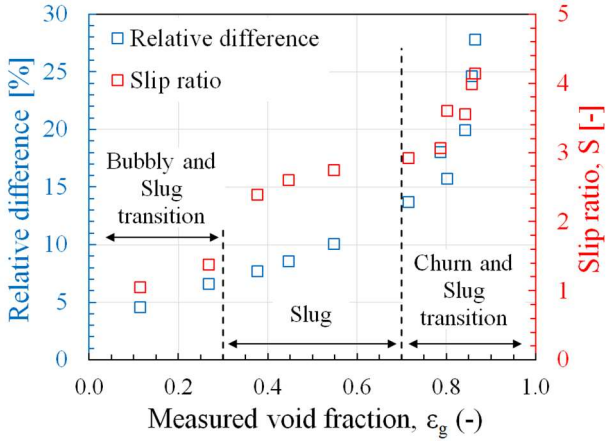

Figure 11: Impact of the two-phase flow pattern and slip ratio on void fraction predictions.

V. CONCLUSION

A differential pressure in a vertical ascending single and two-phase flow has been measured. From the obtained pressure drop results, the void fraction was predicted from a model derived from energy conservation. The calculated void fraction data were compared to those measured experimentally from the conductance probe sensor. To evaluate the accuracy of the predicted void fraction from the energy conservation model, the statistical parameters RMS and ABE have been used.

The analysis of the two statistical parameter results showed that the bubbly flow pattern exhibits the most accurate results with RMS and ABE of 3.63% and 2.57%, respectively. For the slug and the churn flow, ε_g>0.3, the deviation between the theoretical and the experimental void fraction increases significantly. The results also showed that the frictional pressure drop between gas and liquid phases significantly affected the void fraction prediction accuracy. The latter cannot be neglected when the slip ratio between phases is beyond unity.

REFERENCES

[1] Y. T. Shah, B. G. Kelkar, S. P. Godbole, and W. D. Deckwer, "Design parameters estimations for bubble column reactors," AIChE J., vol. 28, no. 3, pp. 353–379, 1982, doi: 10.1002/aic.690280302.

[2] K. C. Ruthiya et al., "Detecting regime transitions in slurry bubble columns using pressure time series," AIChE J., vol. 51, no. 7, pp. 1951–1965, 2005, doi: 10.1002/aic.10474.

[3] G. Matsui, "Identification of flow regimes in vertical gas-liquid two-phase flow using differential pressure fluctuations," Int. J. Multiph. Flow, vol. 10, no. 6, pp. 711–719, 1984, doi: 10.1016/0301-9322(84)90007-7.

[4] G. B. Wallis, One-dimensional two-phase flow. New York, 1969.

[5] C. Tang and T. J. Heindel, "Estimating gas holdup via pressure difference measurements in a cocurrent bubble column," Int. J. Multiph. Flow, vol. 32, no. 7, pp. 850–863, 2006, doi: 10.1016/j.ijmultiphaseflow.2006.02.008.

[6] A. Shafquet, I. Ismail, and M. N. Karsiti, "Study of void fraction measurement in a two phase flow by using differential pressure and Electrical Capacitance Tomography," in AMS2010: Asia Modelling Symposium 2010 - 4th International Conference on Mathematical Modelling and Computer Simulation, 2010, pp. 408–413, doi: 10.1109/AMS.2010.87.

[7] A. H. A. M. Hasan, "Measurement of a void fraction in bubbly gas-water two phase flows using differential pressure technique," Appl. Mech. Mater., vol. 152–154, pp. 1221–1226, 2012, doi: 10.4028/www.scientific.net/AMM.152-154.1221.

[8] J. Jia, A. Babatunde, and M. Wang, "This is a repository copy of Void Fraction Measurement of Gas-Liquid Two-Phase Flow from Differential Pressure. Void Fraction Measurement of Gas-Liquid Two-Phase Flow from Differential Pressure," Flow Meas. Instrum., vol. 41, pp. 75–80, 2015, doi: 10.1016/j.flowmeasinst.2014.10.010.

[9] S. Kara, B. G. Kelkar, Y. T. Shah, and N. L. Carr, "Hydrodynamics and Axial Mixing in a Three-phase Bubble Column," Ind. Eng. Chem. Process Des. Dev., vol. 21, no. 4, pp. 584–594, 1982.

[10] A. Zeghloul, H. Bouyahiaoui, A. Azzi, A. H. Hasan, and A. Al-sarkhi, "Experimental Investigation of the Vertical Upward Single- and Two-Phase Flow Pressure Drops Through Gate and Ball Valves," J. Fluids Eng., vol. 142, no. February, pp. 1–14, 2020, doi: 10.1115/1.4044833.

[11] A. Zeghloul, A. Messilem, N. Ghendour, A. Al-sarkhi, A. Azzi, and A. Hasan, "Theoretical study and experimental measurement of the gas liquid two-phase flow through a vertical Venturi meter," Proc IMechE Part C J Mech. Eng. Sci., vol. 0, no. 0, pp. 1–18, 2020, doi: 10.1177/0954406220947118.

[12] A. Zeghloul, A. Azzi, F. Saidj, A. Messilem, and B. J. Azzopardi, "Pressure Drop Through Orifices for Single- and Two-Phase Vertically Upward Flow - Implication for Metering," J. Fluids Eng. Trans. ASME, vol. 139, no. 3, pp. 1–12, 2017, doi: 10.1115/1.4034758.

[13] A. Zeghloul, A. Azzi, A. Hasan, and B. J. Azzopardi, "Behavior and pressure drop of an upwardly two-phase flow through multi-hole orifices," Proc. Inst. Mech. Eng. Part C J. Mech. Eng. Sci., vol. 232, no. 18, pp. 3281–3299, 2018, doi: 10.1177/0954406217736081.

[14] F. Saidj, A. Hasan, H. Bouyahiaoui, A. Zeghloul, and A. Azzi, "Experimental study of the characteristics of an upward two-phase slug flow in a vertical pipe," Prog. Nucl. Energy, vol. 108, no. June, pp. 428–437, 2018, doi: 10.1016/j.pnucene.2018.07.001.

[15] A. Messilem, A. Azzi, A. Zeghloul, F. Saidj, H. Bouyahiaoui, and A. Al-sarkhi, "Single- and two-phase pressure drop through vertical Venturis," Proc. Inst. Mech. Eng. Part C J. Mech. Eng. Sci., vol. 0, no. 0, pp. 1–11, 2020, doi: 10.1177/0954406220906424.

[16] H. Bouyahiaoui, A. Azzi, A. Zeghloul, A. H. Hasan, A. Al-Sarkhi, and M. Parsi, "Vertical upward and downward churn flow: Similarities and differences," J. Nat. Gas Sci. Eng., vol. 73, pp. 1–14, 2020, doi: 10.1016/j.jngse.2019.103080.

[17] G. Costigan and P. B. Whalley, "Slug flow regime identification from dynamic void fraction measurements in vertical air-water flows," Int. J. Multiph. Flow, vol. 23, no. 2, pp. 263–282, 1997, doi: 10.1016/s0301-9322(96)00050-x.

[18] O. Shoham, Mechanistic Modelling of Gas–Liquid Two-Phase Flow in Pipes. USA, 2006.

[19] B. J. Azzopardi, H. K. Do, A. Azzi, and V. Hernandez Perez, "Characteristics of air/water slug flow in an intermediate diameter pipe," Exp. Therm. Fluid Sci., vol. 60, pp. 1–8, 2015, doi: 10.1016/j.expthermflusci.2014.08.004.

Ammar ZEGHLOUL received the Ph.D. degree in Mechanical Engineering Energy Mechanics option, from University of Sciences and Technology Houari Boumediene (USTHB), Algiers. Algeria. in 2016. He is currently a lecturer at the Department of preparatory cycle, Ecole Nationale Polytechnique (ENP) in Algiers, Algeria. and member of Laboratory of multiphase Transport and Porous Media, LTPMP-USTHB. His main research interests are in multiphase flow assurance which applications in oil and gas industry.

Abdelwahid Azzi is Professor and Director of research at the University of Sciences and Technology Houari Boumedien, Algiers (USTHB). He carried a large part of his Ph.D. thesis at the Technical University of Hamburg Harburg (TUHH), Germany. After the accomplishment of his PhD, he was appointed at the same university (TUHH) for conducting researches on the sudden depressurization of two-phase foaming flow from a chemical reactor. Then he re-joined the USTHB University where he led for several years the Two-phase flow group in the Multiphase Flow and Porous Media Laboratory Flow and Porous Media Laboratory LTPMP (USTHB). During more than 30 years of research he was involved in several research activities most of them linked to multiphase flow. These activities find application in oil and gas production/transportation, design and safety process of chemical plants, wastewater treatment, thermal hydraulic plants and solar energy.

Nabil GHENDOUR received his M.Sc. degree in aeronautic engineering from the Institute of Aeronautics and Space Studies, Blida, Algeria, in 2015. He is currently pursuing the Ph.D. degree in mechanical engineering at the University of Sciences and Technology Houari Boumedien (USTHB), Algiers, Algeria. His research topics includes conductive sensing, sensor modeling and multiphase flow. He involved in several research works linked to multiphase flow measurement.

Abdallah Sofiane Berrouk was awarded a Ph.D. degree from The University of Manchester (UK) in the area of Computational Fluid Dynamics (CFD) and turbulence modelling. Before joining the Petroleum Institute in Abu Dhabi (PI) in October 2008, he worked as Senior Research/Teaching Associate at City University of Hong Kong. He has twelve years of university lecturing experience. He taught different courses in different departments both at the undergraduate and graduate levels.